Technical Physics, Vol. 46, No. 8, 2001, pp. 1001–1008. Translated from Zhurnal Tekhnicheskoĭ Fiziki, Vol. 71, No. 8, 2001, pp. 72–79.

OPTICS, QUANTUM ELECTRONICS

Cooperation of Traveling and Quasi-Cutoff Waves in a Cyclotron-Resonance Maser

V. L. Bratman, N. G. Kolganov, A. V. Savilov, S. V. Samsonov, and A. É. Fedotov

Institute of Applied Physics, Russian Academy of Sciences, Nizhni Novgorod, 603600 Russia

Received September 13, 2000

Abstract—A new version of a cyclotron-resonance maser is studied theoretically and experimentally. Here, a spatially periodic helical electron beam couples traveling (autoresonance) and quasi-cutoff (gyrotron) waves of the same frequency, interacting with them at different cyclotron harmonics. The theory and early experimental results show that this maser can effectively generate a traveling wave with low quasi-cutoff wave excitation losses using a very simple feedback system. *© 2001 MAIK "Nauka/Interperiodica".*

INTRODUCTION

It is well known [1–5] that, among cyclotron-resonance masers (CRMs) operating with relativistic particles, a cyclotron-autoresonance maser (CARM) is one of the most attractive designs. In this device, electrons, following helical trajectories in a magnetic field, generate a copropagating traveling wave whose frequency, as in free-electron lasers, may significantly exceed the frequency of electronic oscillation (in this case, the cyclotron frequency) due to the Doppler effect. Therefore, CARMs can use weaker magnetic fields than gyrotrons—another popular CRM version in which electrons interact with a standing wave (quasi-critical waveguide mode) at the cyclotron frequency or at its harmonic. Another advantage of the CARM is the partial mutual compensation of off-resonance conditions due to changes in the electron energy and the electron translational velocity (the autoresonance effect [6, 7]). This allows electrons to be in resonance with the wave for a long time. Theoretically [1, 2], if the beam quality is high, a high efficiency can be reached due to this compensation. However, CARM efficiency is still low [8–14], and it has not yet gained acceptance as wide as the gyrotron. The low efficiency is attributed to the high sensitivity of the device to the electron velocity spread and to spurious gyrotropic oscillations, which, as a rule, suppress the interaction with the autoresonance waves.

A CARM with an efficiency as high as 26%, which is close to the theoretical value for a perfect electron beam, has been implemented only once [15]. Later, it has been found [16] that, in that experiment, along with the traveling (autoresonance) wave, being in resonance with the electrons at the fundamental cyclotron harmonic, the quasi-cutoff (gyrotron) wave was excited at the same frequency but for the second cyclotron harmonic. It is remarkable that the gyrotron wave did not suppress the generation of the autoresonance wave; instead, it favored this process. Note that such an interpretation of the experiment [15] was not evident because the gyrotron wave was confined within the cavity and the autoresonance wave alone was observed at the exit. Nevertheless, the masing frequency and to a great extent the high efficiency were likely to be determined just by the gyrotron wave. We emphasize that such an interaction (cooperation) of the waves is only possible for an equiphase electron beam, where the electrons gyrate with nearly the same phases unlike beams in weakly relativistic gyrotrons. Appropriate calculations [16] have shown that the cooperation of the modes offers a number of attractive features that may significantly simplify the feedback and improve the efficiency. In this paper, we theorize about the cogeneration of the autoresonance and gyrotron waves and report experiments on the implementation of a CARM gyrotron—a device based on this principle.

INTERPRETATION OF EXPERIMENT [15]

To produce a dense electron beam in the experiment [15], we employed an explosive emission diode gun placed in a strong magnetic field (Fig. 1). The whole diode current was 3–5 kA. A cylindrical anodic particle selector was used to separate out the most rectilinear central portion of the beam, where the particle current and energy were 100 A and 500 keV. Then, the beam was set swinging (acquired the transverse velocity component) in the transverse nonadiabatic magnetic field of a kicker—a current-carrying coil inclined to the system's axis of symmetry. The kicker generated a magnetic field having both longitudinal and the transverse components. The electron beam swung and the traveling TE_{11} wave interacted in the cavity under the conditions of fundamental cyclotron resonance:

$$\omega \approx h v_{\parallel} + \omega_B. \quad (1)$$

Here, ω and h are the frequency and the longitudinal wave number of the TE_{11} wave, and $v_{\parallel}$, $\omega_B = eB/mc\gamma$, and $\gamma = 1/\sqrt{1-(v/c)^2}$ are the longitudinal velocity,

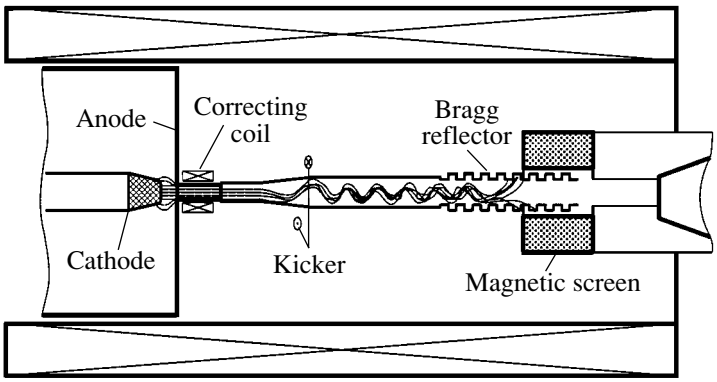

Fig. 1. Experimental high-efficiency CARM [14].

cyclotron frequency, and Lorentz factor of the electrons. The cavity had the form of a circular waveguide with the below-cutoff taper at its cathodic end and the Bragg reflector at the collector end. Due to this improved beam-forming system, which provides a small particle velocity spread, the high (up to 26%) efficiency was achieved in [15]. However, some experimental results have not been convincingly explained. In particular, when the efficiency was the highest, the masing frequency was outside the reflection band of the Bragg reflector. This casted strong doubt upon the feasibility of feedback for the operating wave, although the structure of the output radiation closely followed that of the TE_{11} wave. It was assumed [15] that the masing frequency and the cold cavity frequency diverge because of a change in the Bragg reflector frequency in the presence of a high-current electron beam. This explanation, however, has not been confirmed by detailed calculations.

Another explanation of the fact that the masing frequency goes beyond the reflection band of the Bragg reflector, while the transverse structure of the output radiation remains unchanged, has been suggested in [16]. This explanation relied on the experimental result that the maser frequency was close to the cutoff frequency of the TE_{21} wave, for which the cyclotron resonance condition at the second harmonic was satisfied (Fig. 2):

$$\omega \approx 2\omega_B. \tag{2}$$

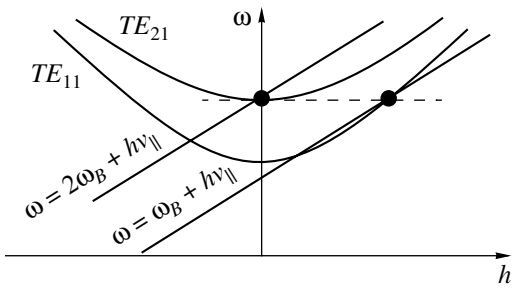

Fig. 2. Dispersion diagram for the simultaneous interaction of electrons resonating with traveling TE_{11} wave at the fundamental cyclotron frequency and with standing TE_{21} wave at the second cyclotron harmonic.

Thus, the electron beam could, in principle, interact at the same frequency both with the traveling TE_{11} wave under the autoresonance conditions and with the quasi-cutoff TE_{21} wave under the gyrotron conditions at the second cyclotron harmonic. Less trivial is the assumption [16] that the two waves were generated simultaneously because this interaction is only possible when the electrons of the beam gyrate in phase. This assumption, however, is consistent with the technique used to form the electron beam: the kicker was placed inside the cavity and the electrons did start interacting with the rf field having no time to change the phase. This was validated by directly measuring the phase spread of the particles, as described below. Once the possibility of the simultaneous excitation of the autoresonance and gyrotron waves has been understood, other aspects of the experiment and the role of each of the waves become clear. A composite oscillation comprising both partial resonance waves (TE_{11} and TE_{21}) was presumably excited in the cavity. The TE_{21} wave was not radiated from the cavity because the inner diameter of the corrugation in the Bragg reflector was smaller than the cutoff diameter of the waveguide for this wave. As a result, the transverse structure of the output radiation was like that of the TE_{11} wave, while the TE_{21} wave, providing efficient feedback, was absorbed by the cavity walls and scattered by the electron beam into the TE_{11} wave of the same frequency. The scattering was efficient because the electrons gyrated in phase, making the beam spatially periodic. The spatial periodicity coupled the waves with the different spatial field structures. The TE_{11} wave extracted the RF power from the cavity almost reflectionlessly.

It should be noted that the situation when the electrons are in double resonance with the traveling operating wave and with the quasi-cutoff (or counterpropagating) spurious wave at the same frequency but at differ-

ent harmonics is common in CARMs. In fact, CARMs often use the operating conditions under which the dispersion characteristics of the beam and the wave almost coincide ("touch" one another). Since the cyclotron resonance band under these conditions is sufficiently wide, it seems very likely that conditions for synchronism with another mode at a higher cyclotron harmonic will be satisfied for one of the frequencies within this band. Also note that the effect of spurious synchronism with the counterpropagating wave in a CRM where the operating wave is copropagating has also been studied in [17] for another situation, namely, for the waves weakly coupled by a nonequiphase electron beam (in which the electrons are uniformly distributed in initial gyration phase).

The conditions under which an equiphase electron beam interacts simultaneously with the autoresonance wave and with the gyrotron wave may significantly increase the efficiency. In this case, the gyrotron wave provides initial beam bunching and feedback. Then, the resulting signal is amplified in the electron beam–traveling wave system. The electrodynamic system of a CARM gyrotron may have the form of a usual gyrotron cavity—a tapered waveguide. At its cathodic end, the waveguide is evanescently tapered for the gyrotron wave, and, at the collector end, it is tapered so that the autoresonance wave can freely leave the cavity (Fig. 3).

The new design has much in common with a dual-section multimode CRM [18]. In the first section of this device, the quasi-cutoff wave is excited at the frequency ω_1. In the next section, this wave is transformed into the traveling wave with the multiple frequency $\omega_2 = n\omega_1$. According to [18], the theoretical efficiency of such a system that is based on Doppler multiplication of frequency is no more than 10% even for a perfect electron beam. A similarity also exists between the CARM gyrotron and the new version of a gyro-TWT [19, 20]. In the latter, the standing and the traveling waves are coupled not by a helical electron beam, but through a helical corrugation on the wall of the operating waveguide.

COUPLING BETWEEN THE TRAVELING AND STANDING WAVES BY AN EQUIPHASE ELECTRON BEAM

Let the electrons simultaneously interact with the traveling TE_{11} wave of frequency ω at the fundamental cyclotron resonance frequency and with the standing (quasi-cutoff) TE_{21} wave of the same frequency at the second cyclotron harmonic (Fig. 2). The waves may efficiently couple through an equiphase electron beam in which all particles possess the same initial cyclotron phase φ_0. This condition holds, for example, for a thin paraxial beam (all its electrons encircle the waveguide axis) produced by swinging a rectilinear beam with a kicker. The shape of such a beam is close to a helix that is traced by an electron in the magnetic field. The beam

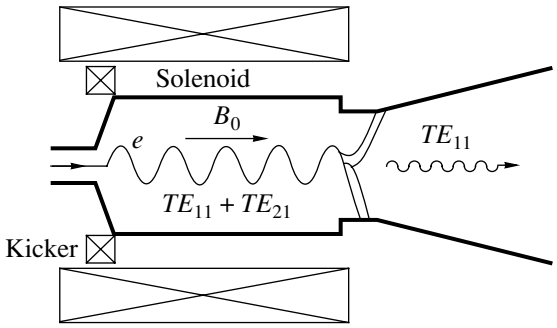

Fig. 3. Simplest oscillator operating with coexcited traveling and standing waves (CARM gyrotron).

exhibits a longitudinal periodicity (the period equals the Larmor pitch of an electron) and an azimuthal periodicity. Because of this, when resonance conditions (1) and (2) hold, waves with different longitudinal wave numbers and different azimuthal indices couple even in the linear approximation. Coupling between the two waves due to an equiphase electron beam (and the absence of such coupling in the linear regime for a mixed-phase beam) becomes clearer if we consider electron bunches created by either wave. Specifically, the quasi-cutoff wave synchronized with the second cyclotron harmonic tends to bunch the particles of the mixed-phase paraxial beam into two straight lines parallel to the magnetic field and located oppositely on the Larmor cylinder. The traveling wave synchronized with the fundamental cyclotron harmonic confines such a beam into a helix with the pitch $L_w = 2\pi/h$ on the surface of the same Larmor cylinder (Fig. 4a). Since the limit shapes of the electron bunches in these two cases are significantly different, the waves do not couple by the mixed-phase beam. In contrast, in the case of the equiphase paraxial beam, the electron bunches represent a periodic set of points that are cut from the respective bunches of the mixed-phase helical beam by the helical trajectory of an electron (Fig. 4b). When the resonance frequencies (1) and (2) of these two waves are equal, the electron bunches created by them in the equiphase beam have the same shape. As a result, the bunches created by one of these waves efficiently excite the other, which is indicative of efficient coupling.

Formally, this effect also follows from the fact that the initial phases of the electrons relative to both waves are equal. In fact, the phase of an electron relative to the traveling wave is $\Theta_1 = \omega t - hz - \varphi$, while the phase relative to the standing wave is $\Theta_2 = \omega t - 2\varphi$. Here, z is the longitudinal coordinate, t is time, and φ is the azimuthal angle. For a perfectly thin beam ($\varphi_0 = 0$), the initial phases of the electrons relative to both waves are equal: $\Theta_1(0) = \Theta_2(0) = \omega t_0$, where t_0 is the time instant when an electron enters the interaction space. If resonance conditions (1) and (2) are satisfied simultaneously, the particle phases with respect to both waves will remain approximately equal even as the particle moves through

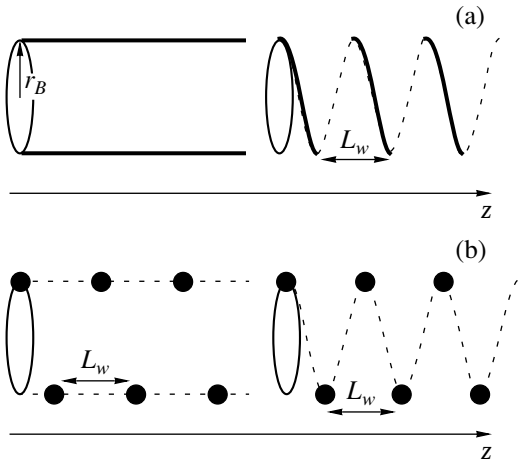

Fig. 4. Shape of electron bunches that are created in the paraxial beam by the gyrotron wave at the second cyclotron harmonic (on the left) and by the autoresonance wave at the fundamental cyclotron harmonic (on the right): (a) beam with mixed initial phases and (b) equiphase beam.

the interaction space. Thus, the electron bunch that excites one of the waves will also excite the other, coupling them together. The coupling weakens as the spread in the initial phases of the cyclotron gyration of the electrons increases and becomes loose for a randomly mixed hollow paraxial beam.

SIMULATION OF CARM GYROTRON

The electron–wave interaction can be described in terms of equations that are a simple generalization of the well-known CRM equations averaged over rapid cyclotron gyration [3]. To this end, it is convenient to represent the electron Lorentzian factor as $\gamma = \gamma_0(1 + w_1 + w_2)$, where w_1 and w_2 describe the energy exchange between an electron and a traveling (autoresonance) wave at the fundamental cyclotron frequency and between an electron and a standing (gyrotron) wave at the second harmonic, respectively. We have

$$\frac{dw_1}{d\zeta} = -\kappa_1 \mathrm{Im}(a_1 e^{i\Theta_1}),$$
$$\frac{dw_2}{d\zeta} = -\kappa_2 \sin(\pi\zeta/\hat{L})\mathrm{Im}(a_2 e^{i\Theta_2}). \quad (3)$$

Here, $\zeta = kz$ is the normalized longitudinal coordinate, $k = \omega/c$, $a_{1,2}$ are the normalized amplitudes of the waves, $\kappa_1 = p_\perp/2p_z$ and $\kappa_2 = p_\perp^2/2p_z$ are the electron–wave coupling coefficients, $p_{\perp,z} = \gamma v_{\perp,\parallel}/\gamma_0 c$ are the normalized components of the electron momentum, and $\hat{L}$ is the normalized length of the cavity. The longitudinal structure of the gyrotron wave is assumed to be sinusoidal. The longitudinal particle momentum is changed only by the traveling wave and is related to the particle energy through the well-known relationship [6, 7]

$$p_z = -\beta_{z_0} = w_1/\beta_{ph}. \quad (4)$$

Here, $\beta_{ph} = k/h$ and $\beta_{z_0} = v_{\parallel 0}/c$ are, respectively, the phase velocity of the traveling wave and the initial longitudinal velocity of the electrons, both being normalized by the velocity of light. The equations for the electron phases relative to both waves have the form

$$\frac{d\Theta_1}{d\zeta} = \frac{-\delta_1 - (1-\beta_{ph}^{-2})w_1 - w_2}{p_z} - F,$$
$$\frac{d\Theta_2}{d\zeta} = \frac{-\delta_2 - w_1 - w_2}{p_z} - 2F. \quad (5)$$

Here, $\delta_1 = 1 - \beta_{z_0}/\beta_{ph} - \omega_{B_0}/\omega$ and $\delta_2 = 1 - 2\omega_{B_0}/\omega$ quantify the off-synchronism conditions between the electrons and both waves, ω_{B_0} is the initial cyclotron frequency of the electrons, and the quantity

$$F = \chi_1 \mathrm{Re}(a_1 e^{i\Theta_1}) + \chi_2 \sin(\pi\zeta/\hat{L})\mathrm{Re}(a_2 e^{i\Theta_2}) + eB_z/mc\gamma_0\omega p_z$$

on the left sides of Eqs. (5) is responsible for so-called "force" electron bunching. Also, $\chi_1 = (1/\beta_z - 1/\beta_{ph})/2p_z$, $\chi_2 = 1/2\beta_z$, and β_z is the total longitudinal magnetic field of the two waves. The initial conditions for Eqs. (5) are

$$\Theta_1(0) = \omega t_0 - \varphi_0, \quad \Theta_2(0) = \omega t_0 - 2\varphi_0, \quad (6)$$

where the initial cyclotron phases φ_0 of the electrons are distributed uniformly in the interval $0 \le \varphi_0 \le \Delta\varphi_0$ ($\Delta\varphi_0 = 0$ for a perfect equiphase beam and $\Delta\varphi_0 = 2\pi$ for a mixed-phase beam).

The slow-varying amplitude of the gyrotron wave interacting with the electron beam is described by the equation

$$\frac{da_2}{d\tau} + \frac{a_2}{2Q_2} = i\frac{G_2}{\hat{L}}\int_0^{\hat{L}} \sin(\pi\zeta/\hat{L})\langle \chi_2 e^{-i\Theta_2}\rangle_{t_0,\varphi_0} d\zeta, \quad (7)$$

where $\tau = \omega t$, Q_2 is the Q factor of the wave, and angle brackets mean averaging over the initial parameters t_0 and φ_0.

For the traveling wave, reflection from the cavity ends is absent and its excitation is described by the steady-state equation

$$\frac{da_1}{d\zeta} = iG_1\langle \chi_1 e^{-i\Theta_1}\rangle_{t_0,\varphi_0} \quad (8)$$

with the zero amplitude at the entrance to the cavity:

$$a_1(\zeta = 0) = 0. \quad (9)$$

In Eqs. (7) and (8),

$$G_1 = \frac{2I\beta_{ph}(1-\beta_{ph}^{-2})}{I_A N_1 \gamma_0}, \quad G_2 = \frac{8I}{I_A N_2 \gamma_0}$$

are the wave excitation factors, I is the beam current, $I_A = mc^3/e$, and $N_{1,2}$ are the wave norms.

The partial efficiencies of interaction of the electron beam with the traveling and the quasi-cutoff waves are defined by the expressions

$$\eta_{1,2}(\tau) = \frac{-\langle w_{1,2}(\tau)\rangle_{t_0,\varphi_0}}{1-\gamma_0^{-1}}.$$

In calculations, we considered a CARM gyrotron with a perfectly phased paraxial electron beam. The device operated at the TE_{11} and TE_{21} modes of the cylindrical gyrotron cavity (Fig. 3). According to the calculations, at sufficiently high initial transverse electron velocities, $\beta_{\perp_0} = v_{\perp_0}/c = 0.60$–$0.65$, the electron-to-traveling wave energy transfer efficiency of the device may be as high as 40–60% in a wide range of parameters (beam current, initial energy and pitch factor of the electrons, and Q factor of the gyrotron wave). Figure 5 shows the efficiency of an oscillator with a particle energy of 500 keV, a current of 50 A, and a cavity Q factor of 3000 (which is equal to its ohmic Q) versus magnetic induction with the transverse particle velocity taken as a parameter. The electron-to-gyrotron wave energy transfer efficiency is less than 1%. When the cavity Q factor decreases, the electron energy transferred to the gyrotron wave grows but remains much smaller than the energy gained by the traveling wave.

The spread in the initial cyclotron phases of the particles decreases the efficiency of the CARM gyrotron (Fig. 6). Nevertheless, if the particle phases are mixed only slightly ($\Delta\varphi_0 < \pi/2$), the device is weakly sensitive to the initial phase spread. A further increase in the beam width decreases the energy given up by the electrons to the traveling wave and increases the energy given up to the gyrotron wave.

The efficiency of a CRM using standing and traveling waves may thus be significantly higher than that of a conventional cyclotron autoresonance maser operating as an oscillator. One reason is that a CARM gyrotron has a better longitudinal structure of the RF field of the traveling wave. It is similar to the field structure in a CRM-based traveling wave amplifier (gyro-TWT). Another reason for the high efficiency of a CARM gyrotron is its capability of maintaining synchronism between the electrons and the traveling wave for a long time due to the interaction with the standing wave. Consider the variation of the electron phase relative to the traveling wave under the simplifying assumption that inertial bunching prevails:

$$\frac{d\Theta_1}{d\zeta} \approx \frac{-\delta_1 - \nu_1 w_1 - \nu_2 w_2}{p_z}. \qquad (10)$$

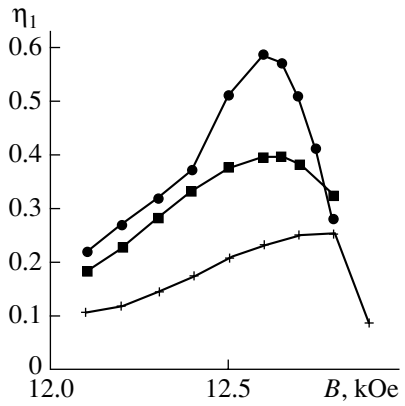

Fig. 5. Efficiency of the CARM gyrotron versus magnetic field at $\beta_\perp$ = (+) 0.57, (■) 0.60, and (●) 0.63.

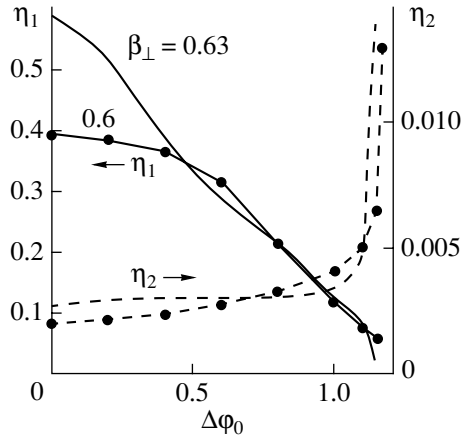

Fig. 6. Efficiency of the CARM gyrotron versus spread in the initial cyclotron phases of beam particles.

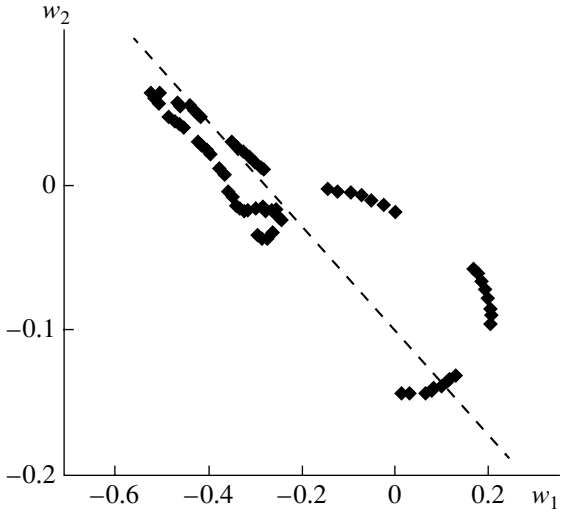

Fig. 7. Distribution of the particles over changes in their energy that are caused by the traveling and the quasi-cutoff waves at the exit from the interaction space.

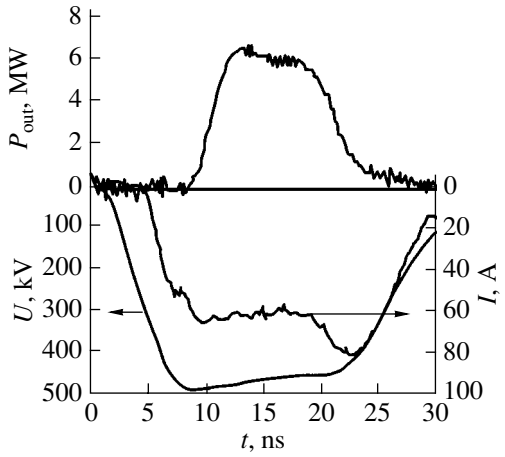

Fig. 8. Current, voltage, and output power pulses of the CARM gyrotron.

In this case, the term F, responsible for force bunching in the first equation in (5), can be neglected. Here, $\nu_i = 1 - \beta_{ph}^{-2}$ and $\nu_2 = 1$ are the coefficients of inertial bunching, which take into account the energy exchange between the electrons and the autoresonance and gyrotron waves, respectively. Since the phase velocity β_{ph} of the autoresonance wave is close to the velocity of light, $\nu_1 \ll \nu_2$. Thus, having gained a small amount of energy Δw_2 from the gyrotron wave, the electron may radiate a significantly greater amount of energy $\Delta w_1 = -\Delta w_2 \nu_2/\nu_1$ into the traveling wave, remaining in synchronism with it. This effect is illustrated in Fig. 7, which shows the distribution of the electrons over changes in their energies w_1 and w_2 at the exit from the interaction space. It can be seen that the majority of the particles are near the dashed line $\nu_1 w_1 + \nu_2 w_2 = \text{const}$.

EXPERIMENTAL STUDY OF A CRM OSCILLATOR WITH SIMULTANEOUSLY EXCITED AUTORESONANCE AND GYROTRON WAVES

Experiments with the CARM gyrotron were conducted in a Sinus-6 accelerator equipped with a diode-type explosive emission gun. The accelerator generated an ≈20-ns electron beam with a current of 3–8 kA and a particle energy of 300–600 keV. The experimental setup was similar to that used in the above experiment with the high-electron-efficiency CARM [15]. However, the parameters of the electron beam and of the electromagnetic system in these two experiments somewhat differed. As in [14], reasonable current and particle velocity spread were provided by cutting the most rectilinear portion of the beam created by the diode gun (Fig. 1) with the 1.5-mm-diam. aperture in the anode. After passing through the aperture, the rectilinear electron beam was set swinging in the transverse magnetic field of the kicker. The swung beam entered the cavity—a circular waveguide with evanescent taping at its cathodic end. At the collector end, the waveguide either expanded or tapered so that the quasi-cutoff TE_{21} wave alone was confined.

The first set of new experiments used a 460-keV 60-A electron beam. The cavity diameter and length were 7.7 and 60 mm, respectively (the cutoff frequency for the TE_{21} wave was 37.8 GHz). At the collector end, the cavity was bounded by a circular waveguide 7.1 mm in diameter (its cutoff frequency for the TE_{21} wave was 41 GHz). The reflection of the traveling TE_{11} wave at the exit from the cavity was negligible; at the same time, the Q factor of the TE_{21} gyrotron wave was very high. Maser radiation at 40 ± 1 GHz with the transverse structure similar to that of the TE_{11} wave was obtained in the experiment. A maximal power of 6 MW and an efficiency of 22% (Fig. 8) were obtained at a longitudinal magnetic field of 11.0 to 11.3 kOe and at a pitch factor $\beta_\perp/\beta_\parallel$ of about 1. The difference between the masing frequency and the cutoff frequency of the TE_{21} wave in the cavity can be associated with the excitation of the gyrotron TE_{21} wave with a high longitudinal index.

The second set of experiments used a 400-keV 50-A electron beam. To be sure that the simultaneous excitation of the autoresonance and gyrotron waves takes place, i.e., that the TE_{21} wave is present, we compared masing with open and closed resonators of the same diameter (8.1 mm; the cutoff frequency of the TE_{21} wave was 36.0 GHz) and length (90 mm). The open resonator expanded at the exit; the closed one tapered so that the first longitudinal TE_{21} mode alone was confined. The length of electron–wave interaction could be varied by moving the magnetic screen (a thick copper ring shielding the pulsed field of the solenoid), which directed the electron beam onto the waveguide wall.

The device mased at 36.0 ± 0.5 GHz with either resonator. The CARM gyrotron with the closed resonator and the 5.5-cm-long interaction length featured a 3.5-MW output power, which corresponded to a 17% efficiency. The transverse structure of the output radiation was similar to that of the TE_{11} wave. The CARM gyrotron with the open resonator was studied for interaction lengths of 9, 7, and 5.5 cm. In compliance with the masing mechanism elaborated in this work, the major portion of the power was emitted from the open cavity by the TE_{11} wave but the TE_{21} wave was also observed at the same frequency under certain conditions. The highest power radiated through the TE_{11} wave was 4 MW, which corresponded to a 20% efficiency, was achieved at the smallest interaction length (5.5 cm). A further decrease in the interaction length was impossible in the design under study. For electron–RF field interaction lengths of 7 and 9 cm, the output power was 3.1 and 1.3 MW, respectively. When the magnetic field was varied to optimize the pitch factor (Fig. 9), the maximum masing power was observed at 11.2 kOe, which corresponded to the optimal off-syn-

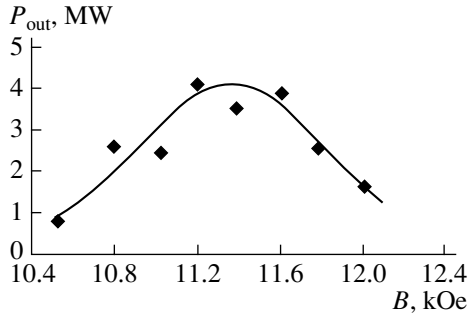

Fig. 9. Output power of the CARM gyrotron versus magnetic field for the 5.5-cm interaction length.

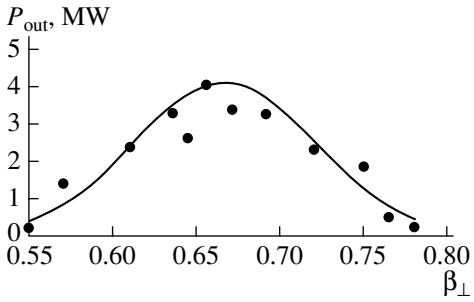

Fig. 10. Output power of the CARM gyrotron versus transverse electron velocity at an interaction length of 5.5 cm and a magnetic field of 11.2 kOe.

chronism conditions between the electrons and the traveling wave. At a transverse electron velocity of 0.65 c, which corresponded to the maximal efficiency (Fig. 10), the pattern of the output radiation was in good agreement with that of the TE_{11} wave. As the transverse particle velocity increased with the masing frequency remaining unchanged, the portion of the power that was extracted with the TE_{21} mode grew. At a transverse velocity of 0.75 c, the radiation pattern corresponded to the TE_{21} wave with a minor portion of the TE_{11} wave because the latter fell out of resonance with the electron beam.

An important evidence in favor of the mechanism of wave cogeneration considered is the experimental result obtained when the cyclotron gyration phases of the electron beam were mixed at the entrance to the cavity. The phase spread was achieved by increasing the kicker–cavity distance to 7 cm. After traveling this distance, the electrons acquired a velocity spread and thus became uniformly mixed over cyclotron gyration phases. As a result, the beam entering the cavity was not equiphase. In this case, no generation of the TE_{11} wave was observed.

CONCLUSION

The simultaneous interaction of a thin equiphase electron beam with the traveling (autoresonance) wave at the fundamental cyclotron resonance frequency and with the standing (gyrotron) wave at the same frequency but at the second harmonic allows the implementation of a new high-efficiency CARM gyrotron. Its efficiency (up to 60% theoretically and 20–25% obtained in the early experiments) is much higher than that of a single-mode CARM. In the new oscillator, the gyrotron wave provides feedback and forms electron bunches; the resulting signal is efficiently converted into the autoresonance wave, amplified, and extracted from the interaction space in a convenient form. This configuration may employ very simple gyrotron-type cavities instead of complicated Bragg cavities.

The idea reported in this work has recently been extended further [21, 22]: an oscillator based on a combination of a gyro-BWT and a gyro-TWT has been implemented. It uses a counterpropagating wave instead of the gyrotron wave and can be tuned in a wide frequency band. Its efficiency exceeds that of a usual gyro-BWT.

It should be noted that wave coupling by an electron beam is likely to be used not only in CRMs, but also in free-electron lasers [23]. The latter use forced, rather than free, oscillations of electrons in a spatially periodic magnetic field; therefore, the electron beam is always equiphase.

ACKNOWLEDGMENTS

This work was supported by the Russian Foundation for Basic Research (grant nos. 98-02-17068 and 99-02-16361).

REFERENCES

1. M. I. Petelin, Izv. Vyssh. Uchebn. Zaved., Radiofiz. **16**, 902 (1974).
2. V. L. Bratman, N. S. Ginzburg, and M. I. Petelin, Opt. Commun. **30**, 409 (1979).
3. V. L. Bratman, N. S. Ginzburg, G. S. Nusinovich, *et al.*, in *High-Frequency Relativistic Electronics* (Inst. Prikl. Fiz. Akad. Nauk SSSR, Gorki, 1979), Vol. 1, pp. 157–216.
4. V. L. Bratman, G. G. Denisov, N. S. Ginzburg, *et al.*, IEEE J. Quantum Electron. **19**, 282 (1983).
5. J. L. Vomvoridis, J. Electron. **53**, 555 (1982).
6. A. A. Kolomenskiĭ and A. N. Lebedev, Dokl. Akad. Nauk SSSR **145**, 1259 (1962) [Sov. Phys. Dokl. **7**, 745 (1963)]; Zh. Éksp. Teor. Fiz. **44**, 261 (1963) [Sov. Phys. JETP **17**, 179 (1963)].
7. V. Ya. Davydovskiĭ, Zh. Éksp. Teor. Fiz. **43**, 886 (1962) [Sov. Phys. JETP **16**, 629 (1963)].
8. I. E. Botvinnik, V. L. Bratman, A. B. Volkov, *et al.*, Pis'ma Zh. Éksp. Teor. Fiz. **35**, 418 (1982) [JETP Lett. **35**, 516 (1982)].
9. V. A. Bogachenkov, V. L. Bratman, G. G. Denisov, *et al.*, Kratk. Soobshch. Fiz., No. 6, 38 (1983).
10. G. Bekefi, A. DiRienzo, C. Leibovitch, *et al.*, Appl. Phys. Lett. **54**, 1302 (1989).

11. A. W. Fliflet, R. B. McCowan, C. A. Sullivan, *et al.*, Nucl. Instrum. Methods Phys. Res. A **285**, 233 (1989).
12. M. Caplan, B. Kulke, G. A. Westenskov, *et al.*, in *Induction-Linac-driven, Millimeter-ware CARM Oscillator* (Lawrence Livermore National Laboratory, Livermore, 1990), pp. 53689–53690.
13. S. Alberti, B. G. Danly, G. Gulotta, *et al.*, Phys. Rev. Lett. **71**, 2018 (1993).
14. V. L. Bratman, G. G. Denisov, M. M. Ofitserov, *et al.*, Int. J. Infrared Millim. Waves **13**, 1857 (1992).
15. V. L. Bratman, G. G. Denisov, B. D. Kol'chugin, *et al.*, Phys. Rev. Lett. **75**, 3102 (1995).
16. A. V. Savilov, V. L. Bratman, A. D. R. Phelps, *et al.*, Phys. Rev. E **62**, 4207 (2000).
17. G. S. Nusinovich and J. Zhao, Phys. Rev. E **58**, 1002 (1998).
18. A. F. Aleksandrov, S. Yu. Galuzo, V. I. Kanavets, *et al.*, Radiotekh. Élektron. (Moscow) **29**, 1788 (1984).
19. S. J. Cooke and G. G. Denisov, IEEE Trans. Plasma Sci. **26**, 519 (1998).
20. G. G. Denisov, V. L. Bratman, A. D. R. Phelps, *et al.*, IEEE Trans. Plasma Sci. **26**, 508 (1998).
21. V. L. Bratman, A. E. Fedotov, and A. V. Savilov, IEEE Trans. Plasma Sci. **28**, 1742 (2000).
22. V. L. Bratman, A. E. Fedotov, N. G. Kolganov, *et al.*, Phys. Rev. Lett. **85**, 3424 (2000).
23. A. V. Savilov, N. Yu. Peskov, and S. V. Samsonov, Nucl. Instrum. Methods Phys. Res. A **445**, 284 (2000).

Translated by A. Khzmalyan

Technical Physics, Vol. 46, No. 8, 2001, pp. 1009–1013. Translated from Zhurnal Tekhnicheskoĭ Fiziki, Vol. 71, No. 8, 2001, pp. 80–84.

OPTICS, QUANTUM ELECTRONICS

Spatially Coherent Radiation from a Coaxial Free-Electron Laser with a Resonator Composed of One-Dimensional and Two-Dimensional Bragg Mirrors

N. S. Ginzburg, N. Yu. Peskov, and A. S. Sergeev

Institute of Applied Physics, Russian Academy of Sciences, Nizhni Novgorod, 603600 Russia

e-mail: peskov@appl.sci-nnov.ru

Received September 14, 2000

Abstract—It is shown that the application of a resonator composed of one-dimensional and two-dimensional coaxial Bragg mirrors provides a spatially coherent radiation from a hollow electron beam with a transverse size several orders of magnitude larger than the wavelength. The two-dimensional Bragg mirror placed at the cathodic end of the resonator synchronizes the radiation across the hollow electron beam. The standard one-dimensional Bragg mirror placed at the collector end closes the feedback loop and reduces ohmic losses to as low as 5–10% of the lasing power. © *2001 MAIK "Nauka/Interperiodica".*

INTRODUCTION

It has been proposed [1, 2] to use two-dimensional (2D) distributed feedback (DF) to obtain a spatially coherent radiation from high-power ribbon-shaped [3, 4] or hollow [5] electron beams. This feedback mechanism can be implemented with so-called 2D planar or coaxial Bragg resonators. In essence, these resonators are waveguides of the respective geometry with a doubly periodic corrugation on their inner surfaces. It has been shown [6, 7] that a free-electron laser (FEL) with the 2D Bragg resonators may operate under steady-state single-frequency lasing conditions at an almost arbitrary width of the electron beam. To date, the efficiency of the new feedback approach has been experimentally demonstrated in a planar 4-mm-range free-electron maser [8, 9] based on the ÉLMI accelerator (Institute of Nuclear Physics, Siberian Division, Russian Academy of Sciences). A coaxial version of the FEL with 2D DF based on the high-current accelerator (Strathclyde University, Glasgow, United Kingdom) is now under development [10].

It should be noted that the implementation of this feedback poses difficulties associated primarily with a number of design constraints. For example, for planar FELs, the best situation is when the system is open in the transverse direction, so that transverse (relative to the translational motion of the electron beam) electromagnetic energy fluxes are extracted. However, for early pilot 2D DF FELs, such a configuration seems to be too complex; simpler systems closed in the transverse direction and providing unidirectional radiation extraction are needed. For coaxial FELs, problems associated with unidirectional energy extraction do not arise. Here, a major part of the energy radiated by the electrons is extracted in the direction of the translational motion of the electron beam. Nevertheless, if the 2D Bragg structure occupies the whole interaction space, ohmic losses associated with azimuthal energy fluxes appear to be high. A possible design of the two-mirror arrangement is that where two doubly periodic Bragg structures (mirrors) are separated by a regular waveguide. In this configuration, however, the azimuthal energy fluxes prove to be sufficiently high in the mirror located near the collector end of the system. This may ultimately cause rf breakdown.

Therefore, the FEL design with a resonator composed of 2D and 1D Bragg mirrors (Fig. 1) seems to be optimal. A 2D Bragg mirror at the cathode synchronizes the radiation across the hollow electron beam. Then, a conventional 1D Bragg mirror at the opposite (collector) side that partly reflects the output radiation and closes the feedback loop will suffice. With the parameters chosen optimally, the reflection from the exit mirror is not too high, the radiation is amplified mostly after the entrance mirror, and the amplitude of the azimuthal energy flux in the first 2D mirror proves to be relatively small. Hence, the ohmic losses due to these waves also become small and their effect on the

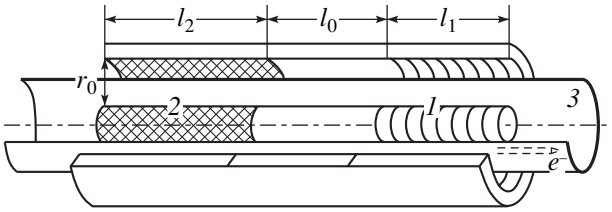

Fig. 1. FEL with a resonator composed of (*1*) 1D and (*2*) 2D Bragg mirrors. (*3*) Hollow relativistic electron beam.

1063-7842/01/4608-1009$21.00

energy balance is insignificant. The optimum choice also removes the above breakdown problem.

In this work, the FEL design with the composite coaxial two-mirror resonator (Fig. 1) is analyzed.

THE MODEL AND BASIC EQUATIONS

Consider a quasi-planar model of the coaxial FEL. We assume that the radii of the inner and the outer cylinders of the coaxial waveguide are much larger than the wavelength and the distance between the cylinders. Then, the azimuthal dependence of the field can be described in terms of the Cartesian variable $x = R\varphi$.

Let a shallow 2D corrugation

$$r = r_2 \cos(\bar{h}_2 z)\cos(\bar{h}_2 x), \tag{1}$$

where $2r_2$ is the corrugation depth, be applied on the entrance mirror. This corrugation couples four partial waves and provides their mutual scattering. Two of these waves ($\mathcal{A}_\pm$) copropagate and counterpropagate with the beam (in the $\pm z$ directions), while the other two ($\mathcal{B}_\pm$) propagate in the transverse (azimuthal) directions ($\pm x$ directions):

$$\mathbf{E} = \mathbf{E}\mathrm{Re}([\mathcal{A}_+ e^{-ihz} + \mathcal{A}_- e^{ihz} + \mathcal{B}_+ e^{-ihx}\mathcal{B}_- e^{ihx}]e^{i\bar{\omega}t}). \tag{2}$$

Let the propagation constants h of the partial waves meet the Bragg resonance condition

$$h \approx \bar{h}_2. \tag{3}$$

In formulas (2) and (3), $\bar{h}_2 = \sqrt{2}\,\pi/d_2$; d_2 is the corrugation period; $\mathcal{A}_\pm(x, z, t)$ and $\mathcal{B}_\pm(x, z, t)$ are slowly varying functions; and $\bar{\omega} = \bar{h}_2 c$ is the Bragg frequency, which is taken as the carrier. The function $\mathbf{E}_0(r)$ describes the transverse (radial) wave structure and coincides with a mode of the regular waveguide. The mutual scattering of these waves by Bragg structure (1) with allowance for the electron-beam excited synchronous wave $\mathcal{A}_+$ can be described by the system of equations [6, 7]

$$\begin{aligned}
&\left(\frac{\partial}{\partial Z} + \beta_{\mathrm{gr}}^{-1}\frac{\partial}{\partial \tau}\right)A_+ + \sigma A_+ + i\alpha_2(B_+ + B_-) = J,\\
&\left(\frac{\partial}{\partial Z} - \beta_{\mathrm{gr}}^{-1}\frac{\partial}{\partial \tau}\right)A_- + \sigma A_- + i\alpha_2(B_+ + B_-) = 0,\\
&\left(\frac{\partial}{\partial X} \pm \beta_{\mathrm{gr}}^{-1}\frac{\partial}{\partial \tau}\right)B_\pm + \sigma B_\pm + i\alpha_2(A_+ + A_-) = 0.
\end{aligned} \tag{4}$$

In formulas (4), we use the normalized variables $Z = zC\bar{\omega}/c$, $X = xC\bar{\omega}/c$, $\tau = tC\bar{\omega}$, and $(A_\pm, B_\pm) = (\mathcal{A}_\pm, \mathcal{B}_\pm)eK\mu/\gamma mc\bar{\omega}C^2$. Here, $K \approx \beta_\perp/2\beta_\parallel$ is the electron–wave coupling parameter, $\mu \approx \gamma^{-2}$ is the parameter of inertial bunching [11], γ is the relativistic mass factor of the electrons, $\beta_\parallel$ is the translational particle velocity, and β_{gr} is the wave group velocity. The amplification parameter (Pierce parameter) C is given by

$$C = \left(\frac{eI_0}{mc^3}\frac{\lambda^2\mu K^2}{8\pi\gamma r_0}\right)^{\frac{1}{3}},$$

where I_0 is the beam current per unit length, r_0 is the spacing between the cylinders, α_2 is the coefficient of wave coupling by the Bragg structure (it is proportional to the corrugation depth [6, 7]), and σ describes ohmic loss.

It is significant that the presence of losses for the confined waves $\mathcal{B}_\pm$ is imperative for steady-state oscillations to set up. If ohmic losses are absent, losses may be caused by the diffraction spread of the wave beams $\mathcal{B}_\pm$ in the z direction. Equations (4) ignore diffraction effects because they assume that the transverse dimension L_x of the wave beams $\mathcal{B}_\pm$ far exceeds the wavelength, so that the geometrical optics approximation is valid.

In the exit 1D Bragg mirror, like in the regular part of the resonator, only two partial waves that propagate in and in opposition to the direction of the beam's translational velocity are present:

$$\mathbf{E} = \mathbf{E}\mathrm{Re}([\mathcal{A}_+ e^{-ihz} + \mathcal{A}_- e^{ihz}]e^{i\bar{\omega}t}). \tag{5}$$

These waves are scattered by the 1D Bragg structure

$$r = r_1 \cos(\bar{h}_1 z) \tag{6}$$

subject to the condition

$$h \approx \bar{h}_1/2, \tag{7}$$

where $\bar{h}_1 = 2\pi/d_1$ and $2r_1$ and d_1 are the depth and the period of the 1D corrugation, respectively. The scattering is described by the equations

$$\begin{aligned}
&\left(\frac{\partial}{\partial Z} + \beta_{\mathrm{gr}}^{-1}\frac{\partial}{\partial \tau}\right)A_+ + \sigma A_+ + i\alpha_1 A_- = J,\\
&\left(\frac{\partial}{\partial Z} - \beta_{\mathrm{gr}}^{-1}\frac{\partial}{\partial \tau}\right)A_- + \sigma A_- + i\alpha_1 A_+ = 0,
\end{aligned} \tag{8}$$

where α_1 is the coefficient of wave coupling by the 1D Bragg structure [12].

In the regular part of the resonator, the amplification of the wave $\mathcal{A}_+$ is described by an equation similar to (8) with the zero coupling coefficient.

The boundary conditions for Eqs. (4) and (8) under which the external electromagnetic energy flux into the resonator is zero have the form

$$A_+(X, Z = 0) = 0, \quad A_-(X, Z = L_z) = 0, \tag{9a}$$

where $l_z = l_2 + l_0 + l_1$ is the full length of the resonator (Fig. 1).

Next, the amplitudes of the partial waves $\mathcal{A}_\pm$ should be continuous at the boundaries between different sec-

tions. In the transverse direction, we have the cyclic boundary conditions for the partial waves:

$$\begin{aligned} B_{\pm}(X + L_x, Z) &= B_{\pm}(X, Z), \\ A_{\pm}(X + L_x, Z) &= A_{\pm}(X, Z), \end{aligned} \tag{9b}$$

where $l_x = 2\pi R$ is the perimeter of the system and $L_{x,z} = l_{x,z}C\bar{\omega}/c$.

In view of (9b), we can expand the fields into the Fourier series:

$$A_{\pm}(X, Z) = \sum_{m=-\infty}^{\infty} A_{\pm}^{m}(Z)e^{imsX},$$

$$B_{\pm}(X, Z) = \sum_{m=-\infty}^{\infty} B_{\pm}^{m}(Z)e^{imsX},$$

where $s = 2\pi/L_x$. Each of the harmonics can be treated as the mth azimuthal mode. The averaged motion of the particles in the field of the synchronous wave $\mathcal{A}_+$ is described by the equation [11]

$$\left(\frac{\partial}{\partial Z} + \beta_{\parallel}^{-1}\frac{\partial}{\partial \tau}\right)^2 \Theta = \mathrm{Re}(A_+ e^{i\Theta}) \tag{10}$$

with the boundary conditions

$$\begin{aligned} \Theta|_{Z=0} &= \Theta_0 \in [0, 2\pi), \\ \left(\frac{\partial}{\partial Z} + \beta_{\parallel}^{-1}\frac{\partial}{\partial \tau}\right)\Theta|_{Z=0} &= \Delta, \end{aligned} \tag{11}$$

where $\Theta = \bar{\omega}t - hz - h_w z$ is the electron phase relative to the synchronous wave, $\Delta = (\bar{\omega} - hv_{\parallel} - h_w v_{\parallel})/\bar{\omega}C$ is the initial detuning of undulatory synchronism at the carrier frequency, $h_w = 2\pi/d_w$, and d_w is the undulator period. From Eq. (10), we obtain the electron current

$$J = \frac{1}{\pi}\int_0^{2\pi} e^{-i\Theta}d\Theta_0,$$

which excites the synchronous wave and enters the right-hand sides of Eqs. (4) and (8). In terms of the new variables, the electron efficiency is given by

$$\eta = \frac{C}{\mu(1-\gamma_0^{-1})}\hat{\eta},$$

where

$$\hat{\eta} = \frac{1}{2\pi L_x}\int_0^{L_x}\int_0^{2\pi}\left(\frac{\partial\Theta}{\partial Z} + \frac{1}{\beta_{\parallel}}\frac{\partial\Theta}{\partial\tau} - \Delta\right)\Big|_{Z=L_z} d\Theta_0 dX. \tag{12}$$

In Eqs. (4), (8), and (10), it is assumed that the 2D [Eq. (3)] and 1D [Eq. (7)] Bragg resonance conditions are satisfied simultaneously. Clearly, this is possible if $\bar{h}_2 = \bar{h}_1/2$, which is valid when the corrugation periods are related as $d_2 = \sqrt{2}\,d_1$.

NUMERICAL RESULTS

Figures 2 and 3 show results of simulation for the system of Eqs. (4), (8), and (10). The parameters were close to those used in experiments with the 8-mm-range FEL that are being carried out on the high-current accelerator at the Strathclyde University [10]. The entrance (2D) and exit (1D) Bragg mirrors were, respectively, 23 and 13 cm long; the regular part of the resonator was 38 cm long; the average diameter was $2R = 7$ cm; and the spacing between the cylinders was $r_0 = 1$ cm. The corrugation amplitude was 0.3 mm in the entrance resonator and 0.1 mm in the exit one. The beam current per unit length was 50–100 A/cm, the particle energy was 0.5 MeV, the undulator period was 4 cm, and the oscillatory velocity of the particles in the undulator field was $\beta_{\perp} \approx 0.2$–$0.3$. Under these conditions, the Pierce parameter was $C \approx 7 \times 10^{-3}$; the dimensionless lengths of different sections were $L_2 = 1.4$, $L_0 = 2.4$, and $L_1 = 0.8$; and the perimeter of the system $L_x = 1.4$. The loss parameter was set equal to $\sigma = 0.02$, which corresponded to a duralumin resonator. In the simula-

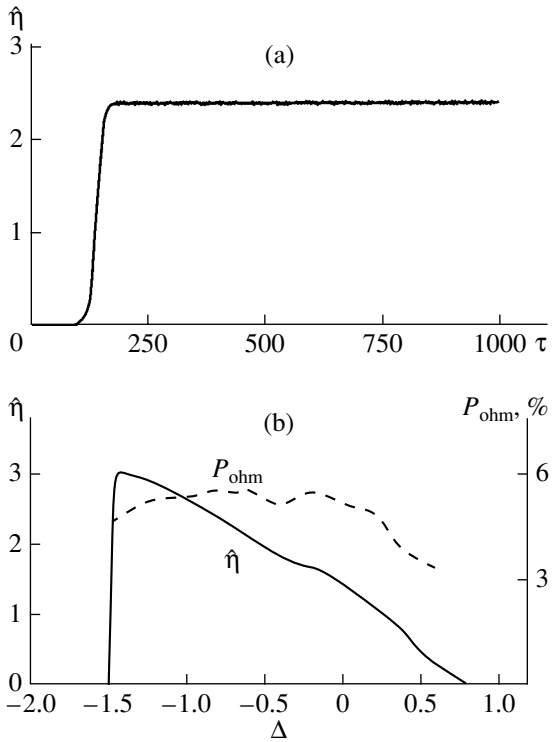

Fig. 2. Simulated self-excitation in the coaxial FEL with a composite Bragg resonator at $L_2 = 1.4$, $L_0 = 2.4$, $L_1 = 0.8$, $L_x = 1.4$, $\alpha_2 = 0.5$, $\alpha_1 = 0.3$, and $\sigma = 0.02$. (a) Normalized electron efficiency versus time at the optimal detuning parameter $\Delta = -1.0$ and (b) steady-state maximal efficiency and relative ohmic losses versus Δ.

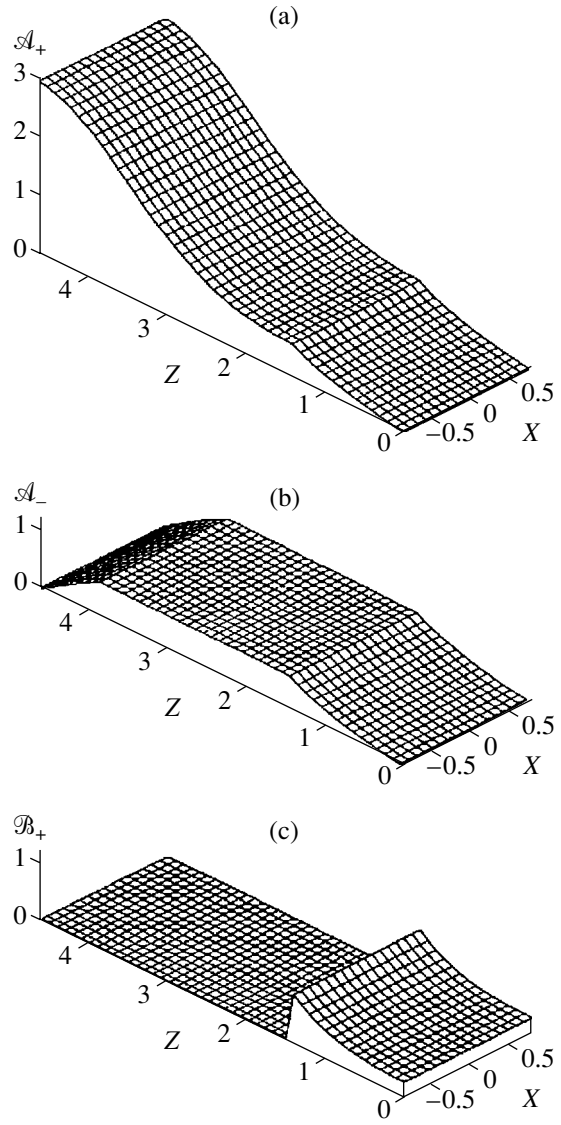

Fig. 3. Steady-state spatial distribution of the partial wave amplitudes $\mathscr{A}_\pm$ and $\mathscr{B}_+$ for the same FEL parameters as in Fig. 2a.

tions, the translational velocity of the particles was assumed to equal the group velocity of the copropagating synchronous wave.

Figure 2a plots the normalized electron efficiency versus time. It shows that steady-state lasing can be obtained in this FEL configuration. The maximal efficiency is attained at negative off-synchronism parameters Δ near the self-excitation band edge (Fig. 2b). As a result, at the above parameters, the FEL efficiency was 15–20% and the output power was 100–200 MW.

Figures 3a–3c illustrate the spatial distributions of the partial wave amplitudes in the steady-state lasing mode. It is important that the amplitude of the synchronous wave $\mathscr{A}_+$ is constant throughout the transverse coordinate, which indicates that only the axisymmetric wave ($m = 0$) is excited. In this case, all portions of the electron beam give up the same amount of energy, thereby providing the sufficiently high average efficiency. The amplitudes $\mathscr{B}_\pm$ of the transverse waves propagating in the entrance mirror were found to be not too high in this case. On the one hand, this eliminates the rf breakdown problems. On the other hand, the ohmic losses due to the finite conductivity of the resonator walls prove to be sufficiently small. These losses can be defined as the difference between the beam power entering the resonator and the power radiated from the resonator:

$$P_{\text{ohm}}(\%) = 1 - \frac{\int_0^{L_x} (|A_+(X, Z = L_z)|^2 + |A_-(X, Z = 0)|^2) dX}{4\hat{\eta}}.$$

According to our simulations, the ohmic losses at the above parameters is no more than 5–6% for any Δ (Fig. 2b). It is yet significant that the steady-state lasing mode cannot set up in this FEL design if the ohmic (or any other, for example, diffraction) losses for the confined waves $\mathscr{B}_\pm$ are completely absent (see [7] for details).

It should be emphasized that the transient behavior remained identical to that shown in Fig. 2 when the resonator diameter was increased to 50–70 cm and the normalized perimeter, accordingly, to $L_x \approx 10$–15. The maximum perimeter at which steady-state lasing was observed, was limited only by the RAM capacity. Importantly, the steady-state lasing mode was independent of the initial longitudinal and azimuthal field distributions.

Thus, using a resonator composed of 1D and 2D coaxial Bragg mirrors provides a spatially coherent radiation from a hollow electron beam whose cross size is several orders of magnitude larger than the wavelength. The steady-state spatial distribution of the laser radiation coincides with that of one of the axisymmetric modes in the coaxial waveguide.

REFERENCES

1. N. S. Ginzburg, N. Yu. Peskov, and A. S. Sergeev, Pis'ma Zh. Tekh. Fiz. **18** (9), 23 (1992) [Sov. Tech. Phys. Lett. **18**, 285 (1992)].
2. A. V. Arzhannikov, N. S. Ginzburg, V. S. Nikolaev, *et al.*, in *Proceedings of the 14th International FEL Conference, Kobe, Japan, 1992*, p. 214.
3. A. V. Arzhannikov, V. S. Nikolaev, S. L. Sinitsky, and M. V. Yushkov, J. Appl. Phys. **72**, 1657 (1992).
4. A. V. Arzhannikov, V. B. Bobylev, V. S. Nikolaev, *et al.*, in *Proceedings of the 10th International Conference on High-Power Particle Beams, San Diego, USA, 1994*, Vol. 1, p. 136.

5. A. N. Bastrikov, S. P. Bugaev, I. N. Kiselev, *et al.*, Zh. Tekh. Fiz. **58**, 483 (1988) [Sov. Phys. Tech. Phys. **33**, 291 (1988)].

6. N. S. Ginzburg, N. Yu. Peskov, A. S. Sergeev, *et al.*, Nucl. Instrum. Methods Phys. Res. A **358**, 189 (1995).

7. N. S. Ginzburg, N. Yu. Peskov, and A. S. Sergeev, Opt. Commun. **112**, 151 (1994).

8. N. V. Agarin, A. V. Arzhannikov, V. B. Bobylev, *et al.*, in *Proceedings of the IV International Workshop "Strong Microwaves in Plasmas," Nizhni Novgorod, Russia, 1999*, p. S24.

9. N. V. Agarin, A. V. Arzhannikov, V. B. Bobylev, *et al.*, in *Abstracts of the 21st International FEL Conference, Hamburg, Germany, 1999*, p. Mo-O-03.

10. A. D. R. Phelps, A. W. Cross, G. R. M. Robb, *et al.*, in *Proceedings of the 19th International FEL Conference, Beijing, China, 1997*, p. II-122.

11. V. L. Bratman, G. G. Denisov, N. S. Ginzburg, and M. I. Petelin, IEEE J. Quantum Electron. **19**, 282 (1983).

12. N. F. Kovalev, I. M. Orlova, and M. I. Petelin, Izv. Vyssh. Uchebn. Zaved., Radiofiz. **11**, 783 (1968).

Translated by A. Khzmalyan

Technical Physics, Vol. 46, No. 8, 2001, pp. 1014–1019. Translated from Zhurnal Tekhnicheskoĭ Fiziki, Vol. 71, No. 8, 2001, pp. 85–91.

Computer Simulation of Magnetic Force Microscopy Images with a Static Model of Magnetization Distribution and Dipole–Dipole Interaction

D. V. Ovchinnikov and A. A. Bukharaev

Zavoĭskiĭ Physicotechnical Institute, Kazan Scientific Center, Russian Academy of Sciences, Sibirskiĭ trakt 10/7, Kazan 29, 420029 Tatarstan, Russia

e-mail: dovchinnikov@dionis.kfti.knc.ru

Received August 9, 2000

Abstract—An algorithm for computer simulation of images obtained by magnetic force microscopy (MFM) is suggested. It is based on the Brown formalism and takes into account the shapes and the magnetic properties of the MFM tip and sample studied. The robustness and efficiency of the algorithm are tested by simulating the MFM image of a point magnetic dipole for the case where the tip is approximated by a nonmagnetic truncated cone covered by a thin uniformly magnetized layer. From the computer simulation of the MFM images of the dipole, the optimum parameters of the MFM probe are obtained. © *2001 MAIK "Nauka/Interperiodica".*

INTRODUCTION

The last decades have marked an extensive search for novel media for data recording and storage. In spite of the great advances in optical recording techniques, micron and submicron magnetic structures continue to attract considerable interest because they hold much promise for creating quantum magnetic disks and other media for ultrahigh-density magnetic data recording [1, 2].

The properties of such objects, which are prepared on or near the surface of solids, are being studied by scanning probe microscopy to an increasing extent [3, 4]. The basic sensitive element of these microscopes is a flexible cantilever with a probing tip fixed at its edge. Scanning probe microscopy images result from the interaction of the tip with the surface structures. In the atomic force mode, when the tip touches the surface, the surface image (topography) represents the tip–surface relief convolution. This substantially distorts the resulting pattern. The distortions are due to the fact that, when scanning, the tip touches the surface by its different parts. To avoid this problem, researchers perform computer analysis of the experimental images by using special deconvolution algorithms, which enable the noticeable suppression of the distortions [5, 6].

The use of magnetic probes (magnetic force microscopy, MFM) makes it possible to study the magnetic properties of the surface structures with a submicron resolution [4, 7]. If the two-pass technique is combined with the lifting mode of MFM operation, one can simultaneously obtain both the surface topography and the magnetic image of the same area on the sample. The essence of the lifting mode is that the tip traverses this area twice. In the first pass, it touches the surface and its path is memorized. Then, the tip is raised through a given height and moves along the path memorized, sensing only magnetic effects. The resulting magnetic contrast either maps the forces of magnetic interaction between the surface structures and the tip (dc mode of microscope operation, cantilever does not vibrate) or displays the gradient of probe–surface magnetic interaction forces (ac mode, cantilever vibrates at its natural frequency) [4].

Magnetic interactions are long-range; therefore, in the case of MFM, the effect of the tip on imaging becomes still more significant and should be taken into account by means of special analytic approaches. The probe may affect the image through the shape of the tip or its magnetic part [8]. The magnetic properties of the probe, for example, the magnetization distribution over the volume of its magnetic part, may also be a factor [9, 10]. The geometry of the tip can be reconstructed by special deconvolution algorithms if the profile of the surface studied is known or test samples with known geometric parameters are used [5, 6]. To find the magnetization distribution over the magnetic part of the tip is a more intricate challenge. In the majority of cases, however, the tip is assumed to be uniformly magnetized with its total magnetic moment aligned with the probe axis.

Analysis of experimental MFM data implies the computer-aided simulation of MFM images. Its essence is the evaluation of the interaction between the tip and the magnetic field produced by surface structures of the sample. Deconvolution algorithms for experimental MFM images can be found in the literature (for example, the use of Fourier analysis for extracting the "true" magnetic image that bears information only on the poles and domain walls of the sample [11]). However, most researchers apply direct simulation algorithms to

1063-7842/01/4608-1014$21.00

MFM images based on tentative models of the geometric and magnetic characteristics of the tip and surface area under study. Historically, at the stage MFM maturing, its objects were largely thin magnetic films used as magnetic recording media. Once digital information of one type (1 or 0) has been written on such a carrier, its magnetic structure becomes periodic. The magnetic field above this sample can analytically be estimated by integrating over its volume [12–15] or by applying Fourier analysis [16]. An analytical approach is also possible in some special cases, for example, in the case of an individual domain wall [17, 18]. The tip can roughly be approximated by a point-contact magnetic dipole; then, its magnetic interaction with the sample surface can be evaluated by using the formula for point dipole–magnetic field interaction [12, 13, 16, 17, 19] or the Green function formalism [20]. However, the "actual" size of the tip involved in the magnetic interaction with the surface is rather large. Therefore, if the magnetic part of the tip were approximated by a figure whose shape is closer to the real size of the tip [14, 15, 18, 21, 22], computer simulation would provide results more adequate to experiment. In this case, the evaluation of tip–sample magnetic interaction can be made by integrating over the magnetic volume of the probe. However, analytic integration applies only to a limited number of the tip geometries. To simplify the associated computations, integration is replaced by summation over small subvolumes into which the initial magnetic volume of the probe is divided; in other words, we pass to the Brown formalism [22, 23]. Of particular interest here is that such an approach to simulating MFM images may take into consideration dynamic magnetic processes arising when the magnetization of the tip or of the sample changes because of their interaction [24]. However, it requires a high computer power and has not yet found wide recognition in simulating MFM images.

In this work, we pioneer in-depth analysis of the potentialities and restrictions of the Brown formalism as applied to computer simulation of MFM images. With the algorithm elaborated and numerical experiments, we also try to optimize the MFM tip parameters in order to provide the tradeoff between the spatial resolution and the sensitivity of a magnetic force microscope.

COMPUTATIONAL ALGORITHM FOR TIP–SURFACE INTERACTION IN MFM

In the absence of induced currents, the force gradient of tip–surface magnetic interaction at a given position $\mathbf{r}$ of the probe in a coordinate system related to the sample is given by

$$\frac{\partial}{\partial z}F_z(\mathbf{r}) = \frac{\partial}{\partial z}\int\limits_{\text{tip volume}}\int\int(\mathbf{M}_t(\mathbf{r}_t)\nabla)H_z(\mathbf{r}+\mathbf{r}_t)dV_t, \quad (1)$$

where $\mathbf{M}_t(\mathbf{r}_t)$ is the magnetization per unit volume of a magnetic tip material at a point $\mathbf{r}_t$, $H_z(\mathbf{r}+\mathbf{r}_t)$ is the field induced at this point, ∇ is the del operator, and $\mathbf{M}_t(\mathbf{r}_t)\nabla$ is the scalar product.

The magnetic volumes of the tip and the sample are divided into small subvolumes according to the Brown formalism. Their size should exceed the range within which the effect of microscopic (atomic) processes is significant and, at the same time, be sufficiently small, i.e., such that the macroscopic behavior of a solid is adequately described at a local level. For the sake of simplicity, we assume that all the subvolumes have an equal size and, hence, volume. Each of the partition elements has a cubic shape and is approximated by a point-contact magnetic dipole with the magnetic moment

$$\mathbf{m}_t^i = \mathbf{M}_t V_t^i, \quad (2)$$

where V_t^i is the volume of a partition element.

To simplify the analysis, we do not take into account the variation of the magnetizations of the tip and the sample when the probe moves over the surface. In other words, we assume that both the tip and the sample are absolutely magnetically hard (a static model of magnetization). In addition, it is suggested that only dipole–dipole interaction between the tip and the sample takes place; that is, the jth sample dipole located at a point $\mathbf{r}_s^j$ produces the magnetic field

$$H_z^{ij}(\mathbf{r}+\mathbf{r}_t^i-\mathbf{r}_s^j) = \frac{3(z+z_t^i-z_s^j)(\mathbf{m}_s^j\cdot(\mathbf{r}+\mathbf{r}_t^i-\mathbf{r}_s^j))}{\left|\mathbf{r}+\mathbf{r}_t^i-\mathbf{r}_s^j\right|^5} - \frac{m_{s_z}^j}{\left|\mathbf{r}+\mathbf{r}_t^i-\mathbf{r}_s^j\right|^3} \quad (3)$$

at the point where the ith dipole of the tip is located. Here, $\mathbf{m}_s^j$ is the magnetic moment of the jth sampling element.

Thus, integration in formula (1) can be replaced by summation, which simplifies the computation and makes it independent of the shape and magnetization of the tip and the sample:

$$\frac{\partial}{\partial z}F_z(\mathbf{r}) = \sum_{\substack{t-\text{tip}\\ j-\text{sample}}}\left((\mathbf{m}_t^i\nabla)\frac{\partial}{\partial z}H_z^{ij}(\mathbf{r}+\mathbf{r}_t^i-\mathbf{r}_s^j)\right). \quad (4)$$

We consider the three-dimensional case. The tip is approximated by a nonmagnetic truncated cone covered by a magnetic layer (Fig. 1a). Such an approximation is adequate to the shape of tips used in MFM [25, 26]. To simulate scanning, the virtual tip is sequentially placed in different sites over the virtual surface. The tip travels according to the lifting mode with regard for the convolution effect. That is, in scanning the surface during the first pass, the geometry of the tip is included, which affects its trajectory in the second pass.

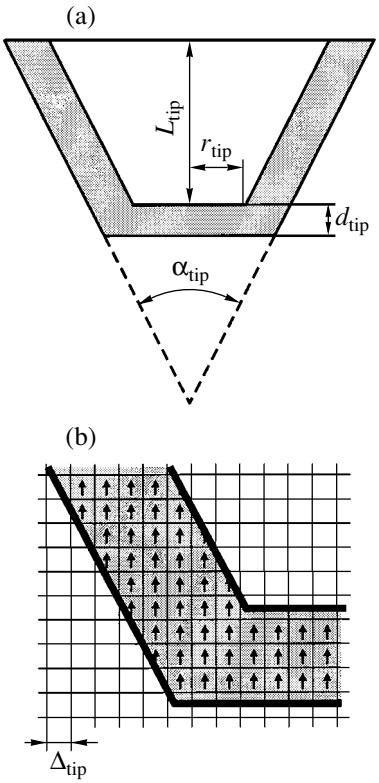

Fig. 1. Approximation of the MFM tip by a nonmagnetic truncated cone covered by a thin magnetic layer. (a) Principal normal section of the three-dimensional model truncated cone with the angle α_{tip} and length L_{tip}; the radius of the truncated part is r_{tip} and the thickness of the magnetic layer is d_{tip}. (b) Partition of the magnetic part of the tip into small subvolumes with the linear dimension Δ_{tip} that are approximated by point magnetic dipoles.

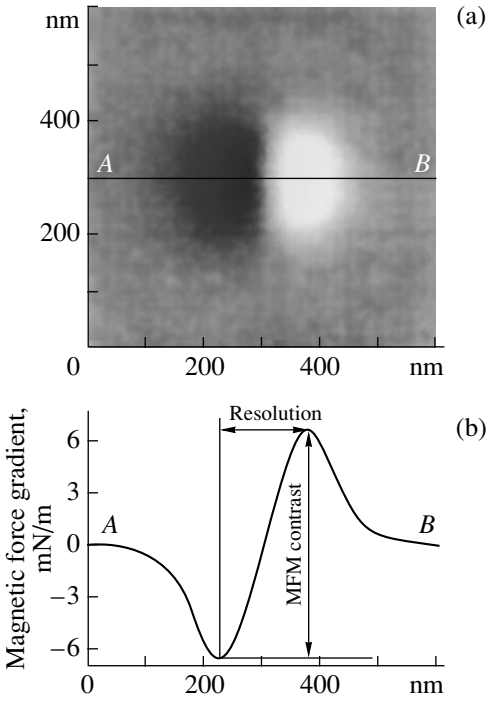

Fig. 2. Computer-aided simulation of the MFM image of a point magnetic dipole for the tip approximated by a nonmagnetic truncated cone covered by a magnetic layer. The tip is uniformly magnetized along the axis normal to the sample surface, and the magnetic moment of the dipole is parallel to the sample surface. (a) Typical image of the dipole and (b) algorithm for the determination of the MFM contrast and resolution along the magnetic moment of the dipole from the image profile simulated.

EFFECTIVE PARAMETERS OF MFM PROBE PARTITION

The integration-to-summation transition causes partition errors in the calculation of tip–sample interaction. They depend largely on the size Δ_{tip} of an element of volume partition (Fig. 1b): the smaller the size, the smaller the error. However, as the size of the element decreases, the number of the elements grows. This makes the computations much more cumbersome and imposes increased requirements to the computer performance, in particular, to the RAM capacity.

We studied the dependences of the model image parameters on Δ_{tip}. The object to be imaged was a single point-contact dipole at the center of the scan area. The dipole was directed parallel to the sample surface and had a magnetic moment of $\approx 2.14 \times 10^{-13}$ G (in this case, the dipole approximates an iron cube of side 50 nm). The tip was assumed to be uniformly magnetized along its axis of symmetry. A typical model MFM image of the dipole for the given parameters is depicted in Fig. 2a. The parameters to be studied are the MFM contrast, which characterizes the sensitivity of the microscope, and the resolution (resolving power). The resolution is defined as the distance between those positions of the tip (those points on the image profile) where the magnetic interaction force gradient along the magnetic moment of the dipole is minimal and maximal. The MFM contrast equals the difference between these two values of the gradient (Fig. 2b).

When simulating the image of the dipole, one can construct a contrast vs. Δ_{tip} curve by varying Δ_{tip}, all other tip parameters being fixed. Since this curve is found for the partitioned magnetic layer of the tip, the MFM contrast for two close values of Δ_{tip} may differ greatly. This difference will decrease with decreasing Δ_{tip} until Δ_{tip} is less than some Δ_{tip}^{eff} below which the contrast remains nearly unchanged. This is evidence for the numerical robustness of the algorithm. Figure 3 shows contrast vs. Δ_{tip} curves for different values of the magnetic layer thickness d_{tip} and the model cone angle α_{tip}. The value of the tip elevation above the surface and the magnetization per unit volume of the magnetic material of the tip are kept constant: D_z = 100 nm and M_{tip} = 1710 G/cm^3 (for iron), respectively. It is seen that Δ_{tip}^{eff} found by the above technique is almost indepen-

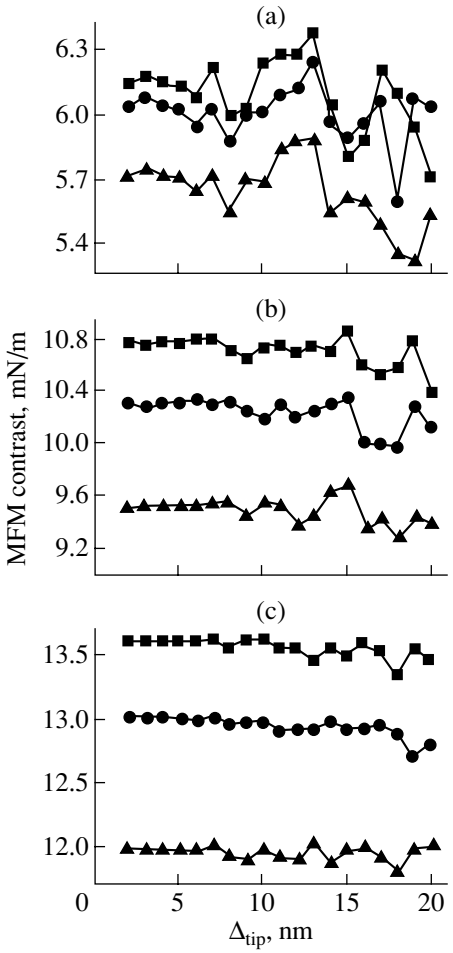

Fig. 3. Computer analysis of the MFM contract in the image of the dipole vs. Δ_{tip} for various values of the model parameters. L_{tip} = 500 nm. d_{tip} = (a) 20, (b) 40, and (c) 60 nm; α_{tip} = (■) 20°, (●) 40°, and (▲) 60°.

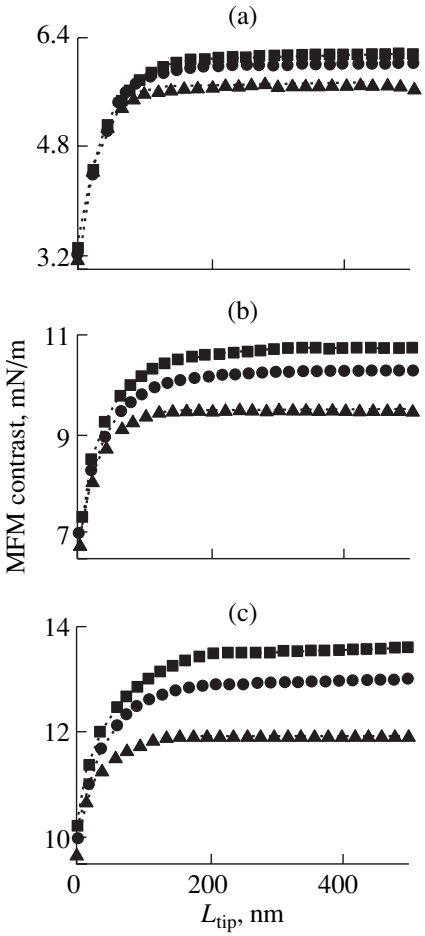

Fig. 4. Computer analysis of the MFM contract in the image of the dipole vs. length of the nonmagnetic part of the truncated cone that is taken into consideration. D_z = 100 nm. d_{tip} and α_{tip} are the same as in Fig. 3.

dent of α_{tip} but strongly depends on d_{tip}. The values of Δ_{tip}^{eff} obtained for different d_{tip} are listed in the table.

As was noted above, magnetic interaction is long-range; therefore, a major part of the tip is responsible for imaging by MFM. Yet, the interaction decreases with increasing distance, and one can take into consideration only the edge (effective) portion of the tip of length L_{tip}^{eff}, ignoring the effect of its remaining part. This greatly simplifies the computation. Contrast vs. L_{tip} curves obtained for D_z = const = 100 nm and M_{tip} = 1710 G/cm^3 indicate that the contrast sharply grows with L_{tip} when L_{tip} is small and remains practically unchanged for $L_{tip} \geq L_{tip}^{eff}$ (Fig. 4). The computer simulation at different d_{tip} and α_{tip} shows that L_{tip}^{eff} is almost independent of d_{tip} and varies with α_{tip} only slightly: from $L_{tip}^{eff} \cong 200$ nm for $\alpha_{tip} = 20°$ to $L_{tip}^{eff} \cong 150$ nm for $\alpha_{tip} = 60°$.

OPTIMAL PARAMETERS OF MFM PROBE

The performance of the probe to a great extent determines the MFM image quality and, hence, the potentialities of MFM. Of concern to us is the question: Which must be probe parameters for a tradeoff between the contract and the resolution to be achieved (in other

Effective linear size Δ_{tip}^{eff} of a subvolume of the magnetic layer for its various thicknesses

d_{tip}, nm	Δ_{tip}^{eff}, nm
20	5–6
30	6–7
40	8–9
50	11–12
60	17–18

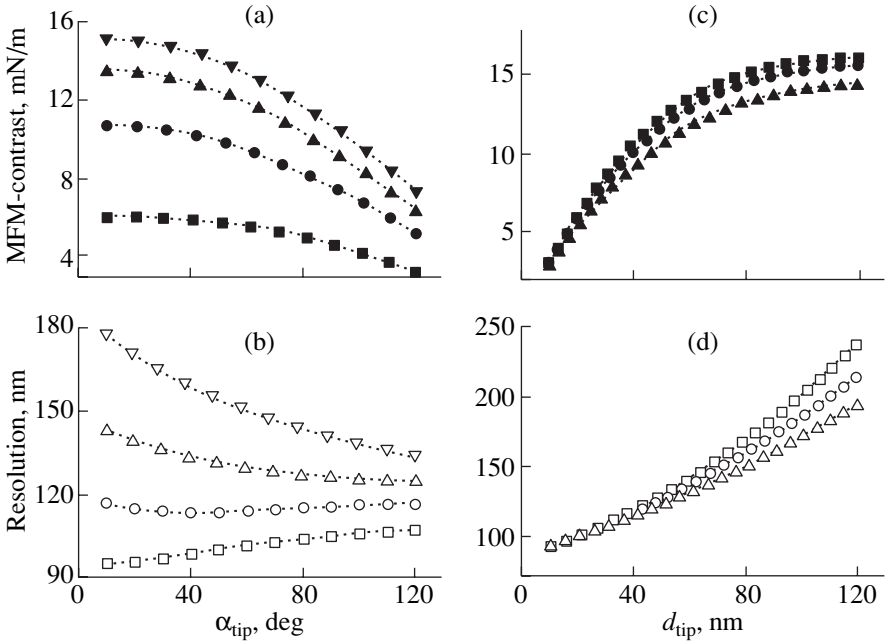

Fig. 5. Computer analysis of the (a, c) MFM contract and (b, d) resolution vs. (a, b) cone angle and (c, d) magnetic layer thickness. Δ_{tip} = 5 nm, D_z = 100 nm, and L_{tip} = 500 nm. (a, b) d_{tip} = (■, □) 20, (●, ○) 40, (▲, △) 60, and (▼, ▽) 80 nm; (c, d) α_{tip} = (■, □) 20°, (●, ○) 40°, and (▲, △) 60°.

words, for both the contrast and the resolution to be at a reasonable level)?

To answer the question, we tried to find the optimal geometry of a nonmagnetic tip covered by a thin magnetic film. It was assumed that the magnetic structure of the tip is homogeneous and geometry-independent. As before, the tip was approximated by a nonmagnetic truncated cone with a magnetic layer (Fig. 1). The parameters under study were those that can be varied by the manufacturers of the cantilevers: d_{tip}, thickness of the magnetic layer; α_{tip}, cone angle; and r_{tip}, radius of the nonmagnetic substrate (truncated part) of the tip.

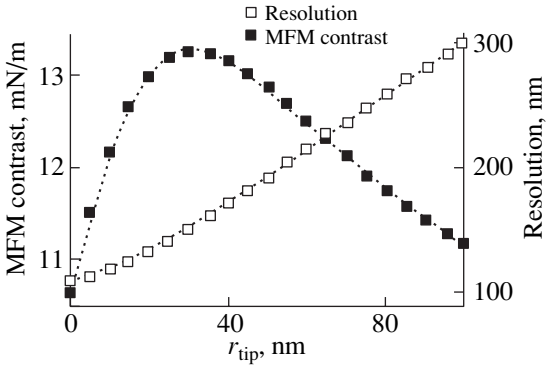

Fig. 6. Computer analysis of the MFM contract and resolution vs. radius of the truncated nonmagnetic part of the cone for α_{tip}^{opt} = 40° and d_{tip}^{opt} = 60 nm. Δ_{tip} = 5 nm, D_z = 100 nm, and L_{tip} = 500 nm.

We simulated the MFM images of the point-contact dipole that were obtained for various d_{tip} and α_{tip} (all other parameters of the tip shape being fixed) and constant tip elevation D_z = 100 nm and magnetization per unit volume of the magnetic material of the tip M_{tip} = 1710 G/cm^3 (for iron). From these images, we constructed contrast and resolution vs. d_{tip} and α_{tip} curves (Fig. 5). From these curves, we deduce the optimal ranges for d_{tip} and α_{tip}; namely, d_{tip}^{opt} = 60–80 nm and α_{tip}^{opt} = 30°–50°.

We also found the optimal value of the tip (nonmagnetic substrate) radius r_{tip} (Fig. 6) for d_{tip}^{opt} and α_{tip}^{opt}. It was found to be $r_{tip}^{opt} \approx 30$ nm.

Thus, our computer simulation proves to be efficient in studying MFM imaging. Tentative data suggest that the computer images (obtained with the above technique) of ferromagnetic nanoparticles and micron-size planar structures correlate well with their experimental images provided that the shape of the magnetic probe and its path are correctly taken into account (i.e., the effect of tip–surface convolution is included). Associated investigations are under way and will be published later.

CONCLUSION

We described an algorithm for computer-aided simulation of MFM images. The algorithm is based on the

Brown formalism and takes into account the shape and the magnetic properties of the tip and the sample.

The efficiency of the algorithm was tested by simulating the MFM image of a point magnetic dipole for the case where the tip is approximated by a nonmagnetic truncated cone covered by a thin uniformly magnetized layer. Algorithm parameters that specify the robustness of our numerical method were found.

From the computer simulation of the MFM images of the magnetic dipole, an interrelation between the tip geometry and the sensitivity and resolution of a magnetic force microscope was derived. Optimum geometric parameters of the MFM probe were obtained.

ACKNOWLEDGMENTS

This work was supported by the Russian Foundation for Basic Research (grant no. 99-02-17462) and the Program "Physics of Solid-State Nanostructures" (grant no. 99-1137).

REFERENCES

1. M. H. Kryder, Sci. Am. **257**, 117 (1987).
2. S. Y. Chou, P. R. Krauss, and L. Kong, J. Appl. Phys. **79**, 6101 (1996).
3. *Scanning Tunneling Microscopy*, Ed. by R. Wiesendanger and H.-J. Güntherodt (Springer-Verlag, Berlin, 1992), Vol. II.
4. A. A. Bukharaev, D. V. Ovchinnikov, and A. A. Bukharaeva, Zavod. Lab., No. 5, 10 (1997).
5. A. A. Bukharaev, N. V. Berdunov, D. V. Ovchinnikov, *et al.*, Mikroélektronika **26**, 163 (1997).
6. P. Markiewicz, S. R. Cohen, A. Efimov, *et al.*, Probe Microsc. **1**, 355 (1999).
7. S. Porthun, L. Abelmann, and C. Lodder, J. Magn. Magn. Mater. **182**, 238 (1998).
8. P. Grütter, D. Rugar, H. J. Mamin, *et al.*, J. Appl. Phys. **69**, 5883 (1991).
9. S. L. Tomlinson, S. R. Hoon, A. N. Farley, *et al.*, IEEE Trans. Magn. **31**, 3352 (1995).
10. P. Rice and S. E. Russek, J. Appl. Phys. **85**, 5163 (1999).
11. J.-G. Zhu, X. Lin, and R. C. Shi, J. Appl. Phys. **83**, 6223 (1998).
12. U. Hartmann, Phys. Status Solidi A **115**, 285 (1989).
13. H. J. Hug, B. Stiefel, A. Moser, *et al.*, J. Appl. Phys. **79**, 5609 (1996).
14. C. Schönenberg and S. F. Alvarado, Z. Phys. B **80**, 373 (1990).
15. A. Wadas and P. Grütter, Phys. Rev. B **39**, 12 013 (1989).
16. S. J. L. Vellekoop, L. Abelmann, S. Porthun, *et al.*, J. Magn. Magn. Mater. **193**, 474 (1999).
17. S. Müller-Pfeifer, M. Schneider, and W. Zinn, Phys. Rev. B **49**, 15 745 (1994).
18. C. D. Wright and E. W. Hill, Appl. Phys. Lett. **67**, 433 (1995).
19. U. Hartmann, Phys. Lett. A **137**, 475 (1989).
20. H. Saito, J. Chen, and S. Ishio, J. Magn. Magn. Mater. **191**, 133 (1999).
21. G. L. Klimchitskaya, R. Prioli, and S. I. Zanette, Surf. Rev. Lett. **6**, 115 (1999).
22. S. L. Tomlinson and A. N. Farley, J. Appl. Phys. **81**, 5029 (1997).
23. J. O. Oti, IEEE Trans. Magn. **29**, 2359 (1993).
24. A. Aharoni and J. P. Jakubovics, J. Appl. Phys. **73**, 6498 (1993).
25. K. Babcock, V. Elings, M. Dugas, *et al.*, IEEE Trans. Magn. **30**, 4503 (1994).
26. V. A. Bukharaev, D. V. Ovchinnikov, N. I. Nurgazizov, *et al.*, Fiz. Tverd. Tela (St. Petersburg) **40**, 1277 (1998) [Phys. Solid State **40**, 1163 (1998)].

Translated by V. Isaakyan

Technical Physics, Vol. 46, No. 8, 2001, pp. 1020–1025. Translated from Zhurnal Tekhnicheskoĭ Fiziki, Vol. 71, No. 8, 2001, pp. 92–97.

The Effect of Low-Energy Ion Bombardment on the Density and Crystal Structure of Thin Films

V. V. Naumov, V. F. Bochkarev, O. S. Trushin, A. A. Goryachev, É. G. Khasanov, A. A. Lebedev, and A. S. Kunitsyn

Institute of Microelectronics and Informatics, Russian Academy of Sciences, ul. Universitetskaya 21, Yaroslavl, 150007 Russia

e-mail: mrsan@mail.ru

Received August 29, 2000

Abstract—The effect of low-energy ion bombardment on the growth and properties of thin films deposited by rf plasma sputtering at low substrate temperatures is studied. The dependences of the film thickness, density, crystal structure, and conductivity on the bias voltage applied to the substrate are obtained. At biases ranging from 0 to –30 V, nickel films are polycrystalline; at higher biases, they exhibit axial (111) texture. At the bias –60 V, the density of the Ni films is close to that of the bulk metal and the crystal structure of the films is the most ordered. With a further increase in the bias, the density of the films drops because of gas (argon and residual gases) atoms incorporated into the films. The same bias dependence of the density is observed for amorphous films of binary alloys of *d* and *f* metals. In this case, the films deposited at the substrate bias –40 V have the highest density. © *2001 MAIK "Nauka/Interperiodica".*

In recent years, low-temperature growth of ordered films stimulated by various electromagnetic [1, 2] and corpuscular [3–13] effects has received much recognition. The stimulation of oriented growth by ion bombardment seems to be particularly promising. The action of a bombarding beam is localized in an extremely narrow surface layer, and its energy and angle of incidence can be varied in a wide range. Of interest here is that, as ion bombardment parameters change, so do the structure and properties of the films. An example is a decrease in the temperature of Si-on-Si epitaxial growth when the energy of bombarding ions was reduced [3]. In [4], the ion treatment improved the quality of ohmic contacts. Ion-beam-assisted deposition (ion–plasma sputtering of films in combination with ion bombardment at an angle to the surface) has also found wide application [5–7]. The basic advantage of this method is the formation of biaxial texture irrespective of the material type and substrate properties. Also, the substrate can be biased (deposition with bias) [8–13]. With this method, the films grown have been shown to be of high purity [8]. In addition, the elemental composition of the films can be controlled when multicomponent targets are sputtered [9, 10], microstresses in the films can be varied [8, 11, 12], and their crystal structure can be modified [3, 5–13]. It has been repeatedly noted [6, 12, 13] that the effect of ion bombardment on the film properties shows up at the early stage of growth. Thus, ion stimulation allows the control of growth conditions and obtaining of films of practical value. In this work, we report the density (determined by X-ray fluorescent analysis), crystal structure, microstresses, and conductivity of nickel films and gadolinium–cobalt alloy as functions of the bias applied to the substrate during their growth.

Pure nickel films were obtained by the rf (13.56 MHz) diode sputtering of a 100-mm-diam. target in argon at a pressure of 1 Pa. The power and the voltage of the dc bias component applied to the target were 300 W and 1600 V, respectively. Substrates were 48×60-mm ST 50 1–10.6 pyroceramic plates. The target–substrate distance was 100 mm. During the process, the substrate was cooled by water. The frequency of the bias applied to the target and to the substrate was the same. A series of the films where the substrate bias was varied from 0 to –180 V (dc component) were prepared. The deposition time was 30 min in all experiments.

The density of thick films can well be measured by the gravimetric method. Using a balance of class II, one can measure the density of a metal film with a thickness of about 300 nm and a surface area of 5 cm^2 up to 0.35 g/cm^3. For thinner films, the gravimetric method is inapplicable. Therefore, we used X-ray fluorescence spectroscopy, which measures the relative values of the density.

For thin films, an X-ray fluorescence signal I_i varies as ρh, where ρ and h are the film density and thickness, respectively. Note that a film is considered to be thin if the condition $\mu\rho h < 0.1$, where μ is the absorption factor, is satisfied [14]. This condition holds, for example, for Ni films thinner than 1000 nm. In this range of thicknesses, the X-ray fluorescence signal from a film is proportional to its mass and the signal intensity is sufficient for analysis of even ultrathin (about 10 nm

1063-7842/01/4608-1020$21.00

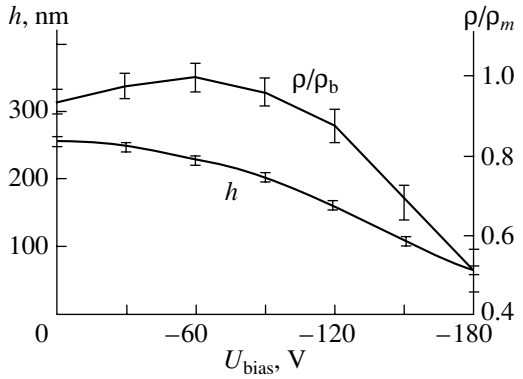

Fig. 1. Density and thickness of the Ni films vs. substrate bias (ρ_b is the density of bulk nickel).

thick) films. Therefore, this method is appropriate for measuring the density of thin films [15]. The signal was calibrated as follows. A reference sample was analyzed by X-ray fluorescence spectroscopy and weighed with a VLR-200 analytic balance with and without a nickel film. The thickness of the films was measured in an STM-2000 tunnel microscope. To do this, a periodic rectangular profile was lithographically patterned on the films. As an etchant, we used a $2H_2SO_4 + 5HNO_3 + 5CH_3COOH + 3H_2O$ solution. The film density was measured by the formula $\rho_i = I_i m_0/(I_0 S_0 h)$, where m_0 is the mass of the reference film, S_0 is its surface area, I_0 is the intensity of its X-ray fluorescence signal, and I_i is the intensity of the signal from a film being analyzed. The relative error in ρ was evaluated according to [16]. The error in measuring the film thickness (6 nm) made a major contribution to the density error. The maximal overall relative density error was found to be 3.8% (for the film deposited at the bias –180 V). The error can be decreased by using smoother substrates.

Figure 1 shows the thickness and density of the nickel films vs. substrate bias relative to the housing of the reactor. The density of bulk nickel is 8.91 g/cm^3 [17]. The maximal density of the film, 8.9 ± 0.7 g/cm^3 was obtained for the bias –60 V. The thickness of the films deposited at small biases grows insignificantly with increasing bias. This is possibly because the films become more compact. With a further rise in the bias voltage, the thickness decreases because of enhanced re-evaporation. The density also drops in this case because of argon and residual gas atoms incorporated into the films.

The crystal structure of the films was analyzed with DRON-3M X-ray diffractometer (FeK_α radiation with the wavelength 0.1938 nm). At the biases 0 and –30 V, the Ni films grew polycrystalline, as indicated by a series of reflections [(111), (200), and others] in the diffraction patterns (Fig. 2, curve *1*). At the other biases, the films exhibit (111) texture, since there are no reflections except (111) and (222) in the diffraction patterns (Fig. 2, curve *2*).

To reveal a preferential direction in the substrate plane, the (200) pole figure was taken [18]. The figure has a ring at the angle $\alpha = 54.7°$; hence, the texture is axial (Fig. 3). The $\langle 111 \rangle$ axis of the texture runs normally to the substrate surface. Figures 4 and 5 depict the (111) reflection intensity reduced to the film thickness, interplanar spacing $d_{(222)}$, size of coherently scattering blocks, and microstresses against bias voltage applied to the substrate. It is seen that the crystallinity (reflection intensity) of the Ni films vs. substrate bias

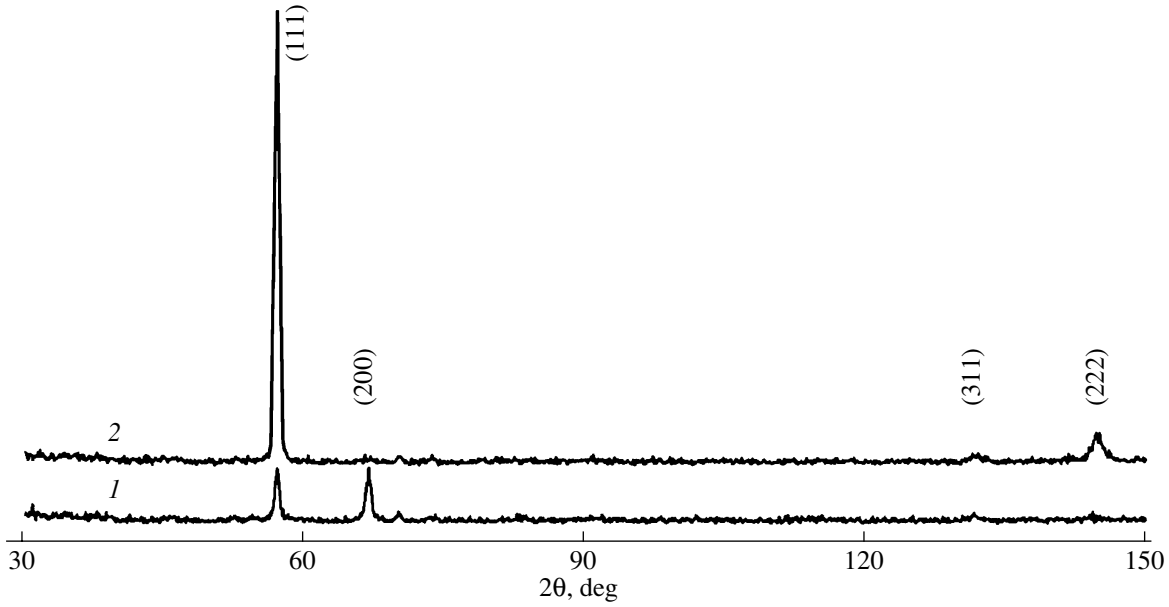

Fig. 2. X-ray diffraction patterns for the Ni films. The substrate bias is (*1*) 0 and (*2*) –90 V.

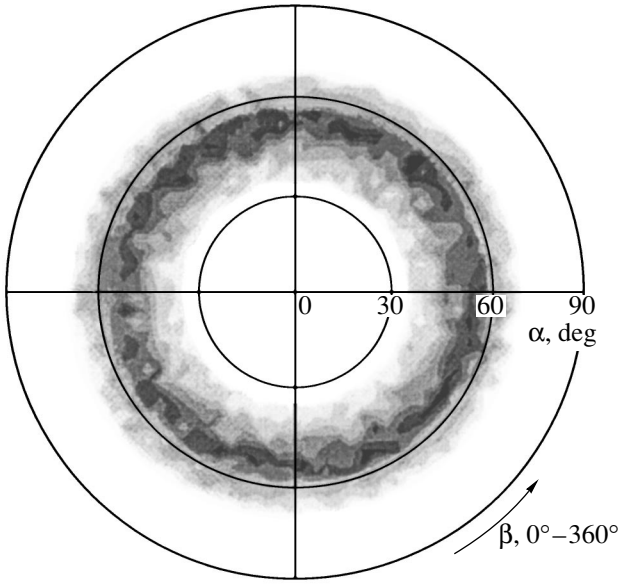

Fig. 3. (200) pole figure for the Ni film. The substrate bias is –60 V.

dependence is similar to the density–bias dependence. There are, however, two essential points worth noting.

First, the maximum of the (111) reflection intensity, i.e., the maximum content of the crystal phase in the film, is observed at the bias –90 V. Then, the half-width of the rocking curves for the (111) reflections is the least (10°) at –90 V. That is, at this bias voltage, the misorientation of the grains relative to the texture axis is the least, 5°. However, the crystal perfection is the best for the films grown at –60 rather than –90 V, which the least microstresses and the largest size of the blocks indicate.

Second, the interplanar spacings $d_{(222)}$ in the films are always smaller than in the bulk metal (0.1017 nm), which was analyzed under the same conditions. The interplanar spacing $d_{(200)}$ in the film obtained at –60 V equals that of the bulk sample. Since the film has the axial (111) texture, the spacing $d_{(200)}$ was determined when it was tilted at an angle of 54.7°. The density of the film estimated from $d_{(222)} = 0.1016$ nm was found to be 8.9 ± 0.1 g/cm^3, which is somewhat larger than that measured by the above technique. This discrepancy may be explained by grain-boundary disordering.

The resistivity is an important parameter that characterizes the material structure. The resistivity of the films was calculated by measuring the sheet resistivity and the thickness. The bias dependence of the resistivity of the Ni films is shown in Fig. 6.

The resistivity of bulk nickel was measured to be 6.14×10^{-6} Ω cm [17]. In the range of small substrate biases, the resistivity of the films drops with increasing substrate bias and attains its minimum at –40 V. Comparing this result with the data of structure analysis, one can assume that the density of defects in the intergranular space is significant at small biases, although the structure of individual grains is more perfect at larger biases (–60…–90 V).

The bias dependences of the film properties can be explained as follows. In general, the film growth can be divided into two competing processes: mass transfer (both to and from the substrate) and atomic ordering of a growing film (or the formation of its crystalline state). Both are sensitive to changes in the physical state of the substrate (both uncovered and covered by a growing film). For example, if the films grow without ion stimulation, a rise in the substrate temperature, as a rule, results in film ordering. At the same time, the rate of reevaporation of the films also increases because the amplitude of thermal vibration grows. That is, with the target atom flux toward the substrate remaining unchanged, the backward atom flux builds up. In our experiment, ion bombardment serves as an alternative to heating. However, the effects of the two processes markedly differ. As the substrate temperature increases during heating, adatoms have more time to migrate over the surface of a growing film. The growth becomes pro-

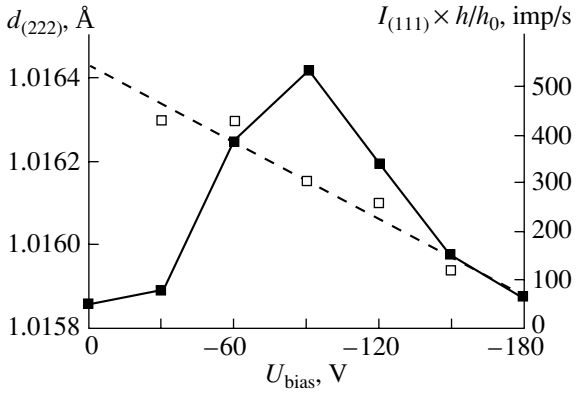

Fig. 4. (■) (111) reflection intensity reduced to the film thickness and (□) interplanar spacing $d_{(222)}$ as functions of substrate bias.

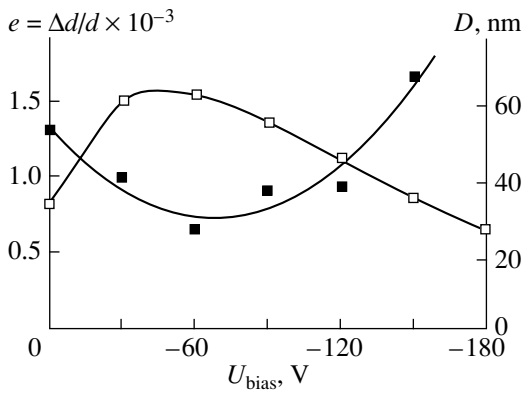

Fig. 5. (□) Size of coherently scattering blocks and (■) microstresses in the Ni films vs. substrate bias.

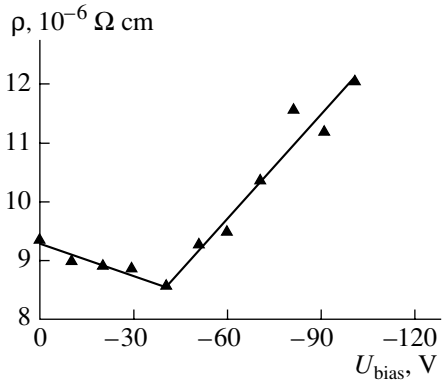

Fig. 6. Resistivity of the Ni films vs. substrate bias.

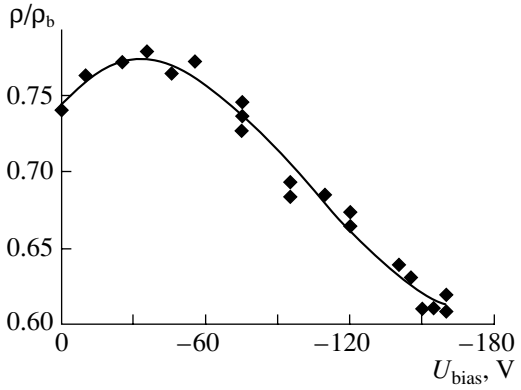

Fig. 7. Relative density of the GdCo films vs. substrate bias.

gressively equilibrium and the films more and more ordered. In most cases, the totally equilibrium epitaxial growth takes place when the substrate temperature is close to two-thirds of the melting point of the film material [19]; that is, when the balance between the rate of material delivery to the substrate, rate of re-evaporation, and time of migration of adatoms is set. At low temperatures (the substrate is cooled by force), the growth is essentially nonequilibrium largely because of the short time of adatom migration. However, the time of migration can be extended by bombarding the growing film surface by low-energy ions of inert gases. In our experiment, this is done by applying an rf bias to the substrate. Moreover, computer simulation shows [20] that ion bombardment causes local stress relaxation at the site of an ion impact and modifies the crystal structure within 1 nm or more away from the film surface (the distance depends on the ion energy). It is also believed [8] that ion bombardment removes primarily foreign, rather than nickel, atoms from the surface, since impurity atoms are weakly bonded to the surface, thereby providing more ordered growth and increasing the conductivity of the films. One advantage of ion-assisted film growth is that ions effectively act only on the near-surface region of the substrate (on the order of several or several tens of atomic layers depending on the ion energy). This enables the application of highly ordered dense films on substrates that cannot be heated because of their degradation.

The energy of Ar ions bombarding the substrate surface can be estimated by the formula $E_i = e|V_p - V_b|$, where e is the charge of an electron, V_p is the plasma potential, and V_b is the dc bias applied to the substrate. The plasma potential was measured with a cylindrical Langmuir probe and turned out to be roughly 15 V in all experiments. The density of the argon ion flux toward the substrate was determined from the formula $P_{Ar} = W/E_{Ar}$, where W is the density of the power flux toward the substrate and E_{Ar} is the ion argon energy. The density of the target-to-substrate atom flux was evaluated

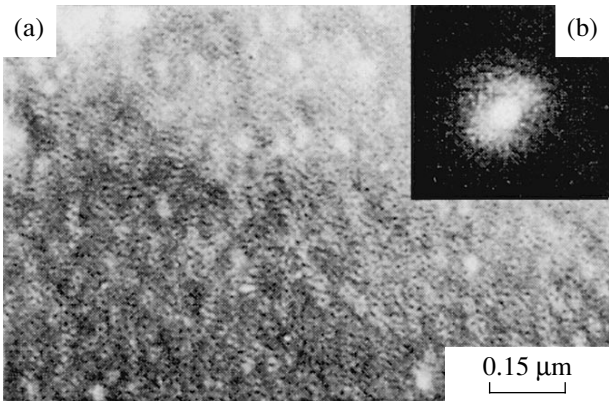

Fig. 8. (a) Bright-field image of the surface morphology of the amorphous GdCo film after amplitude filtration and (b) electron diffraction pattern.

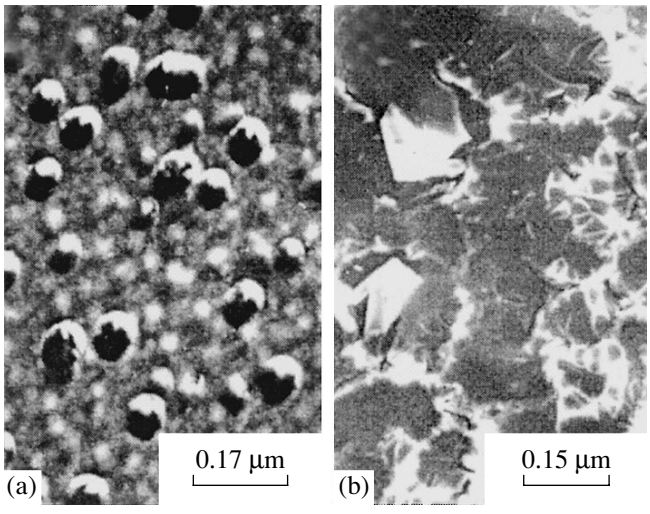

Fig. 9. Bright-field images of the surface morphology of the GdCo films at the biases (a) –90 and (b) –100 V.

Table

Bias, V	Density, g/cm^3	Thickness, nm	Ion flux density, 1/(cm^2 s)	Atom flux density, 1/(cm^2 s)	Re-evaporated atom flux density, 1/(cm^2 s)
0	8.4	254	4.17×10^{14}	1.24×10^{15}	2.46×10^{13}
–30	8.7	249	1.94×10^{15}	1.24×10^{15}	–
–60	8.9	225	2.83×10^{15}	1.24×10^{15}	9.85×10^{13}
–90	8.6	200	3.57×10^{15}	1.24×10^{15}	2.63×10^{14}
–120	7.8	160	3.82×10^{15}	1.24×10^{15}	5.26×10^{14}
–150	6.1	108	4.55×10^{15}	1.24×10^{15}	8.66×10^{14}
–180	4.6	65	4.89×10^{15}	1.24×10^{15}	1.07×10^{15}

by the formula $P_{Ni} = \rho h/(m_A t)$, where ρ and h are the density and the thickness of the film, respectively; m_A is the atomic mass of Ni; and t is the film deposition time. The associated values are summarized in the table.

The atomic flux density listed in the table was determined from the maximal mass of the nickel film. The mass was maximal at the bias –30 V, i.e., when the re-evaporation of the atoms from the substrate is the least. The last column of the table lists the re-evaporation flux density for these conditions.

The same bias dependence of the density was observed for amorphous films of binary alloys of *d* and *f* metals. $Gd_{0.23}Co_{0.77}$ films were obtained by ion–plasma dc sputtering onto water-cooled glass substrates [21]. The argon pressure in the process was 2.25×10^{-2} Pa, and the voltage across the target, 1.5 kV. The thickness of the films that was measured by the Fizeau interferometric method [22] was found to be 80 nm. Ion irradiation was performed at substrate biases ranging from 0 to –160 V relative to the housing of the reactor. Figure 7 plots the relative density of the GdCo films against substrate bias. The density determined experimentally is normalized to the calculated density that is the weighted average of the densities of pure Co (8.9 g/cm^3) and Gd (7.95 g/cm^3).

It is seen that the curve in Fig. 7 is in many ways similar to that for the Ni films. As the bias is raised, the density first increases, peaking at –30…–50 V (ρ/ρ_b = 0.78), and then sharply drops. Figures 8a and 8b show, respectively, a TEM image of the GdCo film obtained at the bias voltage –40 V and an electron diffraction pattern for this film (JEOL-200 transmission electron microscope). It is seen that the biasing of the substrate results in the growth of the films with a complex periodic surface morphology. Fine irregularities (10–30 nm in size) aggregate to form 100- to 150-nm clusters; the latter aggregate into coarser (700–1000 nm) ones; etc. At larger bias voltages, the films become more porous. This can be explained by working and residual gases incorporated into the films (Fig. 9a) and microstresses developed. Eventually, the microstresses result in blistering (Fig. 9b).

Thus, we have shown that the properties of the films can be controlled by using ion stimulation. Specifically, at low substrate biases, the films grow denser and more ordered than those obtained without biasing. At high biases, ion bombardment causes defects in the films; hence, the density lowers and the crystal structure worsens. It has been demonstrated that the effect of ion stimulation on the density is the same for the nickel and GdCo films.

ACKNOWLEDGMENTS

This work was financially supported by the Russian Foundation for Basic Research (grant no. 98-02-16581).

REFERENCES

1. H. Akazava, J. Appl. Phys. **79**, 9396 (1996).
2. H. Gleiter and B. Chalmers, *High-Angle Grain Boundaries* (Pergamon, Oxford, 1972; Mir, Moscow, 1975).
3. W. Shindo and T. Ohmi, J. Appl. Phys. **79**, 2347 (1996).
4. S. P. Morgan and D. V. Morgan, Thin Solid Films **272**, 107 (1996).
5. L. S. Yu, J. M. E. Harper, J. J. Cuomo, *et al.*, J. Vac. Sci. Technol. A **4**, 443 (1986).
6. K. G. Lesler, N. Sonnenberg, and M. J. Cima, J. Electron. Mater. **25**, 35 (1996).
7. Y. Iijima, K. Onabe, N. Futaki, *et al.*, J. Appl. Phys. **74**, 1905 (1993).
8. *Handbook of Thin-Film Technology*, Ed. by L. I. Maissel and R. Glang (McGraw-Hill, New York, 1970; Sov. Radio, Moscow, 1977), Vol. 1.
9. A. Nakagawa, M. Sugiura, and Y. Okabe, Jpn. J. Appl. Phys. **30**, L993 (1991).
10. L. Li and W. B. Nowak, J. Vac. Sci. Technol. A **12**, 1587 (1994).
11. A. Misra and M. Nastasi, Appl. Phys. Lett. **75**, 3123 (1999).
12. K.-F. Chiu, M. G. Blamire, and Z. H. Barber, J. Vac. Sci. Technol. A **17**, 2891 (1999).
13. V. V. Naumov, V. F. Bochkarev, and O. S. Trushin, Neorg. Mater. **34**, 57 (1998).

14. *X-ray Fluorescence Analysis*, Ed. by N. F. Losev (Nauka, Novosibirsk, 1991).
15. O. S. Trushin, V. F. Bochkarev, A. A. Goryachev, *et al.*, Zavod. Lab. **66**, 39 (2000).
16. P. Täubert, *Abschätzung der Genauigkeit von Messergebnissen* (Berlin, 1987; Énergoatomizdat, Moscow, 1988).
17. *Physical Quantities: Handbook*, Ed. by I. S. Grigor'ev and E. Z. Rastorguev (Énergoizdat, Moscow, 1991), p. 99.
18. Ya. S. Umanskiĭ, Yu. A. Skakov, A. N. Ivanov, and L. N. Rastorguev, *Crystallography, X-ray Radiography and Electron Microscopy* (Metallurgiya, Moscow, 1982).
19. L. S. Palatnik, M. Ya. Fuks, and V. M. Kosevich, *Mechanism of Formation and Substructure of Condensed Films* (Nauka, Moscow, 1972).
20. B. Stricklan and C. Roland, Phys. Rev. B **51**, 5061 (1995).
21. V. F. Bochkarev, A. A. Goryachev, and V. V. Naumov, RF Inventor's Certificate No. 2 046 840 (1995).
22. *Physics of Thin Films: Advances in Research and Development*, Ed. by G. Hass and R. Thun (Academic, New York, 1967; Mir, Moscow, 1970), Vol. IV.

Translated by V. Isaakyan

Technical Physics, Vol. 46, No. 8, 2001, pp. 1026–1036. Translated from Zhurnal Tekhnicheskoĭ Fiziki, Vol. 71, No. 8, 2001, pp. 98–108.

EXPERIMENTAL INSTRUMENTS AND TECHNIQUES

On the Longitudinal Stability of Technogenic Ionized Formations

A. P. Elokhin

Received September 4, 2000; in final form, November 10, 2000

Abstract—A mechanism behind the longitudinal stability of technogenic ionized formations in air is considered. Air is ionized by radioactive emergency ejections from dangerous plants. The stability mechanism is based on cloud polarization when unlike heavy ions are separated under the action of the force of gravity. The longitudinal and transverse distributions of the heavy ions (charged water drops), as well as the distribution of their difference, calculated in a cylindrical coordinate system agree well with experimental data found in the literature. The reflection coefficient for electromagnetic waves reflected from an ionized air layer is derived. The wavelength dependence of the absolute value of the reflection coefficient is consistent with experimental and analytic data for the centimeter range of wavelengths. A range where the magnitude of the reflection coefficient sharply grows is found. *© 2001 MAIK "Nauka/Interperiodica".*

It has been shown [1] that ionized formations, plasmoids, appear over the underlying surface polluted by radioactive impurities. They take the form of bodies of revolution, such as cylinders, ellipsoids, truncated cones, etc. The cross size of the plasmoids depends, in general, on the polluted area of the underlying surface. Typically, they measure several tens to several hundred meters across and no less than several hundred meters in height [1]. As follows from natural experiments, these formations are stable against environmental effects (wind, moisture, etc.). In-depth investigation into the effect of reflection of electromagnetic waves from the plasmoids [1] requires some of their parameters, namely, stability, uniformity of the spatial ion distribution, and dependence of the reflection coefficient on the length of a wave scanning the plasmoids, to be refined. The last property is of special importance, since the authors of [2], studying the centimeter range, detected the effect of reflection only when a very sensitive detector was used.

When considering ionized formations in the atmosphere, i.e., in a mixture of gases where oxygen accounts for 21%, it should be recognized that the formations are largely ion–ion, rather than ion–electron, clusters. Indeed, in air, the lifetime of a free electron before it is captured by an oxygen molecule (atom) is $\tau_c \sim 1/k_c N_{O_2} \approx 2 \times 10^{-9}$ s ($k_c = 8.85 \times 10^{-11}$ cm^3/s is the coefficient of capture of a free electron by a neutral atom or molecule, $N_{O_2} = 0.21N_0$ cm^{-3} is the concentration of oxygen molecules in air, and $N_0 = 2.75 \times 10^{19}$ cm^{-3}). The rate k_{ei} of electron–ion recombination is $\approx 10^{-7}$ cm^3/s. Let us assume that, as a result of a radiation accident, an ejection with a dose rate as high as I = 1 R/h (strong accident) takes place. Then, for the radiation yield of electron–ion pairs $G = 2.08 \times 10^9$ R^{-1} cm^{-3}, the concentration of electrons in air will be $N_e = N_+ \approx \sqrt{GI/k_{ei}} = 2.4 \times 10^6$ cm^{-3}. The lifetime of an electron to recombination with an ion is $\tau_r \sim 1/k_{ei}n_e \approx 4$ s. Comparing τ_c and τ_r, we see that, after thermalization, an electron generated as a result of atom or molecule ionization is captured by a neutral oxygen atom or molecule within 2 ns to produce a negatively charged ion. It is easy to check that the resulting concentrations of the positive, N_+, and negative, N_-, ions, as well as the resulting concentration of the electrons N_e, can be estimated (under steady-state radiation conditions) from a set of equations

$$GI - k_{ii}N_+N_- - k_{ei}N_+N_e = 0,$$
$$N_+ = N_- + N_e,$$
$$GI - k_cN_0N_e - k_{ei}N_+N_e = 0$$

up to the spontaneous decay of the negative ions. This set is reduced to the third-order equation

$$k_{ei}N_+^3 + k_cN_0k_{ei}N_+^2 - k_{ei}GIN_+ - GIk_cN_0k_{ei}/k_{ii} = 0.$$

Its solution yields the concentrations

$$N_e = [GI - k_{ei}N_+^2]/[k_cN_0(1 - k_{ei}/k_{ii})],$$
$$N_- = N_+ - N_e.$$

For the constants given above and the ion–ion recombination rate $k_{ii} = 1.6 \times 10^{-6}$ cm^3/s, the associated values are $N_+ = 6.021 \times 10^5$ cm^{-3}, $N_- \approx 6.021 \times 10^5$ cm^{-3}, and $N_e = 1.036 \times 10^{+3}$ cm^{-3}. Such a great difference between the concentrations of the ions and the electrons is due to the fact that, even for such a high dose rate, the concentration of oxygen is 10^{13} times greater than that of the positive ions. Therefore, at the residence time of

1063-7842/01/4608-1026$21.00

the plasmoids in the real atmosphere and especially in its boundary layer, where the plasmoids form, $\tau_{res} = 2$–3 μs, they must be treated as ion–ion, rather than ion–electron, formations.[1] Below, we show that the capture of molecular water ions results in ion–drop formations. Under terrestrial conditions, one can consider electron–ion plasma formations if the lifetime of free electrons is long. Their lifetime can be increased, for example, by decreasing the pressure in the upper atmosphere. This subject, however, is beyond the scope of this report. With regard for the electron and ion concentrations found, the air permittivity in the polluted region of the underlying surface is given by [3]

$$\varepsilon = 1 - \frac{4\pi N_e e^2}{m_e(\omega^2 + \nu^2)} - \frac{4\pi N_+ e^2}{M_+(\omega^2 + \nu^2)} - \frac{4\pi N_- e^2}{M_-(\omega^2 + \nu^2)}$$

$$\approx 1 - \frac{4\pi e^2 N_i}{(\omega^2 + \nu^2)M_i}\left(2 + \frac{N_e M_i}{m_e N_i}\right),$$

where ν is the collision frequency, ω is the electromagnetic wave frequency, $M_+ = M_- = M_i$ is the mass of an ion, m_e is the mass of an electron, and $N_i \approx N_+ \approx N_-$.

Taking the mass of an oxygen molecule as the mass of an ion in the above expression, we find that the effect of electrons on the permittivity is negligible, since $M_i N_e/m_e N_i \approx 10^{-4} \ll 1$ for the values of N_e and N_i found. This inequality holds for the mass of heavy ions up to $10^3 M_i$.

In this work, we take into account that the plasmoids form in the real atmosphere, which is characterized by some humidity and ion composition [4]. These properties must be included in the description of the physical structure of the plasmoids. Moreover, such an approach must provide a better insight into the conditions for plasmoid stability. In fact, the presence of moisture in the region of the accident (it is assumed that either the underlying surface is polluted, an emission of radioactive gases and/or aerosols takes place, or a radioactive gas like radon evolves from breaks in the Earth's crust as a predecessor to an earthquake [5]) must lead to the production of heavy ions. Their mobility and diffusion coefficient are much lower than those of light ions. Accordingly, transfer conditions for the heavy and light ions will also differ. This must affect the condition for longitudinal plasmoid stability. In addition, the heavy ions, unlike the light ones, experience the force of gravity, which causes spatial charge separation. The hypothesis that heavy ions can be separated by the force of gravity (negative ions are heavier) was used by Frenkel to explain the polarization and the mechanical stability of clouds in ascending air [6]. Following [6], we assume that, in the presence of moisture, positive and negative ions produced as a result of air ionization by γ and β sources in the surface area polluted by radioactive aerosols form hydrated complex ions of both signs [4].

[1] Similar conclusions were made in [2].

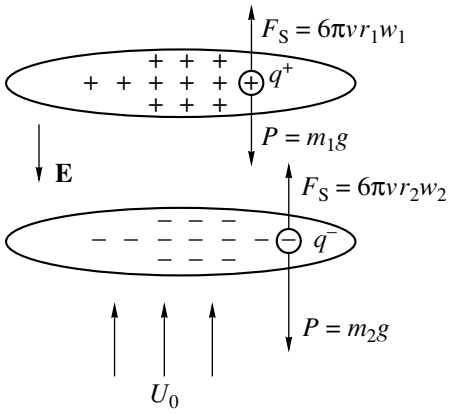

Fig. 1. Polarization of the water cloud in the atmosphere when ions are captured by water drops or dust microparticles.

Let us consider the motion of water drops of masses m_1 and m_2, radii r_1 and r_2 ($r_1 \ll r_2$), and charges q^+ and q^-. When moving, the drops experience the force of gravity mq, Stokes force $F_S = 6\pi\nu r_1 w$, and force of electrostatic interaction $F = Eq^{\pm}$; here, g is the gravitational acceleration, ν is the dynamic air viscosity, w is the velocity of relative motion, and E is the strength of the electric field due to the polarization of an ionized layer. The resulting motion of either drop (Fig. 1) is described by the equations

$$m_1\frac{dw}{dt} = m_1 g - 6\pi\nu r_1 - w_1 + Eq^+,$$

$$m_2\frac{dw}{dt} = m_2 g + -6\pi\nu r_2 w_2 - Eq^-.$$

If initially the drops were at rest, the solutions of the equations have the form

$$w_1 = \frac{m_1 g + Eq^+}{6\pi\nu r_1}\left[1 - \exp\left(-\frac{6\pi\nu r_1 t}{m_1}\right)\right],$$

$$w_2 = \frac{m_2 g - Eq^-}{6\pi\nu r_2}\left[1 - \exp\left(-\frac{6\pi\nu r_2 t}{m_2}\right)\right].$$

For the steady motion at $r_2 = 10^{-3}$ cm and $t \gg \tau_{max} = m_2/6\pi\nu r_2 = 2\rho r_2/9\nu \approx 10^{-3}$ s (i.e., when $w_1 = w_2$), the electric field strength for $m = (4/3)\pi\rho r^3$ is given by

$$E = g\frac{m_2 r_1 - m_1 r_2}{q(r_2 + r_1)} = \frac{4}{3}\pi\rho g r_1 r_2 \frac{r_2 - r_1}{q}.$$

At $r_1 = 10^{-4}$ cm, $r_2 = 10^{-3}$ cm, $\rho = 1$ g cm^{-3}, and $q = e = 1.6 \times 10^{-19}$ C, $E \approx 2.5 \times 10^5$ V/cm, whereas the terrestrial electric field is ≈1.3 V/cm. Note that, as the air humidity rises, so does the breakdown field [7]. The

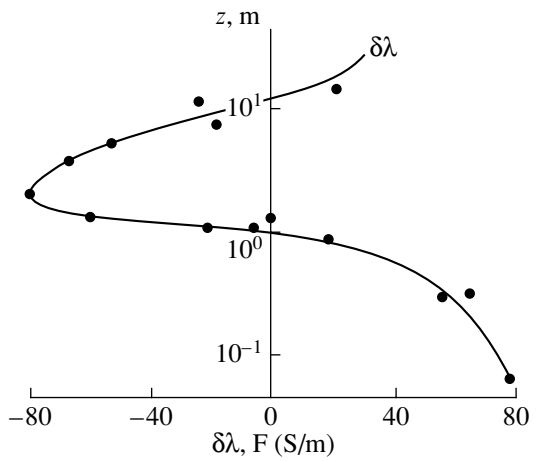

Fig. 2. Height profile of the difference in the air conductivity $\delta\lambda = (\lambda_+ - \lambda_-)$. The testing ground (Institute of Experimental Meteorology) was 7 km from the emergency unit of the Chernobyl nuclear power station (May 18, 1987) [8]. F, conductivity of the background.

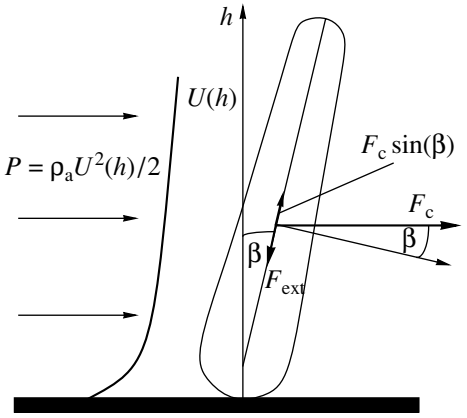

Fig. 3. Illustration of the longitudinal stability of the plasmoids.

velocity of the steady collective motion of the drops is

$$w = \frac{2\rho g}{9\nu}[r_2^2 - r_1 r_2 + r_1^2]$$

or

$$w = \frac{2\rho g}{9\nu} r_2^2$$

at $r_2 \gg r_1$. For the given values of the parameters and $\nu = 1.94 \times 10^{-5}$ kg/(m s), w is about 1 cm/s. Thus, in the presence of moisture or dust, aeroions resulting in the radiation field of a radiation source generate heavy ions, which produce water or dust clouds that polarize under gravity. Compelling evidence in favor of such a mechanism is the height profile of the difference in the conductivity $\delta\lambda = (\lambda_+ - \lambda_-)$ [8] (Fig. 2). According to [6], aeroions are entrained by ascending air (with the typical stream velocity 1 m/s) and are trapped by water drops with the formation of heavy (largely negative) ions. Then, the heavy ions are separated into positive and negative ions under gravity. The positive ions, together with positively charged droplets or dust microparticles adsorbing positive charge from air, and the negative ions form a layered structure. Its longitudinal stability will depend on both the force of electrostatic interaction between the layers and the constancy of the velocity of ascending air. Now we will evaluate the force of electrostatic interaction, considering the structure as a plane capacitor with the surface charge $\sigma = \epsilon\epsilon_0 E$, where E is the electric field strength found earlier and $\epsilon_0 = 8.85 \times 10^{-12}$ F/m. If the weight of the capacitor "plates" cannot be ignored, the energy of their electrostatic interaction ($CU^2/2$, where C is the capacitance and U is the potential difference between the plates) should be counterbalanced by the work of external forces $F_{ext}d$, where d is the equilibrium spacing between the plates. From the equality $CU^2/2 = F_{ext}d$, we find $F_{ext} = CU^2/2d$. For a plane capacitor, $C = \epsilon\epsilon_0 S/d$ and $U = Q/C$, where $Q = \sigma S$. Thus, $F_{ext} = \epsilon\epsilon_0 SE^2/2$. Then, for $\epsilon = 1$ (for air) and $S = \pi R_0^2$ ($R_0 = 5$ m is the plasmoid radius), $F_{ext} = 2.17 \times 10^5$ N. Clearly, this force will increase with drop size, since the field strength grows as the drop radius squared. For an air stream velocity $U_0(h)$, let us find the component of the force F_c that causes the collapse of a plasmoid when it is subjected to the air stream (Fig. 3). At a pressure of the air stream $P = \rho_a U_0^2(h)/2$, where ρ_a is the density of air,

$$F_c = \frac{\rho_a}{2}\int_0^h U_0^2(h)\,ds, \quad \text{where} \quad ds = 2R_0\,dh.$$

Approximating $U_0(h)$ by $u_{z_0}(h/z_0)^m$, we find for $z_0 = 10$ m and $m = 0.5$ [9]

$$F_c = \frac{\rho_a}{2} u_{z_0}^2 2R_0 \left(\frac{h}{z_0}\right)^{2m} \frac{h}{2m+1} \quad \text{and} \quad \bar{F}_c = \frac{1}{H}\int_0^H F_c(h)\,dh.$$

For the given values of the parameters and $H = 500$ m, we obtain

$$\bar{F}_c = \frac{\rho_a u_{z_0}^2 R_0 H}{(2m+1)(2m+2)}\left(\frac{H}{z_0}\right)^{2m}.$$

At $u_{z_0} = 3$–5 m/s, $\bar{F}_c$ makes $(2.25$–$6.25) \times 10^5$ N. When the plasmoid is off the vertical axis by the angle $\beta = 10°$, the collapsing component of $\bar{F}_c$ equals $\bar{F}_c \sin\beta \approx 3.9 \times 10^4$–$1.09 \times 10^5$ N; that is, this component is either much smaller than or comparable to F_{ext}. As the wind velocity increases, so does the inclination. At $\beta = 15°$, $\bar{F}_c \sin\beta \approx 1.62 \times 10^5$ N. Thus, if the wind velocity is such that the deflection of the plasmoid from

the vertical axis is within some limiting value $\beta_{lim} \approx \arcsin(F_{ext}/\bar{F}_c)$, it can be said that the plasmoid is longitudinally stable under given conditions and that such objects of the technogenic origin do exist and form in ascending air.

Now that the basic mechanisms responsible for the stability of the plasmoids have been understood, let us derive a set of equations for concentrations of aeroions and heavy ions, as well as for the amount of condensed moisture, which favors the formation of the ions. Then, we will briefly discuss methods for measuring basic parameters that are necessary to determine the concentrations.

The relative humidity D at a given temperature of ambient air is defined as $D = P/P_{sat}(T)$, where P is the partial vapor pressure at the temperature T (desired quantity), P_{sat} is the partial (saturated) vapor pressure under thermodynamic equilibrium at the given temperature (Table 1), D is the parameter to be measured, and $P = DP_{sat}$. From the Avogadro law $PV = (m/\mu)RT$, where V is the volume considered (hereafter, we consider the unit volume, $V_u = 1$ cm^3), m is the vapor (water) mass, μ is the gram-molecular mass of water ($\mu_{H_2O} = 18$), and R is the gas constant, we obtain $m = PV_u/RT$ or $m = DP_{sat}V_u/RT$. Let us approximate a water drop by a sphere of radius r (the value of r is found by averaging over a drop ensemble with the volume spectrum in the form $f(V) = Ae^{-V/V_0}$; A is determined from the expression $A\int_0^\infty f(V)dV = N_d$, where N_d is the number of drops per unit volume, that is, their concentration [6]). Since $V = 4\pi r^3/3$, the function $f(V)$ in terms of the radius takes the form $f(r) = B\exp(-r/r_0)^3r^2dr$ and we find

$$\bar{r} = \left[\int_0^\infty e^{-(r/r_0)^3} r^3 dr\right] \Big/ \left[\int_0^\infty e^{-(r/r_0)^3} r^2 dr\right].$$

Taking the integral in the numerator, we come to

$$\int_0^\infty e^{-(r/r_0)^3} r^3 dr = \frac{1}{3}\left(\frac{1}{r_0^3}\right)^{-\frac{4}{3}}\Gamma\left(\frac{4}{3}\right) = r_0^4\frac{1}{9}\Gamma\left(\frac{1}{3}\right),$$

where $\Gamma(z)$ is the gamma function and $\Gamma(z + 1) = z\Gamma(z)$.

Calculating the denominator yields $r_0^3/3$, so that we find $\bar{r} = 0.893r_0$. The value of $\bar{r}$ allows us to determine the water mass per unit volume via the expression $m = (4/3)\pi r^3\rho N_d$, where $\rho = \rho(T)$ is the density of water (Table 2). Eventually, N_d is given by

$$N_d = \frac{3DP_{sat}(T)\mu}{4\pi\bar{r}^3\rho(T)RT}V_u.$$

For the relative humidity D ranging from 50 to 100%, $t = 20$°C ($T = 293$ K), $R = 461$ J/(kg K), and $r_0 = 10^{-3}$ cm, N_d is roughly equal to ~10^5. Given the velocity of air rise due to convection $U_0 = 10^2$ cm/s and the steady velocity of drop fall relative to air $w = 1$ cm/s, we will derive a set of equations that describe the forma-

Table 1. Temperature dependence of the saturated water vapor pressure P_{sat} [10]

t, °C	P, kPa	t, °C	P, kPa
–5	0.401	12	1.401
–4	0.437	13	1.497
–3	0.463	14	1.597
–2	0.517	15	1.704
–1	0.563	16	1.817
0	0.611	17	1.937
1	0.656	18	2.062
2	0.705	19	2.196
3	0.757	20	2.337
4	0.813	21	2.486
5	0.872	22	2.642
6	0.953	23	2.809
7	1.005	24	2.984
8	1.072	25	3.168
9	1.148	26	3.361
10	1.227	27	3.565
11	1.312	28	3.780

Table 2. Temperature dependence of the water density ρ [10]

t, °C	ρ, g/cm^3	t, °C	ρ, g/cm^3
0	0.999841	16	0.998943
1	0.999900	17	0.998775
2	0.999941	18	0.998596
3	0.999965	19	0.998406
4	0.999973	20	0.998205
5	0.999965	21	0.997994
6	0.999941	22	0.997772
7	0.999902	23	0.997540
8	0.999849	24	0.997299
9	0.999782	25	0.997047
10	0.999701	26	0.996785
11	0.999606	27	0.996515
12	0.999498	28	0.996235
13	0.999377	29	0.995946
14	0.999244	30	0.995649
15	0.999099		

tion of the plasmoids when the underlying surface area of radius R_0 is polluted by γ and β sources of dose rate H R/s. Assume that the decay period of the radioactive contamination far exceeds the time it takes for aeroions to be entrained by the air flow to a height of 1 km. Then, we are dealing with the steady-state conditions and the terms with the time derivatives of the desired functions can be set equal to zero. Taking into account that fast electrons, whose range in air is 1.5–2.0 m, make a major contribution to ionization, we represent the source of ionizing radiation as a cylinder of radius R_0 and height z_0. In this case,

$$H(r, z) = H_0[\eta(r) - \eta(r - R_0)][\eta(z) - \eta(z - z_0)].$$

Assuming that heavy ions are singly charged[2] and that the equalities $N_0^+ = N_0^- = N_0^\pm = \sqrt{GH/k_r}$ for aeroions are valid, we write a set of equations in terms of the diffusion–drift model:

$$k_c^p N_0^+ N_\mathrm{d}^s - k_r N_\mathrm{d}^+ N_0^- - k_r N_\mathrm{d}^+ N_\mathrm{d}^- - \mu_+^W \mathbf{E}\,\mathrm{grad}(N_\mathrm{d}^+) - \mu_+^W N_\mathrm{d}^+ \mathrm{div}(\mathbf{E}) - \mathbf{U}_1 \mathrm{grad}(N_\mathrm{d}^+) + D_+^W \mathrm{div}[\mathrm{grad}(N_\mathrm{d}^+)] = 0; \quad (1)$$

$$k_c^n N_0^- N_\mathrm{d}^g - k_r N_\mathrm{d}^- N_0^+ - k_r N_\mathrm{d}^+ N_\mathrm{d}^- + \mu_-^W \mathbf{E}\,\mathrm{grad}(N_\mathrm{d}^-) - \mu_-^W N_\mathrm{d}^- \mathrm{div}(\mathbf{E}) - \mathbf{U}_1 \mathrm{grad}(N_\mathrm{d}^-) + D_-^W \mathrm{div}[\mathrm{grad}(N_\mathrm{d}^-)] = 0; \quad (2)$$

$$\mathrm{div}\mathbf{E} = \frac{e}{\varepsilon\varepsilon_0}[N_\mathrm{d}^+ - N_\mathrm{d}^-]; \quad (3)$$

and the quasi-neutrality condition

$$N_\mathrm{d}^+ - N_\mathrm{d}^- = 0. \quad (4)$$

Here, k_r is the recombination coefficient; k_c^p and k_c^n are the coefficients of capture of positive and negative ions by small and large drops, respectively (N_d^s and N_d^l are the respective concentrations of small and large drops); and μ_-^W, μ_+^W, D_-^W, and D_+^W are the mobilities and diffusion coefficients, respectively, for the heavy ions.

With the z axis directed upward, we have $\mathbf{U}_1 = (U_0 - w)\mathbf{e}_z$. For the cylindrical geometry in view of the azimuth homogeneity of the problem,

$$\mathbf{E} = E_z\mathbf{e}_z + E_r\mathbf{e}_r, \quad \mathrm{grad}(N) = \frac{\partial N}{\partial r}\mathbf{e}_r + \frac{\partial N}{\partial z}\mathbf{e}_z;$$

$$\mathrm{div}\mathbf{E} = \frac{1}{r}\frac{\partial}{\partial r}(rE_r) + \frac{\partial}{\partial z}(E_z);$$

$$\mathrm{div}[\mathrm{grad}(N)] = \frac{1}{r}\frac{\partial}{\partial r}\left(r\frac{\partial N}{\partial r}\right) + \frac{\partial^2 N}{\partial z^2}.$$

[2] Heavy ions can also be multiply charged, as shown in [6].

The boundary conditions are as follows:

$$\left.\frac{\partial N_\mathrm{d}^-}{\partial r}\right|_{r=0} = \left.\frac{\partial N_\mathrm{d}^+}{\partial r}\right|_{r=0} = 0, \quad (5)$$

$$N_\mathrm{d}^-(r, z)|_{t\to\infty} = N_\mathrm{d}^+(r, z)|_{t\to\infty} = 0, \quad (6)$$

$$N_\mathrm{d}^-(r, z)\big|_{z\to\infty} = N_\mathrm{d}^+(r, z)\big|_{z\to\infty} = 0. \quad (7)$$

For the radiation yield of ion pairs per unit exposure (1 R) and unit volume (1 cm^3) $G = 2.08 \times 10^9$ R^{-1} cm^{-3}, the concentration of the heavy ions at $z = 0$ is given by

$$N_\mathrm{d}^-(r, z)\big|_{z=0} = N_\mathrm{d}^+(r, z)\big|_{z=0} = \frac{k_c N_\mathrm{d}}{k_r}[\eta(r) - \eta(r - R_0)]. \quad (8)$$

The coefficients of capture of ions by water drops, k_c^p and k_c^n, have the form [8]

$$k_c = 2\pi D_a D_\pm \frac{(1 + \sqrt{|\ln(\mu_+/\mu_-)|})}{1 + 2D_\pm/(D_a c_\pm)}, \quad (9)$$

where $D_\pm$ and $c_\pm$ are the mean diffusion coefficients (≈0.05 cm^2/s) and the thermal velocity of a light aeroions (≈3.0×10^4 cm/s), respectively, and D_a is the diameter of the drops.

Since for the heavy drops $D_a \approx 2 \times 10^{-3}$ cm, $k_c^n \approx 0.63 \times 10^{-3}$ cm^3/s and the time to capture $\tau_c \sim 1/(k_c^n N_\mathrm{d}^\mathrm{l}) = 10^{-2}$ s. Similarly, if for the small drops $D_a \approx 2 \times 10^{-4}$ cm $k_c^p \approx 0.63 \times 10^{-4}$ cm^3/s. Assuming that diffusion in the longitudinal direction (z axis) is negligible in comparison with convection, we omit the longitudinal diffusion terms in Eqs. (1) and (2). Multiplying the vectors scalarwise in our set of equations and having regard for quasi-neutrality condition (4), we come to

$$k_c^p N_0^+ N_\mathrm{d}^s - k_r N_\mathrm{d}^+ N_0^- - k_r N_\mathrm{d}^+ N_\mathrm{d}^- - \mu_+^W E_r \frac{\partial N_\mathrm{d}^+}{\partial r} - \mu_+^W E_z \frac{\partial N_\mathrm{d}^+}{\partial z} + U_1 \frac{\partial N_\mathrm{d}^+}{\partial z} + D_+^W \frac{1}{r}\frac{\partial}{\partial r}\left[r\frac{\partial N_\mathrm{d}^+}{\partial r}\right] = 0; \quad (10)$$

$$k_c^n N_0^- N_\mathrm{d}^\mathrm{l} - k_r N_\mathrm{d}^- N_0^+ - k_r N_\mathrm{d}^- N_\mathrm{d}^+ - \mu_-^W E_r \frac{\partial N_\mathrm{d}^+}{\partial r} - \mu_+^W E_z \frac{\partial N_\mathrm{d}^+}{\partial z} + U_1 \frac{\partial N_\mathrm{d}^+}{\partial z} + D_+^W \frac{1}{r}\frac{\partial}{\partial r}\left[r\frac{\partial N_\mathrm{d}^+}{\partial r}\right] = 0; \quad (11)$$

$$\frac{E_r}{r} + \frac{\partial E_r}{\partial r} + \frac{\partial E_z}{\partial z} = 0; \quad (12)$$

$$N_\mathrm{l}^+ - N_\mathrm{l}^- = 0 \quad (13)$$

with the boundary conditions

$$\left.\frac{\partial N_{\rm d}^-}{\partial r}\right|_{r=0} = \left.\frac{\partial N_{\rm d}^+}{\partial r}\right|_{r=0} = 0, \quad (14)$$

$$N_{\rm d}^-(r,z)\big|_{r\to\infty} = N_{\rm d}^+(r,z)|_{r\to\infty} = 0, \quad (15)$$

$$N_{\rm d}^-(r,z)\big|_{z\to\infty} = N_{\rm d}^+(r,z)|_{z\to\infty} = 0, \quad (16)$$

$$N_{\rm d}^-(r,z)\big|_{z=0} = \frac{k_c^n N_{\rm d}^{\rm l}}{k_r}[\eta(r)-\eta(r-R_0)],$$
$$N_{\rm d}^+(r,z)\big|_{z=0} = \frac{k_c^p N_{\rm d}^{\rm s}}{k_r}[\eta(r)-\eta(r-R_0)]. \quad (17)$$

For the steady motion of the charge carriers, we now find the components of the electric field. The equations of current density for each of the charges in view of the directions of the field and the air velocity (Fig. 1) are written as

$$\mathbf{J}_{\rm d}^+ = \mathbf{E}\mu_+^W N_{\rm d}^+ - \mathbf{U}_1 N_{\rm d}^+ - D_+^W \mathrm{grad}(N_{\rm d}^+),$$
$$\mathbf{J}_{\rm d}^- = -\mathbf{E}\mu_-^W N_{\rm d}^- - \mathbf{U}_1 N_{\rm d}^- - D_-^W \mathrm{grad}(N_{\rm d}^-).$$

If the current densities of the positive and negative ions are equal ($\mathbf{J}_{\rm d}^+ = \mathbf{J}_{\rm d}^-$), we have

$$\mathbf{E}\mu_+^W N_{\rm d}^+ - \mathbf{U}_1 N_{\rm d}^+ - D_+^W \mathrm{grad}(N_{\rm d}^+) = -\mathbf{E}\mu_-^W N_{\rm d}^- - \mathbf{U}_1 N_{\rm d}^- - D_-^W \mathrm{grad}(N_{\rm d}^-)$$

or

$$\mathbf{E}(\mu_-^W N_{\rm d}^- + \mu_+^W N_{\rm d}^+) + \mathbf{U}_1(N_{\rm d}^- - N_{\rm d}^+) = \mathrm{grad}(D_+^W N_{\rm d}^+ - D_-^W N_{\rm d}^-). \quad (18)$$

Writing vector equation (18) componentwise and using the equation for quasi-neutrality [Eq. (13)], we find

$$E_z(r,z) = \left[\frac{\partial}{\partial z}((D_+^W - D_-^W)N_{\rm d}^-)\right]/((\mu_-^W + \mu_+^W)N_{\rm d}^-), \quad (19)$$

$$E_r(r,z) = \left[\frac{\partial}{\partial r}((D_+^W - D_-^W)N_{\rm d}^-)\right]/((\mu_-^W + \mu_+^W)N_{\rm d}^-). \quad (20)$$

These equations are consistent with known results for the one-dimensional electric field. Set (10)–(17), where E_z and E_r are defined by Eqs. (19) and (20), respectively, was solved by the succession-sweep method [11] with respect to Eqs. (10) and (11) for desired concentrations. Estimates were made for R_0 = 10 m, z_0 = 10 m, $r_{\max}$ = 20 m, and $z_{\max}$ = 200 m. The respective diffusion coefficients and the mobilities of the light and heavy charged drops were $D_+^W = 1.63\times10^{-8}$, $D_-^W = 1.37\times10^{-9}$, $\mu_-^W = 0.053\times10^{-5}$, and $\mu_+^W = 0.063\times10^{-4}$. The step in both radial and vertical directions was taken small (d_r = 0.133 m and d_z = 0.25 m) to provide qualitatively correct and reliable results. The iteration method was used because the set of equations is nonlinear. The divergence was determined by the formula

$$\varepsilon = \frac{2}{M}\sum_{i=1}^{M}\left[\left|(N_{\rm d}^+)_{i,j}^{k+1} - (N_{\rm d}^+)_{i,j}^{k}\right|/((N_{\rm d}^+)_{i,j}^{k+1} - (N_{\rm d}^+)_{i,j}^{k})\right]$$

for each layer j along the height (j = 1, 2, …, N) and lay within 10^{-1}–10^{-2}%. The results of calculations are depicted in Figs. 4–7. The height distribution of the concentration of the heavy negative ions is similar to that of the positive ones: a drastic fall at small heights changes to a smooth fall as the height increases (Fig. 4). In the radial direction (Fig. 5), the charge carrier concentration shows a sharp decrease with the transition region width $\Delta r \approx 2$ m. This ensures good reflection of

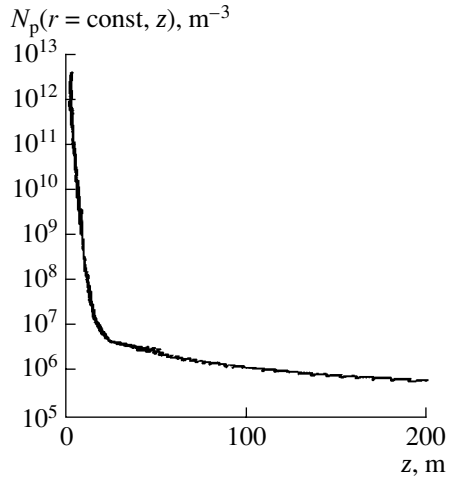

Fig. 4. Distribution of the concentration of the positively charged drops N_p (r = const, z) along the height.

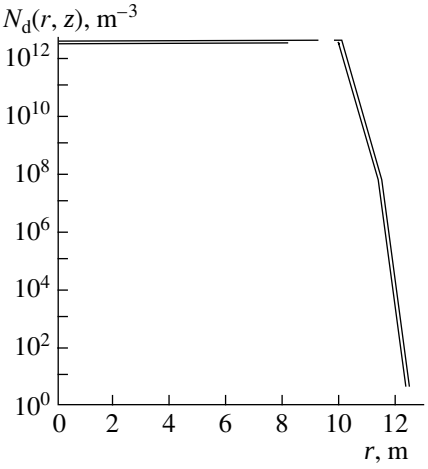

Fig. 5. Radial distribution (z = const) of the concentration of the heavy charge carriers (charged drops).

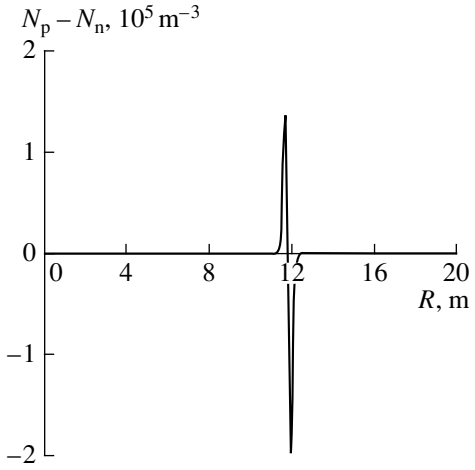

Fig. 6. Radial distribution of the difference in the concentrations of the heavy charge carriers (charged drops).

electromagnetic waves in the meter range. The radial distribution of the difference in the carrier concentrations $\Delta N = N_d^+(r, z) - N_d^-(r, z)$ (z = const) implies that the system as a whole is neutral. At the periphery of the distribution, excess positive charge carriers, which appear because of their higher mobility in comparison with the negative (heavy) charges, are neutralized by an excess of the negative charge. The height distribution of the difference in the concentration of the negative and positive charges (Fig. 7) indicates that the plasmoid has a layered structure (oscillation is associated with the numerical method of solution). Such a picture is consistent with the distribution of the conductivity found in experiments [8]. Moreover, according to our concept, it provides the longitudinal stability of the formations, demonstrating once again that they do actually exist. These findings are circumstantially supported in [12], where the natural electric field of the Earth was measured at a height h = 0.8 m from a surface radioactively polluted with a pollution density Q (Fig. 8). Since the field lines of the electric field $\mathbf{E}_0$ are normally directed toward the soil (the earth is negatively charged), a decrease in the field strength can be associated with excess negative ions due to air ionization by the radioactive products (Fig. 9). The negative charge of the ion cloud induces a positive charge on the soil surface, thus producing a local oppositely directed electric field $\mathbf{E}'(Q)$. The effective field $\mathbf{E} = \mathbf{E}_0 - \mathbf{E}'(Q)$ will decrease with increasing Q (increasing dose rate from the underlying surface), as demonstrated in Fig. 9. The image forces resulting between the negative charge of the ions and the induced positive charge confine the negative charge, preventing its diffusion. On the other hand, by virtue of the quasi-neutrality of a cold plasma, which, in essence, forms by air ionization, an excess concentration of positive ions must occur over the negative ions. The resulting electrostatic forces also contribute to the stability of the plasmoid. Thus, due to the steady processes of air ionization, ion recombination, ion leakage, etc., the ion cloud above the polluted underlying surface segregates into layers. This is a result of the hydration of the negative ions and their gravitational settlement. Measurements of the effective electric field near the radioactive plume from the ventilation pipe of the nuclear power station (Fig. 2) gave the same results. Similar atmospheric effects [13] observed at nuclear explosions at a testing ground (Nevada, USA) were also associated with vertical charge separation in the radioactive cloud.

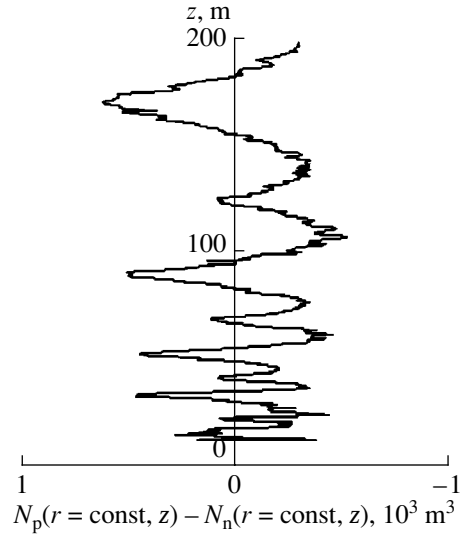

Fig. 7. Distribution of the difference in the concentrations of the heavy charge carriers (charged drops) along the height (r = const).

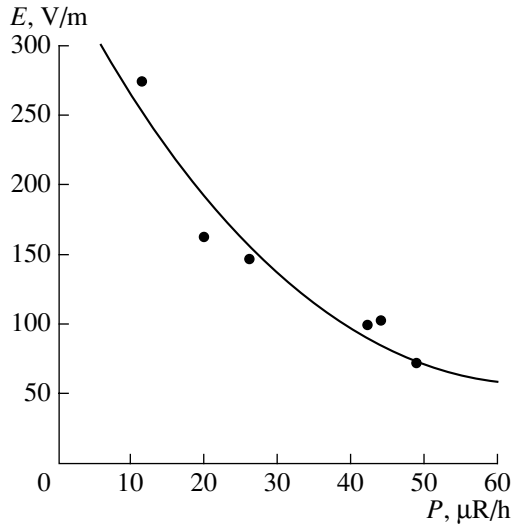

Fig. 8. Natural electric field of the atmosphere vs. radioactive pollution of the soil [12].

The mechanism behind the formation of plasmoids that is considered in this article unambiguously implies that they must have the form of bodies of revolution (ellipsoids, spheres, or cylinders depending on the ion source). Such geometry arises under the action of forces of electrostatic interaction between unlike ions in the transverse and longitudinal directions. The radial distribution of the ions in the plasmoid (Fig. 5) allows us to derive the wavelength dependence of the coefficient of reflection of an electromagnetic wave from a plasmoid. Usually, the reflection coefficient for an electromagnetic wave is found by reducing the Maxwell equations to second-order equations for electric or magnetic field with appropriate boundary conditions. These equations are solved for incident and reflected waves, and then the reflection coefficient $R = A_{ref}/A_{inc}$ or its absolute value $|R| = (A_{ref}/A_{inc})^2 \sim P_{ref}/P_{inc} \sim \sigma_{sc}$ is found. Here, A_{ref}, A_{inc}, P_{ref}, and P_{inc} are, respectively, the amplitudes and the intensities of the reflected and incident waves; σ_{sc} is the scattering cross section.

When estimating the reflection coefficient R, we turn to the results of [14–16] and assume that an electromagnetic wave with a wavelength λ strikes the interface between air and an ionized air layer. In this layer, the ion concentration is symmetric about the plane $z = r_0$ (Fig. 10). In our coordinate system, the plane xy coincides with the interface (the y axis runs normally to the plane of Fig. 10) and the normal to the plane of incidence of the wave makes an angle Θ_0 with the positive direction of the z axis. Note that any plane electromagnetic wave can be represented as a superposition of two waves with the vector **E** in and normal to the plane of incidence.[3] Therefore, we will consider only such waves. The simplest harmonic solution of the Maxwell equations is written as $\mathbf{E}(r, t) = \mathbf{E}_0 e^{i(\mathbf{kr} - \omega t)}$, where $\mathbf{k} = k_x\mathbf{i} + k_y\mathbf{j} + k_z\mathbf{k}$ is the wave vector for which $\mathbf{k}^2 = k_x^2 + k_y^2 + k_z^2$ and $\mathbf{r} = x\mathbf{i} + y\mathbf{j} + z\mathbf{k}$. If our coordinate system is such that $k_y = 0$, then $k_x = x\sin\Theta_0 = \xi$, $k_z = k\cos\Theta_0$ ($k = \omega/c$). We will consider only the wave with the vector **E** normal to the plane of incidence. Since ϵ and σ depend solely on z, we easily find that the x dependence of the electric and magnetic fields is exponential, while their dependence on z is more complex and is to be determined. In this case, $E_x = E_z = 0 \longrightarrow H_y = 0$ and the Maxwell equations written in the Gaussian system have the form

$$\frac{\partial E_y}{\partial z} = -i\frac{\omega}{c}H_x, \quad \xi E_y = (\omega/c)H_z,$$

$$\frac{\partial H_x}{\partial z} - \frac{\partial H_z}{\partial x} = -i\frac{\omega}{c}\epsilon' E_y,$$

[3] The plane of incidence of an electromagnetic wave is that passing through the normal n to the wave front and z axis.

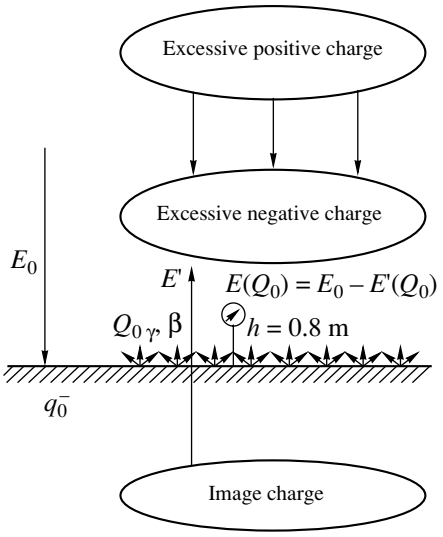

Fig. 9. Vertical separation of the ions generated by radioactive aerosols from the polluted underlying surface [12].

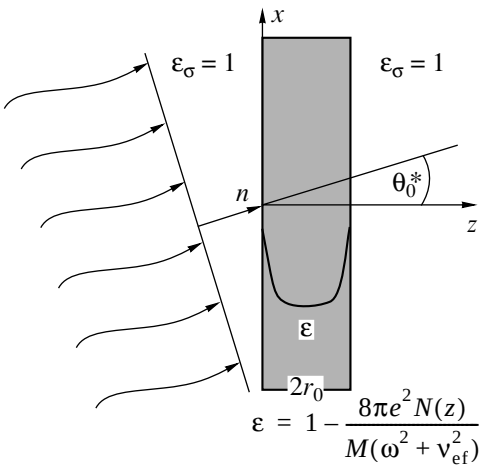

Fig. 10. Reflection of an electromagnetic wave from the ionized air layer.

where

$$\epsilon' = \epsilon + i\frac{4\pi\sigma}{\omega}.$$

Here, we took into account that the differentiation of the components of **E** and **H** with respect to time and x is reduced to multiplying the associated expressions by the factor $-i\omega$ and $i\xi$, respectively.

On straightforward rearrangement, we obtain [14]

$$\frac{\partial H_x}{\partial z} + i\frac{c}{\omega}\left[\left(\frac{\omega}{c}\right)^2\epsilon' - \xi^2\right]E_y = 0, \qquad (21)$$

$$\frac{\partial E_y}{\partial z} + i\frac{\omega}{c}H_x = 0. \qquad (22)$$

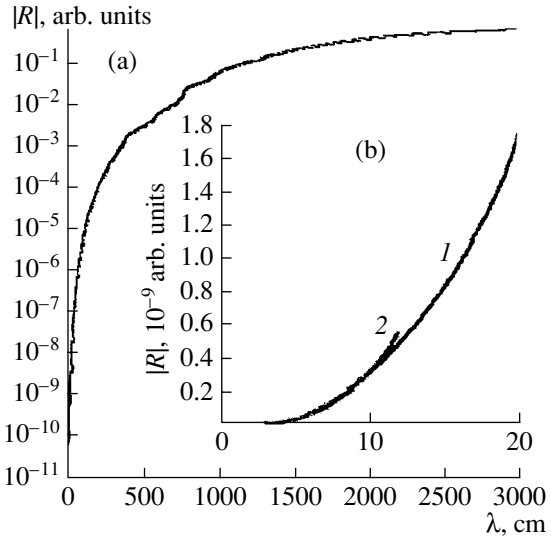

Fig. 11. (a) Absolute value of the reflection coefficient $|R|$ vs. wavelength and (b) comparison of (*1*) author's results with (*2*) experimental data in [17].

A solution of this system is found by introducing the incident wave,

$$E_y = P(z), \quad H_x = -(c/\omega)\beta P(z),$$
$$\beta = \sqrt{\left(\frac{\omega}{c}\right)^2 \varepsilon' - \xi^2}, \tag{23}$$

and the reflected wave,

$$E_y = R(z), \quad H_x = (c/\omega)\beta R(z), \tag{24}$$

where $P(z)$ and $R(z)$ are functions to be found.

Substituting (23) and (24) as the sum of the fields into (21) and (22) yields, after summation and subtraction, the equations for $R(z)$ and $P(z)$:

$$R' = -i\beta R + \gamma(P - R), \tag{25}$$
$$P' = i\beta P - \gamma(P - R), \tag{26}$$

where $\gamma = \beta'/2\beta$.

For arbitrary z, the reflection coefficient $V(z)$ is defined as the ratio $V(z) = R(z)/P(z)$. Multiplying (25) by P and (26) by R, subtracting one from the other, and dividing the difference by P^2, we arrive at the Riccati equation for $V(z)$:

$$V' = -2i\beta V + \gamma(1 - V^2). \tag{27}$$

The boundary condition for a solution of (27) is

$$V(z)|_{z\to\infty} = 0, \tag{28}$$

since the reflected wave does not penetrate into the layer. A similar equation is obtained for the waves the vector **E** of which lies in the plane xz. Analytically, Eq. (27) is solved by the method of successive approximations [14]. To find the solution with a numerical technique, we will consider the normal incidence of an electromagnetic wave on an ionized layer ($\Theta_0 = 0$) and represent the desired function $V(z)$ in the complex form

$$V(z) = u(z) + iv(z), \tag{29}$$

where $u(z)$ and $v(z)$ are real functions of the real argument z that are to be found.

The dependences of the permittivity $\epsilon(z)$ and the conductivity $\sigma(z)$ on the ion concentration in the ionized layer are written as

$$\varepsilon = 1 - \frac{8\pi e^2 N(z)}{M(\omega^2 + \nu_{ef}^2)}; \quad \sigma = \frac{2e^2 \nu_{ef} N_i(z)}{M(\omega^2 + \nu_{ef}^2)},$$

where $\omega = 2\pi c/\lambda = 1.884 \times 10^{11}/\lambda$ and $\nu_{ef} = 4 \times 10^9 \sqrt{T/300}$, s^{-1} [3]. Then, β as a complex function of the real argument z has the form

$$\beta = \frac{\omega}{c}\sqrt{\varepsilon'} = \frac{\omega}{c}\sqrt{\varepsilon + i\frac{4\pi\sigma}{\omega}}.$$

Since

$$\frac{8\pi e^2 N(z)}{M(\omega^2 + \nu_{ef}^2)} \ll 1,$$

we apply the de Moivre formula to β to find

$$\beta = \frac{\omega}{c}\sqrt{\varepsilon^2 + \left(\frac{4\pi\sigma}{\omega}\right)^2}\left(\cos\frac{\varphi_0}{2} + i\sin\frac{\varphi_0}{2}\right),$$

$$\varphi_0 = \arctan\frac{4\pi\sigma}{\omega\varepsilon} \approx \frac{8\pi e^2 \nu_{ef} N(z)}{\omega M(\omega^2 + \nu_{ef}^2)}.$$

Eventually, for β and γ, we have

$$\beta = \frac{\omega}{c}\left[1 + i\frac{4\pi e^2 \nu_{ef} N(z)}{\omega M(\omega^2 + \nu_{ef}^2)}\right],$$
$$\gamma = \frac{\frac{d\beta}{dz}}{2\beta} = \frac{\frac{d\varepsilon'}{dz}}{4\varepsilon'} \approx -\frac{2\pi e^2}{M(\omega^2 + \nu_{ef}^2)}\frac{dN}{dz}\left(1 - i\frac{\nu_{ef}}{\omega}\right). \tag{30}$$

Substituting (29) and the complex expressions for γ and β into (27) and separating the real and imaginary parts yields

$$u' = 2(du + c_1 v) - a[1 - (u^2 - v^2)] + 2buv, \tag{31}$$

$$v' = -2(c_1 u + dv) + b[1 - (u^2 - v^2)] + 2auv, \tag{32}$$

where

$$a = \frac{2\pi e^2}{M(\omega^2 + \nu_{ef}^2)}\frac{dN}{dz}; \quad b = \frac{2\pi e^2 \nu_{ef}}{\omega M(\omega^2 + \nu_{ef}^2)}\frac{dN}{dz};$$

$$c_1 = \frac{\omega}{c}; \quad d = \frac{4\pi e^2 \nu_{ef} N(z)}{cM(\omega^2 + \nu_{ef}^2)}.$$

The boundary conditions remain the same:

$$u(z)|_{z\to\infty} = 0, \quad v(z)|_{z\to\infty} = 0. \tag{33}$$

The set (31), (32) with boundary conditions (33) were solved by a routine based on the Runge–Kutta method. The magnitude of the reflection coefficient $|R| = u^2 + v^2$ calculated as a function of wavelength λ is shown in Fig. 11, where the analytical curve $|R| = f(\lambda)$ (Fig. 11a) is compared with the experimental dependence $\sigma_{sc}(\lambda)$ for the centimeter range [17] (Fig. 11b). Here, σ_{sc}, the effective scattering cross section, is directly determined from the radar equation. Both curves behave in a similar manner: the absolute value of the reflection coefficient grows with wavelength. From Fig. 11a follows that $|R|$ grows most rapidly in the range 1–10 m.

Finally, let us derive an R vs. q_0 dependence where R is the coefficient of reflection from an ionized air layer and q_0 is the surface density of radioactive pollutants on the underlying surface. Since the radial distribution of the ions is sufficiently sharp, we can represent the reflection coefficient as a discontinuity (jump) of the derivative at the air–ionized layer interface [3]; that is,

$$R = \frac{\lambda_0 e^2}{4M\omega^2}\left(\frac{dN_d^+}{dr}\right).$$

Now we find the radial derivative of the charged drop concentration from (10) and (11), leaving only the chemical kinetics terms in them, subject to $N_d^+ \approx N_d^-$:

$$(N_d^\pm)^2 + N_d^\pm N_0^\pm - N_0^\pm(k_e^p N_d^s + k_c^n N_d^l)/2k_r = 0.$$

Putting $N_0^\pm = \sqrt{GH/k_r}$ and assuming that the dose rate is low, i.e., that

$$2(k_c^p N_d^s + k_c^n N_d^l)/k_r \gg N_0^\pm, \tag{34}$$

we have $N_d^\pm \approx (N_0^\pm[k_c^p N_d^s + k_c^n N_d^l]/2k_r)^{1/2}$.

Differentiation yields

$$\frac{dN_d^\pm}{dr} = \frac{[(k_c^p N_d^s + k_c^n N_d^l)/2k_r]^{1/2}}{\sqrt{(N_0^\pm)}}\frac{dN_0^\pm}{dr}$$

$$= \left(\frac{G}{k_r}\right)^{\frac{1}{4}}\frac{\sqrt{(k_c^p N_d^s + k_c^n N_d^l)/2k_r}}{2(H)^{3/4}}\frac{dH}{dr}.$$

Writing the expression for the dose rate in the case of a disk with point radioactive sources of specific activity q_0 [18] that are uniformly distributed over its surface in the form $H(r, z) = K\varphi(r, z)$, where $K = q_0\pi K_\gamma$ (q_0 is the desired quantity), we have

$$H(r, z_0) = K\ln\left[\frac{z_0 + \sqrt{4r^2 + z_0^2}}{2z_0}\right] = K\varphi(r, z_0)$$

and, hence,

$$R = K^{1/4}\frac{1}{8}\frac{\lambda_0 e^2}{M\omega^2}\left(\frac{G}{k_r}\right)^{1/4}$$

$$\times (2/(k_c^p N_d^s + k_c^n N_d^l)/k_r)^{1/2}\frac{1}{\varphi^{3/4}}\frac{d\varphi}{dr},$$

where $d\varphi/dr$ and φ are calculated at the boundary of the region polluted.

From the last expression, it follows that the reflection coefficient varies as the fourth root of q_0. Hence, we can determine q_0 by measuring R and the other parameters of the atmosphere [19]. It can be shown that, with condition (34) met, the dependence of the reflection coefficient on the intensity P_{ej} of an ejection from a volume source also follows the 1/4 power law: $P_{ej}[R \sim P_{ej}^{1/4}]$. In the general case (with regard for the temperature and the humidity of the boundary atmospheric layer), this dependence will have the form $R \sim P_{ej}^{\Delta}$, where $0.25 \le \Delta \le 0.5$. The same range of the exponent is valid for the R vs. q_0 dependence.

REFERENCES

1. A. P. Elokhin and E. N. Kononov, At. Énerg. **80**, 129 (1996).
2. A. N. Didenko, Yu. P. Usov, Yu. G. Yushkov, *et al.*, At. Énerg. **80**, 47 (1996).
3. V. L. Ginzburg, *The Propagation of Electromagnetic Waves in Plasmas* (Nauka, Moscow, 1967; Pergamon, Oxford, 1970).
4. V. V. Smirnov, in *Proceedings of the Institute of Experimental Meteorology*, Vol. 19: *Ecological–Geophysical Aspects of Nuclear Power Station Monitoring* (Gidrometeoizdat, Moscow, 1992), pp. 45–60.
5. K. Kato, in *Collection of Reports of Society of Earthquake Forecast* (1984), No. 33, pp. 184–186.
6. Ya. I. Frenkel', *Theory of Phenomena of Atmospheric Electricity* (GITTL, Moscow, 1949).
7. G. A. Vorob'ev, *Physics of Dielectrics, Strong Fields Region* (Tomsk. Univ., Tomsk, 1977).
8. V. V. Smirnov in *Proceedings of the Institute of Experimental Meteorology*, Vol. 19: *Ecological–Geophysical Aspects of Nuclear Power Stations Monitoring* (Gidrometeoizdat, Moscow, 1992), pp. 111–122.
9. *Calculation of Radioactive Material Propagation in the Environment and Radiation Dose for Population*

(MKhO Interatoménergo, Moscow, 1992), p. 59; p. 248.
10. H. Kuchling, *Physik* (Fachbuchverlag, Leipzig, 1980; Mir, Moscow, 1982).
11. A. A. Samarskiĭ, *The Theory of Difference Schemes* (Nauka, Moscow, 1977).
12. É. Ya. Begun, E. S. Dmitriev, A. B. Ivanov, and G. P. Markov, in *Radiation: Latent Ecological Problems* (ANRI, 1998), No. 1, pp. 15–19.
13. R. Holzer, in *Nuclear Explosion in Space, on the Earth, and under Water* (Voenizdat, Moscow, 1974), pp. 219–234.
14. L. M. Brekhovskikh, *Waves in Layered Media* (Nauka, Moscow, 1973; Academic, New York, 1980).
15. L. M. Brekhovskikh, Zh. Tekh. Fiz. **19**, 1126 (1949).
16. P. H. van Cittert, Physica **6**, 840 (1939).
17. K. A. Boyarchuk, E. N. Kononov, and G. A. Lyakhov, Pis'ma Zh. Tekh. Fiz. **19** (6), 67 (1993) [Tech. Phys. Lett. **19**, 184 (1993)].
18. N. G. Gusev, E. E. Kovalev, D. P. Osanov, and V. I. Popov, *Radiation Protection against from Distant Source* (Gosatomizdat, Moscow, 1961), Part II.
19. A. P. Elokhin, RF Inventor's Certificate No. 2147137 (2000).

Translated by V. Isaakyan

Technical Physics, Vol. 46, No. 8, 2001, pp. 1037–1039. Translated from Zhurnal Tekhnicheskoĭ Fiziki, Vol. 71, No. 8, 2001, pp. 109–111.

BRIEF COMMUNICATIONS

Formation of Resistive Properties of Two-Phase Semiconductor–Metal Systems Based on $FeSi_{1+x}$ with Small Deviations from Stoichiometry

A. A. Povzner, A. G. Andreeva, I. N. Sachkov, and V. V. Kryuk

Ural State Technical University, Yekaterinburg, 620002 Russia

Received June 1, 2000

Abstract—Using the method of finite elements it has been found that in a two-phase system a semiconductor–metal concentrational transition takes place. Specific features of the dependence on concentration and temperature of the effective electrical conductivity in a FeSi–$FeSi_2$ system are studied in the vicinity of critical concentrations. *© 2001 MAIK "Nauka/Interperiodica".*

Some resistive materials are multiphase compositions having *U*-shaped polytherms with the specific resistance $\rho(T)$ [1–3]. Typically, these exist at a certain temperature T_c at which ρ acquires a minimum value and the sign of the temperature coefficient of resistance (TCR) changes from negative to positive. In the vicinity of T_c the absolute values of TCR are small. One of the main objectives of studies on resistor materials is the search for systems where this condition can be attained. Metal–semiconductor metallic systems are very attractive as a basis of resistive materials in the form of two-phase alloys of the silicides of transition metals, which have good operational characteristics [4, 5].

The analysis of statistical systems in [6] demonstrated the possibility of forming a *U*-shaped polytherm of electrical resistance, but only in systems where the conductivities of the metallic and semiconductor phases differed by about an order of magnitude. Finding matching components for such systems is a difficult task. In this study, systems with a matrix structure are considered in which inclusions of the second phase are distributed rather nonuniformly, for example, accumulated at grain boundaries as components of a eutectic. A FeSi–$FeSi_2$ system has been analyzed in detail.

The diagram of stable phase states of $FeSi_{1+x}$ alloys is well known [4, 7]. At temperatures below 1400°C and $0 < x < 0.016$, the thermodynamically stable phase is ε-FeSi. If the alloy is rich in silicon, $0.016 < x < 1$, a two-phase system is formed containing iron disilicide embedded in iron monosilicide. In contrast to the study [6] cited above, we take into account that the $FeSi_2$ particles can be distributed essentially nonuniformly, accumulating as fringes at the grain boundaries and forming eutectics.

To find out the consequences of nonuniform distribution of $FeSi_2$ inclusions, we consider a current flow through a simplified system of cubic FeSi grains separated by accumulations of the FeSi–$FeSi_2$ eutectic (Fig. 1). The grain is $2h$ in size; the thickness of its two-phase boundary region is $2D$. It will be taken into account that the conductivities of FeSi and $FeSi_2$ at 300 K are 0.321 and 5–10 $(\Omega\ \mathrm{m})^{-1}$, respectively; i.e., they differ by four orders of magnitude.

The concentration of semiconductor phase in the region of a two-phase boundary is readily obtained from the expressions

$$C_b = C_0\mu, \quad \mu = \frac{h^3}{h^3 - (h-D)^3}, \qquad (1), (2)$$

where C_0 is the average disilicide concentration in the sample; C_b is the disilicide concentration in the eutectic; and μ is a geometrical parameter characterizing the "looseness" of the boundary.

We allow for the fact that the eutectic medium, in turn, has a matrix structure; the cross sections of different matrices are shown in Fig. 2. In matrix scheme *a*, the semiconducting particles of $FeSi_2$ are separated by

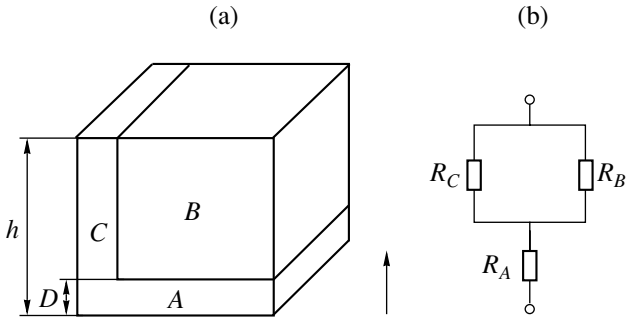

Fig. 1. (a) Schematic unit cell of a polycrystalline two-phase FeSi–$FeSi_2$ system; regions *A* and *C* are filled with eutectic; *B* is the single-phase monosilicide; *h* is the half the grain dimension; and *D* is the thickness of the two-phase boundary of grains. (b) Equivalent electrical circuit of the unit cell of a grain.

1063-7842/01/4608-1037$21.00

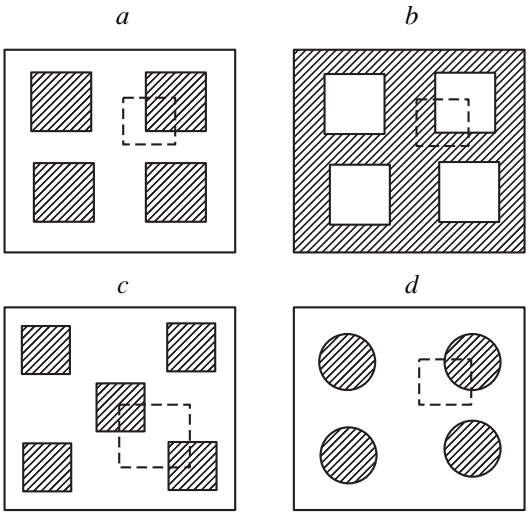

Fig. 2. Schematic cross sections of eutectic regions. Cross-hatched areas are $FeSi_2$. Dashed lines are boundaries of unit cells used in calculating σ_{be}.

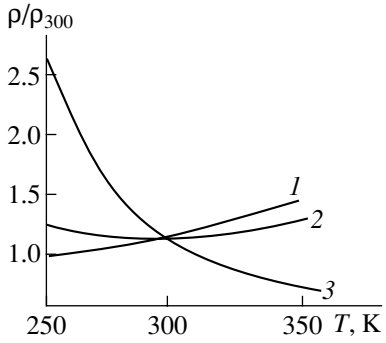

Fig. 3. Polytherms of the relative resistance in various systems: (*1*) single-phase monosilicide; (*2*) iron disilicide; (*3*) FeSi–$FeSi_2$ system having a eutectic structure *c* at C_0 = 0.0015 and δ = 0.01. Arrows indicate critical concentrations of disilicide.

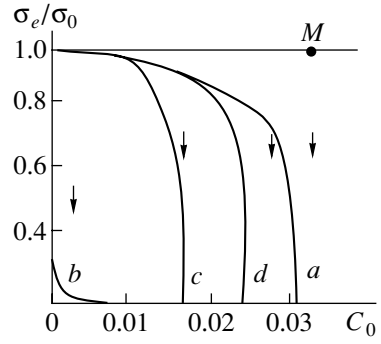

Fig. 4. Effective conductivity as a function of concentration in two-phase systems with a different geometry of eutectic subsystems for a relative boundary thickness of δ = 0.01.

thin continuous layers of the $FeSi_2$ semiconductor component. Structure *b* is a dual *a*, with layers of monosilicide enveloping the disilicide. System *c* contains square inclusions of $FeSi_2$ in a checkerboard pattern. In conducting medium *d* the particles of the semiconductor phase have a spherical shape.

We now consider the behavior of the specific resistance of the above systems as a function of concentration and temperature. When the current flows in the direction indicated by arrow in Fig. 1, the unit cell can be divided by equipotential and adiabatic planes into regions *A*, *B*, and *C*. In a regular, macroscopically uniform, isotropic system like this one, the effective specific conductivity σ_e is equal to that of the unit cell. It can be conveniently determined in two steps. The first step is to calculate the conductivity σ_{be} of the eutectic systems *a*–*d* using an approach based on the method of finite elements [8, 9]. The spatial distribution of the current density is determined from the condition of the extremum of the functional

$$\chi = \int_{V_0} J^2 \sigma dV, \tag{3}$$

where J and σ are the local current density and conductivity of a heterogeneous medium, respectively, and V_0 is the volume of the unit cells highlighted in Fig. 2 with dashed lines.

Next, using the range of J values determined, we calculate the effective conductivity of the eutectic

$$\sigma_{be} = \langle J \rangle / \langle J/\sigma \rangle, \tag{4}$$

where $\langle\rangle$ denotes averaging over the sample volume V_0.

The effective conductivity of the unit cell and, correspondingly, the entire macroscopic isotropic system σ_e can now be calculated by the Dul'nev method [10]. For this calculation we use the equivalent electrical circuit of the unit cell shown in Fig. 1b. It should be taken into account that region *B* is monophase and regions *A* and *C* containing grain boundaries are microscopically heterophase regions. Thus,

$$R_A = \frac{D}{h^2 \sigma_{be}}, \tag{5}$$

$$R_B = \frac{1}{(1-D)\sigma_1}, \tag{6}$$

$$R_C = \frac{D}{(L-D)^2 \sigma_{be}}, \tag{7}$$

where σ_1 and σ_{be} are the conductivities of the monosilicide and the FeSi–$FeSi_2$ eutectic, respectively.

The values of the partial conductivity of FeSi determined by the method described in [1] will be used to calculate the temperature dependences $\sigma_e(T)$. The conductivity polytherm of $FeSi_2$ will be approximated by the usual exponential dependence for a semiconductor with a bandwidth of E_g = 0.2 eV [4].

Figure 3 shows the curves of the effective relative conductivity of the above heterogeneous systems as a function of volume concentration of iron disilicide calculated for a relative thickness of the boundary region of $\delta = D/L = 0.01$, σ_0 being the conductivity of monosilicide at 300 K. It can be seen that the conductivity of the systems considered has an exceptionally sharp dependence on the concentration of the second phase.

In [8], $\sigma_e(C_0)$ dependences have been determined for a system with a regular homogeneous distribution of inclusions of various forms. It was shown that at $C_0 < 0.3$ the effective conductivity of matrices with square or round particles weakly depended on concentration, that it was practically independent of the form of particles, and that it could be described by the known Maxwell formula with an accuracy of not lower than 1% [12]. The Maxwellian dependence is shown in Fig. 3 as curve *M*. It is readily seen that under the conditions considered here, the conductivity of the above systems depends markedly on the form of the disilicide particles at concentrations $C_0 < 0.03$, i.e., an order of magnitude lower than in the case of homogeneous distribution. This dependence is most pronounced in system *b* and least, in system *a*. At concentration C_c indicated by arrows in Fig. 4 and corresponding to disilicide particles in the eutectic bonding, a drastic drop in conductivity and a metal–semiconductor transition occur. It can be seen that C_c values depend markedly on the geometry of the eutectic particles.

In the vicinity of C_c, functions $\sigma_e(T)$ of the two-phase systems considered also experience considerable changes. In Fig. 3, typical polytherms of the relative specific resistance of a two-phase FeSi–$FeSi_2$ film of structure *d* having a eutectic region of relative width $d = 0.01$ are presented for various concentrations of the disilicide. As seen in Fig. 3, as the content of the second phase changes, the dependence $\rho(T)$ typical of FeSi (curve *1*) transforms to a semiconductor-type polytherm (curve *3*). At concentrations around C_c, a transitional U-shaped polytherm is observed (curve *2*) with a typical extended portion of low TCR values.

By summing up the results of calculations for the polytherms, the following conclusions can be made. The $\rho(T)$ function is significantly dependent on three parameters: the initial concentration C_0 of the semiconductor phase, the boundary looseness parameter μ, and the shape of inclusions constituting it. It should be noted that by varying the film synthesis technology, various combinations of these parameters can be produced to optimize the resistive properties of the films. It should be taken into account that the morphology and geometrical parameters of the second phase particles of these systems depend substantially on the synthesis conditions. In particular, by varying the crystallization rate and modes of subsequent thermal treatments, the resistivity parameters of such materials can be controlled.

Nonuniform distribution of the inclusions of the second phase can significantly affect critical concentrations and should be taken into account in interpreting the results of experiments on semiconductor–metal transitions in two-phase systems.

This study explains the considerable scatter in the specific resistance of iron monosilicide, which was observed in [13–15]. It appears that it was caused by small, uncontrollable deviations of composition from the stoichiometry and multiphase structure of the samples. The effect of nonhomogeneity in the second phase distribution may also be important for studies into the details of electrical charge transport in a number of other materials, where the specific resistances of the two phases are appreciably different.

REFERENCES

1. K. I. Martyushov, *Reviews on Electron Technique*, Ser. 5: *Radio Details and Components* (TsNII Élektronika, Moscow, 1985), No. 1108.
2. V. B. Lazarev, V. G. Krasov, and I. S. Shaplygin, *Electroconductivity of Oxide Systems* (Nauka, Moscow, 1979).
3. R. S. Saĭfullin, *Inorganic Composite Materials* (Khimiya, Moscow, 1983).
4. P. V. Gel'd and F. A. Sidorenko, *Silicides of Transition Metals of Fourth Period* (Metallurgiya, Moscow, 1971).
5. S. Murarka, *Silicides for VLSI Applications* (Academic, New York, 1983; Mir, Moscow, 1986).
6. O. L. Vasilenko, A. L. Maĭer, V. A. Chashchin, *et al.*, Inzh.-Fiz. Zh. **49**, 477 (1985).
7. A. E. Vol, *Structure and Properties of Double Metallic Systems* (Nauka, Moscow, 1972), Vol. 2.
8. I. N. Skachkov, Zh. Tekh. Fiz. **66** (12), 48 (1996) [Tech. Phys. **41**, 1225 (1996)].
9. I. N. Skachkov and E. A. Mityushov, Pis'ma Zh. Tekh. Fiz. **22** (1), 22 (1996) [Tech. Phys. Lett. **22**, 14 (1996)].
10. G. N. Dul'nev and V. V. Novikov, *Transport Processes in Inhomogeneous Media* (Énergoatomizdat, Leningrad, 1990).
11. V. P. Gel'd, A. A. Povzner, Sh. Sh. Abel'skiĭ, and L. F. Romasheva, Dokl. Akad. Nauk SSSR **313**, 1107 (1990) [Sov. Phys. Dokl. **35**, 758 (1990)].
12. E. A. Mityushov, P. V. Gel'd, and R. A. Adamesku, *Generalized Conductivity and Elasticity of Macrohomogeneous Heterogeneous Materials* (Metallurgiya, Moscow, 1992).
13. V. N. Igishev and P. V. Gel'd, Izv. Vyssh. Uchebn. Zaved., Chern. Metall., No. 2, 90 (1960).
14. V. S. Neshpor and G. V. Samsonov, Fiz. Tverd. Tela (Leningrad) **2**, 2202 (1960) [Sov. Phys. Solid State **2**, 1966 (1960)].
15. L. P. Andreeva and P. V. Gel'd, Fiz. Met. Metalloved. **19**, 70 (1965).

Translated by B. Kalinin

Technical Physics, Vol. 46, No. 8, 2001, pp. 1040–1044. Translated from Zhurnal Tekhnicheskoĭ Fiziki, Vol. 71, No. 8, 2001, pp. 112–116.

BRIEF COMMUNICATIONS

Results of Visual Investigations of the Magnetoplasma Compressor Emission in Air

Yu. Ya. Volkolupov, M. A. Krasnogolovets, M. A. Ostrizhnoĭ, V. G. Nesterenko, O. I. Kharchenko, and V. I. Chumakov

Kharkov State Technical University of Electronics, Kharkov, Ukraine

Received October 10, 2000

Abstract—An efficient source of pulsed electromagnetic radiation in the range 0.3–10.2 μm is described. The parameters of the device and the results from studies of the radiation characteristics are presented. © *2001 MAIK "Nauka/Interperiodica"*.

Plasma sources of electromagnetic radiation have a high electrical efficiency. It is well known that the emission power and the plasma density and temperature in such sources depend on the energy deposited in the discharge and, consequently, on the discharge current [1–4]. Studies of the spatial distribution of the temperature in the discharge make it possible to optimize the parameters of the power supply as well as the design of the radiation source in order to achieve the maximum emission efficiency.

In experimental devices for the generation and acceleration of a dense plasma, a capacitive energy storage is usually used as a power supply. In this case, the maximum current is limited by the capacitor inductance and the parasitic inductance of the wiring (bus bars connecting the capacitor electrodes to the plasma accelerator electrodes). Minimizing the inductance allows one to achieve a storage discharge mode close to aperiodic and approach the maximum possible level of discharge currents in experimental devices.

In this paper, we present results from experimental studies of a high-power pulsed radiation source based on the end coaxial magnetoplasma compressor (MPC). Experimental dependences are obtained for the parameters of an experimental device with a busless supply circuit, which makes it possible to achieve high emission efficiency. The dependences of the radiation parameters and the results from studies of the radiation characteristics in the optical wavelength range are presented.

The experimental layout is shown in Fig. 1. The electrodes of a coaxial MPC were mounted on metal plates connected to the corresponding electrodes of the storage capacitors. The charging of the storage from a high-power rectifier allowed us to obtain voltages in the range 2–3.6 kV. The device was activated with the help

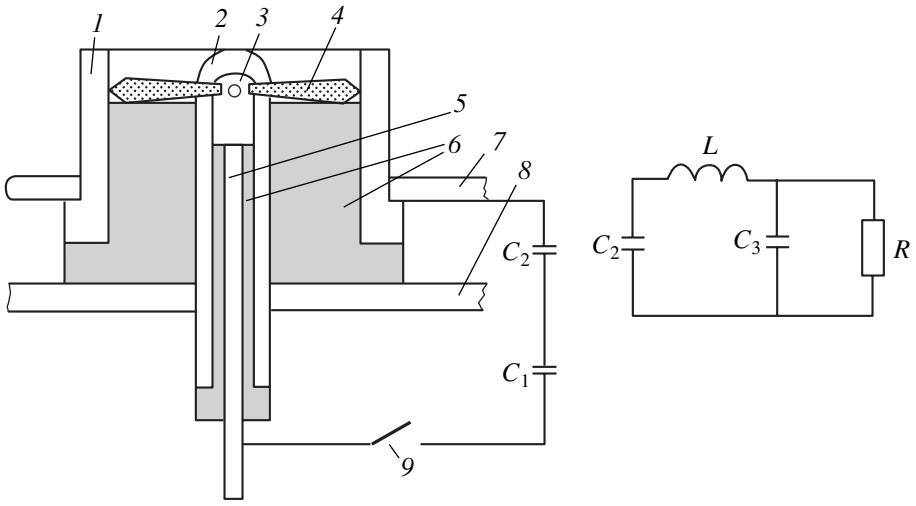

Fig. 1. Schematic of an MPC with foreplasma injection: (*1*) outer electrode, (*2*) central electrode, (*3*) chamber K1 for the formation of a foreplasma, (*4*) plasma jets, (*5*) additional electrode, (*6*) fluoroplastic insulators, (*7*) anode plate of the energy storage, (*8*) cathode plate of the energy storage, and (*9*) spark gap.

1063-7842/01/4608-1040$21.00 © 2001 MAIK "Nauka/Interperiodica"

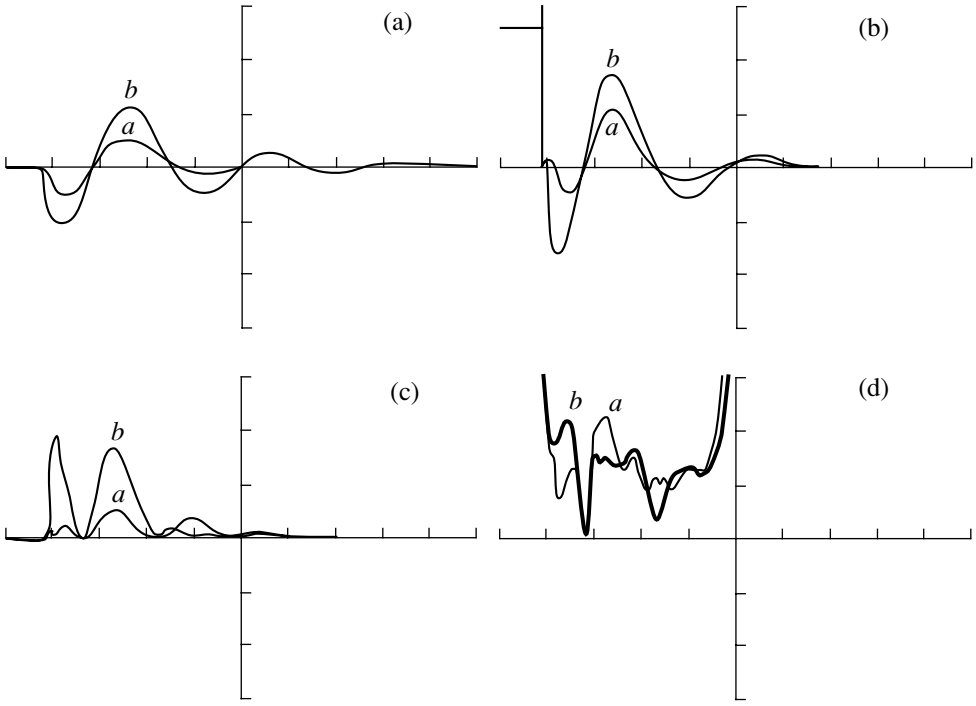

Fig. 2. Typical waveforms of (a) discharge current (325 kA/div, 20 μs/div), (b) voltage across the load (0.75 kV/div, 20 μs/div), (c) power deposited in the discharge (250 MW/div, 20 μs/div), and (d) discharge resistance (2.35 mΩ/div, 20 μs/div) at storage voltages of (*a*) 20.0 and (*b*) 3.2 kV.

of an auxiliary plasma (foreplasma) source, whose electrode was axially positioned inside the central electrode of the MPC. When an additional capacitor (C_f = 60 μF) was discharged through this electrode, a foreplasma was produced inside chamber K1. Under the action of the thermal pressure, the foreplasma was injected through holes in the central electrode of the MPC in the form of individual jets into the discharge gap. The energy of the charged particles of the foreplasma was sufficient for the discharge to bridge the discharge gap, which resulted in the discharging of the capacitive storage. Individual plasma jets formed a uniform plasma disc, which then transformed χ into a current-carrying plasma shell typical of the end MPCs. The polarity of the MPC electrodes was chosen according to the recommendations in [3].

The parameters of the experimental device are as follows: the storage capacitance is 1400 μF, the voltage is 2–3.6 kV, the discharge current is 200–400 kA, the inductance of the discharge circuit is 8.75 nH, the maximum emission power is 55 MW, and the discharge pulse duration is 22 μs.

Let us consider the results of the measurements of the source characteristics. Figure 2a shows the waveforms of the discharge current of the capacitive storage, and Fig. 2b shows the waveforms of the voltage at the MPC electrodes. We note that the discharge is oscillatory with a high damping rate equal to $\ln I_m(t)/I_m(t + T) \cong 1.39$. Using the waveforms $i(t)$ and $u(t)$, we can find the time dependences of the discharge power $p(t) = u(t)i(t)$ and resistance $r(t) = u(t)/i(t)$ (Figs. 2c, 2d). When obtaining these dependences, a correction was made for the deformation introduced by the parameters of the resistive–capacitive voltage divider, whose time constant (~10 μs) is comparable with the duration of the processes under study. We note that the power is always positive, and, consequently, the discharge resistance is ohmic in character.

The dependences of the discharge current on the charging voltage of the energy storage U_2 and on the stored energy

$$W_2 = \frac{1}{2}CU_2^2$$

are shown in Fig. 3. The current increases linearly with increasing voltage; i.e., we can assume that the integral resistance of the discharge circuit ($R = \Delta U/\Delta I \cong 9.4 \times 10^{-3}$ Ω) and the mean power loss in the energy range under study remain constant. The current can also be evaluated by integrating the current waveform in Fig. 2a over the first half-period and comparing the result obtained with the charge stored in the capacitor. Hence, we obtain

$$I_m = \frac{CU_2}{\int_0^{\tau_1} f(t)dt},$$

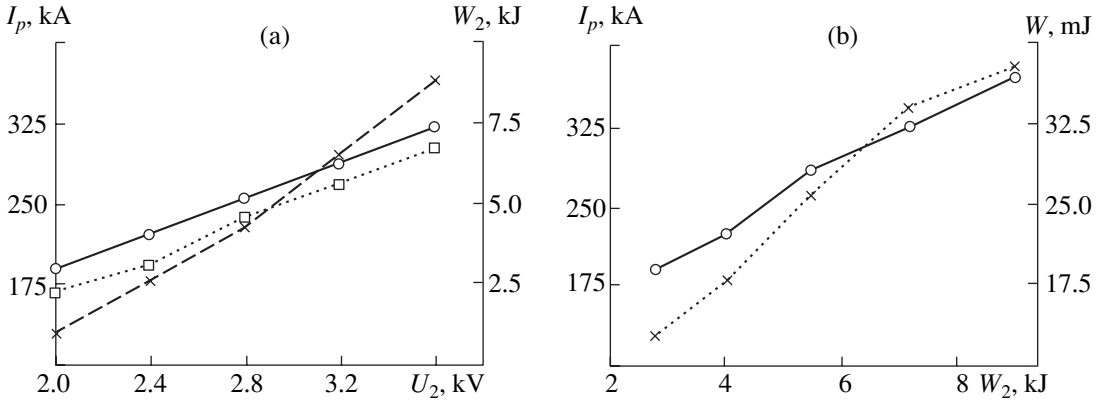

Fig. 3. (a) Dependences of the current through the load (the solid curve and the symbols correspond to calculations and experiment, respectively) and the stored energy (dashed curve) on the charging voltage; (b) the dependences of the current through the load and the radiation power density on the stored energy.

where τ_1 is the duration of the first current half-period and $f(t)$ is the function describing the time dependence of the current. Figure 3 also shows the calculated dependences of the discharge current on the charging voltage; in calculating these dependences, the shape of the current waveform during the first half-period was assumed to be $i(t) = I_m \sin \omega t$.

The radiation energy in the range $0.3 \le \lambda \le 10.2$ μm was measured with an IMO-2N laser radiation power meter. Figure 3 shows the radiation power density at a distance of 1 m from the source as a function of the charging voltage and the stored energy. The bend of the dependence of the radiation energy and the decrease in its slope can be explained by the fact that the maximum of the temperature distribution curve (the Planckian curve) of the radiating plasma is displaced into the UV region and goes beyond the meter passband as the deposited energy (and thus the plasma temperature) increases. The corresponding value of the discharge current is $I_p \cong 260$ kA. At this current, the magnetic pressure $\mu H^2/2$ (where H is the strength of the magnetic field produced by the current) substantially exceeds the thermal pressure of the plasma column $\sim 2nkT$ (where n is the electron density in the plasma column, k is the Boltzmann constant, and T is the temperature), which leads to the formation of constrictions, the onset of instability, and the formation of a plasma focus (PF) [1–5]. The temperature can be estimated from the Bennett relation for an equilibrium plasma configuration with allowance for only the azimuthal magnetic field produced by the current,

$$\frac{\mu H_p^2}{2} = 2nkT,$$

where charged particles are assumed to be distributed uniformly across the plasma column and $H_p = I_p/2\pi r_p$ is the magnetic field at the boundary of the plasma column of radius r_p. Substituting $r_p = 1$ cm and $n = 5 \times 10^{18}$ cm^{-3}, we obtain $T \cong 7.8 \times 10^4$ K.

The radiation energy of the high-temperature region for the given temperature and density is equal to nearly 102 J. The total radiation energy evaluated by integrating the flux density within the directional pattern of the radiation source is equal to $W_1 = 1.744$ kJ. Hence, the efficiency of the radiation source is equal to 0.19. When evaluating the radiation energy, the angular distribution of the radiation energy in the azimuthal and meridional planes was assumed to be proportional to the PF cross section.

The spatial temperature distribution in the discharge and the effects accompanying the high-current MPC discharge can be estimated from photographs made with optical filters (Fig. 4). We note that the high-temperature region of the discharge is located near the end of the central electrode and has a spindlelike shape typical for a PF [2, 3]. The upper boundary of the passband of a UFS-6 filter is 410 nm; thus, it is reasonable to suggest that the PF is actually formed. In addition, the discharge is accompanied by a high-power shock wave at the outlet from the plasma accelerator.

The measurements carried out with lower frequency filters show that the regions with lower temperatures have larger sizes; in the red spectral region, the discharge is diffuse in character. In Fig. 4a, we can see the effects of intense erosion on the central electrode; i.e., the temperature of the metal sputtered during erosion is $T_1 < 5500$ K. In some cases, the discharge was asymmetrical in shape because of the nonuniform injection of the foreplasma into the discharge gap.

The spatial temperature distribution is seen most clearly in Fig. 4a. We can distinguish four characteristic regions: (i) the high-temperature PF region at the end of the central electrode (the size of this region is equal to the electrode diameter d, and its height is on the order of (2–2.5)d); (ii) the internal region between the electrodes, which occupies most of the discharge volume and includes the PF; (iii) the current-carrying plasma shell; and (iv) the external low-temperature region

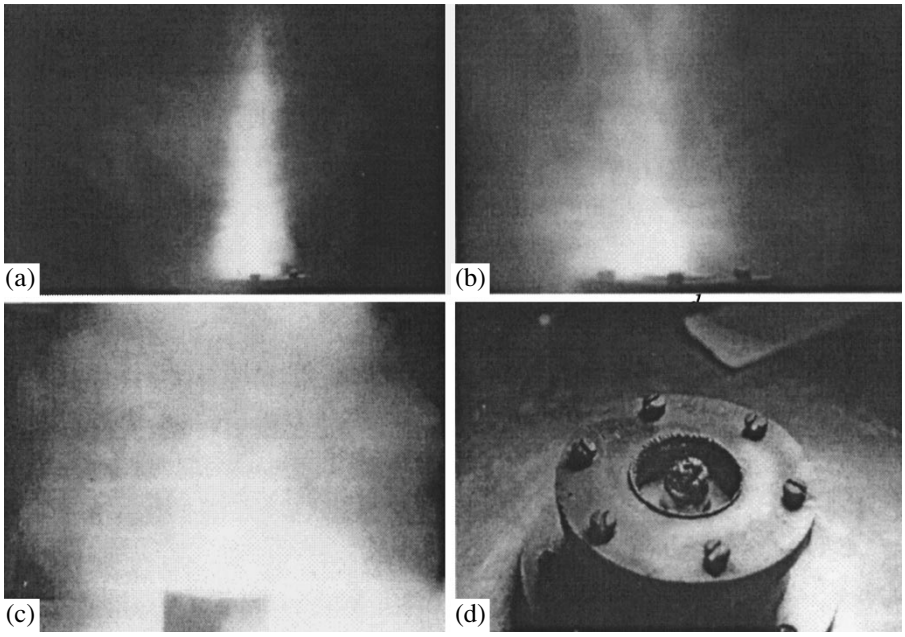

Fig. 4. Photographs of a high-current MPC discharge obtained with (a) TS-2, (b) NS-10, (c) NS-13 filters and (d) the view of the MPC electrodes.

occupied by a heated gas mainly consisting of neutral molecules.

A detailed pattern of the spatial temperature distribution is presented in Fig. 5. To visualize discharge regions with different temperatures, we applied the algorithm of searching the contour lines of the image brightness and the subsequent computer processing of photographs with the help of the Corel PhotoPaint program package. The computer processing makes it possible to distinguish a fairly wide spectrum of brightness gradations in the discharge, which, in fact, represent the isotherms of the temperature distribution.

Among the ways of increasing the power of pulsed optical radiation, we can distinguish two directions. The first direction is related to the methods for increasing the pulsed radiation power by increasing the capacitance of the storage capacitor C_2 and/or by increasing the charging voltage U_2 at the storage capacitor (which results in the increase in the pulse energy). The second direction is related to the methods for shortening the radiation pulse at a constant energy deposited in the discharge. These methods include the decrease in the parasitic inductance of the capacitor elements and current-carrying elements, e.g., by using small-inductance capacitors and current-carrying elements made in the form of metal plates, by selecting the shape and material of the electrodes in order to minimize the plasma resistance in the discharge, and using speedup capacitors in the energy storage.

We briefly describe the method using speedup capacitors. A speedup capacitor is a low-inductance capacitor (a set of capacitors) connected in parallel to the main capacitors of the energy storage and posi-

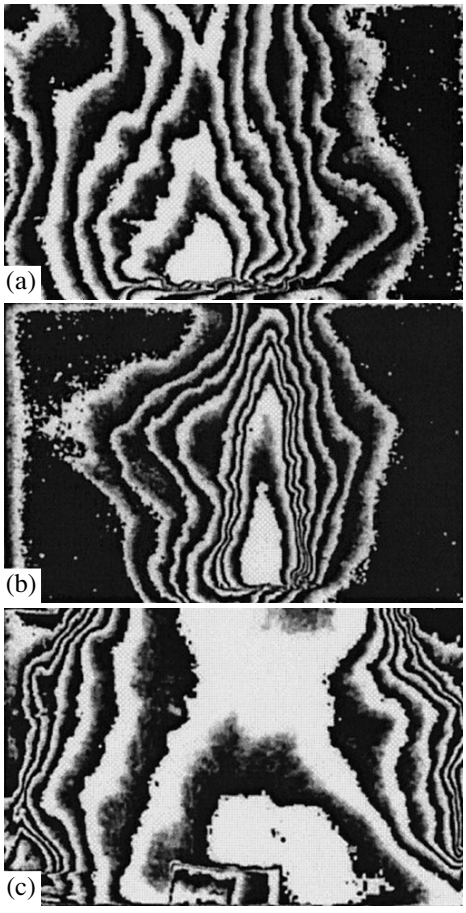

Fig. 5. The qualitative picture of the spatial temperature distribution in the discharge; images (a)–(c) correspond to Figs. 4a–4c.

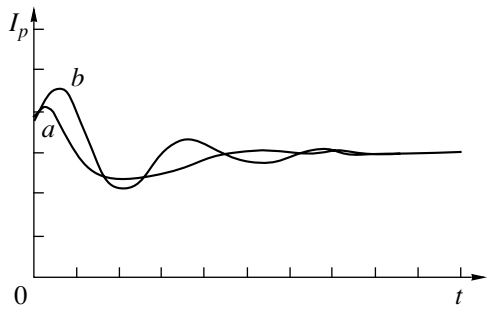

Fig. 6. The waveforms of the discharge current for a circuit with a speedup capacitor: (*a*) an aperiodic mode and (*b*) oscillatory mode.

tioned as closely to the MPC as possible. The capacitance of the speedup capacitors is chosen from the condition $C_4 = (0.001–0.01)C_2$. In this case, the discharge circuit is described by a third-order differential equation. Solving the differential equation for this circuit assuming that the active resistance of the discharge plasma is constant (R_p = const), which is true for discharges with foreplasma ignition systems, we arrive at the following results:

(i) For an aperiodic process, the discharge current $I_{p(t)}$ is described by the equation

$$I_{p(t)} = K_1 e^{-\alpha t} + K_2 e^{-\beta t} + K_3 e^{-\gamma t},$$

where K_1, K_2, K_3, α, β, and γ are constants depending on the initial conditions and the circuit elements.

(ii) For an oscillatory process, the discharge current $I_{p(t)}$ is described by the equation

$$I_{p(t)} = K_1 e^{-\alpha t}\sin\beta t + K_2 e^{-\alpha t}\cos\beta t + K_3 e^{-\gamma t},$$

where K_1, K_2, K_3, α, β, and γ are also constants depending on the initial conditions and the circuit elements. The shape of the discharge current for two cases (the aperiodic and oscillatory modes) is shown in Fig. 6. It is seen in the figure that, in the initial stage, the current in the circuit under consideration is not zero, but is equal to a certain value I_0, which depends on both the capacitance of the speedup capacitor and the initial number of ionized particles in the discharge gap. In this case, ionization and heating occur in the discharge gap in the initial stage of the discharge; hence, the growth rate of the discharge current is higher than in systems without speedup capacitors.

We have developed and created a source of broadband optical plasma radiation based on a high-current discharge in air. The source is capable of producing pulses with a power of up to 55 MW. The source efficiency with respect to the energy deposited in the discharge is on the order of 19%. The use of the busless connection of the MPC electrodes to the capacitors of the energy storage allowed us to obtain fairly short current pulses with a duration of ~20 μs and to enhance the radiation power. The results of photographic studies of the emission from the high-current discharge in different spectral regions allowed us to analyze the spatial radiation distribution in the discharge and estimate the spatial temperature distribution. The results obtained can be used to develop a fairly simple method for qualitatively estimating the plasma temperature distribution in high-current high-voltage pulsed discharges.

REFERENCES

1. N. I. Kozlov, Teplofiz. Vys. Temp. **11**, 191 (1973).
2. V. D. Zvorykin, A. S. Kamrukov, A. D. Klementov, *et al.*, Kvantovaya Élektron. (Moscow) **4**, 290 (1977).
3. A. S. Kamrukov, N. P. Kozlov, and Yu. S. Protasov, Pis'ma Zh. Tekh. Fiz. **1**, 419 (1975) [Sov. Tech. Phys. Lett. **1**, 196 (1975)].
4. *Plasma Accelerations and Ionic Injectors*, Ed. by I. P. Kozlov and A. I. Morozov (Moscow, 1984).
5. S. N. Shostko, I. S. Shostko, Yu. F. Lonin, *et al.*, in *Proceedings of the 7th International Crimean Conference "Microwave Engineering and Telecommunication Technology," Sevastopol, 1997*, Vol. 1, p. 271.

Translated by N. Larionova

Technical Physics, Vol. 46, No. 8, 2001, pp. 1045–1048. Translated from Zhurnal Tekhnicheskoĭ Fiziki, Vol. 71, No. 8, 2001, pp. 117–120.

BRIEF COMMUNICATIONS

The Effect of He^+, O^+, B^+, and Cd^+ Implantation on the Surface Structure of Magnesium Oxide Substrates for HTSC Films

Yu. M. Yakovlev, G. A. Nikolaĭchuk, N. M. Shibanova, T. A. Krylova, L. A. Kalyuzhnaya, and V. V. Petukhova

Domen Research Institute, St. Petersburg, 196084 Russia

Received October 13, 2000

Abstract—The surface structure and the morphology of polished MgO(100) substrates after ion implantation and laser annealing are studied. It is shown that ion implantation, combined with subsequent laser annealing, modifies the surface of the MgO(100) substrate, producing a single-crystal surface layer. According to electron diffraction analysis data, this layer is continuous only in case of Cd^+ implantation. © *2001 MAIK "Nauka/Interperiodica".*

INTRODUCTION

One of the most promising materials for modern cryoelectronics is the high-temperature superconductor (HTSC) $YBa_2Cu_3O_{7-\delta}$, which is conventionally used either as thin films on insulating substrates [1] or as $YBa_2Cu_3O_{7-\delta}$/MgO(100) heterostructures. The quality of the heterostructures depends on both the superconducting thin-film technique and on the surface condition of the insulating substrate. For example, the nonplanarity of substrates prepared by finish grinding, followed by chem–mech polishing, impairs the performance of YIG–superconductor devices [2]. Therefore, alternative surface processing techniques that leave the properties of the damaged surface layer on the MgO(100) substrate close to those of the bulk material are of both scientific and practical interest. In this paper, we studied the structure and the morphology of the MgO(100) substrates subjected to ion implantation and laser annealing.

EXPERIMENTAL

Single-crystal MgO(100) substrates were mechanically cut from ingots, ground, and polished with diamond powder of a grain size no more than 0.5 μm until a scratch-free surface with a roughness $R_z \le 0.05$ μm was obtained. The misorientation angle between the substrate surface and the (100) plane was within 1°. The surface layer was found to contain misorientations indicative of its quasi-polycrystalline structure.

The energy and dose of He^+, O^+, Cd^+, and B^+ ions were $E = 50$–300 keV and $D = 10^{13}$–10^{16} cm^{-2}. Both the as-polished and the as-implanted substrates were subjected to laser annealing at a coherent radiation wavelength of 10.6 μm and a power of 25 W.

The surface structure of the as-polished MgO(100) substrates, the implantation-induced damage, and the surface structure of the annealed (recrystallized) substrates were studied by He^+ Rutherford backscattering (E_0 = 860 keV, Θ = 165°) in the channeling mode. Related spectra were taken for the ion beam aligned with the ⟨100⟩ direction. The structure of the surface layer was analyzed by X-ray diffraction (DRON-2 diffractometer, CuK_α radiation) and reflection electron diffraction (performed in an electron microscope equipped with a diffraction attachment).

The surface layer can be amorphous, polycrystalline, or single-crystalline. It is known that amorphous layers do not give distinct diffraction rings on electron diffraction patterns, whereas polycrystalline layers do. Electron diffraction patterns from single-crystal surfaces consist of symmetrically arranged spots, or reflections.

We studied the surface structure of the polished MgO(100) substrates subjected to different processings: (1) as-prepared (mechanically polished) substrates, (2) laser-annealed mechanically polished substrates, (3) as-implanted substrates, and (4) laser-annealed implanted substrates.

The quality of the substrate surface can be judged, in addition to other criteria, from the superconducting properties of HTSC films synthesized on it. $YBa_2Cu_3O_{7-\delta}$ HTSC films were deposited on differently pretreated MgO(100) substrates by pyrolysis of the ceramic charge with an organic binder. The charge was chemically synthesized from yttrium, barium, and copper nitrate solutions [3]. From the samples resulted, temperature dependences of the resistance $R(T)$ were taken in the range of 77–300 K by the conventional four-probe method at the direct current 100 μA.

1063-7842/01/4608-1045$21.00

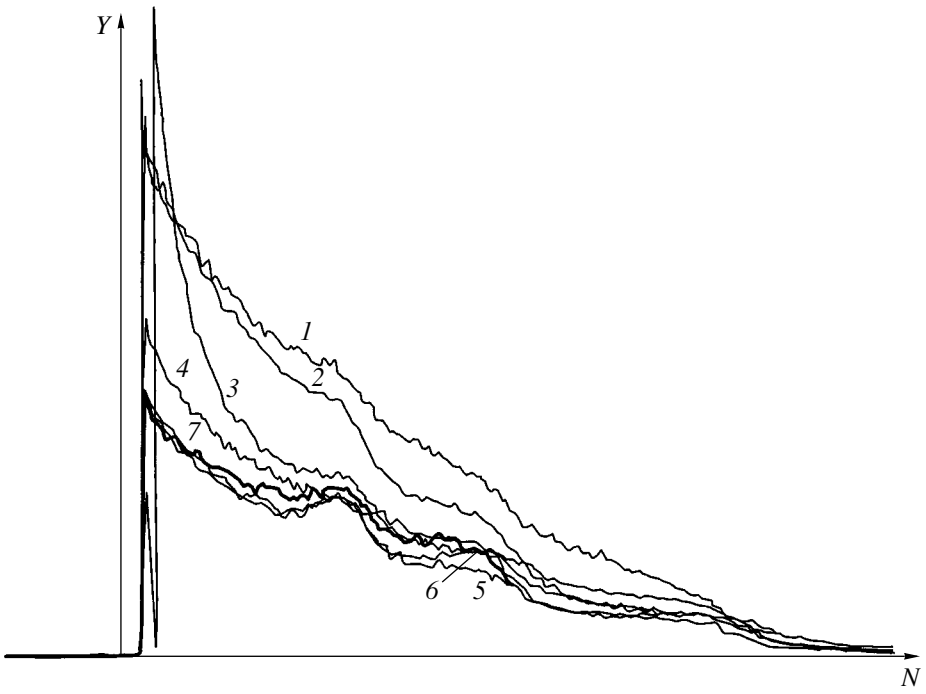

Fig. 1. Energy spectra of He^+ Rutherford backscattering in the channeling mode (E_0 = 860 keV) from the MgO(100) single-crystal substrates: (*1*) random spectrum; (*2–6*) after 100-keV He^+ implantation with respective doses of 1×10^{16}, 5×10^{15}, 1×10^{15}, 5×10^{14}, and 1×10^{14} cm^{-2}; and (*7*) as-prepared substrate. *Y* is the backscattering yield, and *N* is the channel no.

MODIFICATION OF SUBSTRATE SURFACE BY ION IMPLANTATION AND LASER ANNEALING

(a) **He^+ implantation.** The Rutherford backscattering spectra were taken from the substrates doped by different doses of 100-keV He^+ ions (Fig. 1). In the channeling mode, spectrum *7* for the initial (undoped) substrate is similar to those for the substrates doped by doses of 1×10^{15} (spectrum *3*), 5×10^{15} (spectrum *4*), and 1×10^{16} cm^{-2} (spectrum *2*); i.e., the surface damage due to the mechanical polishing within the 0.28-μm-thick surface layer remains nearly the same. At depths of 0.28 μm or more, the damage is small compared to the amorphization. The weak effect of the dose on the surface structure of the MgO(100) substrates is supported by the small variation of the superconducting properties of the underlying films. The room-temperature resistance was found to be between 0.7 and 0.8 Ω, and the superconducting transition temperature, within the range from 77 to 79 K.

It is worth noting that the spectra obtained at different sites of the substrate surface are somewhat different (Fig. 2). This may indicate the presence of slightly misoriented mosaic blocks, which is typical of single-crystal magnesium oxide. The X-ray diffraction data confirm this supposition (Fig. 3). The size of inhomogeneities is comparable to the probing beam size (about 1 mm^2). According to the electron diffraction data, an increase in the energy from 50 to 300 keV at a constant dose of 10^{14} cm^{-2} leaves the surface damage unchanged. These results suggest that, because of their small weight, helium ions cannot damage the surface to an extent close to amorphization. The electron diffraction data for the laser-annealed MgO(100) substrates

The effect of the MgO(100) substrate treatment on the superconducting properties of $YBa_2Cu_3O_{7-\delta}$ films

Treatment	Superconducting transition temperature, K			Resistance, Ω
	T_R	$T_{R=0}$	ΔT_C	
B^+ implantation (E = 300 keV, $D = 10^{15}$ cm^{-2})	85	<77	>8	1.6
B^+ implantation (E = 300 keV, $D = 10^{15}$ cm^{-2}) with subsequent laser annealing	85	83	2	0.3
As-prepared reference sample	86	77	9	0.84

Note: T_R is the initial superconducting transition temperature, $T_{R=0}$ corresponds to the zero sample resistance, ΔT_C is the transition width.

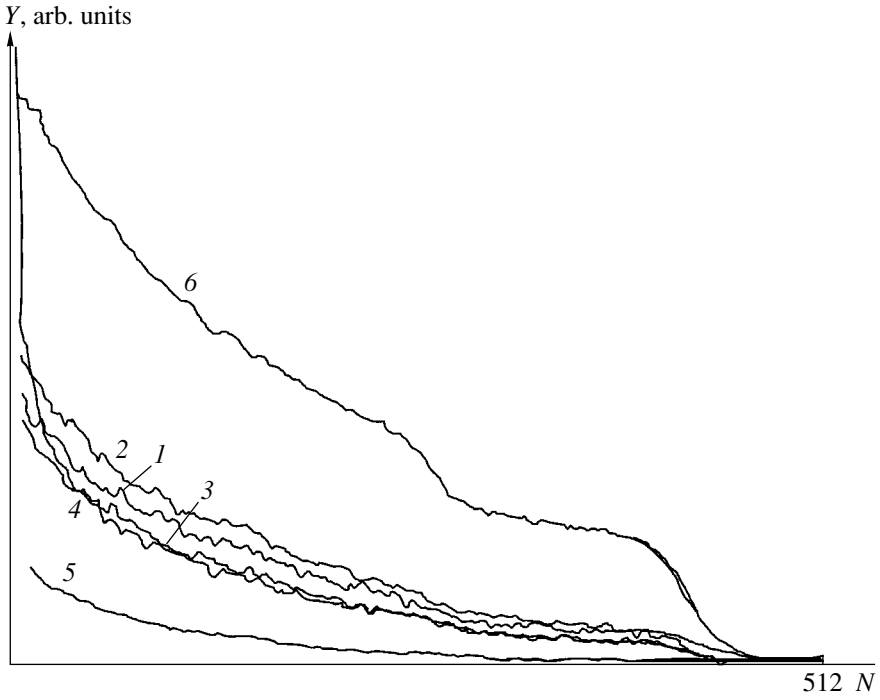

Fig. 2. Energy spectra of He^+ Rutherford backscattering in the channeling mode (E_0 = 860 keV) from the MgO(100) substrates with (*1–4*) polycrystalline and (*5*) single-crystal surface structure; (*6*) random spectrum.

show that both as-prepared and helium-doped surfaces retain the polycrystalline structure.

(b) **O^+ implantation.** As follows from the electron diffraction data for the substrates doped with O^+ ions (E = 100 keV, $5 \times 10^{13} \le D \le 10^{15}$ cm^{-2}), their surface is nearly amorphous. The electron diffraction patterns taken from the O^+-doped substrates subjected to laser annealing contain reflections indicative of the single-crystal structure of the surface layer.

(c) **B^+ and Cd^+ implantation.** The surface structure of both as-implanted substrates and laser-annealed implanted substrates varied as in the case of the O^+ implantation. It should be noted, however, that, unlike the lighter ions, the implantation of heavy cadmium ions (E = 200 keV and $D = 5 \times 10^{15}$ cm^{-2}) results in the appearance of single-crystal reflections throughout the MgO surface. The islandlike modification of the surface structure in the B^+- and O^+-doped substrates is evidently due to the smaller weights of these ions as compared to that of Cd^+, since similar structure modifications were also observed after B^+ and O^+ implantation into YIG substrates [4].

Since the maximum surface temperature provided by the scanning laser (2000°C) is much lower than the MgO melting point (2800°C), the formation of the single-crystal surface layer through solid-phase recrystallization seems to be a possibility.

(d) **Superconducting properties of $YBa_2Cu_3O_{7-\delta}$ films on the implanted substrates.** The effect of the MgO(100) surface structure on the electrical properties of HTSC films was studied on samples of two types: $YBa_2Cu_3O_{7-\delta}$/MgO(100) films doped by B^+ and Cd^+ ions (E = 300 keV, $D = 10^{15}$ cm^{-2}) (type I) and similarly doped $YBa_2Cu_3O_{7-\delta}$/MgO films subjected to laser annealing (type II).

To control the process of HTSC film fabrication and to obtain a database for comparative analysis, reference samples $YBa_2Cu_3O_{7-\delta}$ films deposited on the substrates immediately after the mechanical polishing) of both types were also prepared. They were thermally treated together with the samples of the corresponding

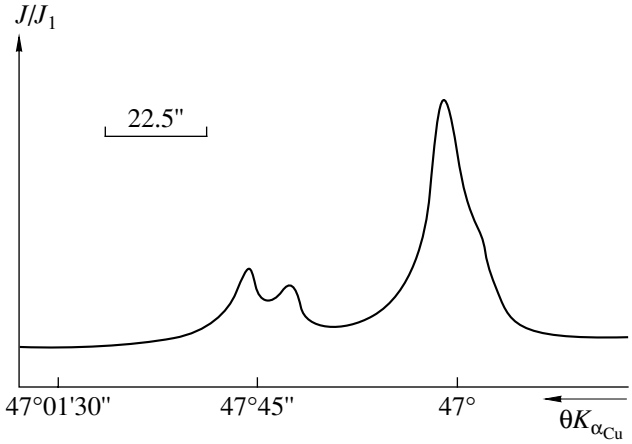

Fig. 3. Diffraction pattern from the MgO(100) single-crystal substrate.

type. The initial superconducting transition temperature turned out to be equal for all of the samples. The superconducting properties were better for the HTSC films on the B^+- or Cd^+-doped substrates subjected to laser annealing: they offer a higher final superconducting transition temperature and a lower electrical resistance at room temperature. The superconducting properties of the films obtained on the B^+-doped substrates are listed in the table.

Thus, we have demonstrated that the single-crystal surface layer on polished MgO(100) substrates can be produced by ion implantation, followed by laser annealing. According to the electron diffraction analysis, the continuous single-crystal layer was obtained only on the Cd^+-doped substrates.

REFERENCES

1. Z.-Y. Shen, *High Temperature Superconducting Circuits* (Artech House, Nortwood, 1994).
2. L. V. Lutsev and S. V. Yakovlev, J. Appl. Phys. **83**, 7330 (1998).
3. G. A. Nikolaĭchuk, S. V. Yakovlev, T. A. Krylova, *et al.*, Neorg. Mater. **34**, 718 (1998).
4. B. M. Lebed', S. V. Yakovlev, G. A. Nikolaĭchuk, *et al.*, Pis'ma Zh. Tekh. Fiz. **22** (10), 18 (1996) [Tech. Phys. Lett. **22**, 395 (1996)].

Translated by A. Sidorova-Biryukova

Technical Physics, Vol. 46, No. 8, 2001, pp. 1049–1052. Translated from Zhurnal Tekhnicheskoĭ Fiziki, Vol. 71, No. 8, 2001, pp. 121–124.

BRIEF COMMUNICATIONS

Subnormal Glow Discharge in a Xe/Cl_2 Mixture in a Narrow Discharge Tube

A. K. Shuaibov, A. I. Dashchenko, and I. V. Shevera

Uzhhorod State University, Pidgirna str. 46, Uzhhorod, 88000 Ukraine

Received October 13, 2000

Abstract—Electrical and optical characteristics of a subnormal glow discharge in a short (L = 10 cm) discharge tube with an inner diameter of 5 mm are investigated. The dependences of the discharge current–voltage characteristic, the energy deposition in the discharge, the plasma spectral characteristics in the 130- to 350-nm wavelength range, the emission intensities of the XeCl(D–X) 236-nm and XeCl(B–X) 308-nm bands, and the total emission intensity in the range 180–340 nm on the pressure and composition of the Xe/Cl_2 mixture are studied. Two modes of glow discharge are shown to exist: the low-current mode at a discharge current of $I_{ch} \leq$ 2 mA and the high-current mode at $I_{ch} >$ 2 mA. The transition from one mode to another occurs in a stepwise manner. The increase in the chlorine content causes the discharge voltage and the energy deposition in the plasma to increase. At low pressures of the Xe/Cl_2 mixture ($P \leq$ 0.7 kPa), stationary strata form in the cathode region. The lower the discharge current, the greater the volume occupied by the strata. This longitudinal discharge acts as a powerful source of continuous broadband emission in the range 180–340 nm, which forms due to overlapping the XeCl(D, B–X) and Cl_2^* bands with edges at λ = 236, 308, and 258 nm. The intensity of the 236-nm band is at most 20% of the total intensity of UV radiation. The maximum power of UV radiation (3 W at an efficiency of 8%) is attained at a xenon partial pressure of 250–320 Pa and a total pressure of the mixture of 2 kPa. © *2001 MAIK "Nauka/Interperiodica".*

INTRODUCTION

Systematic studies of longitudinal low-pressure glow discharges in the mixtures of heavy gases (Ar, Kr, and Xe) with chlorine began more than 20 years ago [1, 2]. Interest in this type of discharge is related to the wide applications of noble-gas plasmas with small admixtures of halogen-containing molecules in plasmochemistry [3, 4], quantum electronics, and other fields of science and technology. The first studies of these discharges were carried out with Ar/Cl_2 [1] and Kr/Cl_2 [2] mixtures at pressures $P \leq$ 130 Pa in discharge tubes with lengths of L = 50 cm and diameters of 14–30 mm and were aimed mainly at determining the electron energy distribution functions and electrical parameters of the positive column.

The longitudinal low-pressure glow discharge in the Xe/Cl_2 and Kr/Cl_2 mixtures was first proposed as an efficient source of continuous UV radiation and optimized in [5–7]. The discharge was ignited in cylindrical quartz tubes with lengths of L = 17–28 cm and inner diameters of 1.2–3.0 cm. At discharge currents of I_{ch} = 20–30 mA and pressures of P = 0.6–4 kPa, the emission power of an excimer lamp attained 10–20 W at an efficiency of 12–23%. The longitudinal and transverse distributions of the densities of XeCl* and KrCl* molecules in the discharge tube were found to be nonuniform: most of the excimer molecules were produced in the anode region and in the central part of the tube [6]. The maximum generation efficiency of UV radiation was attained at relatively low discharge currents ($I_{ch} \leq$ 10 mA), when the voltage drop across the discharge tube was maximum. Such a high-voltage mode of a longitudinal dc discharge occurs when passing over from the dark Townsend discharge to the normal glow discharge and is called the subnormal glow discharge (SGD) [8]. An SGD in a 40-cm-long coaxial tube enabled an excimer lamp with an emission power of 8 W at an efficiency of 30% to be created.

In this paper, we continue studying the low-pressure ($P \leq$ 30 kPa) electric-discharge excimer lamps based on the mixtures of Ar, Kr, and/or Xe with molecular chlorine [9–14]. The most attention is concentrated on achieving the steady-state pump mode and a further decrease in the mixture pressure. The electrical, spectral, and energy characteristics of low-pressure SGDs in Xe/Cl_2 mixtures in a short narrow discharge tube are determined.

EXPERIMENTAL SETUP

A glow discharge was ignited in a thin-walled quartz tube with an inner diameter of 5 mm. The distance between the 10-mm-long, 5-mm-wide cylindrical nickel electrodes was 100 mm. The electrodes were placed inside the discharge tube near its open ends. The

1063-7842/01/4608-1049$21.00

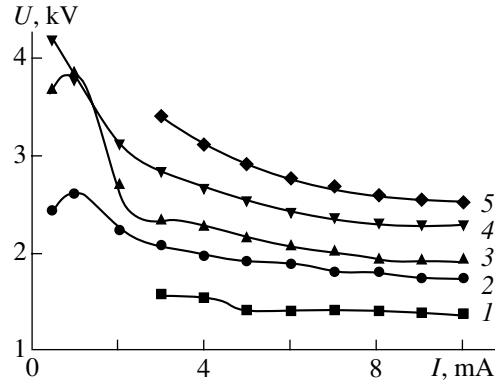

Fig. 1. Current–voltage characteristics of SGDs in Xe/Cl_2 mixtures: P_{Xe}/P_{Cl_2} = (*1*) 0.60/0.08, (*2*) 2.00/0.04, (*3*) 2.00/0.16, (*4*) 2.00/0.40, and (*5*) 2.00/0.56 kPa.

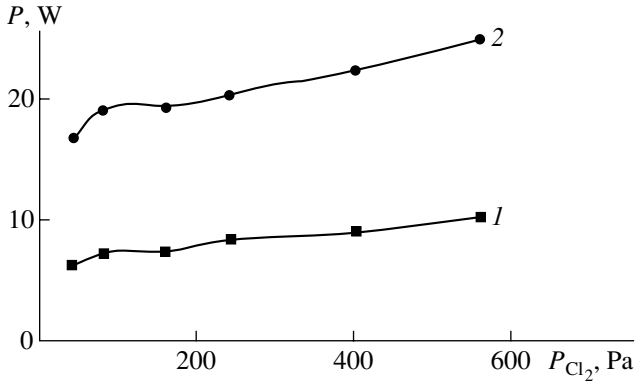

Fig. 2. Power deposition in an SGD in a Xe/Cl_2 mixture vs. the chlorine partial pressure for P_{Xe} = 2.0 kPa and I_{ch} = (*1*) 3 and (*2*) 10 mA.

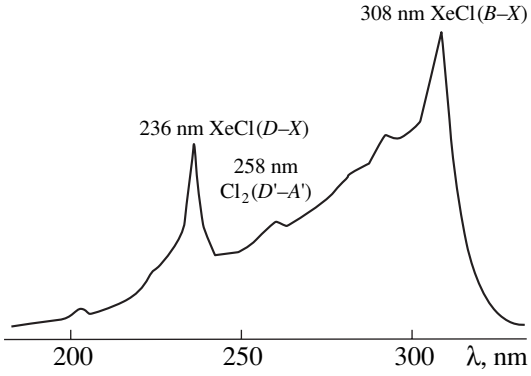

Fig. 3. Emission spectrum from an SGD in a Xe/Cl_2 mixture.

discharge tube was placed in a sealed 10-l buffer chamber with a CaF_2 window and three quartz windows 5 cm in diameter. The chamber was connected via the CaF_2 window to a 0.5-m-long Seya–Namioka vacuum monochromator equipped with a 1200-line/mm diffraction grating. The discharge tube was positioned so that its center was at the same level as the centers of the entrance and exit monochromator slits. An FÉU-142 photomultiplier with an LiF window served as a radiation detector. The residual pressure in both the monochromator and photomultiplier compartment was 10^{-3}–10^{-4} Pa. The operating range of the spectrophotometer was 130–350 nm. The relative calibration of the monochromator–photomultiplier system was performed with the help of the emission continuum of molecular hydrogen in the range 165–350 nm. The system for recording the photodetector signal was the same as in [10–14]. The SGD was powered by a high-voltage dc power supply ($U_{ch} \le 30$ kV, $I_{ch} \le 100$ mA); a positive voltage was applied to the anode through a ballast resistor (r_b = 400–700 kΩ). The discharge currents were in the range I_{ch} = 0.5–30 mA. Absolute measurements of the SGD emission power were carried out with a Kvarts-01 detector by the procedure described in [9]. Between the Kvarts-01 detector and the aperture on the discharge tube surface, a filter with a 200- to 400-nm passband was installed. In the measurements, the relative spectral sensitivity of the detector was taken into account.

ELECTRICAL AND OPTICAL CHARACTERISTICS

An SGD existed in the low-current and high-current modes. A stepwise transition from one mode to another occurred at I_{ch} = 0.5–1.5 mA; in some current–voltage characteristics, the transition manifested itself as a hump at low discharge currents (Fig. 1). At larger currents, the rate at which U_{ch} decreased progressively slowed, which corresponded to the voltage stabilization and the transition to the normal mode of a glow discharge. At $I_{ch} \ge 10$ mA, the current–voltage characteristics measured in our experiments were similar to those obtained in [15] with a 9-mm-diameter and 23-cm-long coaxial tube at I_{ch} = 10–80 mA. At low currents, the current–voltage characteristics were also similar to those of an SGD in a coaxial tube [9]. The increase in the mixture pressure and/or the xenon content led to an increase in both U_{ch} and the power deposition in the discharge (Fig. 2). The decrease in the pressure of the Xe/Cl_2 mixture to 0.5–0.7 kPa resulted in the formation of stationary strata in the cathode region of the discharge tube. When the discharge current decreased from 10 to 3 mA, the strata occupied the entire positive column. Stratified SGDs are of importance for developing special UV radiation sources with a controlled regular distribution of the emission intensity over the source surface. Such sources can be used to draw regular geometric figures on the surfaces of photosensitive materials and prepare special photomasks.

Figure 3 shows the emission spectrum from an SGD in a Xe/Cl_2 mixture. The spectrum contains strongly broadened XeCl(*D*–*X*), XeCl(*B*–*X*), and Cl_2(*D*'–*A*')

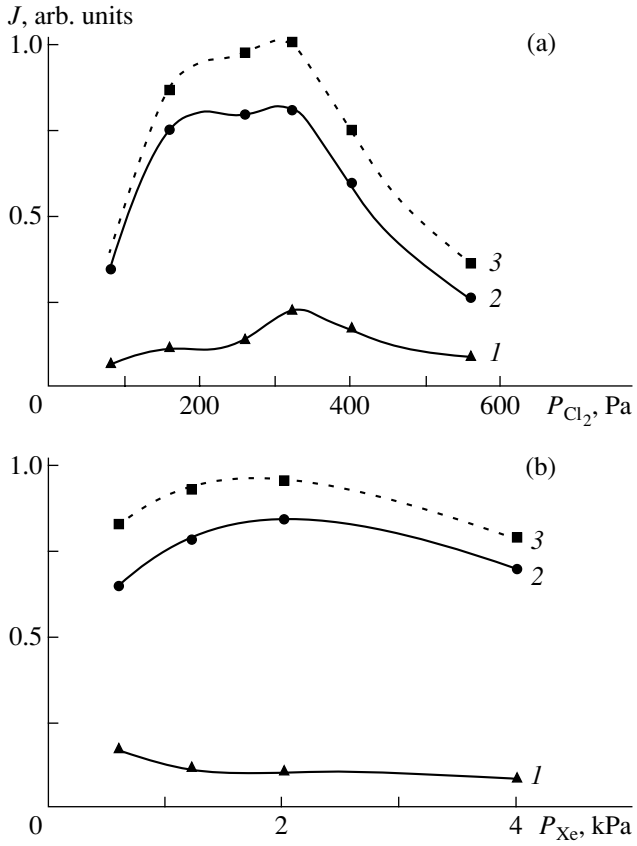

Fig. 4. Intensities of the XeCl(*D*, *B*–*X*) bands with λ = (*1*) 236 and (*2*) 308 nm and (*3*) the total emission intensity of from the SGD in the range 180–340 nm vs. (a) the chlorine partial pressure at P_{Xe} = 2.0 kPa and (b) the xenon partial pressure at P_{Cl_2} = 80 Pa for I_{ch} = 8 mA.

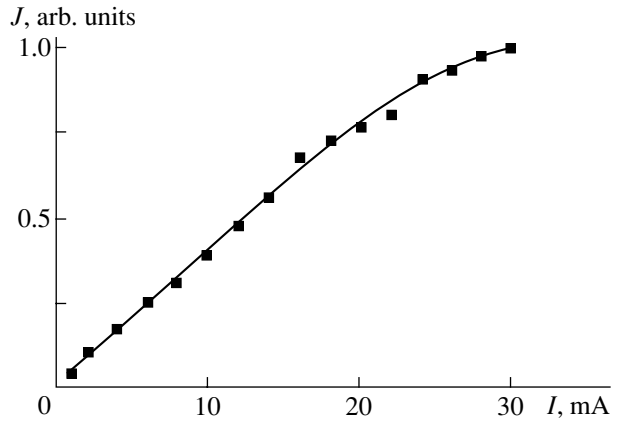

Fig. 5. Intensity of the XeCl(*D*–*X*) 236-nm band in the Xe/Cl_2 = 3.6/0.24-kPa mixture vs. the SGD current.

bands with edges at λ = 236, 308, and 258 nm, respectively. Due to the broadening and overlapping of these bands, the discharge can be regarded as a broadband (180–340 nm) radiation source. The entire spectrum can be divided into two bands: the XeCl(*B*–*X*) band together with Cl_2^* 258-nm bands and the XeCl(*D*–*X*) band (joining them results in the spectrum recorded). For each mixture, we determined the intensities of the XeCl(*D*, *B*–*X*) bands and the integral intensity in the range 180–340 nm. The band intensity was defined as the area below the corresponding profile of the emission spectrum, which was corrected for the relative spectral sensitivity of the monochromator–photomultiplier system.

The dependences of the intensity of a Xe/Cl_2 SGD excimer lamp on the chlorine and xenon partial pressures are shown in Fig. 4. The intensity of the XeCl(*D*–*X*) band is at most 10–20% of the integral intensity of UV radiation from the SGD plasma. The optimum partial pressure of Cl_2^* lies in the range 250–320 Pa. The dependence of the intensity of the 236-nm band on the discharge current is linear in the range 1–20 mA and then saturates (Fig. 5). Such a shape of the dependence $J = f(I_1)$ is similar to that of the integral intensity of UV radiation from the longitudinal glow discharge in a wide tube [5], in which the UV intensity starts decreasing at discharge currents of $I \geq 30$ mA. The maximum averaged radiation power in the range 180–340 nm is 3 W at an efficiency of 8%.

CONCLUSION

It is shown that an SGD in a Xe/Cl_2 mixture in a short narrow discharge tube acts as an efficient source of continuous UV emission in the wavelength range 180–340 nm (P = 3 W at an efficiency of 8%). Due to the strong overlapping of the XeCl(*D*, *B*–*X*) and Cl_2(*D*–*A*) molecular bands, the emission spectrum has the form of a continuum with peaks at λ = 236, 258, and 308 nm. The intensity of the XeCl(*D*–*X*) 236-nm band is at most 20% of the total intensity of UV radiation. The optimum partial pressures of chlorine and xenon are 250–320 Pa and 2 kPa, respectively.

REFERENCES

1. V. V. Zaĭtsev, E. Yu. Zverevskaya, Ya. I. Zukher, and P. D. Netyagov, Teplofiz. Vys. Temp. **16**, 1152 (1978).
2. V. V. Zaĭtsev, P. D. Netyagov, and N. V. Bozhko, Teplofiz. Vys. Temp. **18**, 944 (1980).
3. B. S. Danilin and V. Yu. Kireev, *Application of Low-temperature Plasma for Etching and Cleaning Materials* (Énergoatomizdat, Moscow, 1987).
4. A. M. Efremov, A. I. Kupriyanovskaya, and V. I. Svettsov, Khim. Vys. Énerg. **27** (1), 88 (1993).
5. A. P. Golovitskiĭ, Pis'ma Zh. Tekh. Fiz. **18** (8), 73 (1992) [Sov. Tech. Phys. Lett. **18**, 269 (1992)].
6. A. P. Golovitskiĭ and S. N. Kan, Opt. Spektrosk. **75**, 604 (1993) [Opt. Spectrosc. **75**, 357 (1993)].

7. A. P. Golovitskiĭ and S. V. Lebedev, Opt. Spektrosk. **82**, 251 (1997) [Opt. Spectrosc. **82**, 227 (1997)].
8. Yu. P. Raizer, *Gas Discharge Physics* (Nauka, Moscow, 1987; Springer-Verlag, Berlin, 1991).
9. A. N. Panchenko and V. F. Tarasenko, Opt. Spektrosk. **84**, 389 (1998) [Opt. Spectrosc. **84**, 337 (1998)].
10. A. K. Shuaibov, L. L. Shimon, A. I. Dashchenko, *et al.*, Pis'ma Zh. Tekh. Fiz. **25** (11), 29 (1999) [Tech. Phys. Lett. **25**, 433 (1999)].
11. A. K. Shuaibov, L. L. Shimon, A. I. Dashchenko, and I. V. Shevera, in *Problems of Economical and Social Development of the Region and the Practice of Scientific Experiments* (Karpaty, Kiev, 2000), Vol. 16, p. 185.
12. A. K. Shuaibov, Pis'ma Zh. Tekh. Fiz. **26** (9), 1 (2000) [Tech. Phys. Lett. **26**, 357 (2000)].
13. A. K. Shuaibov and A. I. Dashchenko, Kvantovaya Élektron. (Moscow) **30**, 279 (2000).
14. A. K. Shuaibov and A. I. Dashchenko, Prib. Tekh. Éksp., No. 3, 101 (2000).
15. M. I. Lomaev, A. N. Panchenko, É. A. Sosnin, and V. F. Tarasenko, Zh. Tekh. Fiz. **68** (2), 64 (1998) [Tech. Phys. **43**, 192 (1998)].

Translated by N. Ustinovskiĭ

Technical Physics, Vol. 46, No. 8, 2001, pp. 1053–1055. Translated from Zhurnal Tekhnicheskoĭ Fiziki, Vol. 71, No. 8, 2001, pp. 125–127.

BRIEF COMMUNICATIONS

On the Possibility of Diagnostics of High-Energy Proton Beams Using Parametric X-ray Radiation Excited in Single Crystals

M. D. Bavizhev, L. Sh. Dokumova, R. M. Goshokov, É. A. Merker, and V. V. Kaplin

Institute for High-Energy Physics, Russian Federal Research Center, Protvino, Moscow oblast, 142281 Russia

e-mail: emerker@oea.ihep.su

Received October 23, 2000

Abstract—The possibility of diagnosing high-energy proton beams with the help of parametric X-ray radiation generated in single crystals is considered. © *2001 MAIK "Nauka/Interperiodica".*

To date, numerous experiments on the use of the effect of channeling of relativistic charged particles in single crystals have been performed [1]. With great success, crystallooptic systems are applied as particle deflectors based on bent crystals for the ejection and forming of beams in modern accelerators [2, 3]. Single crystals also received wide application for beam diagnostics.

In this paper, we discuss the technique of beam diagnostics based on the detection of specific radiation that arises when a relativistic proton passes through an oriented single crystal. Because of the periodicity of crystals structures, single crystals can with success be applied as radiators of monochromatic polarized parametric X-ray radiation (PXR) with a controlled frequency. This radiation is a result of the diffraction of pseudophotons of the self-field of a relativistic proton [4].

The PXR of relativistic electrons was first observed in a diamond single crystal in Tomsk [5]; later, similar investigations were performed in Kharkov [6] and Erevan [7]. In these investigations, this type of radiation has been studied for the electron energies from 20 MeV to 4.6 GeV and for the energies of generated photons from a few keV to several hundred keV. No such investigations have been made for protons. At the same time, the possibility of using PXR for the production of beams of polarized X-ray photons can substantially widen the circle of applications of proton accelerators and storage rings. An important thing in this case is the possibility of obtaining greater Θ_γ angles of PXR ejection, up to $\pi/2$ with respect to the direction of the proton motion, as compared to, e.g., transition radiation, where $\Theta_\gamma \approx \gamma^{-1}$.

The advantage of protons over electrons is their substantially smaller (in fractions of the characteristic angle γ^{-1}) scattering in the crystals, which makes it possible to obtain high-intensity coherent radiation using thick crystals or, on the contrary, to use thin crystals that only weakly disturb the proton beam. The PXR photons are emitted along the direction of the particle propagation $\Theta_\gamma = \Theta_0$ (central reflection) and in the direction $\Theta_\gamma = 2\Theta_0$ (side reflection).

Figure 1 displays the geometry of the angular distribution of PXR emitted into the side diffraction reflection. The plane of the drawing coincides with the plane formed by the proton-momentum and reciprocal-lattice vectors.

Experimental investigations [8] show that the degree of linear polarization for some directions can reach 90%. We calculated the angular and energy distributions of PXR produced by 70-GeV protons in a (110) silicon crystal 1 mm thick according to the theory [9]. The results of the calculations of $\Theta_{\gamma x}$ distributions for $\Theta_0 = 40°$ and 10° with respect to the (110) plane of the silicon crystal are given in Fig. 2; the $\Theta_{\gamma y}$ distributions are similar. It is seen that the intensity of the PXR reflection has a narrow minimum in the direction $\Theta_{\gamma x} = \Theta_{\gamma y} = 0$. The angle of the maximum intensity of PXR in the calculated distributions is close to the effective angle of radiation emission determined as $\Theta_{ph} = (\gamma^{-2} + \omega_p^2/\omega^2 + \Theta_m^2)^{1/2}$, where Θ_m is the root-mean-square angle of multiple scattering of a proton in the crystal, ω_p is the plasma frequency of the material, and ω is the photon-emission frequency. In our case, we have $\Theta_{ph} \approx$

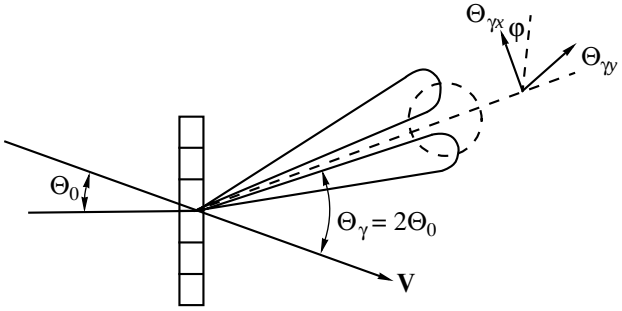

Fig. 1. Geometry of the angular distribution of X-ray photons in a side diffraction reflection of PXR.

1063-7842/01/4608-1053$21.00

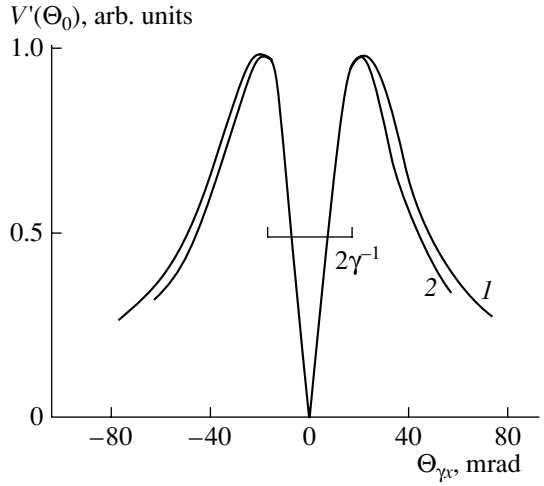

Fig. 2. Angular distributions of PXR photons into the side reflection for a silicon crystal 1 mm thick. Proton energy 70 GeV; $\Theta_0 = 40°$ (*1*) and 10° (*2*).

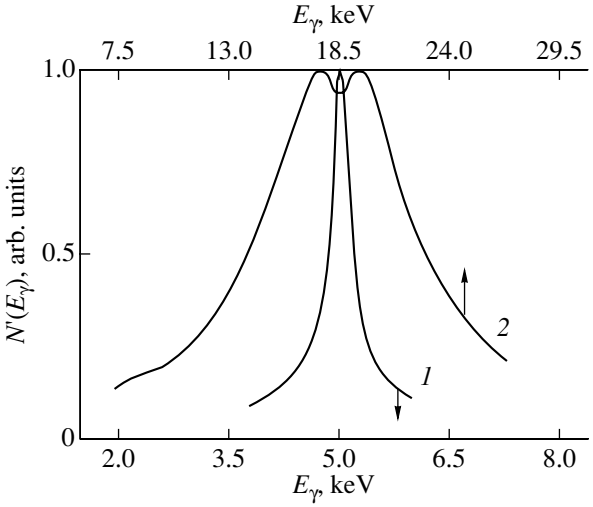

Fig. 3. Spectra of PXR photons (excited by protons with an energy of 70 GeV) emitted into the side reflection for a silicon crystal 1 mm thick.

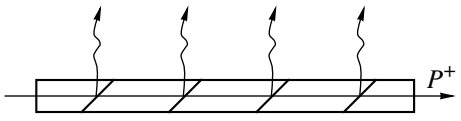

Fig. 4. Asymmetrical geometry of crystal irradiation upon the generation of PXR (Laue–Bragg transition).

γ^{-1}, since ω_p^2/ω^2 and Θ_m^2 are much smaller than γ^{-2}; therefore, the shape of the distributions shown in Fig. 2 only weakly depends on the angle Θ_0. The densities of radiation in the maximum are $\sim 1.2 \times 10^{-5}$ and $\sim 3.8 \times 10^{-3}$ photon/(p Ω) for $\Theta_0 = 40°$ and 10°, respectively.

Figure 3 shows the total spectra of emission produced by protons with an energy of 70 GeV in a silicon crystal calculated according to the theory [9] for $\Theta_0 =$ 40° (curve *1*) and 10° (curve *2*) with respect to the plane (110). In contrast to the angular distributions, the shape of the total spectra of PXR in the side reflection substantially depends on the angle Θ_0. At $\Theta_0 = 40°$, the spectral distribution of PXR represents a sharp peak at the photon energy $E_\gamma = 5$ keV with the FWHM $\Delta E_\gamma/E_\gamma \approx$ 6% and with the spectral density of radiation in the maximum $\sim 6.3 \times 10^{-9}$ photon/(p eV). At $\Theta_0 = 10°$, the radiation spectrum represents a wide two-hump distribution centered at $E_\gamma = 18.5$ keV with relative FWHM $\approx$45%, and maximum spectral density $\sim 3.7 \times 10^{-9}$ photon/(p eV). The total photon yield is $\sim 3.8 \times 10^{-6}$ photon/p for $\Theta_0 = 40°$ and $\sim 3 \times 10^{-5}$ photon/p for $\Theta_0 = 10°$.

Because of the absorption of photons in the crystal, it is expedient to use an asymmetrical geometry of crystal irradiation (Fig. 4), namely, the so-called Laue–Bragg transition case. Thus, if a 70-GeV proton moves inside a crystal at a distance less than the photon absorption length from the crystal surface, the spectral density of emission will be $\sim 6 \times 10^{-9}$ photon/(p eV) at $\Theta_0 = 40°$ and $\sim 3.5 \times 10^{-7}$ photon/(p eV) at 10° per 1 mm of the path.

It is obvious that this geometry is the most promising, since it permits one, using a peripheral portion of the proton beam, to organize an additional channel to work with X-ray radiation. Taking into account the small absorption of photons in the asymmetrical geometry in comparison with the Laue geometry, longer crystals can be employed for the production of X-ray radiation with the greatest intensity. In the case when the absorption of photons is insignificant, the rate of spectral, angular, and spectral-angular density of PXR is substantial until the root-mean-square angle of the multiple scattering satisfies the condition $\Theta_m^2 \leq \gamma^{-2} + \omega_p^2/\omega^2$; a further increase in the crystal length leads to an effective increase in the width of the angular and spectral distributions and, as a consequence, to the saturation of the growth of these radiation characteristics.

Thus, in the case of protons, crystals that are longer by a factor of $(\gamma_e/\gamma_p)^2$ than in the case of electrons of the same energy can be used for the generation of PXR beams. Therefore, as a factor that restricts the thickness of the crystal used for radiation generation, nuclear interaction should be regarded in the case of protons, and, now, the nuclear length L_N rather than the radiation length L_R is the parameter that determines the optimum length of the crystal. In our case, $L_N = 30$ cm and, at $\Theta_0 \approx 10°$, the yield of X-ray photons can reach $\sim 10^{-2}$ photon/p.

When using PXR for the diagnostics of relativistic protons, the sufficiently high intensity and the directivity of the radiation make it possible to take crystals of very small size, which virtually do not disturb the beam to be analyzed. Moving a thin crystal in the beam and measuring the yield of PXR, one can determine the pro-

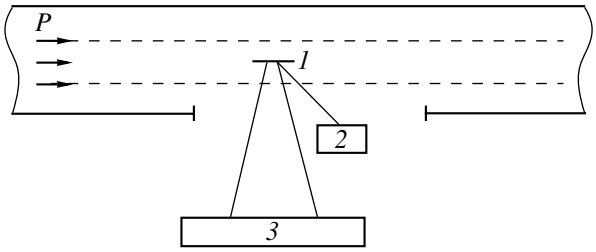

Fig. 5. Diagnostics of relativistic proton beams using PXR (schematic): (*1*) crystal, (*2*) goniometer, and (*3*) *x–y* position detector of X-ray radiation.

ton-intensity distribution over the cross section of the beam with a resolution determined by the width of the crystal, which can be specified to an accuracy of a few microns. An advantage of this method is the simplicity and compactness of the construction for the beam diagnostics, which consists of a goniometer with a fixed crystal and a detector of γ photons (Fig. 5).

Taking into account that the angular distribution of PXR substantially depends on the divergence of the primary beam, this method of diagnostics can also be successfully applied for measuring angular characteristics of proton beams, since an increase in the angular divergence of the beam to be analyzed leads to a broadening of the peak and a decrease in the narrow dip in the center of the angular distribution of PXR. Estimates show that the resolution of this method of measuring angular divergence of the beam can be $\sim 0.1\gamma^{-1}$. This does not exceed the possibilities of the method that can be realized, e.g., with the use of coherent transition radiation [10] in a layered target, but the simplicity of the fabrication and the compactness of the crystal radiator, as well as the high energy and large angles of ejection of the radiation with respect to the direction of the proton beam, make PXR more preferable for measurements of this kind.

The combined measurement of the intensity of a fraction of the beam upon displacement of the crystal and of the angular distribution of the particles of this fraction can be used for measuring the emittance of the beam at a definite place in the channel.

The accuracy of measuring the parameters of the proton beam and the resolution of this diagnostic method can be substantially improved by focusing [11] the generated X-ray radiation using a bent crystal. Thus, many principles of controlling radiation that have long been harnessed in X-ray diffraction optics can also be successfully applied for forming PXR beams.

REFERENCES

1. V. M. Biryukov, V. I. Kotov, and Yu. A. Chesnokov, Usp. Fiz. Nauk **164**, 1017 (1994) [Phys. Usp. **37**, 937 (1994)].
2. A. A. Aseev, M. D. Bavizhev, *et al.*, Preprint No. 87-57, Inst. Fiz. Vysokikh Énergii (IFVÉ) (Serpukhov, 1989).
3. A. G. Afonin, V. M. Biryukov, *et al.*, Preprint No. 98-15, Inst. Fiz. Vysokikh Énergii (IFVÉ) (Serpukhov, 1998).
4. V. G. Baryshevskiĭ, *Channeling, Radiation, and Reactions in Crystals under High Energies* (Beloruss. Gos. Univ., Minsk, 1982).
5. S. A. Vorob'ev, B. N. Kalipin, S. Pak, *et al.*, Pis'ma Zh. Éksp. Teor. Fiz. **41**, 3 (1985) [JETP Lett. **41**, 1 (1985)].
6. D. I. Adeĭshvili, S. V. Blazhevich, *et al.*, Dokl. Akad. Nauk SSSR **298**, 844 (1988) [Sov. Phys. Dokl. **33**, 117 (1988)].
7. R. O. Avakyan, A. É. Avetisyan, Yu. N. Adishchev, *et al.*, Pis'ma Zh. Éksp. Teor. Fiz. **45**, 313 (1987) [JETP Lett. **45**, 396 (1987)].
8. Yu. N. Adishchev, V. A. Verzilov, *et al.*, Nucl. Instrum. Methods Phys. Res. B **44**, 130 (1989).
9. J. D. Feranchuk and A. V. Jvashin, J. Phys. (Paris) **46**, 1981 (1985).
10. M. A. Piestrup, D. G. Boyers, Qiand Li, *et al.*, IEEE Trans. Nucl. Sci. **35**, 464 (1988).
11. S. A. Vorob'ev, V. V. Kaplin, and Pak Sen-De, USSR Inventor's Certificate No. 1 302 933 (1985).

Translated by S. Gorin

Technical Physics, Vol. 46, No. 8, 2001, pp. 1056–1059. Translated from Zhurnal Tekhnicheskoĭ Fiziki, Vol. 71, No. 8, 2001, pp. 128–131.

BRIEF COMMUNICATIONS

Temperature Dependence of Viscosity

R. L. Fogel'son and E. R. Likhachev

Voronezh State University, Universitetskaya pl. 1, Voronezh, 394693 Russia

e-mail: phssd18@main.vsu.ru

Received November 13, 2000

Abstract—A correction to the simple exponential temperature dependence of viscosity arises because of a difference between the real and ideal conditions for a viscous fluid flow. This correction is similar to those to pressure and volume in the real gas law. As a result, the expression for viscosity takes the form

$$\eta = \eta_0 \exp\left(\frac{E}{k(T + T_0)}\right).$$

Literature experimental data for the viscosity of various fluids verify this dependence. © *2001 MAIK "Nauka/Interperiodica".*

In the study of polymeric glasses under deformation [1], the following dependence of limit stress σ on temperature T and strain rate v was obtained:

$$\sigma = (A + B\ln v) - (C + D\ln v)T, \quad (1)$$

where A, B, C, and D are constants. Since viscosity $\eta = \sigma/v$ under experimental conditions, the temperature dependence of viscosity is given by

$$\eta = \sigma \exp\left(\frac{U - a\sigma}{k(\theta - T)}\right), \quad (2)$$

where $U = k(A - CT)/D$, $a = k/D$, and $\theta = B/D$.

The only difference of expression (2) from the Eyring formula [2], obtained theoretically in the case of large stresses, is that, in (2), the difference $(\theta - T)$ appears instead of temperature T. The same difference in the expression for viscosity has been empirically found elsewhere [3, 4].

The appearance of the difference in the exponential dependence of viscosity may be explained in the following way. The specific heat at constant volume c_v of monoatomic fluids is close to $3R$ [5], where R is the gas constant. Therefore, in the ideal case, such fluids, like solids, are equivalent to a system of noninteracting harmonic oscillators that obeys the Boltzmann statistics. According to Eyring [2], particles in a viscous fluid flow must overcome potential barriers. In the classical case, a potential barrier of energy E can be overcome only by particles with an energy of no less than E. Therefore, the probability of passing through the barrier is proportional to the number of particles with an energy $\varepsilon \geq E$. As is shown in the Appendix, for a set of harmonic oscillators, this number is proportional to

$$\exp(-E/kT). \quad (3)$$

The probability of the particles passing through the barrier is proportional to the same function.

Real fluids essentially differ from ideal monoatomic fluid, since, in the former, the particle motion is much more intricate than oscillations about a fixed center. Moreover, the Boltzmann statistics applies to an equilibrium system, whereas a viscous fluid flow is a nonequilibrium process. Therefore, the probability that a system will penetrate the barrier should differ from (3). One can assume that, in the first approximation, a correction T_0 to temperature must appear in expression (3) much as corrections to pressure and volume appear in the real gas law. As a result, expression (3) takes the form

$$\exp\left(-\frac{E}{k(T + T_0)}\right). \quad (4)$$

Eyring employed function (3) in his theory. Substituting (4) for (3) yields Eq. (2) for the viscosity of a polymeric glass (the case of large external forces), where $T_0 = -\theta$. Then, for the viscosity of ordinary fluids (small external forces), we will have

$$\eta = \eta_0 \exp\left(\frac{E}{k(T + T_0)}\right). \quad (5)$$

A lot of experimental data for the viscosities of various fluids has been analyzed to verify Eq. (5). By varying the parameters η_0, E, and T_0, we found the minimum of the quantity

$$\delta = \frac{1}{n}\sum_n \left|\frac{\eta_e - \eta_t}{\eta_e}\right|, \quad (6)$$

which is the mean relative deviation between the calculated and the experimental values. Here, η_e is the experimental viscosity; η_t, theoretical viscosity calculated by

Table 1

Fluid	T, K	n	m	η_0, 10^{-5} Pa s	E, kJ/mol	T_0, K	δ, %	Reference
Nonane	253–423	18	6.6	1.78	8.24	–25	0.36	[7, 8]
Undecane	253–473	18	13.6	2.07	8.07	–54	0.85	[7, 8]
Benzene	285–400	24	3.6	0.705	12.02	27	0.85	[7]
n-xylene	283–403	13	3.2	1.11	11.2	39	0.27	[7]
Toluene	253–393	13	4.3	0.774	13.09	71	0.5	[7, 8]
Ethylbenzene	253–393	13	4.4	1.34	10.48	29	0.33	[7, 8]
Freon-21	209–329	31	4.6	1.45	7.14	–2	0.08	[7]
Freon-113	241–333	24	3.9	1.14	10.17	3.7	0.07	[7]
Freon-114	209–333	32	5.2	1.63	7.71	0.5	0.08	[7]
Methyl alcohol	183–333	15	25.4	1.22	8.67	–24	1.14	[7]
Ethyl alcohol	183–348	25	60.5	0.198	17.82	42	1.15	[8]
Diethyl alcohol	153–313	17	21.4	3.80	3.66	–58	1.94	[7]
Acetone	183–333	16	9.1	2.16	6.22	–17	1.13	[8]
Nitrobenzene	273–480	19	9.5	4.49	6.54	–87	0.91	[8]
Acetic acid	283–383	11	3.4	2.71	7.34	–61	0.33	[8]
Bromine	273–333	13	1.8	6.73	5.64	–41	0.14	[8]
Sodium	371–1200	10	4.6	5.71	11.21	170	0.39	[7]
Zinc	723–973	6	1.7	32.60	15.56	100	0.045	[8]
Mercury	253–1073	24	2.6	53.52	2.613	0.75	0.035	[7]
Sodium chloride	1098–1273	8	2.0	4.37	19.15	–440	0.66	[8]
Gasoline	223–573	28	25.5	0.447	14.49	70	1.2	[7]
Kerosene	223–573	28	72.3	3.96	5.88	–97	3.2	[7]
Saltpeter mixture	423–823	41	15.3	28.86	6.97	–219.5	0.082	[7]
BM-4 oil	243–373	24	1×10^5	6.52	7.5	–186	10	[7]
Resin	282–373	20	2×10^8	8.25	14.65	–226	14	[3]
Aqueous solution of sodium chloride (20 wt %)	263–353	10	7.2	6.39	3.48	–162	1.1	[7]

Table 2

Fluid	P, Bar	T, K	n	m	η_0, 10^{-5} Pa s	E, kJ/mol	T_0, K	δ, %	Reference
Water	1	273–363	10	5.6	2.4152	4.7428	–139.86	0.0046	[7]
Water	20	273–483	22	13.7	2.4180	4.7460	–139.70	0.021	[7]
Hydrogen	10	15–30	12	3.5	0.00475	3.16	47	1.46	[7]
Nitrogen	30	65–120	12	7	0.0985	5.3	48	2.43	[7]

(5); and n, the amount of experimental viscosities used in the calculations. The gas constant was set equal to $R = 8.31441$ J/(mol K) [6].

The calculations showed that Eq. (5) adequately describes the temperature dependence of the fluid viscosity. The results calculated for various fluids are listed in Tables 1 and 2. These tables summarize the calculated parameters η_0, E, T_0, and δ, along with temperature intervals in which the measurements were conducted, the number of viscosity values employed in the calculations (n), the maximum-to-minimum viscosity ratio (m) in the interval specified, and associated references. In Table 2, the pressure p under which the measurements were made is listed as well.

In the case of high-viscosity fluids, δ runs to 10–15%. However, the experimental values of viscosity randomly deviate from the calculated curve. In the $\log\eta$ vs. T plot, data points would appear on both sides of the curve. Hence, the large values of δ are associated with relatively large experimental errors in this case.

Sometimes, the extreme values of the experimental viscosity (those measured near the melting point and

Table 3

T_0, K	η_0, 10^{-5} Pa s	E, kJ/mol	δ, %
10	39.85	12.64	0.134
30	38.14	13.26	0.098
60	35.82	14.19	0.062
70	35.02	14.52	0.055
80	34.26	14.85	0.047
100	32.60	15.56	0.045
120	31.27	16.23	0.049
140	30.13	16.87	0.058
150	29.70	17.16	0.071
180	27.80	18.24	0.092
220	25.72	19.65	0.126

Table 4

T_0, K	η_0, 10^{-5} Pa s	E, kJ/mol	δ, %
–8	54.118	2.515	0.176
–3	53.775	2.570	0.083
–1	53.665	2.591	0.049
0	53.590	2.603	0.037
0.5	53.555	2.609	0.035
0.75	53.520	2.613	0.035
1	53.500	2.616	0.035
1.5	53.477	2.621	0.037
2.5	53.425	2.631	0.046
5	53.300	2.656	0.079
10	52.941	2.715	0.162

above the temperature of vaporization of the material) deviated from the calculated curve much more than the other values. These values and the corresponding temperatures are not given in the tables.

If the viscosity varies only slightly and the number of data points is small, the minimum of δ diffuses and there appear many number triples η_0, E, and T_0, resulting in equally good agreement between the calculated and the experimental values. In such cases, even minor measurement errors may cause substantial errors in the parameters calculated. Table 3, where the results for zinc are listed, exemplifies the strong smearing of the minimum of δ. The parameters for zinc listed in Table 1 are taken at the center of the dip. The same situation takes place for sodium chloride in Table 1. The smearing of the minimum of δ is observed for most metals and inorganic compounds. However, if the temperature range is wide enough and, accordingly, the number of viscosity measurements is large, the minimum of δ turns out to be sharp and the parameters η_0, E, and T_0 are determined fairly accurately. An example is Table 4, where the calculations for mercury are listed.

Tables 1 and 2 show that the correction to temperature T_0 may be both positive and negative. Presumably, factors violating the ideal conditions in the system give corrections of different sign. The resulting sign depends on the predominant factor. One may suppose that the temperature correction is negative when a system comes out of equilibrium. This is supported by the following facts. First, in another kinetic phenomenon, diffusion, where the temperature dependence of diffusion coefficient is analogous to (4), the correction T_0 is always positive [9]. It is known that diffusion in solids and liquids is much closer to equilibrium than viscous flow [10]. Second, polymeric glasses under deformation experience large forces and, therefore, the deviation from equilibrium is large. In this case, the absolute value of the negative correction T_0 even exceeds the temperatures at which the polymer is in the glassy state. For instance [1], $\theta = 415$ K for polymethylmethacrylate and $\theta = 388$ K for polystyrene. These temperatures are close to the softening temperatures of the materials.

To conclude, we note that the potential barrier height U may be a linear function of temperature: $U = U_0 - \beta T$ [1]. In this case, the experimentally found energy E for ordinary fluids will not only define the potential barrier height but will also depend on T_0: $E = U_0 + \beta T_0$.

APPENDIX

Consider a system consisting of N oscillators with a frequency ω. Let us find the number of oscillators n_E that have an energy $\varepsilon \geq E$ at a temperature T. In the framework of the Boltzmann statistics, using the normalized probability that an oscillator is in the nth state with the energy

$$\varepsilon_n = \hbar\omega\left(n + \frac{1}{2}\right),$$

we arrive at

$$n_E = N\frac{\sum_{n=n_0}^{\infty}\exp(-n\hbar\omega/kT)}{\sum_{n=0}^{\infty}\exp(-n\hbar\omega/kT)} = N\exp(-E/kT). \quad \text{(A1)}$$

Here, we have taken into account that $\hbar\omega$ is very small compared to E, and hence, the equality $n_0\hbar\omega = E$ is satisfied with a sufficiently high accuracy. Expression (A1) is also valid when the oscillators have various frequencies, since the exponential is independent of the frequency.

REFERENCES

1. Yu. S. Lazurkin and R. L. Fogel'son, Zh. Tekh. Fiz. **21**, 267 (1951).
2. S. Glasstone, K. J. Laidler, and H. Eyring, *Theory of Rate Processes* (McGraw-Hill, New York, 1941; Inostrannaya Literatura, Moscow, 1948).
3. E. Hatschek, *The Viscosity of Liquids* (G. Bell, London, 1928; ONTI, Moscow, 1935).
4. A. V. Tobolsky, *Properties and Structure of Polymers* (Wiley, New York, 1960; Khimiya, Moscow, 1964).
5. M. I. Shakhparonov, *Introduction to the Molecular Theory of Solutions* (GITTL, Moscow, 1956).
6. Advisable Value of Physical Constants, Usp. Fiz. Nauk **115**, 623 (1975).
7. N. B. Vargaftik, *Tables of Thermophysical Properties of Liquids and Gases* (Nauka, Moscow, 1972; Halsted Press, New York, 1975).
8. *Handbook of Chemist* (Khimiya, Leningrad, 1971), Vol. 1.
9. R. L. Fogel'son and E. R. Likhachev, Fiz. Met. Metalloved. **90**, 62 (2000).
10. R. L. Fogel'son, *Thermodynamic and Kinetic Theory of Diffusion* (Voronezh. Gos. Univ., Voronezh, 1992).

Translated by M. Fofanov

Technical Physics, Vol. 46, No. 8, 2001, pp. 1060–1062. Translated from Zhurnal Tekhnicheskoĭ Fiziki, Vol. 71, No. 8, 2001, pp. 132–133.

BRIEF COMMUNICATIONS

Stationary Thermomagnetic Waves in Superconductors

N. A. Taĭlanov and U. T. Yakhshiev

Research Institute of Applied Physics, National University of Uzbekistan,
Universitetskaya ul. 95, Vuzgorodok, Tashkent, 700174 Uzbekistan
e-mail: taylanov@iaph.silk.org

Received December 4, 2000

Abstract—The propagation of a nonlinear stationary thermomagnetic wave in superconducting media is qualitatively analyzed in view of the effect of an external magnetic field. The velocity and the thickness of the wave front are estimated. It is demonstrated that the inclusion of an external magnetic field affects the thermomagnetic wave profile only slightly. © *2001 MAIK "Nauka/Interperiodica".*

The evolution of Joule heat during the dissipative motion of a magnetic flux gives rise to pronounced nonlinear effects showing up as various wave processes. These processes define the dynamics of thermal and electromagnetic perturbations in superconducting media [1–3]. The stationary propagation of a nonlinear shock thermomagnetic wave in the resistive state of a superconductor is an example. As is shown [1], the dispersive, nonlinear, and dissipative processes in superconducting media result in the formation of stable thermoelectric, **E**, and/or thermomagnetic, **H**, waves depending on the surface conditions. It was assumed that the critical current density $\mathbf{j}_c$ is independent of the local value of the external magnetic field **H** (Bean's model of critical state [4]). However, in sufficiently strong fields, this dependence cannot be disregarded (see, e.g., [5]) and its effect on the nonlinear thermomagnetic wave should be taken into account.

In this paper, we studied the structure of a shock thermomagnetic wave for an arbitrary dependence of the critical current density $\mathbf{j}_c$ on the external magnetic field **H**. Expressions for the velocity and the thickness of the wave front were obtained.

The propagation of a thermomagnetic wave in a superconducting medium along the x axis with a constant velocity v is described by the nonlinear heat conduction equation (with the self-simulated variables $\xi(x, t) = x - vt$) [1]

$$-\nu v\frac{dT}{d\xi} = \frac{d}{d\xi}\left[k\frac{dT}{d\xi}\right] + jE, \qquad (1)$$

Maxwell equations

$$\frac{dE}{d\xi} = -\frac{4\pi v}{c^2}j, \quad E = \frac{v}{c}H, \qquad (2), (3)$$

and the related equation of critical state

$$j = j_c(T, H) + j_r(E). \qquad (4)$$

Here, ν and k are the specific heat capacity and the thermal conductivity, respectively, and j_r is the resistive current density.

In the weak heating approximation $(T - T_0) \ll (T_c - T_0)$, the resistive current density j_r in the range of viscous flow ($E > E_{\text{eff}}$, where E_{eff} is the effective field [5]) is a linear function of the vortex electric field; i.e., $j_r \approx \sigma_{\text{eff}}E$, where σ_{eff} is the effective conductivity and T_0 and T_c are the equilibrium and the critical superconductor temperatures, respectively. For weak fields ($E < E_{\text{eff}}$), the dependence $j_r(E)$ is substantially nonlinear and may be attributed to the thermally activated motion of the magnetic flux (flux creep [5]).

In the range between two critical magnetic fields $H_{c_1} \ll H \ll H_{c_2}$, the dependence of the critical current j_c on T and H can be approximated as the product of two functions of single variable:

$$j_c = j_c(T, H) = j_c(T)\Phi(H). \qquad (5)$$

Here, $j_c(T) = j_c(T_0) - a(T - T_0)$, $j_c(T_0) = j_0$ is the equilibrium current density, a characterizes the thermal reduction of Abrikosov vortex pinning on crystal defects, and Φ will be determined below for different values of the external field H. The thermal and electrodynamic boundary conditions for Eqs. (1)–(5) are given by

$$\begin{aligned} &T(\xi \longrightarrow +\infty) = T_0, \quad \frac{dT}{d\xi}(x \longrightarrow -\infty) = 0, \\ &E(\xi \longrightarrow +\infty) = 0, \quad E(\xi \longrightarrow -\infty) = E_e, \end{aligned} \qquad (6)$$

where E_e is the constant external electric field.

Jointly solving Eqs. (1)–(5) with boundary conditions (6) yields the following equation for the E wave:

$$\frac{d^2E}{dz^2} + F\left(E, \frac{dE}{dz}\right) + \frac{dU}{dE} = 0, \qquad (7)$$

1063-7842/01/4608-1060$21.00

where

$$F = \beta(1+\tau) - \frac{c}{v\Phi}\frac{d\Phi}{dE}\left[\beta\tau\frac{j_r(E)}{\sigma_d} + \frac{dE}{dz}\right]\frac{dE}{dz}, \quad (8)$$

$$U = \beta^2\tau\int_0^E\left[1 + \frac{j_0}{j_r}\Phi\right]\frac{j_r}{\sigma_d} - \frac{E^2}{2E_k}\Phi dE. \quad (9)$$

Here, $z = \xi/L$, $\beta = (vt_k)/L$, $\tau = (4\pi\sigma_{\text{eff}}k)/c^2\nu$, $t_k = (\nu L^2)/k$, $E_k = k/(aL^2)$, $L = (cH_e)/(4\pi j_0)$ is the magnetic penetration depth, σ_d is the differential conductivity, and H_e is the external magnetic field.

Following [6], let us represent the equation for stationary points in the phase plane (E, dE/dz) as

$$\beta^2\tau\frac{j_r}{\sigma_d}\left[1 + \frac{j_0}{j_r}\Phi\right] - \frac{E^2}{2E_k}\Phi = 0. \quad (10)$$

In not-too-strong fields, when $H \ll H_{c_2}$, the $\Phi\left(\frac{c}{v}E\right)$ function can be chosen in terms of the Kim–Anderson model [7]. In our situation, Eq. (10) has two equilibrium states: a stable node, $E_0 = 0$, and a saddle, $E = E_1$. The phase portrait illustrating these equilibrium states is plotted in Fig. 1. The separatrix AB, connecting these two singular points, corresponds to the "overfall"-type solution with the amplitude E_e.

With the boundary conditions $E = E_e$ at $z \longrightarrow -\infty$, this equation can be written as the equation for wave velocity v_e:

$$1 - \Omega_0 V_E = X_0(V_E) = \Omega_E V_E^2, \quad (11)$$

where

$$\Omega_0 = 2\tau c\frac{t_k^2}{L^2}\frac{E_k}{H_0}\left[1 - \frac{j_0}{\sigma_d E_e}\right], \quad \Omega_E = 2\tau\frac{t_k^2}{L^2}\frac{E_k}{E_e}, \quad (12)$$

and H_0 is a constant parameter.

Common points of the $X_0(V_E)$ function and the quadratic parabola $\Omega_E E^2$ yield the velocity v_E we are interested in:

$$v_E = \frac{cE_e}{2H_0}\left[1 - \frac{j_0}{\sigma_d E_e}\right] \times\left[\left(1 + \frac{2L^2}{c^2t_k^2}E_k\frac{H_0^2}{\tau E_e}\left[1 - \frac{j_0}{\sigma_d E_e}\right]^2\right)^{1/2} - 1\right]. \quad (13)$$

The corresponding plot is depicted in Fig. 2. Only the positive value v_E^+ is physically meaningful. In the limit $H_0 \longrightarrow \infty$ (Bean's model [4]), the wave velocity is

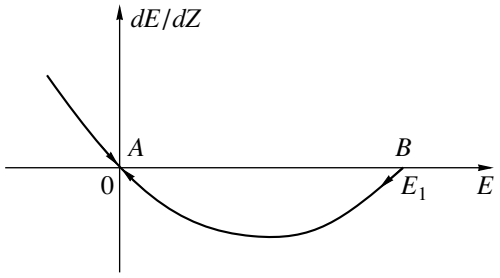

Fig. 1. Phase portrait of Eq. (10).

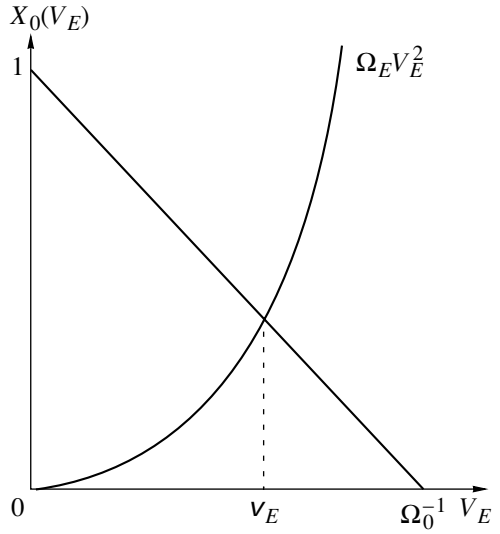

Fig. 2. Graphical solution of Eq. (11).

defined by

$$v_E = \frac{L}{t_k}\left[\frac{E_e}{2\tau E_k}\right]^{1/2}. \quad (14)$$

In the reverse case, when $H_0 \longrightarrow 0$, the velocity is largely small and is almost independent of the wave amplitude E_e:

$$v_e \approx \frac{L^2}{ct_k^2}\frac{H_0^2}{2\tau E_k E_e}\left[1 - \frac{j_0}{\sigma_d E_e}\right]^{-1}. \quad (15)$$

For the field H approaching H_{c_2}, the following approximation is valid:

$$v_E \approx c\frac{j_0 E_e}{j_1 H_{c_2}}\left(\ln\frac{E_e}{E_0}\right)^{-1}. \quad (16)$$

In conclusion, our results suggest that taking into account an arbitrary dependence of j_c on H has a minor effect on the wave profile, since the phase portrait remains nearly the same. The qualitative analysis presented above may be useful for experimentally studying the penetration of a magnetic flux into a superconductor placed into an external magnetic field. Improv-

ing the protection of superconducting devices at the design stage is another possible application of our results.

REFERENCES

1. I. L. Maksimov, Yu. N. Mastakov, and N. A. Taĭlanov, Fiz. Tverd. Tela (Leningrad) **28**, 2323 (1986) [Sov. Phys. Solid State **28**, 1300 (1986)].
2. N. A. Taĭlanov and S. Kuchkarov, Zh. Tekh. Fiz. **61** (7), 197 (1991) [Sov. Phys. Tech. Phys. **36**, 838 (1991)].
3. N. A. Taĭlanov and S. Kuchkarov, Fiz. Tverd. Tela (Leningrad) **33**, 1873 (1991) [Sov. Phys. Solid State **33**, 1052 (1991)].
4. C. P. Bean, Phys. Rev. Lett. **8**, 250 (1962).
5. R. G. Mints and A. L. Rakhmanov, *Instability in Superconductors* (Nauka, Moscow, 1984).
6. V. I. Karpman, *Nonlinear Waves in Dispersive Media* (Nauka, Moscow, 1973).
7. P. W. Anderson and Y. B. Kim, Rev. Mod. Phys. **36**, 36 (1964).

Translated by A. Sidorova-Biryukova

Technical Physics, Vol. 46, No. 8, 2001, pp. 1063–1067. Translated from Zhurnal Tekhnicheskoĭ Fiziki, Vol. 71, No. 8, 2001, pp. 134–138.

BRIEF COMMUNICATIONS

Structural Stability of a Nonparaxial Singular Mode Beam

A. V. Volyar, V. G. Shvedov, and T. A. Fadeeva

Vernadsky National University, Simferopol, 95007 Ukraine

e-mail: volyar@ccssu.crimea.ua

Received October 31, 2000

Abstract—The exact explicit solution of the Maxwell equations for nonparaxial singular beams propagating in free space or in a homogeneous isotropic medium is considered. It is shown that, in the paraxial approximation, such solutions for mode beams of both lower and higher orders may turn into the solutions for guided modes or vortices of optical fibers. It is found that a variation of the Rayleigh length for a mode beam does not change the structure of phase and polarization singularities; it merely transforms their coordinates. In the paraxial limit, the singularities are shifted off the axis to regions with negligible light fluxes. © *2001 MAIK "Nauka/Interperiodica".*

The propagation of a real laser beam is always related to external perturbations, which usually induce changes in its structure. Changes in the field structure can be conveniently characterized within the concept of structural stability of the Mors functions [1]. In singular-beam optics, the change in the number of wavefront dislocations in response to small variations of the beam parameter, e.g., the Rayleigh length z_0, may serve as a descriptive qualitative characteristic of structural stability. From this standpoint, the birth and/or death of dislocations (dislocation reactions [2]) at small variations of z_0 may be considered as an example of structural instability of the wave field. In [2], a nonparaxial beam in which elementary plane waves have various real directions of propagation and the magnitudes of the wave vectors are modulated by the Gaussian function has been considered. The elementary wave spectrum was limited to uniform fields only, whereas the evanescent waves were neglected. As a result, edge diffraction by "numerical aperture" arises and dislocation rings form. Any small variation of the Rayleigh length z_0 induces the birth–death of the ring dislocations. Although the sum of the topological indices of the characteristic surface remains constant (Poincaré–Hopf theorem [3]), the total number of dislocations changes. Hence, the beam is structurally unstable. For a beam to be structurally stable, one has to take into account fields for which the sum of the squares of the direction cosines of elementary waves is other than unity, i.e., to take into account the evanescent waves of free space. We have considered this problem for lower-order nonparaxial vector beams in [4]. However, the Davis boundary conditions, employed in the paper, did not allow us to pass to the limit of higher-order paraxial beams.

The aim of this paper is to study structurally stable mode beams carrying phase and polarization singularities. As boundary conditions, we require that, in the vicinity of the focal plane $z = 0$, the electric and magnetic field components of nonparaxial singular beams transform, in the paraxial approximation, into the fields of the eigenmodes and the vortices of a weakly guiding optical fiber with the axisymmetrically distributed refractive index.

In order to solve the problem, we take advantage of the method of Whittaker potentials [4] and represent the scalar potentials in the form

$$\begin{aligned}\Psi_1 &= A_m^{(l)} P_m^{(l)}(\cos\theta) j_m(kR)\cos(l\varphi),\\ \Psi_2 &= A_m^{(l)} P_m^{(l)}(\cos\theta) j_m(kR)\sin(l\varphi).\end{aligned} \tag{1}$$

Here, $P_m^{(l)}(\cos\theta)$ are the associated Legendre polynomials, $j_m(kR)$ are the mth-order spherical Bessel functions of the first kind, $R = \sqrt{x^2 + y^2 + (z + iz_0)^2}$ is the complex radius, $\cos\theta = (z + iz_0)/R$, $A_m^{(l)}$ is a normalization factor, k is the wave number, and φ is azimuth angle.

Such a choice of scalar potentials (1) is dictated by the symmetry requirement for the fields at the input to a weakly guiding fiber [5]. Note that the associated Legendre polynomials have the form

$$\begin{aligned}P_m^{(l)}(\zeta) &= (1-\zeta^2)^l \frac{d^l P_m}{d\zeta^l} \quad \text{and}\\ P_m(\zeta) &= \frac{1}{2^m m!}\frac{d^m}{d\zeta^m}(\zeta^2-1)^m,\\ \zeta &= \cos\theta.\end{aligned} \tag{2}$$

Besides, in the paraxial approximation, we have

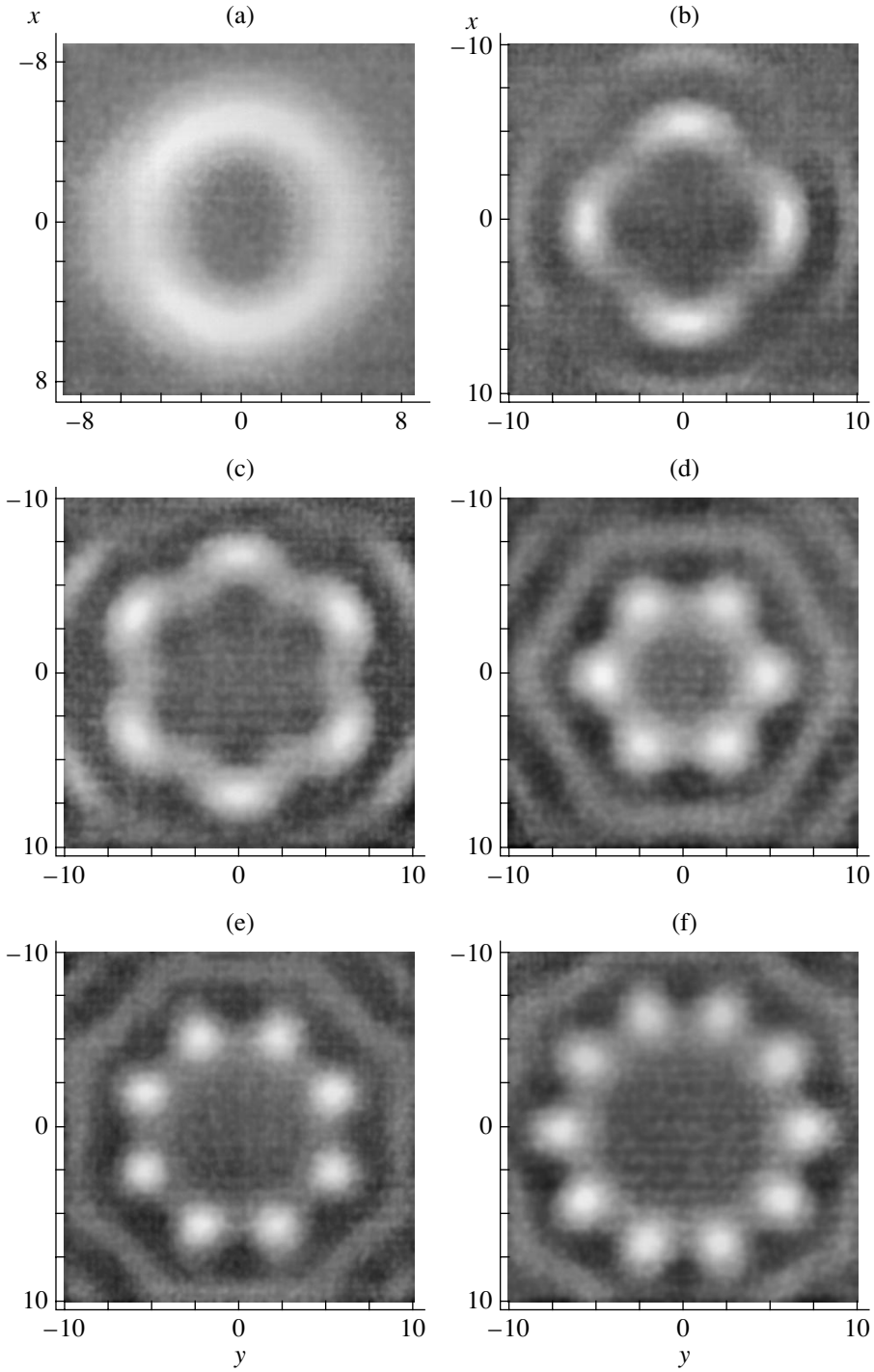

Fig. 1. Distribution of the light intensity in the waist plane $z = 0$ of the singular beam in free space for (a) EH_{12}^{ev}, (b) EH_{23}^{ev}, (c) EH_{34}^{ev}, (d) HE_{32}^{ev}, (e) HE_{43}^{ev}, and (f) HE_{54}^{ev} modes. The Rayleigh length $kz_0 = 1$. The coordinates are measured in units of the wave number k.

$kz_0 \gg 1$ and

$$\frac{j_m(R)}{R^m} \propto G_0(x, y, z),$$

where

$$G_0(x, y, z) = \frac{1}{\xi}\exp\left(-\frac{r^2}{\rho^2\xi}\right); \quad \xi = 1 + i\frac{z}{z_0}$$

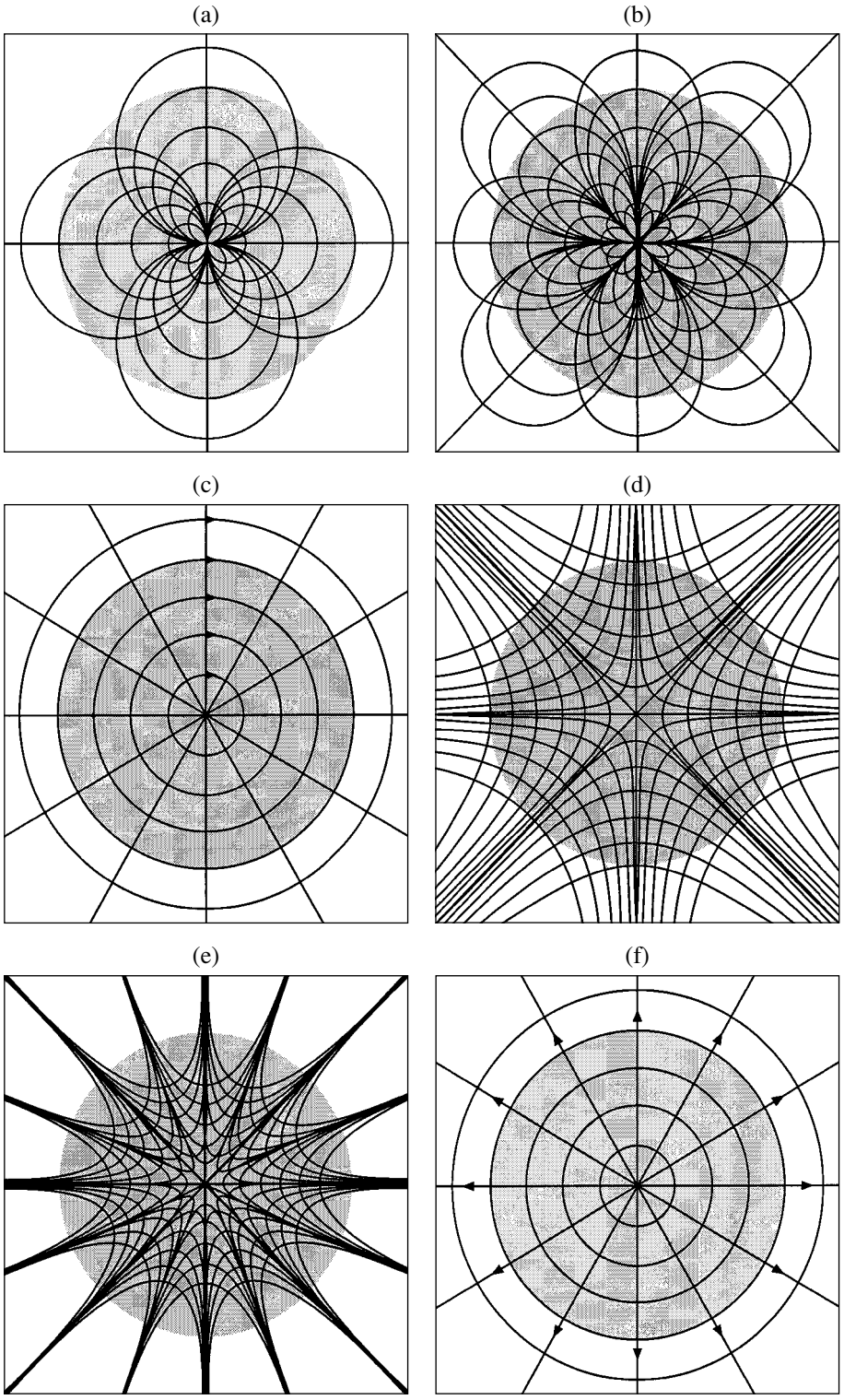

Fig. 2. Distribution of the electric (black lines) and magnetic (gray lines) field lines of singular beams with $kz_0 = 1$ in the plane $z = 0$ for (a) EH_{12}^{ev}, (b) EH_{23}^{ev}, (c) TE_{01}, (d) HE_{21}^{ev}, (e) HE_{43}^{ev}, and (f) TM_{01} modes. The gray circle marks out the beam region with the waist radius $\rho = \sqrt{2z_0/k}$.

Eigenmodes of higher-order nonparaxial singular beams ($m = l$)

	$\mathbf{e}_r$	$\mathbf{e}_\varphi$	$\mathbf{e}_z$	$\mathbf{h}_r$	$\mathbf{h}_\varphi$	$\mathbf{h}_z$
$\mathbf{HE}_{l+1}^{ev}$	$-i(z+iz_0)r^l\cos(l+1)\varphi F_{l+1}$	$i(z+iz_0)r^l\sin(l+1)\varphi F_{l+1}$	$ir^{l+1}\cos(l+1)\varphi F_{l+1}$	$r^l\sin(l+1)\varphi(\Im_1+r^2F_{l+2})$	$r^l\cos(l+1)\varphi\Im_1$	$(z+iz_0)r^{l+1}$ $\times\sin(l+1)\varphi F_{l+2}$
$\mathbf{HE}_{l+1}^{od}$	$-i(z+iz_0)r^l\sin(l+1)\varphi F_{l+1}$	$-i(z+iz_0)r^l\cos(l+1)\varphi F_{l+1}$	$ir^{l+1}\sin(l+1)\varphi F_{l+1}$	$-r^l\cos(l+1)\varphi(\Im_1+r^2F_{l+2})$	$r^l\sin(l+1)\varphi\Im_1$	$-(z+iz_0)r^{l+1}$ $\times\cos\{(l+1)\varphi\}F_{l+2}$
$\mathbf{EH}_{l-1}^{ev}$	$-i(z+iz_0)r^l\cos(l-1)\varphi F_{l+1}$	$-i(z+iz_0)r^l\sin(l-1)\varphi F_{l+1}$	$-ir^l\cos(l-1)\varphi\,\Im_3^{(l)}$	$-r^l\sin(l-1)\varphi(\aleph^+-\Im_2)$	$-r^l\cos(l-1)\varphi$ $\times(\aleph^- -\frac{l-1}{k}\mathrm{F}_{l+1})$	$(z+iz_0)r^l$ $\times\sin(l-1)\varphi\Im_3^{(l+1)}$
$\mathbf{EH}_{l-1}^{od}$	$-i(z+iz_0)r^l\sin(l-1)\varphi F_{l+1}$	$i(z+iz_0)r^l\cos(l-1)\varphi F_{l+1}$	$-ir^l\sin(l-1)\varphi\,\Im_3^{(l)}$	$r^l\cos(l-1)\varphi(\aleph^+-\Im_2)$	$-r^l\sin(l-1)\varphi$ $\times(\aleph^- -\frac{l-1}{k}\mathrm{F}_{l+1})$	$-(z+iz_0)r^l$ $\times\cos(l-1)\varphi\Im_3^{(l+1)}$
$\mathbf{CV}^{hom}$	$-i(z+iz_0)r^l\exp(i\sigma(l+1)\varphi)\mathrm{F}_{l+1}$	$i\sigma(z+iz_0)r^l\exp(i\sigma(l+1)\varphi)F_{l+1}$	$ir^{l+1}\exp(i\sigma(l+1)\varphi)F_{l+1}$	$-i\sigma(\Im_1+r^2F_{l+2})$ $\times r^l\exp(i\sigma(l+1)\varphi)$	$r^l\exp(i\sigma(l+1)\varphi)\Im_1$	$-i\sigma(z+iz_0)r^{l+1}$ $\times\exp(i\sigma(l+1)\varphi)F_{l+2}$
$\mathbf{CV}^{in}$	$-i(z+iz_0)r^l\exp(i\sigma(l-1)\varphi)F_{l+1}$	$-\sigma(z+iz_0)r^l\exp(i\sigma(l-1)\varphi)F_{l+1}$	$-ir^l\exp(i\sigma(l-1)\varphi)\,\Im_3^{(l)}$	$i\sigma(\aleph^+-\Im_2)$ $\times r^l\exp(i\sigma(l-1)\varphi)$	$-r^l(\aleph^- -\frac{l-1}{k}\mathrm{F}_{l+1})$ $\times\exp(i\sigma(l-1)\varphi)$	$-i\sigma(z+iz_0)r^l\Im_3^{(l+1)}$ $\times\exp(i\sigma(l+1)\varphi)$

$$\Im_1 = F_1 - \frac{l+1}{k}F_{l+1},\ \Im_2 = \frac{(3l+1)}{k}F_{l+1} - r^2F_{l+2},\ \aleph^{\pm} = \left\{\frac{2l(l-1)}{(kr)^2} \pm 1\right\}F_l,\ \Im_3^{(l+1)} = \frac{2l}{kr}F_{l+1} - \frac{r}{k}F_{l+2}$$

is the wave function of the fundamental mode of the Gaussian beam.

Then, for $l = m$, we have $P_l^{(l)} = \sin^l\theta = (r/R)^l$, and scalar potentials (1) are given by

$$\Psi_{1,2} \propto \left(\frac{r}{\xi}\right)^l G_0(r, z)\begin{Bmatrix}\cos l\varphi\\ \sin l\varphi\end{Bmatrix}. \quad (3)$$

In the plane $z = 0$, expression (3) exactly coincides with the wave functions of the even and odd linearly polarized (*LP*) modes of a weakly guiding optical fiber with the parabolic profile of the refractive index [5]. According to [5], the even and odd *LP* modes polarized along the *x* and *y* axes can be combined into hybrid *HE* and *EH* modes as

$$\begin{aligned} HE^{ev}_{l+1,l} &= LP^x(e_x) + LP^y(e_y),\\ HE^{od}_{l+1,l} &= LP^y(e_x) - LP^x(e_y),\\ EH^{ev}_{l-1,l} &= LP^x(e_x) - LP^y(e_y),\\ EH^{od}_{l-1,l} &= LP^y(e_x) + LP^x(e_y). \end{aligned} \quad (4)$$

Expressions (4) are written for the fields of electric type. Corresponding expressions for fields of magnetic type can be found in a similar way. The *y* and *x* superscripts at the *LP* modes correspond to even and odd modes, respectively. The subscript denotes the direction of the predominant linear polarization. Using the relation [4] between potentials (1) and the electric and magnetic fields, we obtain, in view of (4), a set of structurally stable *E* fields of the free space eigenmodes. These fields are in agreement with those of the eigenmodes of a weakly guiding fiber in the paraxial approximation (see table). Note that a similar approach can be applied to finding the fields of nonparaxial singular beams with unequal indices, $l \neq m$. However, in the table, we list expressions for the fields with equal indices only because of the awkwardness of the mathematical expressions in the other case. Also, for the fields with equal indices, the transition to a paraxial singular beam takes place throughout the *z* axis, while for those with unequal indices, such a transition is possible only for a combination of nonparaxial singular beams in the vicinity of the beam waist $z = 0$. However, inside a fiber, such fields exist along its whole length.

Figure 1 shows intensity distributions for nonparaxial higher-order singular beams for two groups of *HE*- and *EH*-modes. Figure 2 illustrates the distribution of the electric and magnetic field lines for these groups. The maximum distortion of the cross section of the nonparaxial beam is observed in the direction of the asymptotes to the electric field lines. In the case of the *TE* and *TM* modes that result from the even and the odd *EH* modes at $l = 1$, the field lines have the symmetric distribution. The intensity distribution in the focal plane is also symmetric. It is worthy to note that the *HE* and *EH* modes have a singular line (a polarization disclination) with the index $\nu = -1/2$ for *HE* modes and $\nu = 1/2$ for *EH* modes on the optical axis. The polarization disclination can be transformed into a purely screw dislocation with the topological charge *l* by considering the superposition of the even and the odd *HE* and *EH* modes. The fields of such a superposition are homogeneous and inhomogeneous optical vortices in the states $CV^{(hom)} \Rightarrow |+1, l\rangle, |-1, -l\rangle \Rightarrow HE^{ev}_{l+1,l} + i\sigma HE^{od}_{l+1,l}$ and $CV^{(un)} \Rightarrow |-1, l\rangle, |1, -l\rangle \Rightarrow EH^{ev}_{l-1,l} + i\sigma EH^{od}_{l-1}$ ($\sigma = \pm 1$ is the helicity), respectively. An increase in the Rayleigh length kz_0 reduces the distortion of the *HE* and *EH* modes, so that the singular beam becomes axisymmetric near the optical axis for $kz_0 \gg 1$. Away from the axis, the shape of the singularity lines remains the same, but the energy flux near them is negligible.

If one uses the paraxial approximation $kz_0 \gg 1$, the wave functions for the field components will be substantially simplified. In this case, the expressions for the fields of the singular beam modes structurally coincide with the expressions for the eigenmodes of a weakly guiding fiber that are listed in Table 14.1 of [5]. However, the radial function $F_l(\tilde{R})$ (R is the normalized fiber radius) takes the form $F_l(R) = j_l(R)/R^l$.

It should be emphasized that, in both singular nonparaxial and singular paraxial vector beams, there exists a strict relation between the sign of topological charge *l* and the polarization helicity σ. This relation serves to discriminate between homogeneous and inhomogeneous vortices. This difference is the most pronounced in the shape of Poynting vector lines.

REFERENCES

1. T. Poston and I. Stewart, *Catastrophe Theory and Its Applications* (Pitman, London, 1978; Mir, Moscow, 1980).
2. M. V. Berry, J. Mod. Opt. **45**, 1845 (1998).
3. A. S. Mishchenko and A. T. Fommenko, *Course of Differential Geometry and Topology* (Mosk. Gos. Univ., Moscow, 1980).
4. A. V. Volyar, Pis'ma Zh. Tekh. Fiz. **26** (13), 71 (2000) [Tech. Phys. Lett. **26**, 573 (2000)].
5. A. W. Snyder and J. D. Love, *Optical Waveguide Theory* (Chapman and Hall, London, 1983; Radio i Svyaz', Moscow, 1987).

Translated by M. Fofanov

Technical Physics, Vol. 46, No. 8, 2001, p. 1068. Translated from Zhurnal Tekhnicheskoĭ Fiziki, Vol. 71, No. 8, 2001, p. 139.

In Memory of Mikhail B. Golant

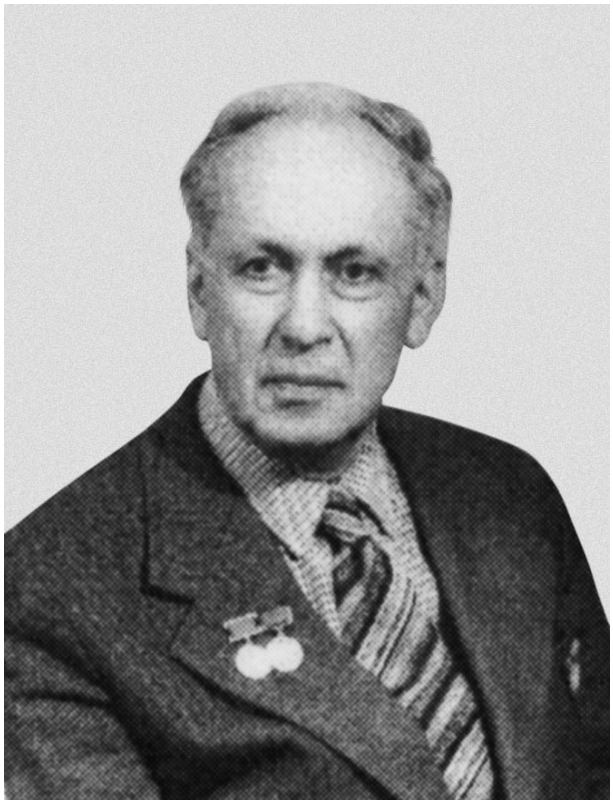

Mikhail B. Golant, Dr. Sci. (Tech.), a Lenin and State Prize winner, a participant of the Great Patriotic War, died on February 7, 2001, at the age of 79.

The contribution of Golant, an outstanding scientist and engineer, to the development of contemporary science is difficult to overestimate. Along with significant achievements in electronic science and technology, his name is associated with a new age in the physics of millimeter and submillimeter waves. The novel approach to designing backward-wave tubes (BWTs) that was suggested by Golant in the late 1950s and early 1960s allowed researchers to develop milliwatt coherent sources radiating in the millimeter and submillimeter ranges. The development of BWTs, which still remain at the leading edge of technology by a number of their parameters, can, without exaggeration, be thought of as one of the greatest advances in world electronics. This breakthrough made it possible to perform unique microwave experiments in radio physics, biology, and medicine and also gave rise to the evolution of a new field in experimental physics—millimeter- and submillimeter-wave BWT spectroscopy.

Golant always defended his scientific ideas to the end. The peak of his activity fell at the onset of semiconductor electronics and laser physics. At that time, experimentation with low-power vacuum tubes appeared to be out of date. It was becoming clear that milliwatt-power vacuum tubes would be ousted by semiconductor devices. However, BWTs designed by Golant still remain a basic tool for physical research in the millimeter- and submillimeter-wave ranges.

The same is true for biophysical investigations into the effect of low-intensity microwaves on living organisms. He directed these investigations and took active part in them by himself. Results obtained do not fit today's ideas and concepts but will undoubtedly revolutionize our knowledge about information processing and transfer in the cells of living organisms.

Golant's life and activity have shown that purposefulness, fresh insight into problems posed, seeing significant points, and the capability of discovering "strangeness" in conventional modes of thought are the key to success in science. Scientists should not be afraid of risk.

A.M. Prokhorov, Academician, Nobel Prize winner

E.M. Dianov, Academician

1063-7842/01/4608-1068$21.00

Technical Physics, Vol. 46, No. 8, 2001, pp. 929–940. Translated from Zhurnal Tekhnicheskoĭ Fiziki, Vol. 71, No. 8, 2001, pp. 1–12.

ATOMS, SPECTRA, RADIATION

Kinetic Mechanisms for the Initiation of Supersonic Combustion of a Hydrogen–Air Mixture behind a Shock Wave under the Excitation of Molecular Vibrations in Initial Reagents

A. M. Starik and N. S. Titova

Baranov Central Institute of Aviation Motors, Moscow, 111250 Russia

e-mail: star@ciam.ru

Received November 22, 2000

Abstract—Mechanisms for the initiation of autoignition in hydrogen–air mixtures in a supersonic flow behind a shock at temperatures ≤700 K when the H_2 and N_2 molecule vibration is selectively excited are considered. By exciting molecular vibration in the gases, one can initiate detonation combustion behind the shock front even at weak shocks at gas temperatures ≤500 K. It is established that even a small (<0.15%) amount of vibrationally excited ozone present in the reacting mixture may considerably shrink the induction zone. © *2001 MAIK "Nauka/Interperiodica".*

INTRODUCTION

Initiating the combustion of $H_2 + O_2$ (air) mixtures in a supersonic flow behind a shock wave is a subject of much investigation [1–5]. This problem is of interest because of the possibility of designing hypersonic ramjets with detonation combustion [6, 7]. In the majority of theoretical works, it was assumed that the delayed excitation of molecular vibrations behind the shock front and the excitation of molecules produced by the chemical reactions do not change the basic parameters of the process. Recently, however, it has been shown [5] that molecular vibrations may sometimes significantly alter the length of induction and combustion zones when an H_2 + air mixture is ignited by an inclined shock. Moreover, the nonequilibrium preexcitation of the vibrational degrees of freedom of H_2, O_2, and even N_2 molecules may markedly accelerate the process and shrink the combustion zone.

Yet, the problem of supersonic combustion under the preexcitation of initial components has not been adequately understood. Specifically, mechanisms of how molecular vibrations of initial reagents initiate combustion in a low-temperature supersonic flow behind a shock and how the vibrations influence the threshold for autoignition still remain unclear. It is the purpose of this work to throw light on these points.

STATEMENT OF THE PROBLEM AND BASIC EQUATIONS

Consider an inclined shock wave behind which the gas velocity remains supersonic [1–3]. We assume that the rotational and translational degrees of freedom of molecules are in thermodynamic equilibrium. At temperatures typical of the combustion of H_2 + air mixtures (<3000 K), the Boltzmann distribution of molecules is established behind the shock front for lower vibrational levels of each of the modes. In this case, we can apply the model of local vibrational temperatures to describe relaxation processes [8, 9]. Then, the equations that govern the flow of a reacting mixture in the relaxation zone of the shock along the $0X$ axis (the $0X$-axis direction is aligned with the gas velocity vector behind the front) are given by

$$\frac{d(\rho u)}{dx} = 0, \quad u\frac{du}{dx} + \frac{1}{\rho}\frac{dP}{dx} = 0,$$

$$\frac{dH}{dx} + \sum_{i=1}^{S}\frac{de_V^i}{dx} + u\frac{du}{dx} = 0,$$

$$u\frac{d\gamma_i}{dx} = G_i - \gamma_i\sum_{j=1}^{M_1} G_j \quad u\frac{d\varepsilon_\xi}{dx} = Q_V^\xi + Q_{Ch}^\xi,$$

$$P = \rho RT/\mu,$$

$$G_i = \sum_{q=1}^{M_2} S_{iq}, \quad S_{iq} = \frac{(\alpha_{iq}^- - \alpha_{iq}^+)}{N}[R_q^+ - R_q^-],$$

$$R_q^{+(-)} = k_{+(-)q}/N_A^{(n_q^{+(-)}-1)}\prod_{j=1}^{n_q^{+(-)}} N_j^{\alpha_{jq}^{+(-)}},$$

$$Q_V^\xi = N\left[\sum_{p=1}^{L_1}\frac{l_\xi}{g_\xi^{l_\xi} g_p^{l_p}} L_{\xi,p} W_{\xi,p} - (\varepsilon_\xi - \varepsilon_{\xi 0})(1 - y_{\xi 0})\sum_{i=1}^{M_1} W_{\xi,0}^i \gamma_i\right],$$

1063-7842/01/4608-0929$21.00

$$Q_{Ch}^{\xi} = \sum_{r=1}^{M_2} \frac{(\alpha_{ir}^{-} - \alpha_{ir}^{+})}{N_i}$$

$$\times [(\chi_{r\xi}^{+} - \varepsilon_\xi)R_r^{+} - (\chi_{r\xi}^{-} - \varepsilon_\xi)R_r^{-}],$$

$$L_{\xi,p} = \varepsilon_\xi^{l_\xi}(g_p + \varepsilon_p)^{l_p} - \varepsilon_p^{l_p}(g_\xi + \varepsilon_\xi)^{l_\xi}\exp\left(\frac{l_\xi\Theta_\xi - l_p\Theta_p}{T}\right), \quad (1)$$

$$\chi_{r\xi}^{+(-)} = (E_r/k\Theta_\xi)\eta_{r\varepsilon}^{+(-)}, \quad \eta_{r\xi}^{+} = \beta_{r\xi}^2/\sum_{j=1}^{b_r}\beta_{rj}^2,$$

$$\eta_{r\xi}^{-} = \beta_{r\xi}^2 T_\xi^2 \sum_{j=1}^{b_r}\beta_{rj}^2/\left(\sum_{j=1}^{b_r}\beta_{rj}^2 T_j\right)^2,$$

$$\varepsilon_\xi = g_\xi y_\xi/(1-y_\xi), \quad y_\xi = \exp(-\Theta_\xi/T_\xi),$$

$$e_V^i = \frac{R}{\mu}\gamma_i\sum_{j=1}^{Z}\Theta_{ij}\varepsilon_{ij},$$

$$H = \sum_{i=1}^{M_1} h_{0i}\gamma_i + C_{RT}T,$$

$$C_{RT} = \left(\frac{5}{2} + \sum_{i=1}^{L}\gamma_i + \frac{3}{2}\sum_{i=L+1}^{S}\gamma_i\right)\frac{R}{\mu},$$

$$E_r = \alpha_r E_{ar}^{+}, \quad \alpha_r = \frac{E_{ar}^{+}}{E_{ar}^{+} + E_{ar}^{-}}, \quad \gamma_i = N_i/N,$$

$$N = \sum_{i=1}^{M_1} N_i, \quad \mu = \sum_{i=1}^{M_1}\mu_i\gamma_i,$$

$$\varepsilon_{\xi 0} = \varepsilon_\xi(y_\xi = y_{\xi 0}), \quad y_{\xi 0} = y_\xi(T_\xi = T_{\xi 0}).$$

Here, P, ρ, T, and u are, respectively, the pressure, density, temperature, and velocity of the gas; R is the gas constant; N_A is the Avogadro number; N_i is the concentration of molecules of the ith sort; μ_i is their molecular mass; M_1 is the number of molecular and atomic components in the mixture; L is the number of components consisting of linear molecules; S is the total number of molecular components; Z is the number of modes for the molecules of the ith sort; h_{0i} is the enthalpy of formation of molecules (atoms) of the ith species at T = 298 K; M_2 is the number of reactions that produce (or remove) the ith component; Θ_ξ and T_ξ are the characteristic and local vibrational temperatures, respectively, of the ξth mode; g_ξ is the multiplicity of its degeneracy; l_ξ is the number of vibrational quanta lost or acquired by the mode ξ at vibrational–vibrational V–V' exchange (the number of the exchanges is L_1); $W_{\xi,p} = \sum_{i=1}^{M_1} W_{\xi,p}^i\gamma_i$ for the case of intramolecular V–V' exchange; $W_{\xi,p} = W_{\xi,p} = W_{\xi,p}\gamma_j$ ($\xi \longleftrightarrow i$, $p \longleftrightarrow j$) for intermolecular V–V' exchange; $W_{\xi,p}^i$ and $W_{\xi,p}$ are the rate constants for intra- and intermolecular V–V' exchanges; $W_{\xi,0}$ is the rate constant of vibrational–translational V–T relaxation at collision with the ith partner; α_{iq}^{+} and α_{iq}^{-} are the stoichiometric ratios of the qth reaction; $n_q^{+(-)}$ is the number of components involved in the forward (+) and back (–) reactions; $k_{+(-)q}$ are the rate constants of these reactions; β_{qj} are the coefficients of expansion of the qth chemical reaction in terms of normal mode coordinates; b_q is the number of modes involved in the qth reaction; k is the Boltzmann constant; E_r is the energy consumed by the vibrational degrees of freedom of a molecule formed by the rth reaction; and $E_{ar}^{+(-)}$ is the energy of activation of the rth chemical reaction that produces (removes) the vibrationally excited molecule.

In the absence of equilibrium between the translational and vibrational degrees of freedom of molecules involved in a reaction, the rate constant of the reaction can be expressed as

$$k_q(T, T_j) = \varphi_q(T, T_j)k_q^0(T), \quad (2)$$

where $k_q^0(T)$ is the rate constant of the qth chemical reaction at $T_j = T$ and $\varphi_q(T, T_j)$ is the factor of deviation from equilibrium.

To calculate $\varphi_q(T, T_j)$ for both dissociation reactions $A_2(V) + M = A + A + M$ and exchange reactions $A_2(V) + BC(V') = AB(W) + AC(W')$ (V, V' and W, W' are the vibrational quantum numbers of the reagents and reaction products, respectively), we used the modified model [10]

$$\varphi_q(T, T_j) = \frac{\prod_{j=1}^{b_q}(1-y_{j0})^{-g_j}}{\prod_{j=1}^{b_q}(1-y_j)^{-g_j}}\exp\left[\frac{E_q^*}{k}\left(\frac{1}{T} - \frac{\sum_{j=1}^{b_q}\beta_{qi}^2}{\sum_{j=1}^{b_q}\beta_{qi}^2 T_j}\right)\right]. \quad (3)$$

Here, E_q^* is the energy of some vibrational level that is a "bottleneck" when vibrationally excited molecules pass to energy quasi-continuum. The value of E_q^* depends on the gas temperature T and also on several parameters of reacting molecules. To date, specific expressions for E_q^* have been deduced only for the dissociation of diatomic molecules [11]. For T = 500–5000 K, E_q^* for H_2, N_2, O_2, and NO molecules can be approximated well by the energy of the highest discrete level in the vibrational spectrum [9]. This parameters has also been determined for polyatomic molecules. For bimolecular exchange reactions like $AB(V)$ +

$CD(V') = AC(W) + BD(W')$, the exact expressions (values) for E_q^* are lacking. Calculations performed within the model of "efficiency of using vibrational energy" showed that $E_q^* \approx E_{aq}^+$ for moderate-temperature exchange reactions like $AB(V) + C = AC + B$, where $AB = H_2O$, OH, H_2, O_2, N_2, NO, or NO_2 [9]. We consider this relationship to be valid also for other bimolecular exchange reactions.

Boundary conditions for system (1) at $x = 0$ are parameters behind the shock front (labeled by subscript 1). They are found from the equations of mass, momentum, and energy conservation under the assumption that the populations of the vibrational levels and the gas composition remain unchanged when passing through a viscous shock.

KINETIC SCHEME

The dynamics of chemical transformations in the system of elements H–O–N is comprehensively described with 152 reversible reactions involving O_2, H_2, O, H, H_2O, OH, HO_2, H_2O_2, O_3, N, N_2, NO, NO_2, NO_3, N_2O, HNO, HNO_2, HNO_3, HNO_4, N_2O_5, NH, NH_2, NH_3, N_2H, N_2H_2, N_2H_3, and N_2H_4 (a total of 27 components) [12]. In our case, however, they are not all equally important in finding mechanisms of combustion initiation. We tried to separate out the minimal set of reactions that adequately characterize the basic dynamic and thermodynamic parameters of the combustion initiation process. Four approaches (schemes) were considered: (1) all 152 reactions involving 27 components, (2) 42 reactions and 13 components (H_2O, H_2, O_2, OH, H, O, N_2, N, NO, NO_2, HO_2, H_2O_2, and O_3), (3) 35 reactions and 12 components (reactions involving O_3 are rejected), and (4) 19 reactions and 10 components (reactions involving HO_2 and H_2O_2 are rejected). It was assumed that the translational, rotational, and vibrational degrees of freedom of the molecules come into equilibrium immediately behind the shock front.

Table 1 lists the temperatures T_1 behind the front, induction zone lengths L_{in}, and combustion zone lengths L_c. Also given are the values of T and M, as well as the mole fractions of H_2O, H_2, O_2, OH, H, O, N_2, N, NO, NO_2, HO_2, H_2O_2, and O_3, at the end of the reaction zone (the associated parameters are labeled by subscript e) for the stoichiometric H_2 + air ($2H_2 + O_2 + 3.76N_2$) mixture. Here, $P_0 = 1197$ Pa and $T_0 = 226$ K (conditions at the altitude $H_g = 30$ km). The front makes the angle $\beta = 20°$ with the velocity vector u_0. The Mach number M_0 of the undisturbed flow was varied. Necessary thermodynamic data and temperatures dependences $k_q^0(T)$ were taken from [13] and [12], respectively. The values of L_{in} are the distances from the front where the concentration of H atoms was the highest; L_c is the distance from the front where $T = 0.99T_e$. As follows from Table 1, only reduced scheme 2 provides sufficiently correct values of L_{in}, L_e, T_e, M_e, and γ_{ie} throughout the range of M_0.

Table 2 lists the reactions involved in scheme 2 and also the factors necessary for calculating the rate constants of the forward, $k_{+q}^0(T)$, and back, $k_{-q}^0(T)$, reactions by the formula $k_q^0 = A_q T^{m_q} \exp(E_{aq}/T)$. Together with chemical reactions (1)–(42), the model includes V–V' exchange processes between the symmetric, deformation, and antisymmetric (ν_1, ν_2, ν_3) modes of an H_2O molecule; between the modes of H_2 (ν_4), O_2 (ν_5), OH (ν_6), N_2 (ν_7), and NO (ν_8) molecules; between the symmetric, deformation, and antisymmetric modes of NO_2 (ν_9, ν_{10}, ν_{11}), HO_2 (ν_{12}, ν_{13}, ν_{14}), and O_3 (ν_{15}, ν_{16}, ν_{17}) molecules; as well as between the modes of an H_2O_2 (ν_{18}, ν_{19}, ν_{20}, ν_{21}, ν_{22}) molecule. Included also are V–T energy relaxations for the modes ν_2, ν_4, ν_5, ν_6, ν_7, ν_8, ν_{10}, ν_{14}, ν_{16}, and ν_{20}. The relaxation equations assume that there exists quasi-equilibrium between the ν_9 and ν_{10} modes: $y_9 = y_{10}^2 \exp[(\Theta_9 - 2\Theta_{10})/T]$. It was also assumed that the modes ν_{15} and ν_{17} of the O_3 molecule, as well as the modes ν_{18}, ν_{20}, ν_{21} and ν_{19}, ν_{22} of the H_2O_2 molecule, are at sharp resonance ($\Theta_{15} = \Theta_{17}$, $\Theta_{18} = 4\Theta_{20} = \Theta_{21}$, and $\Theta_{19} = \Theta_{22}$). Below, we give the channels of vibrational energy exchange (their serial numbers have the letter V) and their associated rate constants $W_{\xi,p}$:

1V. $H_2O(001) + M \longrightarrow H_2O(100) + M$ $W_{3.1}^M$,

2V. $H_2O(001) + M \longrightarrow H_2O(020) + M$ $W_{3.2}^M$,

3V. $H_2O(100) + M \longrightarrow H_2O(020) + M$ $W_{1.2}^M$,

4V. $H_2O(010) + M \longrightarrow H_2O(000) + M$ $W_{2.0}^M$,

5V. $H_2(V = 1) + H_2O(001) \longrightarrow H_2O(001) + H_2(V = 0)$ $W_{4.3}$,

6V. $H_2(V = 1) + H_2O(001) \longrightarrow H_2O(100) + H_2(V = 0)$ $W_{4.1}$,

7V. $H_2O(010) + O_2(V = 0) \longrightarrow H_2O(000) + O_2(V = 1)$ $W_{2.5}$,

8V. $H_2O(001) + OH(V = 0) \longrightarrow H_2O(000) + OH(V = 1)$ $W_{3.6}$,

9V.	$H_2O(100) + OH(V = 0) \longrightarrow H_2O(000) + OH(V = 1)$	$W_{6.1}$,
10V.	$H_2(V = 1) + OH(V = 0) \longrightarrow H_2(V = 0) + OH(V = 1)$	$W_{4.6}$,
11V.	$H_2(V = 1) + M \longrightarrow H_2(V = 0) + M$	$W^M_{4.0}$,
12V.	$O_2(V = 1) + M \longrightarrow O_2(V = 0) + M$	$W^M_{5.0}$,
13V.	$OH(V = 1) + M \longrightarrow OH(V = 0) + M$	$W^M_{6.0}$,
14V.	$N_2(V = 1) + H_2O(000) \longrightarrow N_2(V = 0) + H_2O(010)$	$W_{7.2}$,
15V.	$OH(V = 1) + N_2(V = 0) \longrightarrow OH(V = 0) + N_2(V = 1)$	$W_{6.7}$,
16V.	$N_2(V = 1) + O_2(V = 0) \longrightarrow N_2(V = 0) + O_2(V = 1)$	$W_{7.5}$,
17V.	$NO(V = 1) + H_2O(000) \longrightarrow NO(V = 0) + H_2O(010)$	$W_{8.2}$,
18V.	$NO(V = 1) + O_2(V = 0) \longrightarrow NO(V = 0) + O_2(V = 0)$	$W_{8.5}$,
19V.	$N_2(V = 1) + NO(V = 0) \longrightarrow N_2(V = 0) + NO(V = 1)$	$W_{7.8}$,
20V.	$N_2(V = 1) + M \longrightarrow N_2(V = 0) + M$	$W^M_{7.0}$,
21V.	$NO(V = 0) + M \longrightarrow NO(V = 0) + M$	$W^M_{8.0}$,
22V.	$O_2(V = 0) + NO_2(001) \longrightarrow O_2(V = 1) + NO_2(000)$	$W_{11.5}$,
23V.	$NO_2(001) + H_2O(000) \longrightarrow NO_2(000) + H_2O(010)$	$W_{11.2}$,
24V.	$NO(V = 1) + NO_2(000) \longrightarrow NO(V = 0) + NO_2(V = 1)$	$W_{8.11}$,
25V.	$NO_2(020) + M \longrightarrow NO_2(100) + M$	$W^M_{10.9}$,
26V.	$NO_2(001) + M \longrightarrow NO_2(020) + M$	$W^M_{11.10}$,
27V.	$NO_2(010) + M \longrightarrow NO_2(000) + M$	$W^M_{10.0}$,
28V.	$HO_2(100) + M \longrightarrow HO_2(003) + M$	$W^M_{12.14}$,
29V.	$HO_2(010) + M \longrightarrow HO_2(001) + M$	$W^M_{13.14}$,
30V.	$HO_2(001) + M \longrightarrow HO_2(000) + M$	$W^M_{14.0}$,
31V.	$H_2O(100) + HO_2(000) \longrightarrow H_2O(000) + HO_2(100)$	$W^M_{1.12}$,
32V.	$O_2(V = 1) + HO_2(000) \longrightarrow O_2(V = 0) + HO_2(010)$	$W_{5.13}$,
33V.	$HO_2(010) + NO_2(000) \longrightarrow HO_2(000) + NO_2(100)$	$W_{13.9}$,
34V.	$H_2O(010) + HO_2(000) \longrightarrow H_2O(000) + HO_2(010)$	$W_{2.13}$,
35V.	$O_3(100, 001) + M \longrightarrow O_3(010) + M$	$W^M_{\Sigma.16}$,
36V.	$O_3(010) + M \longrightarrow O_3(000) + M$	$W^M_{16.0}$,
37V.	$H_2O_2\begin{pmatrix}01\,000\\00\,001\end{pmatrix} + M \longrightarrow H_2O_2\begin{pmatrix}10\,000\\00\,400\\00\,010\end{pmatrix} + M$	$W^M_{\Sigma_1.\Sigma_2}$,

38V. $H_2O_2\begin{pmatrix}10\,000\\00\,400\\00\,010\end{pmatrix} + M \longrightarrow H_2O_2(00\,000) + M$ $W^M_{\Sigma_2.0}$,

39V. $H_2O(100) + H_2O_2(00\,000) \longrightarrow H_2O(000) + H_2O_2\begin{pmatrix}10\,000\\00\,400\\00\,010\end{pmatrix}$ $W_{1.\Sigma_2}$,

40V. $O_2(V = 1) + H_2O_2(00\,000) \longrightarrow O_2(V = 0) + H_2O_2\begin{pmatrix}01\,000\\00\,001\end{pmatrix}$ $W_{5.\Sigma_1}$,

41V. $HO_2(010) + H_2O_2(00\,000) \longrightarrow HO_2(000) + H_2O_2\begin{pmatrix}01\,000\\00\,001\end{pmatrix}$ $W_{13.\Sigma_1}$,

42V. $NO_2(100) + H_2O_2(00\,000) \longrightarrow NO_2(000) + H_2O_2\begin{pmatrix}01\,000\\00\,001\end{pmatrix}$ $W_{9.\Sigma_1}$,

43V. $N_2(V = 1) + O_3(000) \longrightarrow N_2(V = 0) + O_3(101)$ $W_{7.\Sigma}$.

The subscripts ξ and p in $W_{\xi,p}$ take the values 0–16, Σ_1, Σ_2, and Σ_3. The numbers 1–16 are mode numbers. The subscript 0 corresponds to the unexcited state of any of the molecules; Σ, to the combined state ($\nu_{15} + \nu_{17}$); Σ_1, to the combined state ($\nu_{19} + \nu_{22}$); and Σ_2, to the combined state ($\nu_{18} + 4\nu_{20} + \nu_{21}$). The temperature dependences $W_{\xi,p}(T)$ for reactions (1V)–(27V) at $M \neq HO_2, H_2O_2, O_3$ were the same as in [12]. The values of $W^M_{3.1}$, $W^M_{3.2}$, $W^M_{1.2}$, $W^M_{2.0}$, $W^M_{4.0}$, $W^M_{5.0}$, $W^M_{6.0}$, $W^M_{7.0}$, $W^M_{8.0}$, $W^M_{10.0}$, and $W^M_{11.10}$ for $M = HO_2, H_2O_2, O_3$ were determined from the formula $W^M_{\xi,p}(T) = W^{H_2O}_{\xi,p}(T)\,W^M_{\xi,p}(P)/W^{H_2O}_{\xi,p}(P)$, where $W^M_{\xi,p}(P)$ and $W^{H_2O}_{\xi,p}(P)$ are expressions for the related rate constants for the V–T and V–V' processes. These expressions are obtained using formulas of the SSH theory or the semiempirical Millikan–White formula [14, 15]. The values of $W^M_{\Sigma.16}$ and $W^M_{16.0}$ for a given temperature were found from the relationship $W^M_{\xi,p}(T) = W^M_{\xi,p}(300\ \mathrm{K})\,W^M_{\xi,p}(P)/W^{MT}_{\xi,p}(300\ \mathrm{K})$, where $W^{MT}_{\xi,p}(300\ \mathrm{K})$ and $W^M_{\xi,p}(300\ \mathrm{K})$ are the calculated and measured values of $W^M_{\xi,p}$ at $T = 300$ K. The values of $W^M_{\Sigma.16}(300\ \mathrm{K})$ and $W^M_{16.0}(300\ \mathrm{K})$ for $M = O_2$, O, and O_3 were taken from [16]; for $M = H_2O$, it was assumed that $W^M_{\Sigma.16} = W^O_{\Sigma.16}$ and $W^M_{16.0} = W^O_{16.0}$; and for $M = H_2$, N_2, H, OH, NO, NO_2, N, HO_2, and H_2O_2, we put $W^M_{\Sigma.16} = W^{O_2}_{\Sigma.16}$ and $W^M_{16.0} = W^{O_2}_{16.0}$ Calculations also showed that the following equalities are approximately fulfilled: $W_{1.12} = W_{5.\Sigma_1} = W_{5.13} = W_{2.13} = W_{3.6}$, $W^M_{12.14} = W^M_{3.1}$, $W_{1.\Sigma_2} = W_{9.\Sigma_1} = W_{13.\Sigma_1} = W_{1.6}$, $W^M_{\Sigma_2.0} = W^M_{2.0}$, and $W^M_{\Sigma_1.\Sigma_2} = W^M_{1.2}$. The values of $W^M_{14.0}$ and $W^M_{13.14}$ were calculated by the formulas $W^M_{14.0} = W^M_{2.0}W^M_{14.0}(P)/W^M_{2.0}(P)$ and $W^M_{13.14} = W^M_{14.0}W^M_{1.2}/W^M_{2.0}$. The value of $W_{7.\Sigma} = 5 \times 10^{-14}$ cm^3/s was found in [17].

RESULTS OF NUMERICAL ANALYSIS

Earlier [5], it was noted that taking into account the slow excitation of molecular vibrations behind the shock front may significantly affect the combustion characteristics. Table 3 summarizes calculated L_{in} and L_c, as well as T_e, P_e, and M_e at different M_0 (given also are the values of T_1 corresponding to M_0), for the combustion of the $2H_2 + O_2 + 3.76N_2$ mixture at $T_0 = 226.5$ K, $P_0 = 1197$ Pa, and $\beta = 20°$ (hereafter, such conditions will be considered). Two kinetic models are analyzed. The former considers only chemical processes involving 13 components (model 1), and the latter also includes the nonequilibrium excitation of molecular vibrations and the effect of the vibrations on the chemical kinetics (model 2). The values of L_{in} and L_c are seen to grow when the molecular vibrations are taken into account. The higher T_1, the greater the growth.

Now we will consider how the preexcitation of H_2 and N_2 molecules influences combustion initiation in a supersonic flow. It is known that vibrations in these molecules are effectively excited in electric discharge [18, 19]. Figure 1 plots L_{in} against the Mach number of

Table 1

	$M_0 = 12$, $T_1 = 931$ K				$M_0 = 10$, $T_1 = 717.8$ K				$M_0 = 8$, $T_1 = 537.2$ K			
Scheme	1	2	3	4	1	2	3	4	1	2	3	4
L_{in}, cm	2.92(2)	2.92(2)	2.95(2)	2.95(2)	1.54(4)	1.54(4)	6.15(7)	4.54(3)	2.37(6)	2.37(6)	>1(8)	3(5)
L_c, cm	5.08(2)	5.01(2)	5.01(2)	6.73(2)	1.56(4)	1.56(4)	6.15(7)	5.01(3)	2.37(6)	2.37(6)		3.01(5)
T_e, K	2552.9	2543	2543	2672	2510.5	2501.4	2501.4	2631.6	2474.7	2465.7		2596.7
M_e	3.57	3.58	3.58	3.5	2.94	2.95	2.95	2.88	2.26	2.26		2.2
γ_e : H_2O	2.37(–1)	2.37(–1)	2.37(–1)	2.46(–1)	2.47(–1)	2.47(–1)	2.47(–1)	2.57(–1)	2.54(–1)	2.54(–1)		2.64(–1)
H_2	5.37(–2)	5.4(–2)	5.4(–2)	5.12(–2)	4.98(–2)	5.03(–2)	5.03(–2)	4.7(–2)	4.73(–2)	4.76(–2)		4.39(–2)
O_2	1.73(–2)	1.74(–2)	1.74(–2)	1.5(–2)	1.7(–2)	1.64(–2)	1.64(–2)	1.39(–2)	1.56(–2)	1.57(–2)		1.31(–2)
OH	3.31(–2)	3.3(–2)	3.3(–2)	3.27(–2)	3.06(–2)	3.01(–2)	3.01(–2)	2.94(–2)	2.8(–2)	2.79(–2)		2.7(–2)
H	3.3(–2)	3.36(–2)	3.36(–2)	2.64(–2)	2.87(–2)	2.87(–2)	2.87(–2)	2.18(–2)	2.52(–2)	2.56(–2)		1.89(–2)
O	1.27(–2)	1.29(–2)	1.29(–2)	1.03(–2)	1.11(–2)	1.08(–2)	1.08(–2)	8.39(–3)	9.38(–3)	9.46(–3)		7.17(–3)
N_2	6.06(–1)	6.06(–1)	6.06(–1)	6.11(–1)	6.12(–1)	6.11(–1)	6.11(–1)	6.16(–1)	6.15(–1)	6.14(–1)		6.19(–1)
B	1.86(–6)	1.68(–6)	1.68(–6)	2.45(–6)	9.79(–7)	1.23(–6)	1.23(–6)	1.77(–6)	1.04(–6)	9.41(–7)		1.36(–6)
NO	6.38(–3)	6.66(–3)	6.66(–3)	7.64(–3)	3.84(–3)	6.05(–3)	6.05(–3)	6.94(–3)	5.33(–3)	5.57(–3)		6.39(–3)
NO_2	1.36(–6)	1.33(–6)	1.33(–6)	1.14(–6)	8(–7)	1.19(–6)	1.19(–6)	1.03(–6)	1.06(–6)	1.04(–6)		9.2(–7)
HO_2	1.1(–5)	1.04(–5)	1.04(–5)		9.66(–6)	8.97(–6)	8.97(–6)		8.23(–6)	7.78(–6)		
H_2O_2	1.41(–6)	1.39(–6)	1.39(–6)		1.26(–6)	1.2(–6)	1.2(–6)		1.06(–6)	1.05(–6)		
O_3	9.88(–10)	1(–9)			8.55(–10)	8.08(–10)			6.5(–10)	6.60(–10)		

Note: Writing $A(n)$ means $A \times 10^n$.

Table 2

Reaction no.	Reaction	k^0_{+q}, $(cm^3/mol)^{n-1}\ s^{-1}$			k^0_{-q}, $(cm^3/mol)^{n-1}\ s^{-1}$		
		A_q	m_q	E_{aq}	A_q	m_q	E_{aq}
	Reactions involving H_2O, OH, O, H, H_2, O_2						
1	$H_2O + M = OH + H + M$	1(24)	–2.2	–59000	2.2(22)	–2	0
2	$H_2 + M = 2H + M$	2.2(4)	0	–48300	9(17)	–1	0
3	$O_2 + M = 2O + M$	2.6(18)	0	–59580	1.1(14)	–1	900
4	$H + O + M = OH + M$	7.1(18)	–1	0	8.5(18)	–1	–50830
5	$H_2 + O = OH + H$	1.8(10)	1	–4480	8.3(9)	1	–3500
6	$O_2 + H = OH + O$	2.2(14)	0	–8455	1.3(13)	0	–350
7	$H_2O + O = 2OH$	5.8(13)	0	–9059	5.3(12)	0	–503
8	$H_2O + H = OH + H_2$	8.4(13)	0	–10116	2(13)	0	–2600
9	$H_2 + O_2 = 2OH$	1.7(15)	0	–24200	1.7(13)	0	–24100
	Reactions involving N, N_2, NO						
10	$N_2 + M = 2N + M$	3.72(21)	–1.6	–113272	7.94(19)	–1.6	0
11	$NO + M = N + O + M$	5.25(17)	–0.5	–75600	1(17)	–0.5	0
12	$O + N_2 = N + NO$	1.74(14)	0	–38455	4(13)	0	–504
13	$O + NO = N + O_2$	1.51(9)	1	–19439	6.46(9)	1	–3147
14	$H + NO = N + OH$	1.7(4)	0	–24500	4.5(13)	0	0
	Reactions involving NO_2						
15	$NO_2 + M = NO + O + M$	1.1(16)	0	–32712	1.1(15)	0	941
16	$OH + NO = H + NO_2$	2(11)	0.5	–15500	3.5(14)	0	–740
17	$O_2 + NO = O + NO_2$	1(12)	0	–23568	1(13)	0	–302
18	$NO_2 + N = 2NO$	3.6(12)	0	0	1.1(11)	0	–39200
19	$2NO_2 = 2NO + O_2$	2(12)	0	–13500	1.2(9)	0	530
	Reactions involving HO_2						
20	$HO_2 + M = H + O_2 + M$	2.1(15)	0	–23000	1.5(15)	0	500
21	$H_2 + O_2 = HO_2$	5.5(13)	0	–29213	2.5(13)	0	–354
22	$H_2O + O = H + HO_2$	4.76(11)	0.372	–28743	1(13)	0	–540
23	$H_2O + O_2 = OH + HO_2$	1.5(15)	0.5	–36600	3(14)	0	0
24	$H_2O + OH = H_2 + HO_2$	7.2(9)	0.43	–36100	6.5(11)	0	–9400
25	$2OH_2 = H + HO_2$	1.2(13)	0	–20200	2.5(14)	0	–950
26	$OH + O_2 = O + HO_2$	1.3(13)	0	–28200	5(13)	0	–500
27	$N + HO_2 = NO + OH$	1(13)	0	–1000	2.69(12)	0	–41630
28	$OH + NO_2 = NO + HO_2$	1(11)	0.5	–6000	3(12)	0.5	–1200
	Reactions involving H_2O_2						
29	$H_2O_2 + M = OH + OH + M$	1.2(17)	0	–22900	9.1(14)	0	2650
30	$H + H_2O_2 = HO_2 + H_2$	1.7(12)	0	–1900	6(11)	0	–9300
31	$H + H_2O_2 = H_2O + OH$	5(14)	0	–5000	2.4(14)	0	–40500
32	$2HO_2 = H_2O_2 + O_2$	1.8(13)	0	–500	3(13)	0	–21600
33	$HO_2 + H_2O = H_2O_2 + OH$	1.8(13)	0	–15100	1(13)	0	–910
34	$OH + HO_2 = H_2O_2 + O$	5.2(10)	0.5	–10600	2(13)	0	–2950
35	$H_2O + O_2 = H_2O_2 + O$	3.4(15)	0.5	–44800	8.4(11)	0	–2130
	Reactions involving O_3						
36	$O_3 + M = O_2 + M$	4(14)	0	–11400	6.9(12)	0	1050
37	$O_3 + H = OH + O_2$	2.3(11)	0.75	0	4.4(7)	1.44	–38600
38	$O_3 + O = O_2 + O_2$	1.1(13)	0	–2300	1.2(13)	0	–50500
39	$O_3 + OH = HO_2 + O_2$	9.6(11)	0	–1000	9(8)	0	0
40	$O_3 + H_2 = HO_2 + OH$	6(10)	0	–10000			
41	$O_3 + HO_2 = OH + O_2 + O_2$	2(10)	0	–1000			
42	$O_3 + NO = NO_2 + O_2$	1.2(12)	0	–1400			

Note: Writing $A(n)$ means $A \times 10^n$.

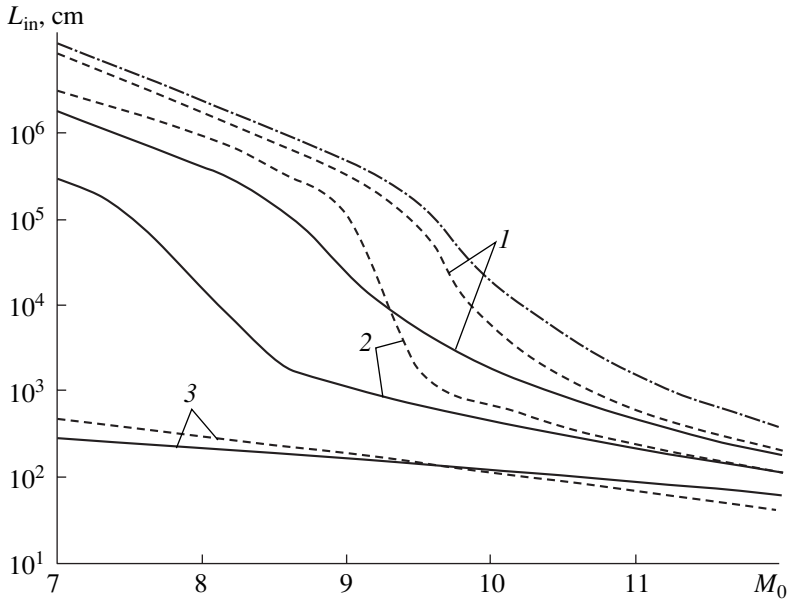

Fig. 1. Induction zone length vs. Mach number in front of the shock for various vibrational temperatures of H_2 and N_2 (dashed and continuous curves, respectively). T_j (j = 4, 7) = (*1*) 1500, (*2*) 2000, and (*3*) 3000 K. Dash-and-dot line depicts the dependence $L_{in}(M_0)$ at $T_{j0} = T_0$.

an undisturbed flow in front of a shock for different vibrational temperatures of the H_2 and N_2 molecules. Even a slight excitation of H_2 or N_2 (T_{40} or T_{70} = 2000 K) significantly shrinks the induction zone. However, at such weak excitations of both H_2 and N_2, there exists a range of M_0 where the shrinkage of the zone is maximal. For $\beta = 20°$ and H = 30 km, this range is M_0 = 9–10.5 at T_{40} = 2000 K and 7.5–10.5 at T_{70} = 2000 K. For example, if M_0 = 9.5, the shrinkage of the induction zone with H_2 excitation is 200 times greater than without H_2 excitation at T_{40} = 2000 K; for M_0 = 9, the difference is only fivefold. As T_{40} or T_{70} rises to 3000 K, the situation noticeably changes. The induction zone considerably shortens at all M_0. Even at M_0 = 7, which corresponds to the temperature T_1 = 460 K behind the front, L_{in} with H_2 excitation equals only 5 m (3 m for N_2 excitation). Without the preexcitation, autoignition at $M_0 < 9.5$ virtually does not occur ($L_{in} > 1$ km). At the same time, at high M_0 ($M_0 > 12$) and, hence, T_1, a decrease in L_{in} is not large even for the strong excitation of H_2 or N_2.

To explain the results obtained, let us consider the formation of chemically active O and H atoms, as well as OH and HO_2 radicals at low T_1 and different levels of H_2 and N_2 excitation. Note that combustion-initiating mechanisms at low ($T_1 < 700$ K) and moderate ($T_1 > 800$ K) temperatures behind the front markedly differ even if H_2 or N_2 molecules are not excited. At both low and high T, the basic reaction that initiates the combustion is reaction 9 (see Table 2), which forms vibrationally excited OH radicals. Then, the radicals dissociate (reaction 4) to produce O and H atoms. At low T_1, this source of H atoms competes with the reaction that is the reverse of reaction 8 and generates H and H_2O. The lat-

Table 3

M_0	8		10		12	
Model	1	2	1	2	1	2
T_1, K	537.2	539.1	717.8	725.9	931	953.2
L_{in}, cm	2.38(6)	2.39(6)	1.55(5)	1.98(4)	2.94(2)	3.77(2)
L_c, cm	2.38(6)	2.39(6)	1.57(4)	2.01(4)	5.01(2)	6.05(2)
T_e, K	2466	2464	2501	2498	2543	2537
P_e, Pa	4.77(4)	4.73(4)	5.45(4)	5.35(4)	6.09(4)	5.87(4)
M_e	2.26	2.16	2.95	2.82	3.58	3.43

Note: Writing $A(n)$ means $A \times 10^n$.

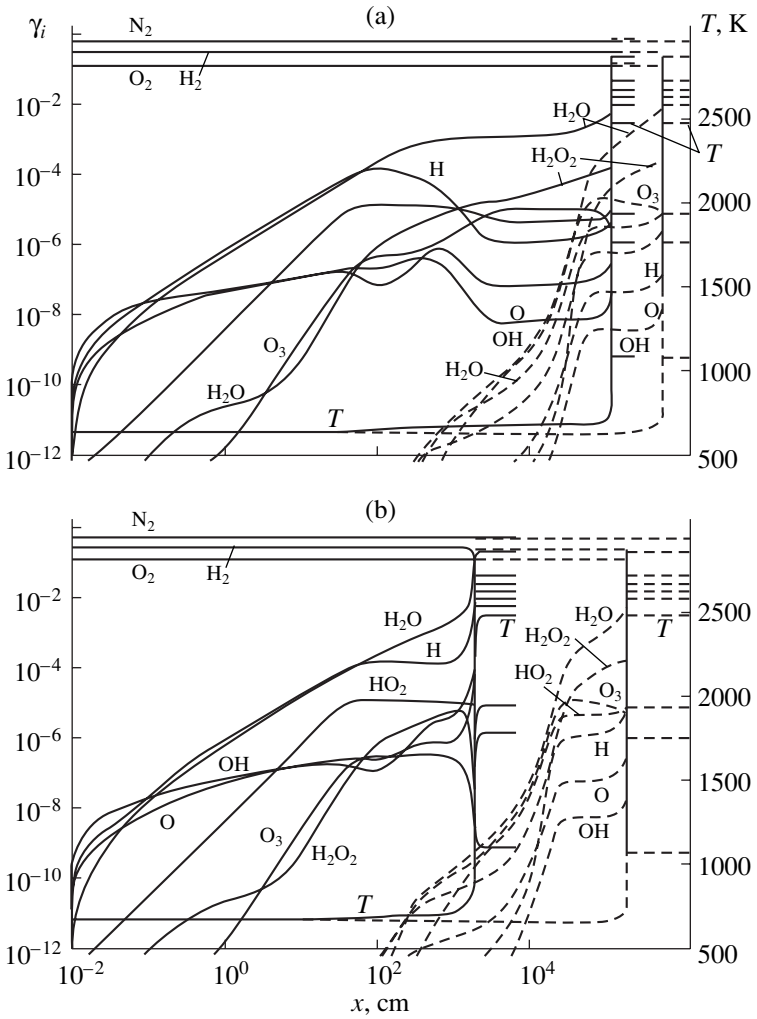

Fig. 2. Variation of γ_i and T along the relaxation zone of the shock with M_0 = (a) 9 and (b) 9.5 for the combustion of the $2H_2 + O_2 + 3.76N_2$ mixture. Continuous curves, H_2 preexcitation (T_{40} = 2000 K); dashed curves, H_2 is not excited.

ter source dominates at high T_1. The H atoms participate in two processes. One produces O atoms (reaction 6) and initiates a chain mechanism of combustion, while the other generates HO_2 (reaction 20). At $T > 800$ K, the rate of the former process exceeds that of the latter; however, at $T < 650$ K, the situation is the reverse and the chain mechanism does not immediately come into play. The production of HO_2 in large amounts at low T_1 triggers vigorous reactions that cause the decomposition of HO_2 (reaction 32 and reverse reactions 25 and 39). In this case, O_3 and H_2O_2 form in large amounts (reactions 39 and 32, respectively). While hydrogen peroxide is a passive component and its accumulation prevents combustion, O_3 dissociates (reaction 36) with the formation of additional O atoms, thereby initiating the chain mechanism through reaction 5.

The excitation of molecular vibrations in H_2 substantially modifies the overall combustion process. The extent of modification depends on the excitation level and also on T_1 and, hence, M_0. This is illustrated in Fig. 2, which shows how a shock wave with M_0 = (a) 9 and (b) 9.5 changes the concentrations of the initial and resulting components in the mixture and the temperature along the relaxation zone at T_{40} = 2000 K. For comparison, dashed lines depict the distributions $\gamma_i(x)$ and $T(x)$ without H_2 excitation. One can see that, for both M_0 = 9 (T_1 = 627 K) and M_0 = 9.5 (T_1 = 675.5 K), the preexcitation of H_2 produces a considerably greater amount of H atoms immediately behind the shock front. First, reaction 9, which generates the OH radicals, and the reverse of reaction 8, which generates the H atoms, are accelerated. Second, a new path for the production of atomic hydrogen appears. This path is associated with the intense dissociation of the vibrationally excited H_2 (reaction 2). Subsequently, the processes in the relaxation zone proceed in a various way depending on T_1. At $T_1 < 650$ K ($M_0 \le 9$), the H atoms are spent on the formation of HO_2 (since, as was indi-

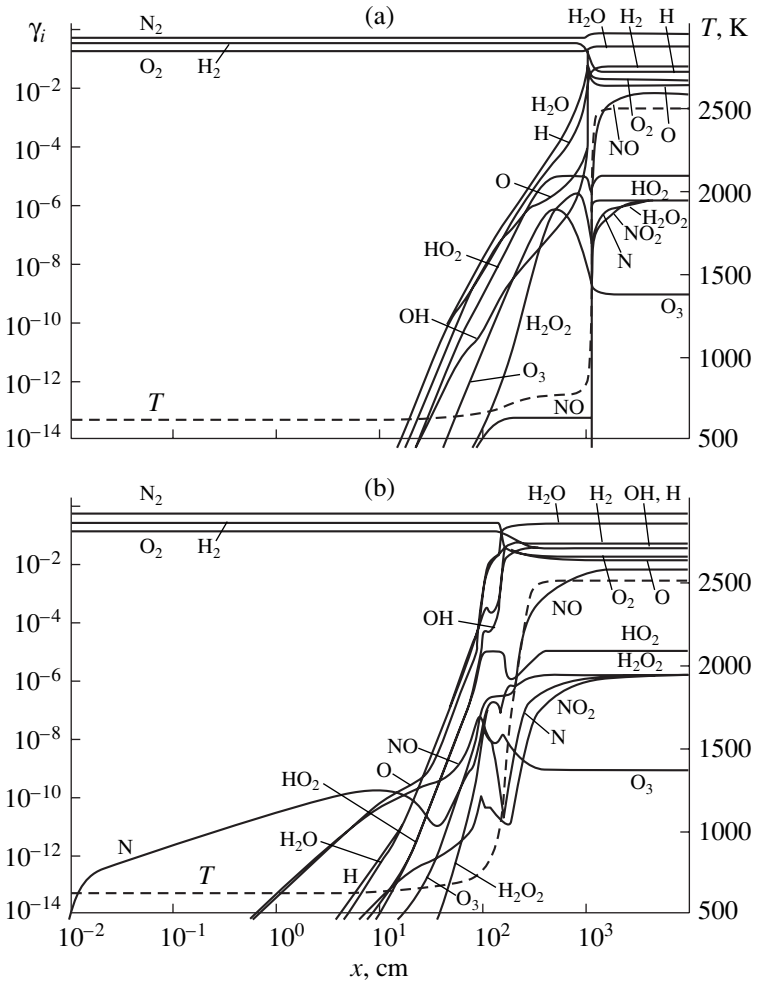

Fig. 3. Variation of γ_i (continuous curves) and T (dashed curves) for the combustion of the $2H_2 + O_2 + 3.76N_2$ mixture behind the shock front with $M_0 = 9$ under the preexcitation of N_2 to T_{40} = (a) 2000 and (b) 3000 K.

cated, the rate of reaction 20 is higher than that of reaction 5) and H_2O_2 (reaction 32). Accordingly, the concentration of H_2O_2 grows and that of the H atoms declines. This considerably inhibits ignition although L_{in} is smaller than that without preexcitation even for $M_0 < 9$.

With increasing T_1 ($T_1 > 650$ K), the rate of reaction 5 increases and that of reaction 32 drops. H–HO_2 interaction forms largely hydroxyl groups (the reaction reverse to reaction 25). However, the concentration of the H atoms does not decrease, since the rate of the reaction reverse to reaction 8 increases because of the resulting OH radicals. Therefore, in the excitation case, the difference in the lengths L_{in} for $M_0 = 9.5$ and $M_0 = 9$ is much greater than in the no-excitation case. The higher degree of H_2 excitation ($T_{40} = 3000$ K) causes the stronger H_2 dissociation and increases the H concentration within the induction zone to a larger extent than at $T_{40} = 2000$ K. Therefore, in the former case, the temperature has a lesser effect on the H and H_2O_2 concentrations; as a result, L_{in} considerably (by a factor of up to 10^4) shrinks in comparison with the equilibrium conditions even at low T_1.

In the case of N_2 preexcitation, the mechanism that intensifies the chain ignition of the H_2 + air mixtures is radically different. Figure 3 demonstrates $\gamma_i(x)$ and $T(x)$ curves for the ignition of the $2H_2 + O_2 + 3.76N_2$ mixture behind a shock at $M_0 = 9$ and different levels of N_2 excitation: $T_{70} = 2000$ and 3000 K. At the higher excitation of N_2 ($T_{70} = 3000$ K), first N atoms form. Then, active O and H atoms, as well as OH radicals, which are responsible for the chain mechanism of combustion, appear. At the lower excitation ($T_{70} = 2000$ K), such a drastic increase in the N concentration at the early stage of combustion initiation does not occur. The concentration of NO is also markedly lower. It is clear that, at $T_{70} = 3000$ K, the high-rate initiation of combustion is associated with the N atoms resulting from the dissociation of the vibrationally excited N_2. This seems to be strange, at first glance, since neither N_2 nor N is imme-

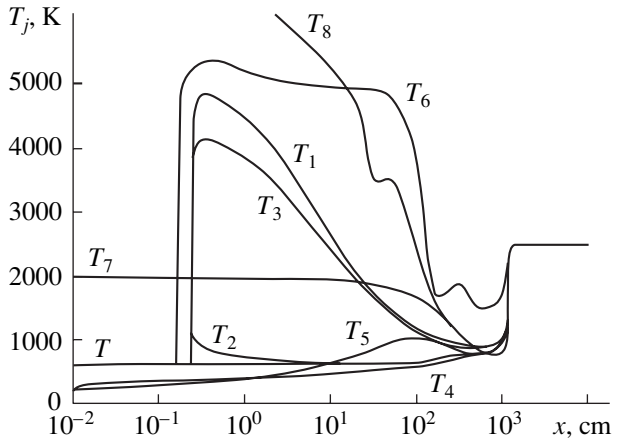

Fig. 4. Variation of the vibrational temperatures T_1–T_8 (the subscripts correspond to the mode nos. of individual molecules) for the combustion of the $2H_2 + O_2 + 3.76N_2$ mixture behind the shock front with $M_0 = 9$ under the preexcitation of N_2 to $T_{70} = 2000$ K.

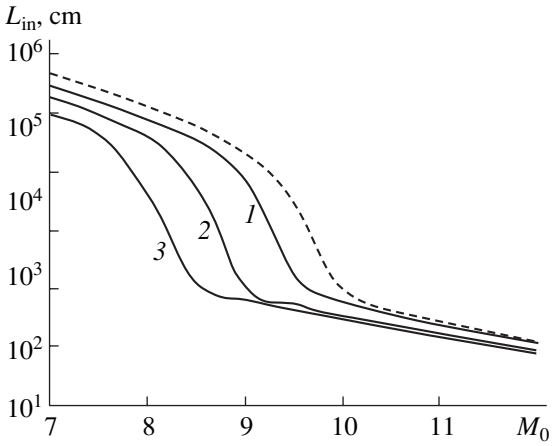

Fig. 5. Induction zone length vs. Mach number in front of the shock for the simultaneous preexcitation of N_2 (T_{70} = 1000 K) and O_3 [T_{170} = (*1*) T_0, (*2*) 2000, and (*3*) 3000 K] (continuous curves). Dashed curve stands for N_2 and O_3 unexcited.

diately involved in the chain mechanism. Combustion, in this case, is initiated as follows. The resulting N atoms combine with O_2 (back reaction 13) to produce O atoms and vibrationally excited NO molecules. The latter rapidly dissociate (reaction 11) into O and N atoms; that is, the chain mechanism, keeping the concentrations of the O and N atoms at a sufficient level, takes place. The O atoms initiate the chain mechanism of combustion (reactions 5 and 6).

At the lower excitation of N_2, dissociation proceeds much more slowly and the above mechanism of formation of O atoms becomes insignificant. Here, the basic factor that intensifies combustion is the presence of vibrationally excited O_2 molecules, which appear (at $x < L_{in}$) behind the shock front because of the V–V' exchange between N_2 and O_2 (reaction 16V). This is distinctly seen in Fig. 4, which shows the variation of the vibrational temperatures T_j (j = 1–8) in the relaxation zone of the shock wave with $M_0 = 9$ at T_{70} = 2000 K. Because of the rise in T_5 ($T_5 > T$), reaction 9, producing OH radicals, and reaction 6 (interaction of molecular oxygen with atomic hydrogen) are accelerated. These reactions also proceed at T_{70} = 3000 K. However, at the high excitation of N_2, they play a minor part. Another important factor that initiates combustion when the N_2 molecules are excited at $T_{70} = 2000$ K is an increase in the translational energy of the gas within the induction zone. This increase is associated with the relaxation of the vibrational energy stored by the N_2. For example, $T = 627$ K immediately behind the shock front against $T = 780$ K at $x > 60$ m. At high T_{70}, this effect is less prominent, because the induction length shrinks (in this case, the characteristic length of relaxation of the N_2 vibrational energy exceeds L_{in}).

The use of an electric discharge is a simple yet the most efficient way of exciting molecular vibrations in N_2. However, if the discharge is initiated in air, a small amount (≤0.15%) of vibrationally excited ozone appears along with excited N_2 [19]. It is therefore of interest to trace its effect on the combustion dynamics in a supersonic flow. The effect of the ozone on the induction zone length is illustrated in Fig. 5 for the mixture $H_2 : O_2 : N_2 : O_3 = 0.299 : 0.147 : 0.553 : 0.00147$ at $T_{70} = 1000$ K (it is assumed that antisymmetric vibrations are excited in the ozone). As the excitation of the ozone increases (the amount of the ozone in the mixture does not exceed 1% in terms of oxygen concentration), the range of M_0 which favors the combustion and cuts L_{in} expands. For example, if only the N_2 vibrations are preexcited ($T_{70} = 1000$ K), the Mach number at which L_{in} equals 10 m is $M_0 = 10$. In the presence of the excited ozone ($T_{170} = 3000$ K), the same value of L_{in} is at $M_0 = 8.5$ ($T_1 = 580$ K).

Thus, a small concentration of excited ozone present in discharge-activated air markedly shrinks L_{in} even for weakly excited N_2. At $M_0 = 9$, the length shrinks by a factor of 100 even at $T_{70} = 1000$ K and $T_{170} = 2000$ K. The reason is that, when the antisymmetric vibrations in O_3 grow, ozone dissociation (reaction 36) proceeds at a higher rate and O atoms in amounts necessary for initiating the chain mechanism of combustion arise very rapidly. Accordingly, OH radicals form. Ozone–hydrogen interaction (reaction 40) also produces OH radicals. Therefore, back reaction 8 again is the basic source of H atoms. When the excitation of N_2 rises to $T_{70} > 2000$ K, the effect of O_3 excitation on the characteristic of supersonic combustion at O_3 concentrations in the mixture as low as mentioned above becomes less

pronounced. The effect is insignificant also at low T_1, when a considerable amount of H_2O_2 is produced.

CONCLUSION

The preexcitation of molecular vibrations in H_2 and N_2 may initiate detonation combustion even behind the front of weak shocks (gas temperatures $T_1 < 500$ K). For the moderate excitation of both H_2 and N_2 and not very high gas temperatures (600–700 K) behind the front, there exists a range of M_0 where the preexcitation of H_2 or N_2 considerably (by a factor of up to 10^3) shrinks the induction zone. As the excitation grows, the range expands toward smaller M_0. Even a small amount of vibrationally excited ozone present in discharge-activated air markedly (by a factor of up to 500) shortens the induction zone and initiates detonation combustion behind the weak shock ($T_1 \sim 500$ K) even if N_2 is low-excited.

ACKNOWLEDGMENTS

This work was financially supported by the Russian Foundation for Basic Research (grant nos. 99-01-01165 and 99-02-18494).

REFERENCES

1. T. Yip, AIAA Pap., No. 89-2567 (1989).
2. N. G. Dautov and A. M. Starik, Fiz. Goreniya Vzryva **32** (1), 94 (1996).
3. D. E. Gonzales, AIAA Pap., No. 96-4960 (1996).
4. C. Li, K. Kailasanath, and E. S. Oran, Combust. Flame **108** (1), 173 (1997).
5. A. M. Starik and N. G. Dautov, Teplofiz. Vys. Temp. **34**, 737 (1996).
6. M. J. Ostrander, J. C. Hyde, M. A. Young, and R. O. Kissinger, AIAA Pap., No. 87-2002 (1987).
7. W. Chinits, AIAA Pap., No. 96-4536 (1996).
8. O. Knab, T. H. Gogel, H. H. Frühauf, and E. W. Messerchmid, AIAA Pap., No. 95-0623 (1995).
9. S. Losev, A. Sergievskaya, A. Starik, and N. Titova, AIAA Pap., No. 97-2532 (1997).
10. N. M. Kuznetsov, *Kinetics Monomolecular Reactions* (Nauka, Moscow, 1982).
11. É. A. Kovach, S. A. Losev, and A. L. Sergievskaya, Khim. Fiz. **14** (9), 44 (1995).
12. A. M. Starik and N. G. Dautov, Kinet. Katal. **37**, 346 (1996).
13. *Thermodynamical Properties of Individual Substances: A Handbook*, Ed. by V. P. Glushko, L. V. Gurvich, G. A. Bergman, *et al.* (Nauka, Moscow, 1978, 1979), Vols. 1, 2.
14. F. J. Tanczaz, J. Chem. Phys. **25**, 439 (1956).
15. R. C. Millikan and D. K. White, J. Chem. Phys. **39**, 3209 (1963).
16. V. V. Lunin, M. P. Popovich, and S. N. Tkachenko, *Physical Chemistry of Ozone* (Mosk. Gos. Univ., Moscow, 1998).
17. K. S. Klopovskiĭ, A. S. Kovalev, D. V. Lopaev, *et al.*, Zh. Éksp. Teor. Fiz. **107**, 1080 (1995) [JETP **80**, 603 (1995)].
18. A. A. Vedenov, *Physics of Electric Discharge CO_2 Lasers* (Énergoizdat, Moscow, 1982).
19. N. G. Basov, V. A. Danilychev, V. A. Dolgikh, *et al.*, Kvantovaya Élektron. (Moscow) **13**, 1161 (1986).

Translated by V. Isaakyan

Technical Physics, Vol. 46, No. 8, 2001, pp. 941–945. Translated from Zhurnal Tekhnicheskoĭ Fiziki, Vol. 71, No. 8, 2001, pp. 13–16.

Motion through a Viscous Liquid of a Heated Spheroidal Solid Particle under Conditions of Uniform Internal Heat Release

N. V. Malaĭ, E. R. Shchukin, and Yu. I. Yalamov

Belgorod State University, Belgorod, Russia

e-mail: malay@bsu.edu.ru

Received November 22, 2000

Abstract—An expression has been derived allowing the drag to be estimated on a spheroidal hydrosol particle moving in a liquid under conditions of an arbitrary temperature difference between the particle surface and a separate region, which takes into account the temperature dependence of the liquid viscosity presented in the form of an exponential power series. © *2001 MAIK "Nauka/Interperiodica".*

FORMULATION OF THE PROBLEM

Consider a spheroidal particle of a solid containing uniformly distributed constant-power heat sources (sinks), which is immersed in an incompressible viscous liquid occupying the whole space. The motion of heated spheroidal particles through viscous liquid and gaseous media was studied in a number of papers [1–5]. A particle is considered heated if the average temperature of its surface is well above the ambient temperature. Heating of the particle surface may be due, for example, to a chemical reaction inside the particle, radioactive decay of the particle matter, and so on. The heated particle significantly influences the thermophysical characteristics of a medium and may appreciably affect the velocity field and the pressure distribution in its vicinity.

The motion of nonspherical particles through liquid and gaseous media under conditions of small relative differences of temperature was considered in papers [6–8].

In this paper, in the framework of the Stokes approximation, an analytical expression for the hydrodynamic force acting on a uniformly heated spheroidal particle has been obtained, which takes into account the temperature dependence of the liquid viscosity represented in the form of an exponential power series, for an arbitrary difference between the temperatures of the particle surface and a separate region.

In the frame of reference with respect to the center of mass of the particle, the problem is reduced to that of a heated immovable oblate (prolate) spheroid placed in a plane-parallel flow of liquid having a velocity $\mathbf{U}_\infty$ (parallel to the symmetry axis of the spheroid). It is assumed that the density, thermal conductivity, and thermal capacity of the liquid and the particle are constant, and the thermal conductivity of the particle is much greater than that of the ambient liquid.

Of the parameters governing the liquid flow, only the dynamic viscosity coefficient strongly depends on temperature [9]. This dependence will be taken into account using the expression

$$\mu_{\text{liq}} = \mu_\infty\left[1 + \sum_{n=1}^{\infty} F_n\left(\frac{T_{\text{liq}}}{T_\infty} - 1\right)^n\right] \times \exp\left\{-A\left(\frac{T_{\text{liq}}}{T_\infty} - 1\right)\right\} \quad (1)$$

(at $F_n = 0$ this formula is reduced to the well-known Reynolds relation [9]). Here A = const; $\mu_\infty = \mu_{\text{liq}}(T_\infty)$; and T_∞ is the liquid temperature away from the particle; the indices "liq" and "p" here and below refer to the parameters of the ambient liquid and the particle, respectively. It is known that the viscosity of a liquid drops exponentially with temperature [9]. An analysis of the known semiempirical formulas has shown that expression (1) best describes viscosity variations in a wide temperature range with any required accuracy.

The flow about the spheroid is presented in spheroidal coordinates $(\varepsilon, \eta, \varphi)$ with the origin at the center of the hydrosol particle. The curvilinear coordinates ε, η, and φ are related to the Cartesian coordinates by the following expressions [10]

$$x = c\sinh\varepsilon\sin\eta\cos\varphi, \quad y = c\sinh\varepsilon\sin\eta\sin\varphi, \quad z = c\cosh\varepsilon\cos\eta \quad (2)$$

or

$$x = c\cosh\varepsilon\sin\eta\cos\varphi, \quad y = c\cosh\varepsilon\sin\eta\sin\varphi, \quad z = c\sinh\varepsilon\cos\eta, \quad (3)$$

where $c = \sqrt{b_0^2 - a_0^2}$ in the case of a prolate spheroid ($a_0 < b_0$, formulas (2)) and $c = \sqrt{a_0^2 - b_0^2}$ for an oblate

1063-7842/01/4608-0941$21.00

spheroid ($a_0 > b_0$, formulas (3)), a_0 and b_0 are the semiaxes of the spheroid, and the z axis of the particle Cartesian coordinate system coincides with the spheroid's axis of symmetry.

For small Reynolds numbers, the distributions of velocity $\mathbf{U}_{liq}$, pressure P_{liq}, and temperature T_{liq} are described by the following set of equations [11]:

$$\nabla P_{liq} = \mu_{liq}\Delta\mathbf{U}_{liq} + 2(\nabla\mu_{liq}\nabla)\mathbf{U}_{liq} + [\nabla\mu_{liq}\times \mathrm{rot}\mathbf{U}_{liq}], \quad \mathrm{div}\mathbf{U}_{liq} = 0, \tag{4}$$

$$\Delta T_{liq} = 0, \quad \Delta T_p = -q_p/\lambda_p. \tag{5}$$

Equations (4) and (5) are solved with the following boundary conditions:

$$\mathbf{U}_{liq} = 0, \quad T_{liq} = T_p, \quad \lambda_{liq}\frac{\partial T_{liq}}{\partial\varepsilon} = \lambda_p\frac{\partial T_p}{\partial\varepsilon} \quad \text{at} \quad \varepsilon = \varepsilon_0, \tag{6}$$

$$\mathbf{U}_{liq} \longrightarrow U_\infty\cos\eta\,\mathbf{e}_\varepsilon - U_\infty\sin\eta\,\mathbf{e}_\eta, \quad T_{liq} \longrightarrow T_\infty, \quad P_{liq} \longrightarrow P_\infty \quad \text{at} \quad \varepsilon \longrightarrow \infty, \tag{7}$$

$$T_p \neq \infty \quad \text{at} \quad \varepsilon \longrightarrow 0. \tag{8}$$

Here, $\mathbf{e}_\varepsilon$ and $\mathbf{e}_\eta$ are the unit vectors of the spheroidal coordinate system, λ is the thermal conductivity, $U_\infty = |\mathbf{U}_\infty|$, and q_p is the (constant) power of the heat sources (sinks) per particle unit volume. Boundary conditions (6) allow for a zero liquid velocity condition at the particle surface, equality of the particle surface and the liquid temperatures, and continuity of the heat fluxes through the particle surface. The particle surface is specified by the coordinate ε_0. At a large distance from the particle ($\varepsilon \longrightarrow \infty$), boundary conditions (7) are valid, and the finiteness of the physical parameters of the particle at $\varepsilon \longrightarrow 0$ is taken into account in (8).

The force exerted by the flow on the particle is defined by the formula

$$F_z = \int_S\Big(-P_{liq}\cos\eta + \sigma_{\varepsilon\varepsilon}\cos\eta - \frac{\sinh\varepsilon}{\cosh\varepsilon}\sigma_{\varepsilon\eta}\sin\eta\Big)dS, \tag{9}$$

where $dS = c^2\cosh^2\varepsilon\sin\eta\,d\eta\,d\varphi$ is a differential surface element, and $\sigma_{\varepsilon\varepsilon}$ and $\sigma_{\varepsilon\eta}$ are the components of the stress tensor in a spheroidal coordinate system [11].

THE FIELD OF VELOCITIES AND THE TEMPERATURE DISTRIBUTION: DETERMINATION OF THE DRAG

To find the force exerted by a liquid on a heated spheroidal solid particle, it is necessary to know the temperature field around the particle. Integrating Eq. (5) under the corresponding boundary conditions gives

$$t_{liq} = 1 + \frac{\gamma}{c}a_0\,\mathrm{arccot}\lambda, \tag{10}$$

$$t_p = B + \frac{\lambda_{liq}}{\lambda_p}\frac{\gamma a_0}{c}\mathrm{arccot}\lambda + \int_{\lambda_0}^{\lambda}\frac{\mathrm{arccot}\lambda}{c}f\,d\lambda - \frac{\mathrm{arccot}\lambda}{c}\int_{\lambda_0}^{\lambda}f\,d\lambda. \tag{11}$$

Here, $\lambda = \sinh\varepsilon$; $t = T/T_\infty$; $\gamma = t_s - 1$ is a dimensionless parameter characterizing the heating of the particle surface; $t_s = T_s/T_\infty$; and T_s is the average surface temperature of the heated spheroid defined by the formula

$$T_s = T_\infty + \frac{a_0 b_0}{3\lambda_{liq}}q_p, \tag{12}$$

$$B = 1 + \left(1 - \frac{\lambda_{liq}}{\lambda p}\right)\gamma\sqrt{1+\lambda^2}\,\mathrm{arccot}\lambda_0, \quad \lambda_0 = \sinh\varepsilon_0,$$

$$f = -\frac{c^2}{2\lambda_p T_\infty}\int_{-1}^{+1}q_p(\lambda^2 + x^2)dx; \quad x = \cos\eta.$$

Taking (10) into account, expression (1) takes the form

$$\mu_{liq} = \mu_\infty\left[1 + \sum_{n=1}^{\infty}F_n\gamma_0^n(\mathrm{arccot}\lambda)^n\right]\exp\{-\gamma_0\,\mathrm{arccot}\lambda\}, \tag{13}$$

where

$$\gamma_0 = \frac{A\gamma}{c}a_0.$$

Making use of the fact that the viscosity depends only on the radial coordinate λ, we solve Eq. (4) by the method of the separation of variables, resolving the velocity and pressure fields into Legendre and Gegenbauer polynomials [10]. In particular, for the components of the mass velocity $\mathbf{U}$ the following expressions satisfying boundary conditions (7) are obtained:

$$U_\varepsilon(\varepsilon,\eta) = \frac{U_\infty}{cH_\varepsilon}\cos\eta[c^2 + A_1G_1 + A_2G_2], \tag{14}$$

$$U_\eta(\varepsilon,\eta) = -\frac{U_\infty}{cH_\varepsilon}\sin\eta[c^2 + A_1G_3 + A_2G_4], \tag{15}$$

where

$$G_1 = -\frac{1}{\lambda^3}\sum_{n=0}^{\infty}\frac{\Theta_n^{(1)}}{(n+3)\lambda^n},$$

$$G_2 = -\frac{1}{\lambda}\sum_{n=0}^{\infty}\frac{\Theta_n^{(2)}}{(n+1)\lambda^n}$$

$$-\frac{\beta}{\lambda^3}\sum_{n=0}^{\infty}\frac{\Theta_n^{(1)}}{(n+3)\lambda^n}\left[(n+3)\ln\frac{\lambda_0}{\lambda}-1\right],$$

$$G_3 = G_1 + \frac{1+\lambda^2}{2\lambda}G_1^{\mathrm{I}}, \quad G_4 = G_2 + \frac{1+\lambda^2}{2\lambda}G_2^{\mathrm{I}},$$

$$\Theta_n^{(1)} = -\frac{1}{n(n+5)}\sum_{k=1}^{n}[(n+4-k)$$

$$\times\{(n+1-k)\alpha_l^{(1)} + \alpha_k^{(2)}\} + \alpha_k^{(3)}]\Theta_{n-k}^{(1)} \quad (n\geq 1),$$

$$\Theta_n^{(2)} = -\frac{1}{(n-2)(n+3)}\left[\sum_{k=1}^{n}\{(n+2-k)\right.$$

$$\times[(n+1-k)\alpha_k^{(1)} + \alpha_k^{(2)}] + \alpha_k^{(3)}\}\Theta_{n-k}^{(2)}$$

$$\left.+\beta\sum_{k=0}^{n}[(2n-2k-3)\alpha_k^{(1)} + \alpha_k^{(1)}]\Theta_{n-k-2}^{(1)} - 6\alpha_n^{(4)}\right]$$

$$(n\geq 3), \quad H_\varepsilon = c\sqrt{\cosh^2\varepsilon - \sin^2\eta},$$

$$\Theta_1^{(2)} = -\frac{1}{4}[2(\alpha_0^{(1)} + \alpha_2^{(2)}) + \alpha_1^{(3)} + 6\alpha_1^{(4)}],$$

$$\Theta_2^{(2)} = 1, \quad \Theta_0^{(1)} = -1, \quad \Theta_0^{(2)} = -1,$$

$$\beta = -\frac{1}{5}[\{3(2\alpha_1^{(1)} + \alpha_1^{(2)}) + \alpha_1^{(3)}\}\Theta_1^2$$

$$-2(\alpha_2^{(1)} + \alpha_2^{(2)}) - \alpha_2^{(3)} - 6\alpha_2^{(4)}],$$

$$\alpha_n^{(1)} = C_n + 12\sum_{k=0}^{\left[\frac{n-2}{2}\right]}(-1)^k\frac{C_{n-2k-2}}{(2k+1)(2k+3)(2k+5)}, \quad (16)$$

$$\Delta_0 = 1,$$

$$\alpha_n^{(2)} = (n-2)C_n - \gamma_0 C_{n-1}$$

$$+12\sum_{k=0}^{\left[\frac{n-2}{2}\right]}(-1)^k\frac{(4k+5)C_{n-2k-2}}{(2k+1)(2k+3)(2k+5)}$$

$$-3\sum_{k=0}^{\left[\frac{n-3}{2}\right]}(-1)^k\frac{1}{(2k+3)(2k+5)}[(n-2k-2)C_{n-2k-2}$$

$$-\gamma_0 C_{n-2k-3} + (n+2k-4)C_{n-2k-4}] \quad (n\geq 1),$$

$$\alpha_n^{(3)} = -2(n+2)C_n + 2\gamma_0 C_{n-1} - 2(n-2)C_{n-2}$$

$$+12\sum_{k=0}^{\left[\frac{n-2}{n}\right]}(-1)^k\frac{C_{n-2k-2}}{(2k+5)} + 6\sum_{k=0}^{\left[\frac{n-3}{2}\right]}(-1)^k$$

$$\times\frac{(k+2)(4k+5)}{(2k+3)(2k+5)}[(n-2k-2)C_{n-2k-2}$$

$$-\gamma_0 C_{n-2k-3} + (n-2k-4)C_{n-2k-4}] \quad (n\geq 1),$$

$$\alpha_n^{(4)} = \frac{1}{n!}[\gamma_0\Delta_{n-1} - (n-1)(n-2)\Delta_{n-2}] \quad (n\geq 1),$$

$$C_k = \sum_{l_1+3l_3+5l_5+\ldots+sl_s=k}\frac{l!}{l_1!l_3!l_5!\ldots l_s!}$$

$$\times F_l f_1^{l_1} f_3^{l_3} f_5^{l_5}\ldots f_s^{l_s},$$

$$s = k - \frac{1+(-1)^k}{2},$$

$$l = l_1 + l_3 + l_5 + \ldots + l_s,$$

$$f_{2k-1} = (-1)^{k-1}\frac{\gamma a_0}{c(2k-1)} \quad (k\geq 1),$$

$[k/2]$ denotes the integer part of $k/2$.

The force acting on the spheroid because of viscous stresses is determined by integrating expression (9) over the spheroid surface and, taking into account (14) and (15), is equal to

$$\mathbf{F}_z = -4\pi\frac{\mu_\infty U_\infty}{c}A_2\exp\left\{-\frac{A\gamma}{c}a_0\operatorname{arccot}\lambda_0\right\}\mathbf{n}_z, \quad (17)$$

where $\mathbf{n}_z$ is the unit vector along the z axis.

Note, that expression (17) for the force was obtained under the assumption of uniform particle motion, which is only possible when the total force acting on a particle is zero. Since force (17) is proportional to the velocity and becomes zero only together with it,

Variation of the coefficient K with the average surface temperature of the spheroid and the ratio of its semiaxes

	T_s, K				a_0/b_0
	293	313	331	353	
K	2.066	2.023	1.818	1.704	1.2
K	0.978	0.649	0.367	0.173	1.4

another force has to be present to balance (17) for uniform motion to be possible.

The integration constants A_1 and A_2 appearing in the expressions for the components of mass velocity are determined from the boundary conditions at the spheroid surface. Then, expression (17) can be represented in the form

$$\mathbf{F}_z = 6\pi a_0 \mu_\infty K U_\infty \mathbf{n}_z, \tag{18}$$

where

$$K = \frac{2}{3}\frac{G_1^{\mathrm{I}}}{\sqrt{1+\lambda_0^2}[G_2 G_1^{\mathrm{I}} - G_1 G_2^{\mathrm{I}}]} \times \exp\left\{-\frac{A\gamma}{c} a_0 \operatorname{arccot}\lambda_0\right\},$$

G_1^{I} and G_2^{I} are the first derivatives of the corresponding functions with respect to λ; and $\boldsymbol{n}_z$ is the unit vector along the z axis.

To obtain an expression for the hydrodynamic drag on an aprolate spheroid it is necessary to substitute $i\lambda$ for λ and $-ic$ for c in formula (18) (i is an imaginary unit).

Thus, formula (18) allows one to estimate the hydrodynamic force acting on a spheroidal particle containing uniformly distributed constant-power heat sources (sinks). This estimation takes into account the dependence of viscosity on temperature expressed in the form of an exponential power series for an arbitrary difference between the temperatures at the particle surface and away from it.

As an example, the table gives the calculation results of the dependence of K on the average temperature of the spheroid surface and the ratio of spheroid semiaxes for granite particles of a radius $R = 2 \times 10^{-5}$ m suspended in water ($T_\infty = 293$ K, $A = 6.095$, $F_n = 0$, $n \geq 1$).

In the limit $\gamma \longrightarrow 0$ (small temperature gradients in the spheroid's vicinity), $a_0 = R$, $K = 1$, and formula (18) transforms into the Stokes formula [10].

Let us consider the motion of a spheroidal particle in a gravitational field. A particle sinking under the action of gravitational force in a viscous liquid ultimately acquires a constant velocity, such that gravity is balanced by hydrodynamic forces.

The gravitational force on the particle, with allowance made for its buoyancy, is

$$F_{\mathrm{g}} = (\rho_p - \rho_{\mathrm{liq}}) g \frac{4}{3}\pi a_0^2 b_0. \tag{19}$$

Equating (18) to (19), we obtain the velocity of the steady fall of a nonuniformly heated spheroidal particle

$$U_\infty = (\rho_{\mathrm{p}} - \rho_{\mathrm{liq}}) g \sqrt{1+\lambda_0^2}\frac{a_0 b_0}{3\mu_\infty}\frac{G_1 G_2^{\mathrm{I}} - G_2 G_1^{\mathrm{I}}}{G_1^{\mathrm{I}}} \times \exp\left\{\frac{A\gamma}{c} a_0 \operatorname{arccot}\lambda_0\right\}.$$

Let us highlight some problems which can be solved using the results obtained. Consider the motion of a particle containing nonuniformly distributed heat sources (sinks) of density q_p. In this case, the average temperature of the spheroid surface is defined by the following relation:

$$\frac{T_s}{T_\infty} = 1 + \frac{1}{4\pi a_0 \lambda_{\mathrm{liq}} T_\infty}\int_V q_p dV,$$

where the integral is taken over the whole volume of the spheroidal particle.

Another case is that of heat sources (sinks) of constant intensity I_0 distributed not in the volume but over the particle surface. It is easy to show that the solution can be obtained if in the above relationships for the case of uniform internal heat release the following substitution is made

$$q_p = \frac{3}{4b_0} I_0 \left[2 + \frac{b_0^2}{\varepsilon a_0^2}\ln\frac{1+\varepsilon}{1-\varepsilon}\right].$$

Here, ε is the spheroid's eccentricity. It is also possible to consider the motion of a uniformly heated particle with an average surface temperature T_s. In particular, if an electromagnetic radiation (having the wavelength λ_0) of intensity I_0 is incident on the spheroid, the absorbed energy is $\pi R^2 I_0 K_n$, where R is the semimajor axis of the spheroid and K_n is the absorption factor [12]. If $\lambda_0 \gg R$, the absorbed energy is uniformly distributed over the particle surface; that is, the particle can be considered uniformly heated. In this case, it is necessary to take that $q_p = 0$ and $T = T_s$ in the boundary conditions (6). The parameter γ takes the form

$$\gamma = \frac{1}{\sqrt{1+\lambda_0^2}}\frac{t_s - 1}{\operatorname{arccot}\lambda_0} \quad (t_s = T_s/T_\infty).$$

REFERENCES

1. D. R. Kassoy, T. C. Adamson, and A. F. Messiter, Phys. Fluids **9**, 671 (1966).
2. V. I. Naĭdenov, Prikl. Mat. Mekh. **38**, 162 (1974).
3. E. R. Shchukin and R. V. Malaĭ, Inzh.-Fiz. Zh. **54**, 630 (1988).

4. E. R. Shchukin, N. V. Malaĭ, and Yu. I. Yalamov, Teplofiz. Vys. Temp. **25**, 1020 (1988).
5. N. V. Malaĭ, Inzh.-Fiz. Zh. **73**, 728 (2000).
6. Yu. I. Yalamov and A. M. Afanas'ev, Zh. Tekh. Fiz. **47**, 1998 (1977) [Sov. Phys. Tech. Phys. **22**, 1163 (1977)].
7. Yu. I. Yalamov and A. M. Afanas'ev, Zh. Tekh. Fiz. **47**, 2001 (1977) [Sov. Phys. Tech. Phys. **22**, 1165 (1977)].
8. Yu. I. Yalamov, V. M. Redchits, and M. N. Gaĭdukov, Zh. Tekh. Fiz. **49**, 1534 (1979) [Sov. Phys. Tech. Phys. **24**, 852 (1979)].
9. St. Bretsznajder, *Properties of Gases and Liquids. Engineering Methods of Calculation* (Wydawnictwo Naukowo-Techniczne, Warsaw, 1962; Moscow, 1966), translated from Polish.
10. J. Happel and H. Brenner, *Low Reynolds Number Hydrodynamics* (Prentice-Hall, Englewood Cliffs, 1965; Mir, Moscow, 1976).
11. L. D. Landau and E. M. Lifshitz, *Mechanics of Continuous Media* (Moscow, 1958).
12. C. F. Bohren and D. R. Huffman, *Absorption and Scattering of Light by Small Particles* (Wiley, New York, 1983; Mir, Moscow, 1986).

Translated by N. Mende

Technical Physics, Vol. 46, No. 8, 2001, pp. 946–951. Translated from Zhurnal Tekhnicheskoĭ Fiziki, Vol. 71, No. 8, 2001, pp. 17–22.

Determination of the Negative Hydrogen Ion Concentration in a Cesium–Hydrogen Discharge

F. G. Baksht, V. G. Ivanov, S. I. Kon'kov, and S. M. Shkol'nik

Ioffe Physicotechnical Institute, Russian Academy of Sciences, Politekhnicheskaya ul. 26, St. Petersburg, 194024 Russia

Received October 31, 2000

Abstract—The concentration N_{H^-} of negative hydrogen ions in a low-voltage cesium–hydrogen discharge plasma N_{H^-} is determined from experiments with laser radiation absorption caused by the photodetachment of electrons from the H^- ions. The resolution of a setup measuring the relative absorption is $\geq 10^{-5}$ for a signal-to-noise ratio of $\sim 10^{-2}$ or less. A heated-cathode diode is used to initiate the discharge at a voltage of $U \leq 10$ V and a current density of $j \leq 5$ A/cm^2 (hydrogen pressure p_{H_2} is equal to several torr, and the cesium concentration in the plasma $N_{Cs}^{(0)} \sim 10^{14}$ cm^{-3}). The absorption due to the photoionization of excited Cs atoms is shown to be negligible. The measured concentration N_{H^-} of the H^- ions is 10^{12}–10^{13} cm^{-3}. Experimental results are consistent with the theory. © *2001 MAIK "Nauka/Interperiodica".*

(1) In modern plasma sources of negative hydrogen ions, the ions are generated by dissociatively attaching thermal electrons to vibrationally excited $H_2^*(v)$ molecules being in the ground electronic state $X^1\Sigma_g^+$ [1, 2]. The necessary concentration of $H_2^*(v)$ is attained mainly by the cascade filling of vibrational states via radiative transitions from excited singlet states of H_2 molecules [3]. Intense filling of the vibrational states is provided in high-voltage electric discharges where electrons emitted by the cathode have an energy $eU \geq 50$ eV. Since electrons with energies of several electronvolts or higher destroy H^- ions, volume plasma ion sources usually consist of two chambers.

In the first chamber, highly excited molecules are generated in the presence of fast electron beams. In the second one, where the dissociative attachment of thermal electrons and the generation of H^- ions take place, the beams are absent. The chambers are separated by either a meshy magnetic filter [2] or a so-called hybrid source [4]. In the latter, fast electrons from the cathode are strictly confined near the chamber walls using electric and magnetic fields of special configuration. The excited hydrogen molecules pass from the walls to the center of the chamber, where H^- ions are generated by dissociative attachment. Thus, H^- ions are generated in the region free of fast electrons.

(2) The goal of this work was to study the generation of H^- ions in Cs + H_2 low-voltage discharges ($U <$ 10 V). In such discharges, cesium ionizes, whereas hydrogen does not, remaining in the ground state. A potential well filled by Maxwellian thermal electrons is formed in the gap. The concentration of the thermal electrons in the gap ($n_e = 10^{13}$–10^{14} cm^{-3}) is considerably higher than the concentration n_e^0 of fast electrons in the cathode beam. Thus, the vibrational kinetics of electrons in the discharge is determined exclusively by the Maxwellian electrons. The temperature T_e of the electrons in the low-voltage Cs + H_2 discharge is close to 1 eV. Such a value is optimum both for the dissociative attachment to vibrationally excited H_2 molecules in the ground state $X^1\Sigma_g^+$ [5] and for the production of the required vibrational distribution function of the H_2 molecules.[1] Thus, all conditions for the intense generation of H^- ions in a single space are met.

According to the theory of low-voltage Cs + H_2 discharge [6–9], a very high concentration of H^- ions ($N_{H^-} \geq 10^{13}$ cm^{-3}) can be attained in the discharge plasma if the emissivity of the cathode is sufficiently high ($j_s \geq 10$ A/cm^2). Therefore, discharges of this type can be used for generating narrow beams of H^- ions with a high current density j_{H^-} (up to 1 A/cm^2). Experimental studies of low-voltage Cs + H_2 discharge [10–14] showed, in particular, that the plasma parame-

[1] As T_e exceeds 1 eV, the vibrational excitation efficiency decreases because of H_2 dissociation and the high-rate generation of atomic hydrogen. This sharply increases the rate of V–T relaxation of H_2 molecules due to atomic hydrogen. As a result, the concentration of H^- ions in the discharge decreases [9].

ters obtained with such discharges are sufficient for attaining high values of N_{H^-}.

In this work, direct measurements of N_{H^-} in the low-voltage Cs + H_2 discharge are reported for the first time. The results of the measurements are compared with calculations.

We studied largely dense-plasma discharges ($3 \le p_{H_2} L \le 12$ torr mm, where p_{H_2} is the hydrogen pressure and L is the interelectrode spacing). Under these conditions, the effect of interaction between $H_2^*(v)$ molecules and the electrode surfaces on the vibrational distribution function is negligible. Therefore, when comparing theoretical and experimental data, one does not need to know the deactivation probabilities for $H_2^*(v)$ on cesium-coated surfaces.

(3) The concentration N_{H^-} was determined from the experimentally measured absorption of the laser radiation. The absorption was caused by the photodetachment of electrons from H^- ions. A continuous-wave $P \cong 10^{-1}$ W semiconductor laser was used. The spectral width of the radiation was approximately 2 nm, and the maximum intensity was at $\lambda_0 = 816$ nm ($h\nu_0 = 1.52$ eV). This wavelength corresponds to the maximum photoionization cross section of H^- ions ($\sigma_0 = 4 \times 10^{-17}$ cm^{-2} [15]). However, the corresponding energy $h\nu_0$ is insufficient for the photoionization of highly occupied discrete levels of Cs ($7S_{1/2}$ or lower). As a result, the photoionization of Cs under the experimental conditions is insignificant (see below). On the other hand, the laser radiation at this wavelength can effectively be filtered out from the discharge radiation, because the former falls within a wide spectral "window" where cesium does not emit.

The diode used in the experiment is shown in Fig. 1a. The face ends of cylinders 12 mm in diameter were used as parallel-sided electrodes. The lateral surfaces of the cylinders were covered by insulating BeO ceramics. The interelectrode spacing L was 3 mm. The Mo cathode cylinder was heated by a radiator placed inside the cylinder. A platinum foil 0.1 mm thick was welded to the face end of the cathode cylinder. The anode cylinder was made of oxygen-free copper. A cylindrical probe made of gilded tungsten was inserted in the interelectrode gap through a hole at the center of the anode. The probe diameter and length were 0.1 and 2 mm, respectively. The axis of the probe was parallel to the electrode surfaces. The diode was mounted in a glass bulb placed in a special thermostat. To prevent cesium condensation, the temperature inside the thermostat was maintained between 550 and 600 K.

The measurements were performed in the pulse-periodic mode. A special source generating regulated voltage pulses of variable amplitude ($U \le 10$ V) and

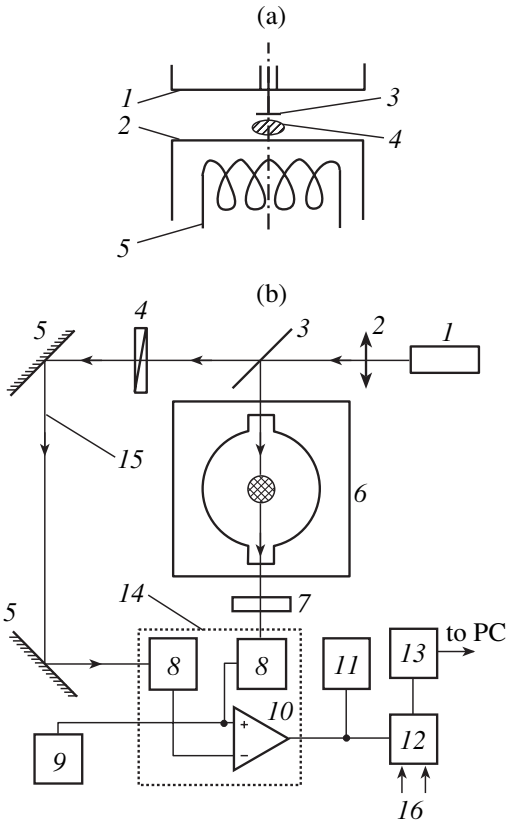

Fig. 1. (a) Diode used in the experiment: (*1*) anode, (*2*) cathode, (*3*) cylindrical probe, (*4*) cross section of laser beam, and (*5*) heater. (b) Experimental setup for optical measurements: (*1*) semiconductor laser, (*2*) focusing lens, (*3*) beam-splitting plate, (*4*) polarizer, (*5*) mirrors, (*6*) thermostat with the diode, (*7*) interference filter, (*8*) FD-24K photodiodes, (*9*) digital voltmeter, (*10*) differential amplifier, (*11*) S1-122A oscilloscope, (*12*) differential integrator, (*13*) analog-to-digital converter, (*14*) bulk thick-wall brass case, (*15*) laser beam, and (*16*) gate pulses.

duration $\tau = 1$ ms was used to sustain the discharge.[2] The permissible current load I of this source did not exceed 10 A. The pulse repetition frequency was varied in the range $10 \le f \le 40$ Hz. Thus, the current pulses of the arc were almost rectangular. During the measurements, the external parameters (cathode temperature, cesium concentration, and hydrogen pressure) were maintained constant. Variations in both the pulse shape and the arc plasma parameters with time (i.e., from pulse to pulse) were negligible. This property of the low-voltage heated-cathode arc allowed the use of gated integration in the measurements. The parameters of the electronic component of the plasma are virtually related to the instantaneous current. The molecular component relaxation time τ_1 did not exceed 0.5 ms [12]. Therefore, the measurements began when the plasma became quasi-stationary, i.e., $\Delta t \ge 0.5$ ms after

[2] The *I–V* characteristic of the low-voltage heated-cathode arc shows that the current saturates at the level of the thermionic current of the cathode. This allows the regulation of the arc voltage.

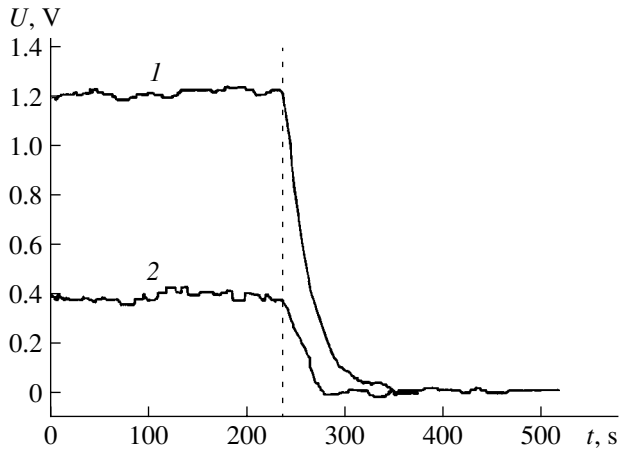

Fig. 2. Laser radiation absorption by the plasma of the low-voltage Cs + H_2 discharge (discharge turn-off time is marked with the dotted line): (*1*) I = 4.0 A, U = 6.6 V, and p_{H_2} = 2 torr; (*2*) I = 3.0 A, U = 5.0 V, and p_{H_2} = 1 torr.

arc initiation. The probe measured the electron temperature and concentration as well as the potential distribution in the gap. The probe measurements were performed simultaneously with the optical measurements. The experimental setup and the procedure of electrical measurements are described in more detail in [10, 14].

The weak absorption of the probe radiation by our plasma object was caused by its small size and also by the small cross section of electron photodetachment from the H^- ions. This imposed severe requirements on the experimental setup and the measuring procedure. It was necessary to provide the detection of weak noisy signals (a signal-to-noise ratio of $\sim 10^{-2}$ or less). Noise was due to the mechanical vibrations of the setup, convective flows of dusty air because of heating the thermostat, etc. The block diagram of the experimental setup for optical measurements is shown in Fig. 1b. The setup uses the method of gated integration to measure the relative absorption of the laser radiation as low as $\Delta P/P_0 \geq 10^{-5}$ (P_0 and ΔP are the incident and absorbed radiation power, respectively).[3] With regard for the fact that the linear size of our plasma object is about 1 cm, the setup can determine N_{H^-} at a level of $\geq 2.5 \times 10^{11}$ cm^{-3}.

Consider the operation of the setup. The beam from laser *1* is split into the probing and reference beams by plate *3*. The probing beam passes through the setup and is partially absorbed by the plasma. Lens *2* inside the laser case focuses the probing beam in the gap so that its cross section becomes elliptic (major semiaxis is 1.0 mm; minor semiaxis, 0.35 mm). The major semiaxis of the ellipse is parallel to the electrode surfaces. The inclination of the beam-splitting plate can be varied with a micrometer screw. In this way, the probing beam moves along the discharge axis. The results discussed below refer to the case when the probing beam was focused between the cathode and the probe (Fig. 1a).

Both beams fall on photodiodes *8*. The plasma radiation is cut off by narrow-band interference filter *7*. The passband maximum lies at the wavelength λ_0. The output signals of photodiodes *8* are applied to the input of differential amplifier (DA) *10* with a gain K_1 = 200. The photodiodes and the DA are enclosed in a bulk thick-wall brass case used to equalize the temperature and protect the high-sensitivity measuring circuit from external electrical noise. The DA is balanced with polarizer *4*. The balancing is monitored using an oscilloscope [11]. The output signal of the DA is applied to the input of differential integrator (DI) *12*. The DI improves the signal-to-noise ratio, i.e., facilitates the extraction of the desired signal.

The DI consists of two gated integrators. The difference signal from the gated integrators is amplified (K_2 = 28) and integrated with an output capacitor. One of the integrators is gated a short time before the initiation of the low-voltage arc. This integrator is used to measure the noise component of the DA output signal. The second integrator is gated during the discharge. It is used to determine the sum of the desired and noise signals. Thus, the DI output signal is proportional to the laser radiation power absorbed by the low-voltage arc plasma. Gate pulses 0.3 ms wide were applied to the DI 0.4 ms before and 0.6 ms after the initiation of the low-voltage arc. For a gating frequency f = 20 Hz, the time constant of the DI was $\sim 10^2$ s. The design and the performance of the DI are detailed in [17]. The output signal of the DI was digitized using an analog-to-digital converter and applied to a PC.

Precautions have been taken to minimize the noise caused by the mechanical vibrations of the elements of the setup. To suppress air convection due to the heating of the thermostat, the reference and probe beams propagated inside small-diameter glass tubes.

Signal readout and digitization were performed every second. For each of the discharge modes, the maximum possible duration of measurement was $\sim 10^3$ s. Signal recording began 200–300 s after the steady conditions had been set and the arc had been initiated. The measurements lasted 200–300 s until the discharge was switched off. Then, the DI output signal corresponding to the zero absorption was recorded for another 200–300 s. Associated records are shown in Fig. 2. The results were statistically processed. To calculate the relative absorption of the laser radiation, the ratio between the absorbed power measured and the incident power was determined. The signal proportional to the incident power was recorded with digital voltmeter *9* (Fig. 1b).

[3] In the study of the magnetochromatic effect in gaseous nitrogen dioxide [16], the absorption of the laser radiation by nitrogen dioxide was measured at a level of $\Delta P/P_0 \approx 5 \times 10^{-6}$. In contrast to our experiments, the measurements in [16] were performed using a single pulse, i.e., without averaging the valid signal. Low noise is the reason for such high sensitivity.

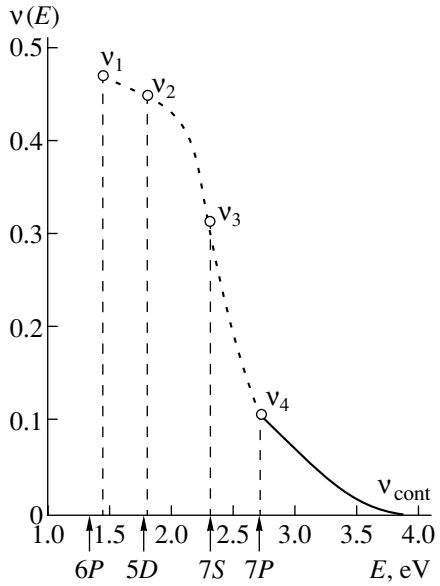

Fig. 3. Relative populations $\nu_i = N_i/N_i^{(B)}$ of the excited levels of a Cs atom for one of the experimentally studied discharge modes: I = 2 A, U = 5.2 V, p_{H_2} = 1 torr, $n_e = 4.7 \times 10^{13}$ cm^{-3}, and T_e = 0.64 eV ($N_i^{(B)}$ is the population of the excited level according to the Boltzmann distribution when the excited level is in equilibrium with the ground level). The solid curve is the population $\nu(E)$ calculated in the Gurevich–Pitaevskiĭ diffusion approximation of quasi-continuous spectrum.

We performed measurements in the presence of the arc and in the absence of the laser radiation to estimate the efficiency of plasma radiation cutoff. It can be argued (within the accuracy of our measuring procedure) that the plasma radiation did not fall on the photodiodes.

(4) The plasma parameters (including the concentration N_{H^-} of the negative ions) were calculated at the midgap ($x = L/2$), i.e., at the site of the probe, using an approximate model described in [7]. The plasma in the gap was assumed to be uniform. A comparison of these approximate calculations with the exact solutions obtained using the procedure described in [8] shows that, for $x = L/2$, they are in fairly good agreement: the respective electron concentrations diverge no more than twofold, and the difference in T_e does not exceed 15%. Given T_e, one can, with the model described in [7], calculate all the parameters of the plasma, namely, the concentrations of the plasma components, the populations N_1 of the excited levels of a Cs atom, and the vibrational function $H_2(v)$ for the distribution of H_2 molecules [9].[4]

[4] The potential drop near the electrodes should be determined from the balance conditions for charged particles and energy at the plasma boundaries. In our case, the form of related expressions depends on the mechanism of cathode beam relaxation in a plasma (cf. [6–8] and [9]). This problem is not considered in this work, because the nonequilibrium (beam) component of the electron distribution function has no effect on the vibrational kinetics of electrons in the plasma.

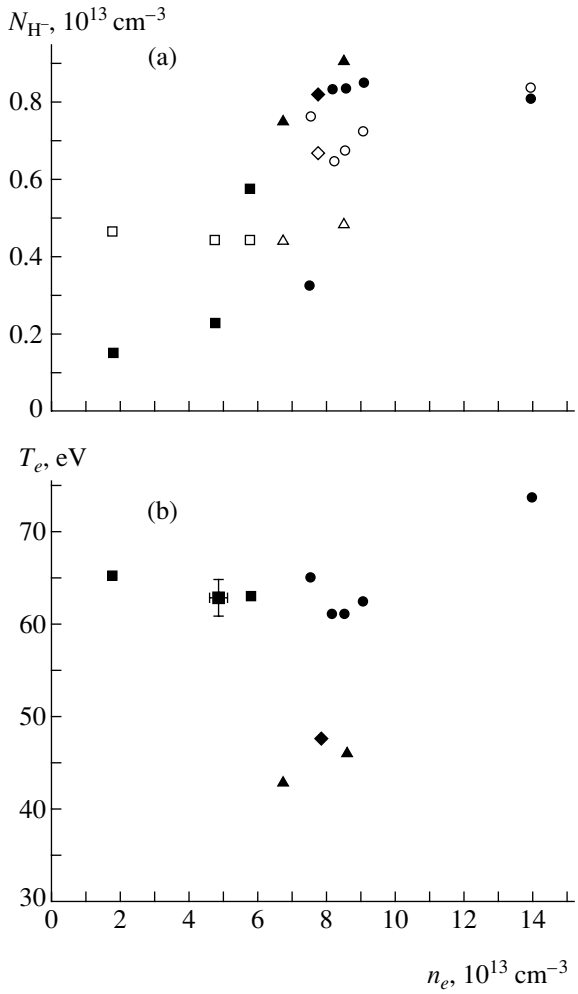

Fig. 4. (a) Concentrations N_{H^-} of negative hydrogen ions in the interelectrode gap for various modes of the low-voltage cesium–hydrogen discharge; (b) plasma parameters n_e and T_e measured with the probe placed at the center of the gap ($x = L/2$) for various modes of the discharge. Closed symbols, experimental data; open symbols, calculations for $x = L/2$ (center of the gap). p_{H_2} = (■, □) 1, (●, ○) 2, (▲, △) 3, and (◆, ◇) 4 torr.

Now let us find N_i and estimate the laser radiation absorption caused by the photoionization of cesium. The cesium spectrum is subdivided into two parts. The lower widely spaced levels (i = 6S, 6P, 5D, 7S, and 7P) will be considered in a discrete spectrum approximation with regard for impacts of the first and second kind, optical transitions (in the effective lifetime approximation [18, 19]), and interactions with H_2 molecules [20] (for more details, see [7]). Highly excited closely spaced levels (from 7P to the ionization threshold) will be considered in the Gurevich–Pitaevskiĭ approximation of quasi-continuous spectrum [21]. Typical dimensionless values of the population $\nu_i = N_i/N_i^{(B)}$ that were calculated for one of the experimentally studied discharge modes (the point corresponding to p_{H_2} = 1 torr,

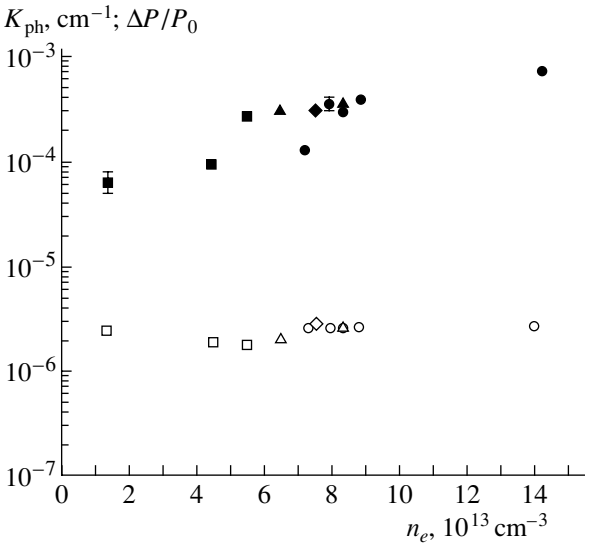

Fig. 5. Filled symbols: experimental values of the relative absorption $\Delta P/P_0$ of the laser radiation in the plasma. They were used to calculate the concentrations N_{H^-} shown in Fig. 4a. Open symbols: calculated factors of absorption caused by the photoionization of excited Cs atoms for the same discharge modes as in Fig. 4a. The values of p_{H_2} are the same as in Fig. 4a.

$n_e = 4.7 \times 10^{13}$ cm^{-3}, and $T_e = 0.64$ eV in Fig. 4b) are shown in Fig. 3 ($N_i^{(B)} = (g_i/g_{6S})N_{6S}\exp\{-E_i/kT_e\}$ is the Boltzmann equilibrium population, and g_i is the statistical weight of a level). For $E \geq E_{7P}$, a continuous function $\nu(E)$ should be used instead of the discrete function $\nu_i(E_i)$. The former is obtained by solving an appropriate diffusion equation [21] and is joined together with the values of ν_{7P} and $\nu_{cont} = n_e n_{Cs}^+ / N_{6S} K_0(T_e)$ at the edges of the quasi-continuous spectrum (n_{Cs}^+ is the concentration of Cs^+ ions, and $K_0(T_e)$ is the equilibrium ionization constant for the 6*S* state). The distribution of the populations of the excited states in Fig. 3 is typical for plasmas where ionization dominates over recombination. It should be noted that this distribution has small values of $\nu(E)$ in the upper part of the spectrum, where the photoionization absorption of the laser radiation occurs.[5] The distribution shown in Fig. 3 is typical of all discharge modes. The value of the photoionization cross section used in the calculations was taken from [22].

(5) The experimental and calculated data are shown in Figs. 4 and 5. The concentrations N_{H^-} for various modes of the low-voltage arc that were determined from the absorption values are shown in Fig. 4a (the laser radiation was assumed to be absorbed in a 1-cm-thick layer of the plasma). The cathode emission was $j_s = 1$–4 A/cm^2. The values of the electron concentration n_e and temperature T_e measured with the probe at the center of the discharge for the same modes are shown in Fig. 4b. In the calculations, they were used as discharge mode parameters. The calculated concentrations N_{H^-} for various discharge modes are also shown in Fig. 4a. The total concentration $N_{Cs}^{(0)}$ of cesium in the gap was determined by calculations, since this value could differ significantly from the concentration N_{Cs} over the liquid phase under experimental conditions. As is seen from Fig. 4, the experimental and calculated data are in satisfactory agreement.

The measured values of the relative absorption $\Delta P/P_0$ (Fig. 5) were used to calculate the concentrations N_{H^-} shown in Fig. 4. In Fig. 5, shown is also the calculated coefficient K_{ph} of absorption (absorption per 1-cm-thick plasma layer) caused by the laser-induced ionization of excited Cs atoms. As is evident from Fig. 5, the measured absorption is greater than the photoionization absorption in cesium by two orders of magnitude. Therefore, the former cannot be due to the photoionization of Cs atoms.

As follows from Fig. 4b, as the concentration n_e and the temperature T_e of the plasma electrons increase, the concentration N_{H^-} grows, approaching ~10^{13} cm^{-3}. According to theoretical predictions, N_{H^-} can exceed the values attained in the experiment. Greater values of N_{H^-} can be obtained using higher-emissivity cathodes (for example, LaB_6 cathodes) or hollow-cathode discharges in a Cs + H_2 mixture [23].

(6) Thus, it has been shown that a high concentration of H^- ions ($N_{H^-} \sim 10^{13}$ cm^{-3}) in a low-voltage cesium–hydrogen discharge plasma is a possibility. The values of N_{H^-} measured are consistent with theoretical predictions.

ACKNOWLEDGMENTS

We are grateful to S.E. Goncharov, Yu.A. Barinov, and N.K. Mitrofanov for their assistance in the experiments.

This work was partially supported by the INTAS Foundation (project no. 94-316).

REFERENCES

1. M. Bacal and G. W. Hamilton, Phys. Rev. Lett. **42**, 1538 (1979).
2. M. Bacal, Nucl. Instrum. Methods Phys. Res. **37/38**, 28 (1989).
3. J. R. Hiskes, J. Appl. Phys. **51**, 4592 (1980).

[5] The possibility of absorption due to transitions from the 7*S* level to the Rydberg 6*P* states of the quasi-continuous spectrum was also analyzed. Absorption of this type was found to be very weak.

4. A. M. Bruneteau, G. Holles, M. Bacal, and J. Bretagne, J. Appl. Phys. **67**, 7254 (1990).
5. J. H. Wadehra, Phys. Rev. A **29**, 106 (1984).
6. F. G. Baksht and V. G. Ivanov, Pis'ma Zh. Tekh. Fiz. **12**, 672 (1986) [Sov. Tech. Phys. Lett. **12**, 278 (1986)].
7. F. G. Baksht, L. I. Elizarov, V. G. Ivanov, and V. G. Yur'ev, Fiz. Plazmy **14**, 91 (1988) [Sov. J. Plasma Phys. **14**, 56 (1988)].
8. F. G. Baksht, L. I. Elizarov, and V. G. Ivanov, Fiz. Plazmy **16**, 854 (1990) [Sov. J. Plasma Phys. **16**, 497 (1990)].
9. F. G. Baksht, V. G. Ivanov, and A. A. Kostin, Zh. Tekh. Fiz. **63** (9), 173 (1993) [Tech. Phys. **38**, 825 (1993)].
10. F. G. Baksht, G. A. Dyuzhev, L. I. Elizarov, *et al.*, Zh. Tekh. Fiz. **62** (9), 148 (1992) [Sov. Phys. Tech. Phys. **37**, 959 (1992)].
11. F. G. Baksht, G. A. Dyuzhev, L. I. Elizarov, *et al.*, Pis'ma Zh. Tekh. Fiz. **19** (22), 39 (1993) [Tech. Phys. Lett. **19**, 716 (1993)].
12. F. G. Baksht, V. G. Ivanov, A. G. Nikitin, and S. M. Shkol'nik, Pis'ma Zh. Tekh. Fiz. **20** (22), 84 (1994) [Tech. Phys. Lett. **20**, 927 (1994)].
13. F. G. Baksht, V. G. Ivanov, A. N. Kostin, *et al.*, Zh. Tekh. Fiz. **65** (8), 186 (1995) [Tech. Phys. **40**, 851 (1995)].
14. A. G. Nikitin and S. M. Shkol'nik, Zh. Tekh. Fiz. **67** (1), 125 (1997) [Tech. Phys. **42**, 110 (1997)].
15. H. S. W. Massey, *Negative Ions* (Cambridge Univ. Press, Cambridge, 1976; Mir, Moscow, 1979).
16. B. A. Zon, V. I. Naskidashvili, G. V. Pakhomov, and S. I. Pruchanskiĭ, Opt. Spektrosk. **66**, 1203 (1989) [Opt. Spectrosc. **66**, 699 (1989)].
17. Yu. A. Barinov and S. I. Kon'kov, Prib. Tekh. Éksp., No. 2, 60 (2001).
18. L. M. Biberman, V. S. Vorob'ev, and I. T. Yakubov, *Kinetics of Nonequilibrium Low-Temperature Plasmas* (Nauka, Moscow, 1982; Consultants Bureau, New York, 1987).
19. *Thermionic Converters and Low-Temperature Plasmas*, Ed. by B. Ya. Moĭzhes and G. E. Pikus (Nauka, Moscow, 1973).
20. M. Lukaszwic'z, Bull. Acad. Pol. Sci., Ser. Sci., Math., Astron. Phys. **23**, 501 (1975).
21. A. V. Gurevich and L. P. Pitaevskiĭ, Zh. Éksp. Teor. Fiz. **46**, 1281 (1964) [Sov. Phys. JETP **19**, 870 (1964)].
22. J. Lahiri and S. T. Manson, Phys. Rev. A **33**, 3151 (1986).
23. F. G. Baksht and V. G. Ivanov, Pis'ma Zh. Tekh. Fiz. **21** (20), 15 (1995) [Tech. Phys. Lett. **21**, 821 (1995)].

Translated by K. Chamorovskiĭ

Technical Physics, Vol. 46, No. 8, 2001, pp. 952–955. Translated from Zhurnal Tekhnicheskoĭ Fiziki, Vol. 71, No. 8, 2001, pp. 23–26.

SOLIDS

Nonlinear Strain Waves and Densities of Defects Induced in Metal Plates by External Energy Fluxes

F. Mirzoev and L. A. Shelepin

Lebedev Institute of Physics, Russian Academy of Sciences, Leninskiĭ pr. 53, Moscow, 117942 Russia

Received January 27, 2000; in final form, October 17, 2000

Abstract—A model of nonlinear periodic traveling strain waves induced in laser-irradiated metal plates with quadratic nonlinearity is proposed. Interaction between the elastic strain fields and the concentration of point defects is taken into account. The effect of generation–recombination processes on the evolution of nonlinear localized waves is considered. An equation for the amplitudes of the nonlinear waves is derived. It is employed to analyze the attenuation of the waves with allowance for low- and high-frequency losses. © *2001 MAIK "Nauka/Interperiodica".*

The generation of various solitary waves (e.g., solitons) is one of the most prominent nonlinear effects when a solid is subjected to intense pulsed action (laser or electron irradiation, shock loading, etc.). This phenomenon has been addressed in numerous theoretical and experimental works [1–6]. The velocities of solitary waves are proportional to their amplitudes, and their shape is virtually time-independent. When studying the evolution of the nonlinear elastic waves in crystals, one should take into account various (intrinsic or induced) lattice defects, giving rise to large strain. Dispersion, due to the finite thickness of a crystal, also significantly influences wave dynamics. Spatial dispersion related to the finiteness of the lattice spacing [7] may play an important role at high frequencies, where the free path of a phonon is smaller than the wavelength. Investigation into the dynamics of the waves with allowance for wave–defect interaction is of great theoretical and practical value, in particular, for the analysis of anomalous mass transfer during laser or ion implantation of metals [8] and the mechanic activation of components in solid-phase chemical reactions.

The purpose of this work was to study the propagation of a longitudinal-strain nonlinear wave in a crystal plate where point defects (vacancies and interstitials) with the bulk concentration $n_j(x, t)$ ($j = v$ for vacancies and $j = i$ for interstitials) are induced by an external energy flux (laser radiation or particle beam). When passing, a longitudinal wave changes the activation energy of defect formation in the tension and compression areas, which leads to the spatial redistribution of the defects [9]. The defects migrate in the crystal and recombine at various centers of density ρ_s, such as dislocations, interstitial impurities, etc. Let the wavelength λ be larger than the plate thickness h. Then, the nonlinear dynamic equation that describes the propagation of elastic waves in an elastic continuum with quadratic nonlinearity is represented as

$$\frac{\partial^2 u}{\partial t^2} - c_s^2\frac{\partial^2 u}{\partial x^2} - \frac{\beta_N}{\rho}\frac{\partial^2 u}{\partial x^2}\frac{\partial u}{\partial x} - l^2\left(\frac{\partial^4 u}{\partial t^2 \partial x^2} - c_\tau^2\frac{\partial^4 u}{\partial x^4}\right) = -\frac{K\Omega_j}{\rho}\frac{\partial n_j}{\partial x}. \quad (1)$$

Here, $u(x, t)$ is the displacement of the medium; $c_s = (E/\rho(1-\sigma^2))^{1/2}$ and $c_\tau = (\mu/\rho(1-\sigma^2))^{1/2}$ are the velocities of the longitudinal and transverse waves, respectively; ρ is the density of the medium; K is the modulus of uniform compression; and Ω_j is the dilatation parameter characterizing a change in the crystal volume upon the formation of one point defect (if $j = v$, $\Omega_j < 0$; if $j = i$, $\Omega_j > 0$). The coefficient of nonlinearity β_N and the dispersion parameter l are given by [10]

$$\beta_N = \frac{3E}{1-\sigma^2} + 3B\left[\frac{1-4\sigma+6\sigma^2}{(1-\sigma)^3}\right] + A\left[1-\left(\frac{\sigma}{1-\sigma}\right)^3\right] + C\left(\frac{1-2\sigma}{1-\sigma}\right)^3,$$

$$l^2 = \frac{h^2\sigma^2}{12(1-\sigma)^2},$$

where A, B, and C are the Landau moduli of the third order; E is the Young modulus; and σ is Poisson's ratio. For the majority of solids (metals and many of the polymers), $\beta_N < 0$.

Samsonov *et al.* [2–4] thoroughly studied Eq. (1) in the absence of concentration stresses (so-called dual-dispersion equation). We used the Hamiltonian approach to generalize this equation to the case of elastic concentration stresses [9].

The distribution of the defects in the medium depends on that of strains and stresses and is deter-

mined by the right-hand side of Eq. (1). Therefore, the comprehensive description of the propagation of an elastic wave requires Eq. (1) to be closed by the equation for the density of defects. Assume that the evolution of the defects with time is governed mainly by generation, recombination, and diffusion. Then, the density of defects n_j obeys the diffusion–kinetic equation

$$\frac{\partial n_j}{\partial t} = q_0 + q_\varepsilon \frac{\partial u}{\partial x} + D_j \frac{\partial^2 n_j}{\partial x^2} - \beta_j n_j, \tag{2}$$

where q_0 is the rate of generation of point defects in the absence of strain, the second term in the right of Eq. (2) represents the contribution of strain into defect generation ($\varepsilon = u_x$ is the strain in the medium), D_j is the diffusion coefficient for a defect of the jth type, and β_j is the rate of recombination at sinks. The bulk recombination of the unlike defects is not taken into account.

The closed system of Eqs. (1) and (2) comprehensively describes the interrelation between the point defect density and the displacement of the medium: the nonuniform distribution of defects affects the displacements, which, in turn, change the distribution of the defects according to Eq. (2).

Eliminating the concentration of defects from the above system of equations, we arrive at the following equation for the displacement:

$$\frac{\partial}{\partial t}\left[\frac{\partial^2 u}{\partial t^2} - c_s^2 \frac{\partial^2 u}{\partial x^2} - \frac{\beta_N}{\rho}\frac{\partial^2 u}{\partial x^2}\frac{\partial u}{\partial x} - l^2\left(\frac{\partial^4 u}{\partial t^2 \partial x^2} - c_\tau^2 \frac{\partial^4 u}{\partial x^4}\right)\right]$$

$$= \frac{K\Omega_j}{\rho} q_\varepsilon \frac{\partial^2 u}{\partial x^2} + D\left[\frac{\partial^4 u}{\partial t^2 \partial x^2} - c_s^2 \frac{\partial^4 u}{\partial x^4} - \frac{\beta_N}{2}\frac{\partial^3}{\partial x^3}\left(\frac{\partial u}{\partial x}\right)^2 - l^2 \frac{\partial^2}{\partial x^2}\left(\frac{\partial^4 u}{\partial t^2 \partial x^2} - c_\tau^2 \frac{\partial^4 u}{\partial x^4}\right)\right] - \beta\left[\frac{\partial^2 u}{\partial t^2} - c_s^2 \frac{\partial^2 u}{\partial x^2} - \frac{\beta_N}{\rho}\frac{\partial^2 u}{\partial x^2}\frac{\partial u}{\partial x} - l^2\left(\frac{\partial^4 u}{\partial t^2 \partial x^2} - c_\tau^2 \frac{\partial^4 u}{\partial x^4}\right)\right]. \tag{3}$$

Equation (3) is a differential analog of equations typical of dissipative media with shape memory (or relaxation) [1]. In the absence of dispersion ($l = 0$) and generation of defects ($q_\varepsilon = \beta = 0$), Eq. (3) is reduced to the equation for a longitudinal wave in free space. In the general case, Eq. (3) can be solved only numerically. However, one can consider the right of Eq. (3) as a small deviation of the wave processes from the "unperturbed" state provided that the dissipation effects are small. Then, assuming that $u_{tt} \approx c_s^2 u_{xx}$ in the zero approximation, we can rewrite Eq. (3) as

$$\frac{\partial^2 u}{\partial t^2} - c_s^2 \frac{\partial^2 u}{\partial x^2} - \frac{\beta_N}{\rho}\frac{\partial^2 u}{\partial x^2}\frac{\partial u}{\partial x} - l^2(c_s^2 - c_\tau^2)\frac{\partial^4 u}{\partial x^4} = -\frac{K\Omega_j}{\rho c_s^2} q_\varepsilon \frac{\partial u}{\partial t} + \frac{\beta l^2}{c_s^2}\frac{\partial^3 u}{\partial x^2 \partial t} - Dl^2 \frac{\partial^5 u}{\partial t \partial x^4}. \tag{4}$$

Equations of this type were theoretically studied in [11–13]. Below, we will consider only the long-wave approximation ($\lambda/h > 1$). Following [13], we pass from Eq. (4) to equations for coupled normal modes. Introducing variables ε_1 and ε_2:

$$\frac{\partial u}{\partial x} = \varepsilon_1 + \varepsilon_2,$$
$$\frac{\partial u}{\partial t} = c_s(\varepsilon_1 - \varepsilon_2) + \frac{l^2 c_s}{2}\frac{\partial^2}{\partial x^2}(\varepsilon_1 - \varepsilon_2), \tag{5}$$

we arrive at the system of equations

$$\frac{\partial \varepsilon_1}{\partial t} - c_s \frac{\partial \varepsilon_1}{\partial x} - \beta_d \frac{\partial^3 \varepsilon_1}{\partial x^3} - \frac{\beta_N}{\rho c_s}\frac{\partial}{\partial x}(\varepsilon_1 + \varepsilon_2)^2 = g(\varepsilon_1 - \varepsilon_2) + \zeta \frac{\partial^2}{\partial x^2}(\varepsilon_1 - \varepsilon_2) + \mu \frac{\partial^4}{\partial x^4}(\varepsilon_1 - \varepsilon_2),$$
$$\frac{\partial \varepsilon_2}{\partial t} + \frac{\partial \varepsilon_2}{\partial x} + \beta_d \frac{\partial^3 \varepsilon_2}{\partial x^3} + \frac{\beta_N}{\rho c_s}(\varepsilon_1 + \varepsilon_2)^2 = g(\varepsilon_2 - \varepsilon_1) + \zeta \frac{\partial^2}{\partial x^2}(\varepsilon_1 - \varepsilon_2) - \mu \frac{\partial^4}{\partial x^4}(\varepsilon_1 - \varepsilon_2). \tag{6}$$

Here, the coefficient $g = q_\varepsilon K\Omega_j/\rho c_s^2$ and two coefficients $\zeta = \beta l^2$ and $\mu = Dl^2$ characterize the dissipation of the wave energy at low and high frequencies, respectively. The third term in the left of (6) describes the energy dispersion ($\beta_d = l^2(c_s^2 - c_\tau^2)/2$ is the dispersion coefficient). The nonlinear term proportional to $\varepsilon\varepsilon_x$ allows the redistribution of the energy between the low- and high-frequency oscillations.

It is seen from system (6) that the functions ε_1 and ε_2 represent two counterpropagating strain waves interacting with each other because of nonlinearity and dissipation.

Consider the evolution of the strain wave $\varepsilon_2 = \varepsilon(x, t)$, propagating from left to right along the x axis. It follows from (6) that

$$\frac{\partial \varepsilon}{\partial t} + c_s \frac{\partial \varepsilon}{\partial x} + \beta_d \frac{\partial^3 \varepsilon}{\partial x^3} + \frac{\beta_N}{\rho c_s}\frac{\partial}{\partial x}\varepsilon^2 = g\varepsilon - \zeta \frac{\partial^2 \varepsilon}{\partial x^2} + \mu \frac{\partial^4 \varepsilon}{\partial x^4}.$$

The energy flux density for the localized perturba-

tions is given by

$$\frac{d}{dt}\left(\int_0^\lambda (\varepsilon^2/2)dx\right) = -g\int_0^\lambda \varepsilon^2 dx + \zeta\int_0^\lambda \varepsilon_x^2 dx - \mu\int_0^\lambda \varepsilon_{xx}^2 dx. \quad (7)$$

Here, $E = \int_0^\lambda (\varepsilon^2/2)dx$ is the energy of the wave. Because of the smallness of the dissipation effects, we will consider nonlinear quasi-stationary modes described by a solution of Eqs. (6) that ignores strain field–defect interaction: $g = \zeta = \mu = 0$. In this case, system (6) is reduced to the Korteweg–de Vries equation allowing solutions in the form of stationary periodic (cnoidal) waves or solitary waves (solitons) [13]. Stationary periodic strain waves depending on the single traveling variable $z = x - Vt$ (V is the velocity of the nonlinear wave) are represented as [13]

$$\varepsilon(z) = -\frac{2a}{m^2}\left(1 - \frac{E(m)}{K(m)}\right) + 2a\,\mathrm{sn}^2[k_m z, m]. \quad (8)$$

Here, a is the amplitude; $r = m^2$ is the coefficient of harmonic distortion ($0 < r < 1$); $K(m)$ and $E(m)$ are the complete elliptic integrals of the first and the second kind, respectively; and $k_m(-\beta_N a/3\rho c_s\beta_d m^2)^{1/2} = k_0 a^{1/2}$ is the analog of the wave number for a nonlinear periodic wave. The amplitude a, coefficient m, and the period of the wave λ are related as $\lambda = \sqrt{-2\beta_d\rho c_s/\beta_N}\, mK(m)a^{-1/2}$.

If the amplitude tends to zero ($r \longrightarrow 0$), expression (8) describes a linear harmonic wave (the elliptic sine is changed to the trigonometric sine: $\mathrm{sn} = \sin x$). In the case of large amplitudes ($a \longrightarrow \infty$, $r \longrightarrow 1$), we are dealing with essentially nonlinear waves, which are close to solitons (the elliptic sine is changed to the hyperbolic tangent: $\mathrm{sn}(x, 1) = \tanh x$). Substituting Eq. (7) into Eq. (8), we arrive at

$$(3g_1 a^{1/2} + 4g_2 a)\frac{da}{dt} + 4g(g_1 a^{3/2} + g_2 a^2) + 4\zeta g_3 a^{5/2} + 4\mu g_4 a^{7/2} = 0, \quad (9)$$

where

$$g_1 = \frac{4}{k_0 m^2 \lambda^2}\int_0^{\lambda k_m} [-2(1 - E/K)\mathrm{sn}^2(y, m) + \mathrm{sn}^4(y, m)]dy,$$

$$g_2 = \frac{4\lambda}{m^4}\left(1 - \left(\frac{E(m)}{K(m)}\right)^2\right),$$

$$g_3 = \frac{16}{k_0\lambda^2}\int_0^{\lambda k_m} \mathrm{sn}^2(y, m)\mathrm{cn}^2(y, m)\mathrm{dn}^2 dy,$$

$$g_4 = \frac{16k_0^3}{\lambda^2}\int_0^{\lambda k_m} [(1 - 2\mathrm{sn}^2(y, m))\mathrm{dn}^2(y, m) - m^2\mathrm{cn}^2(y, m)\mathrm{sn}^2(y, m)]^2 dy.$$

For soliton-like waves (large amplitudes), the amplitude is given by the equation

$$\frac{3}{2}\frac{da}{dt} = -2ga + 7\frac{\beta_N\zeta}{\rho c_s\beta_d}a^2 - \frac{24\mu k_0^4}{\lambda^2}a^3. \quad (10)$$

We neglect the second and the third terms in the right-hand side in Eq. (10), since the energy dissipation at high frequencies is small for the characteristic values of the strain ($\varepsilon \le 10^{-4}$). Then, the amplitude of the nonlinear wave exponentially decays, $a = a_0\exp(-\gamma t)$, with the damping factor $\gamma = 4q_\varepsilon\Omega/3$. If the first two terms dominate, the solution of Eq. (10) is written as

$$a(t) = a(0)\left[e^{\frac{4}{3}q_\varepsilon\Omega t} - \frac{7\zeta\beta_N a(0)}{2\rho c_s\beta_d q_s\Omega}\left(e^{\frac{4}{3}q_\varepsilon\Omega t} - 1\right)\right]^{-1}.$$

In the general case, the amplitude varies according to a complex law and is given by the implicit formula

$$t(a) = \int_{a(0)}^{a} \frac{d\xi}{(21\beta_N\zeta/2\rho c_s\beta_d)\xi^2 - 3g\xi - (36\mu k_0^4/\lambda^2)\xi^3}.$$

From these expressions, we can conclude that the low-frequency (g) and high-frequency (ζ and η) losses affect the properties of the nonlinear waves in essentially different ways.

In the other limiting case ($a \longrightarrow 0$), the amplitude also exponentially decays but with another damping factor $\gamma \sim q_\varepsilon\Omega$, as follows from Eq. (10).

Thus, we obtained an equation describing the propagation of nonlinear localized waves of elastic strain in an elastic medium with allowance for the generation of nonequilibrium defects by external energy fluxes. This equation is a generalization of the well-known Korteweg–de Vries–Burgers equation [14]. Equations for the amplitude of the nonlinear waves were derived, and the damping factors were found.

Of great interest is the propagation of soliton-like solitary waves in a medium that contains clusters of point defects (vacancy voids, loops of interstitials, etc.). Nonlinear interaction of the solitary waves with the clusters can lead to a local increase in the temperature, thereby facilitating recombination processes. Recombination gives rise to local heating and strains in the medium. Investigation into the nonlinear interaction between the strain–temperature fields and lattice defects (both point defects and clusters) is not only of scientific importance. In particular, methods for defect detection in solids can be elaborated.

REFERENCES

1. Yu. K. Éngel'brekht and U. K. Nigul, *Nonlinear Strain Waves* (Nauka, Moscow, 1981).
2. A. M. Samsonov, G. V. Dreĭden, A. V. Porubov, and I. V. Semenova, Pis'ma Zh. Tekh. Fiz. **22** (21), 61 (1996) [Tech. Phys. Lett. **22**, 891 (1996)].
3. G. V. Dreĭden, Yu. I. Ostrovskiĭ, and A. M. Samsonov, Zh. Tekh. Fiz. **58**, 2040 (1988) [Sov. Phys. Tech. Phys. **33**, 1237 (1988)].
4. A. M. Samsonov *et al.*, Phys. Rev. B **57**, 5778 (1998).
5. M. Toda, *Springer Series in Solid State Science*, Vol. 20: *Theory of Nonlinear Lattices* (Springer-Verlag, Berlin, 1981).
6. L. M. Lyamshev, Usp. Fiz. Nauk **135**, 637 (1981) [Sov. Phys. Usp. **24**, 977 (1981)].
7. A. M. Kosevich, *Foundations of Crystal Lattice Mechanics* (Nauka, Moscow, 1972).
8. Yu. A. Bykovskiĭ, *Ion and Laser Implantation of Metals* (Énergoatomizdat, Moscow, 1991).
9. F. Mirzoev, V. Ya. Panchenko, and L. A. Shelepin, Usp. Fiz. Nauk **166**, 3 (1996) [Phys. Usp. **39**, 1 (1996)].
10. A. I. Lur'e, *Nonlinear Theory of Elasticity* (Nauka, Moscow, 1980).
11. A. M. Samsonov, Appl. Anal. **57**, 85 (1995).
12. A. M. Samsonov, Phys. Lett. A **245**, 527 (1998).
13. A. I. Potapov, *Nonlinear Strain Waves in Rods and Plates* (Gorki, 1984).
14. A. S. Davydov, *Solitons in Molecular Systems* (Naukova Dumka, Kiev, 1988; Kluwer, Dordrecht, 1991).

Translated by A. Chikishev

Technical Physics, Vol. 46, No. 8, 2001, pp. 956–961. Translated from Zhurnal Tekhnicheskoĭ Fiziki, Vol. 71, No. 8, 2001, pp. 27–32.

SOLIDS

The Use of a Metal–Insulator–Metal System for the Study of Structural Transitions in Metals

T. G. Zagurenko, V. M. Kornilov, and A. N. Lachinov

Institute of Physics of Molecules and Crystals, Ufa Scientific Center, Russian Academy of Sciences, Ufa, 450075 Bashkortostan, Russia

e-mail: lpp ipmc@anrb.ru

Received September 27, 2000

Abstract—The conductivity of a low-melting metal–polymer–metal system as a function of temperature is studied. A new technique for detecting structural modifications in metals is suggested. Experimental results are discussed within a model of charge instability, which occurs in thin polymer films when boundary conditions are changed. *© 2001 MAIK "Nauka/Interperiodica".*

INTRODUCTION

Diagnostics of structural modifications in metals is one of the hottest problems in metal science. The search for new methods in this field has always led to gaining new knowledge. In this paper, we present experimental results that might lay a foundation for a new technique to study structural modifications in metals.

Extensive research on solid–liquid phase transitions has shown that they are always accompanied by anomalies in physical properties both below the melting point and above the phase transition temperature (ΔT may exceed 100°C [1, 2]). The pre- and postmelting effects were apparently first revealed in [3]. At the stages of pre- and postmelting, heat capacity [4], as well as thermal conductivity and diffusivity [5], show anomalous behavior. These effects attend the melting of metals [6], insulators [7], and semiconductors [8]. To study the pre- and posttransition phenomena, researchers have to use sophisticated and expensive techniques, such as X-ray absorption [6], ellipsometry [9], precision thermography [8], etc. However, there are certain problems related, for example, with the effect of surface impurities or material contacts that are hard to tackle with these techniques.

In this paper, we consider the possibility of detecting structural modifications in metals near the melting temperature by measuring the current through the metal–insulator interface.

Our method measures the current passing through a metal 1–insulator–metal 2 (M_1–I–M_2) structure. A metal under study is M_1, while M_2 is a metal that does not undergo structural modifications in a given temperature range. As a rule, the injection mechanism of charge transfer dominates in such a system [10]. It should be stressed that charge transfer in our conditions does not cause structure modifications or breakdown of the insulator. The injection current depends on parameters of contacting materials such as the work function of the metals and the insulator, the space charge density in the insulator, the trap density in the insulator, the position of the traps in the forbidden gap, and so on. Many of these parameters are temperature-dependent; therefore, the injection current will also vary with temperature.

However, a change in the injection current due to structural transitions in metals is small in the linear approximation. To detect changes in the metal structure parameters, special conditions are needed. For example, if the properties of the insulator being in contact with the metal nonlinearly depend on the space charge density, the injection current can be substantially increased and, thus, reliably detected under the same conditions. A polymer (polyheteroarylene) film can be used as such an insulator. For some polymers of this type, a great nonlinear increase in the permittivity and conductivity at a minor increase in the free carrier concentration has been observed [11, 12].

EXPERIMENT

We used a planar metal–polymer–metal (M_1–P–M_2) structure (Fig. 1). Poly(phthalidylidenebiphenylilene) (PPB) was employed as a polymer. This polymer offers good film-forming properties when applied on metal substrates. It was shown [13] that PPB forms continuous homogeneous films of thickness 0.05–10 μm under certain process conditions. Also, this polymer shows no singularities in the temperature dependence of the conductivity up to the softening temperature (360°C in air). Finally, PPB is the most studied among the polymers where the high-conductivity state has been realized [14–16].

A polymer layer was applied on the electrode M_2 by spinning from a PPB solution in cyclohexanone. The sample thickness was varied in the range of 0.1–5 μm. The quality and the homogeneity of the polymer films

1063-7842/01/4608-0956$21.00

were inspected by the methods of optical, transmission electron, atomic force [17], and scanning tunneling microscopy (STM).

Low-melting metals, such as gallium, Wood alloy, indium, and tin, were used as M_1, since their melting points are lower than the polymer softening temperature. Polished electrodes made of the low-melting metals (M_1) were slightly forced against the polymer film to provide the electrical contact. A copper layer evaporatively deposited onto a polished glass plate was used as M_2.

The cell was placed into a heater where its temperature could be varied with a constant rate in the range from 20 to 350°C. The current through the cell was measured in a way typical of electrical circuits terminated by a load with *S*-type negative resistance. The schematic of the experimental setup is shown in Fig. 2.

EXPERIMENTAL RESULTS

The method allows two ways of detecting dynamical structural modifications in metals near the phase transition temperature: with or without using an electric field source.

1. Measuring circuit with an emf source. Temperature dependences of the current through the polymer film in the M_1–P–M_2 system are presented in Fig. 3 for different M_1 metals. Curves *1–4* correspond to gallium, Wood alloy, indium, and tin, respectively. The cell was heated at a constant rate. In Fig. 3, the sharp increase in the injection current is observed near the melting point of the electrode. Upon further heating, the system remains in the high-conductivity state. When cooled, the system recovers the initial dielectric state at the temperature that coincides with the solidifying point of metal M_1 within the measurement error.

Let us consider in detail the temperature dependence of the current through the M_1–P–M_2 system with indium as the M_1 electrode. At room temperature, the system is in the dielectric state. The resistivity of the polymer film is about 10 GΩ m, so that the current is small. The *I–V* characteristic of the sample is of an exponential form and can be explained in terms of the Frenkel–Pool effect [18], which is typical for charge transfer in insulators. Upon heating, the current through the system remains constant up to temperatures of 130–135°C. Above these temperatures, current fluctuations occur in the measuring circuit. Correspondingly, the voltage across the ballast resistor fluctuates within 1–10% of the applied voltage. The fluctuations persist up to the melting point of the upper electrode.

When the melting point of the M_1 electrode (indium, 156.2°C) is reached, the current in the measuring circuit jumps and the voltage almost entirely drops across the ballast resistor. The resistivity of the M_1–P–M_2 system decreases to 0.1–5 Ω m. In this case, the current through the system is maximal and is limited only by the ballast resistance.

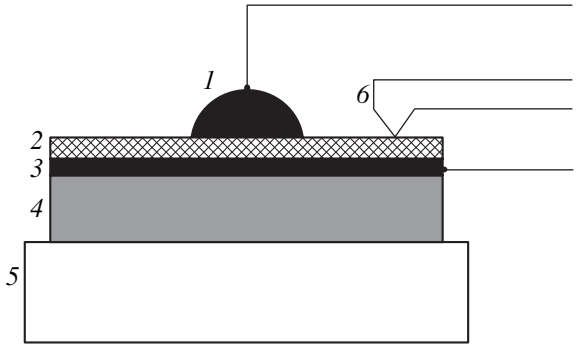

Fig. 1. Measuring cell: (*1*) upper electrode; (*2*) polymer film; (*3*) lower electrode; (*4*) glass substrate; (*5*) heater; and (*6*) thermocouple.

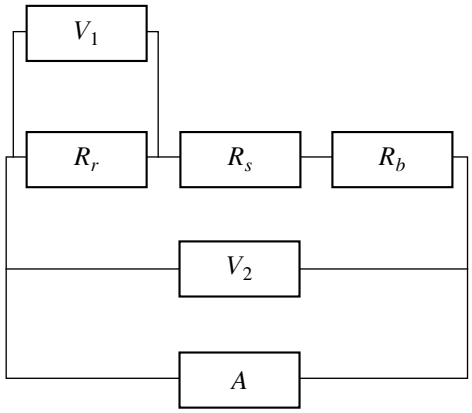

Fig. 2. Electrical circuit for temperature measurements and taking *I–V* characteristics. R_s, sample; R_r, reference resistor; R_b, ballast resistor; $V_{1,2}$, voltmeters; and *A*, power source. $R_s \gg R_r$, $R_s > R_b/100$.

A similar situation arises when gallium, Wood alloy, or tin are used as M_1. The difference is only in that the current singularities occur near the melting points of each of the metals: 29.75°C for gallium, 68°C for Wood alloy, and 232°C for tin.

In the highly conducting state, the temperature dependence of the system is of metallic character. The temperature coefficient of resistance (TCR) of the system is 3×10^{-3} K^{-1}, which coincides with the TCR of the electrodes within the measurement error. In our case, the temperature dependence of the polymer resistance is shadowed by those of the electrodes; however, it never is of activation character.

When the measuring cell is cooled, the current varies in the reverse manner. When the solidifying point of the M_1 electrode is reached, the current in the measuring circuit sharply drops. Sometimes, minor hysteresis was observed, apparently because of the inertia of the measuring cell. As the temperature decreases further,

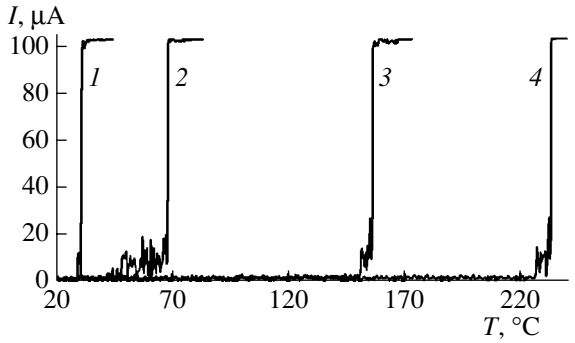

Fig. 3. Temperature dependence of the current through the polymer film for different M_1 metals. Film thickness is 1 μm; applied voltage, 5 V; and heating rate, 5 K/min.

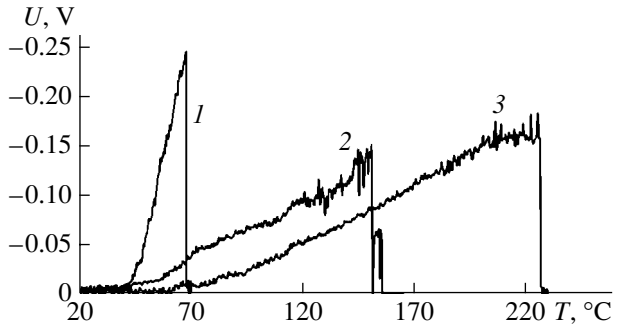

Fig. 4. The same as in Fig. 3 for the contact potential difference.

the current fluctuations appear again and finally the sample recovers the initial dielectric state.

The experimental results are best reproduced when the time between two sequential heating/cooling cycles is no less than 2 h. This may be evidence for the considerable relaxation time of the space charge in the polymer film, which results from injection from the electrode and is captured by long-living traps.

2. Measuring circuit without an emf source. In this case, the measuring circuit differs substantially from the one described above. Here, the state of the cell is monitored with an electrometer connected directly to the electrodes of the M–P–M system.

Typical temperature dependences of the contact potential difference (CPD) in the M_1–P–M_2 system are shown in Fig. 4, where curves *1–3* correspond to Wood alloy, indium, and tin, respectively, used as M_1. At room temperature, the polymer film is in the dielectric state. When it was brought into contact with M_1, a CPD due to the different work functions of the electrodes and the polymer arises. As the temperature grows, the CPD increases exponentially and stops rising 20–30°C below the electrode melting point, when low-frequency CPD fluctuations begin in the structure. Once the metal melting point has been reached, the CPD drastically decreases to the minimum level. The low-frequency oscillations disappear 20–30°C above the melting point.

When the cell is cooled to a temperature 20–30°C above the solidifying point, the low-frequency current oscillations appear again and persist to a temperature 20–30°C below the solidifying point. In this temperature range, the CPD starts growing. With a further decrease in the temperature, the CPD curve gradually converts to the curve corresponding to the heating cycle.

It seems that the nonexponential temperature dependence of the CPD and other temperature singularities also result from the enhanced density of the nonequilibrium space charge in the polymer film. The space charge builds up when the metal–polymer interface conditions change at temperatures that correspond to the pre- and postmelting effects.

The reproducibility of the results strongly depends on the time between sequential heating/cooling cycles. As in the case of the experiments with the field, the results are best reproduced for the time between the cycles no less than 2 h.

DISCUSSION

Let us explain the above phenomenon under the assumption that the injection mechanism dominates. Charge injection from a metal to a polymer under steady-state interface conditions has been studied for a long time [19–21]. According to [19], metal–polymer contacts are ohmic; i.e., the Fermi levels of the materials differ only slightly. This may favor the field injection of the charge to the polymer. In particular, the work function of PPB is about 4.2 eV [11, 22], which corresponds to the mean effective work function (EWF) of a contaminated metal surface.

For an ohmic contact, the distribution of the potential ψ over the polymer volume can be expressed as [23]

$$d\psi/dx = (2q^2 n_s kT/\varepsilon)^{1/2}\{\exp[-(\psi - \varphi_m + \chi)/kT] - \exp[-(\varphi - \varphi_m)/kT]\}^{1/2}, \quad (1)$$

where q is the electron charge; n_s is the surface charge density; k is the Boltzmann constant; T is temperature; ε is the permittivity; φ_m and φ are the EWF of the metal and the polymer, respectively; and χ is the electron affinity.

The residual (nonneutralized) charge in the polymer produces a surface charge of thickness z_0. According to [23], the surface charge density is given by

$$N = \varepsilon(\varphi - \varphi_m)/2\pi(ez_0)^2. \quad (2)$$

The amount and the penetration depth (thickness) of this charge depend on the work functions of the metal and the polymer, the acceptor–donor properties of the polymer, and other parameters of the contacting materials. The value of z_0 varies within the order of magni-

tude depending on the polymer type and the method of estimation [24, 25]. It lies in the range 0.1–3 μm, which is comparable to the polymer film thickness in our experiments. For simplicity, we shall assume that z_0 is constant.

It follows from Eq. (2) that a change in the charge dN in response to a temperature change dT can be expressed as

$$dN/dT \sim (\varphi - \varphi_m)d\varepsilon/dT + \varepsilon d(\varphi_m)/dT. \quad (3)$$

The current density in such a system has the form [26]

$$J = -N\mu d\psi/dx - eDdN/dx. \quad (4)$$

Here, μ is the carrier mobility in the polymer and D is the diffusion coefficient of carriers; the first term in the right of Eq. (4) determines the drift current component, while the second one defines the diffusion component.

Let us estimate the relative change in the charge dN/dT for the metal–polymer contact due to a change in the EWF when the electrode melts. We assume that the ε of the polymer is a weakly varying function of temperature in the range considered and neglect the first term in Eq. (3).

The EWF variation near the phase transition still remains unclear [27, 28]. In particular, it is unknown whether this parameter experiences a jump. We shall rely on the generally accepted fact that the EWF of metals is appreciably nonlinear at the phase transition, the more so as it was shown even in the early work [29] that a sharp change near the melting point is absent only for the true work function when the metal surface undergoes profound cleaning from impurities. It is also known that, near the temperature of structural modifications, the presence of an impurity layer contacting with the metal surface affects the metal emissivity [29–32].

Now we will take advantage of the dependence $\varphi(T)$ [33] to estimate the relative change in the charge density dN/N for the In–PPB contact. In [33], this dependence was obtained for the continuously varying temperature, i.e., under conditions similar to ours for taking the $I(T)$ curve. According these data, the EWF of indium (φ_{In}) increases with temperature and peaks (≈4.1 eV) at the melting point (T_{melt}). A further increase in the temperature leads to a sharp decrease in the EWF of the indium electrode. The drop of φ_{In} at T_{melt} is about 0.1 eV, which corresponds, according to Eq. (3), to $dN/N \approx 80\%$. Obviously, for an initial charge carrier density of 10^{11}–10^{12} cm^{-3} [17], such a value of dN/N is insufficient for the high-conductivity state to set in the polymer.

Apparently, to account for the effect, additional information should be invoked. In particular, it is known that conduction in thin polymer films is essentially anisotropic. Charge transfer is effective only in the direction perpendicular to the film surface along the so-called channels. The channel density has been estimated at 10^4–10^5 cm^{-2}, while the mean diameter, at about 100 nm [34]. Moreover, it has been found [35] that, in the pretransition region under nonsteady heating, the space charge density of the polymer increases by 400–500% of the initial value at room temperature. If it is remembered that the conductivity changes only in the conducting channels, rather than all over the volume of the polymer film, it is natural to assume that a change in the charge carrier density is maximum just in these channels, where it may be as high as 10^{20}–10^{21} cm^{-3}. Then, the 80% increase in the density directly at the melting point takes place not relative to the equilibrium room-temperature value but relative to the nonequilibrium density attained in the vicinity of the melting point. Obviously, such a substantial rise in the surplus charge may considerably enhance the conductivity and cause the highly conducting state in the system.

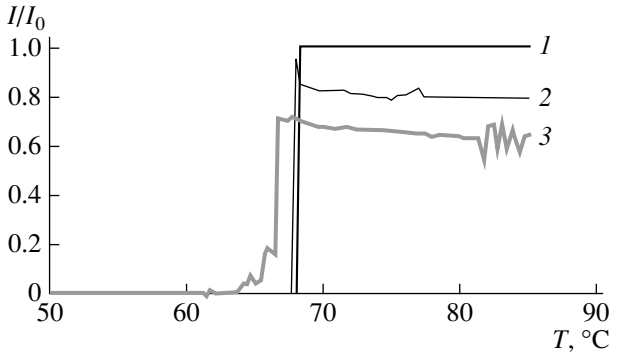

Fig. 5. Temperature dependence of the current through the polymer film at applied voltages (*1*) 5, (*2*) 3, and (*3*) 1.5 V. M_1, Wood alloy; film thickness, 1 μm; and heating rate, 5 K/min.

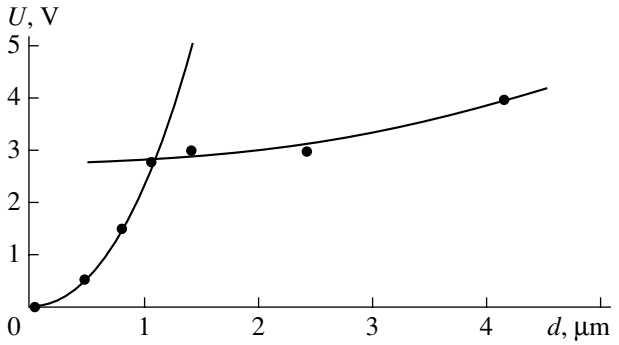

Fig. 6. Threshold voltage vs. thickness of the polymer film. M_1, Wood alloy; heating rate, 8 K/min.

It follows from the aforesaid, in particular, from Eq. (4), that the injection processes play a major part in the low-to-high conductivity state (LCS-to-HCS) transition. We studied the current vs. voltage dependence in the M_1–P–M_2 system. It was found that there exists a switching voltage threshold (U_{th}) below which the polymer remains in the LCS throughout the tempera-

ture range. Near U_{th}, the transition to the HCS is unstable (Fig. 5). Moreover, in this case, for $T > T_{melt}$, the transition to the HCS is not complete.

The values of U_{th} obtained are in fairly good agreement with the threshold voltages for electroluminescence (recombination radiation) [36]. This correlation suggests that U_{th} corresponds to the beginning of double injection. In polymers, intrinsic charge carriers are usually holes; hence, the current singularities are due to electron injection.

The dependence of the threshold voltage on the polymer thickness (Fig. 6) sheds more light on the role of injection in initiating the HCS. The curve has two clear-cut regions separated by the inflection point $d_{th} \approx 1$ μm. Both regions are well approximated by the relationship

$$U_{th}(d) = kd^n, \quad (5)$$

where $n \approx 2$. The coefficient k equals 2.35 for $d_{th} < 1$ μm and ≈0.06 for $d_{th} > 1$ μm.

Such dependences are typical of the injection mechanism. In particular, the voltage at which double injection starts can be defined as [23]

$$U(d) = C\mu^{-1}\tau^{-1}d^n, \quad (6)$$

where μ and τ are the electron mobility and lifetime, respectively, and C is the model coefficient.

Physically, the point of inflection apparently means the penetration depth of the surface charge. It should be noted that the value of d_{th} obtained is in good agreement with the early theoretical estimate for this polymer [17].

As the polymer film thickness increases, the factor k in Eq. (5) changes. In view of Eq. (6), this means a change in either the electron mobility or the lifetime. It is known [19] that there are two, bulk and surface, charging mechanisms in submicron polymer films. Switching from one mechanism to the other occurs as the film thickness increases. The reason is the overlap of surface charge clouds, which is possible at a thickness less than the penetration depth of the surface charge. In this case, image forces between the surface charge and the opposite electrode play an important part. As the thickness increases, the charges are "localized" near their associated electrodes and the middle part of the film becomes depleted. The depleted region prevents the interpenetration of the surface charges. This has been clearly demonstrated in [21]. In terms of this approach, the decrease in the factor k in Eq. (5) may imply the increase in the electron lifetime, since the increase in the mobility can hardly be expected in this case.

Thus, we showed that the use of a thin polymer film like PPB in a M–P–M structure allows one to study surface modifications in metallic electrodes due to structural transitions in the electrodes. The advantages of this method are high sensitivity, simplicity, high reproducibility, and reliability. This technique cannot yet be used for quantitatively describing changes in the metal parameters near the temperatures of structure modifications. Melting is a particular case of phase transitions in materials; however, this technique can be applied to detecting structure modifications in metals. For example, structure modifications in nanocrystalline metals have been revealed by a similar method in [10].

REFERENCES

1. J. W. M. Frenken, P. M. J. Maree, and J. F. van der Veen, Phys. Rev. B **34**, 7506 (1986).
2. W. Theis and K. Horn, Phys. Rev. B **51**, 7157 (1995).
3. A. R. Ubbelonde, Trans. Faraday Soc. **34**, 29 (1938).
4. E. B. Amitin, Yu. F. Minenkov, O. A. Nabutovskaya, and I. E. Paukov, Zh. Éksp. Teor. Fiz. **89**, 2092 (1985) [Sov. Phys. JETP **62**, 1207 (1985)].
5. V. E. Zinov'ev, V. F. Polev, S. G. Taduts, and P. V. Gel'd, Fiz. Tverd. Tela (Leningrad) **28**, 2914 (1986) [Sov. Phys. Solid State **28**, 1639 (1986)].
6. E. A. Stern and Ke Zhang, Phys. Rev. Lett. **60**, 1872 (1988).
7. L. A. Bityutskaya and E. S. Mashkina, Pis'ma Zh. Tekh. Fiz. **21** (17), 85 (1995) [Tech. Phys. Lett. **21**, 763 (1995)].
8. L. A. Bityutskaya and E. S. Mashkina, Pis'ma Zh. Tekh. Fiz. **21** (18), 8 (1995) [Tech. Phys. Lett. **21**, 728 (1995)].
9. K. Dolecki, K. Polanski, and L. Wojtczak, Bull. Soc. Sci. Lett. Lodz, Ser. Rech. Deform. **18**, 119 (1995).
10. A. N. Lachinov, T. G. Zagurenko, V. M. Kornilov, *et al.*, Fiz. Tverd. Tela (St. Petersburg) **42**, 1882 (2000) [Phys. Solid State **42**, 1935 (2000)].
11. A. N. Lachinov, A. Yu. Zherebov, and M. G. Zolotukhin, Synth. Met. **59**, 377 (1993).
12. V. M. Kornilov and A. N. Lachinov, Pis'ma Zh. Éksp. Teor. Fiz. **61**, 902 (1995) [JETP Lett. **61**, 921 (1995)].
13. J. R. Rasmusson, Th. Kugler, R. Erlandsson, *et al.*, Synth. Met. **76**, 195 (1996).
14. A. Yu. Zherebov and A. N. Lachinov, Synth. Met. **44**, 99 (1991).
15. A. N. Lachinov, A. Yu. Zherebov, and V. M. Kornilov, Synth. Met. **44**, 111 (1991).
16. A. N. Lachinov, A. Yu. Zherebov, and V. M. Kornilov, Zh. Éksp. Teor. Fiz. **102**, 187 (1992) [Sov. Phys. JETP **75**, 99 (1992)].
17. V. M. Kornilov and A. N. Lachinov, Zh. Éksp. Teor. Fiz. **111**, 1513 (1997) [JETP **84**, 833 (1997)].
18. G. A. N. Conell, D. L. Camphausen, and W. Paul, Philos. Mag. **26**, 541 (1972).
19. J. G. Simmons, J. Phys. Chem. Solids **32**, 2581 (1971).
20. T. J. Fabish, H. M. Saltsburg, and M. L. Hair, J. Appl. Phys. **47**, 930 (1976).
21. C. B. Duke and N. J. Fabish, Phys. Rev. Lett. **37**, 1075 (1976).
22. C. R. Wu, N. Johansson, A. N. Lachinov, *et al.*, Synth. Met. **67**, 125 (1994).
23. K. C. Kao and W. Hwang, *Electrical Transport in Solids* (Pergamon, Oxford, 1981; Mir, Moscow, 1984), Vols. 1, 2.

24. A. G. Lipson, E. V. Kuznetsova, D. M. Sakov, and Yu. P. Toporov, Poverkhnost, No. 12, 74 (1992).
25. S. A. Nenakhov, G. I. Shcherbina, A. E. Chalykh, and V. M. Muller, Poverkhnost, No. 3, 77 (1994).
26. P. R. Emtage and J. J. O'Dwyer, Phys. Rev. Lett. **16**, 356 (1996).
27. R. E. Vas'kov, A. F. Vladimirov, E. N. Moos, and N. I. Tabunov, Izv. Ross. Akad. Nauk, Ser. Fiz. **62**, 2044 (1998).
28. B. B. Alchagirov, Kh. B. Khokonov, and R. Kh. Arkhestov, Dokl. Akad. Nauk **326**, 121 (1992).
29. V. G. Bol'shov and L. N. Dobretsov, Dokl. Akad. Nauk SSSR **98**, 193 (1954).
30. V. S. Fomenko, *Emission Properties of Materials* (Naukova Dumka, Kiev, 1981).
31. J. Vancea, G. Reiss, D. Butz, and H. Hoffmann, Europhys. Lett. **9**, 379 (1989).
32. J. Ameiser, Z. Phys. **69**, 111 (1931).
33. B. B. Alchagirov, Kh. Kh. Kalazhokov, and Kh. B. Khokonov, Izv. Akad. Nauk SSSR, Ser. Fiz. **52**, 2463 (1991).
34. O. A. Skaldin, A. Yu. Zherebov, A. N. Lachinov, *et al.*, Pis'ma Zh. Éksp. Teor. Fiz. **51**, 141 (1990) [JETP Lett. **51**, 159 (1990)].
35. T. G. Zagurenko, V. M. Kornilov, and A. N. Lachinov, Zh. Tekh. Fiz. **69** (3), 85 (1999) [Tech. Phys. **44**, 345 (1999)].
36. V. A. Antipin, I. L. Valeeva, and A. N. Lachinov, Pis'ma Zh. Éksp. Teor. Fiz. **55**, 526 (1992) [JETP Lett. **55**, 545 (1992)].

Translated by M. Astrov

Technical Physics, Vol. 46, No. 8, 2001, pp. 962–967. Translated from Zhurnal Tekhnicheskoĭ Fiziki, Vol. 71, No. 8, 2001, pp. 33–38.

SOLIDS

Generation and Accumulation of Dislocations on the Silicon Surface under the Action of Pulse–Periodic Emission from a YAG : Nd Laser

A. F. Banishev, V. S. Golubev, and A. Yu. Kremnev

Institute of Problems of Laser and Information Technologies, Russian Academy of Sciences, Shatura, Moscow oblast, 140700 Russia

Received September 26, 2000

Abstract—Solid-phase damage of the silicon surface due to the generation and accumulation of dislocations is studied. The dislocations are generated under the pulse–periodic action of a YAG : Nd laser. The number of laser pulses that causes surface damage vs. power density and pulse repetition period is derived. A mechanism responsible for the generation and accumulation of the dislocations at the surface is suggested. *© 2001 MAIK "Nauka/Interperiodica".*

Intense laser emission is widely used in microelectronics and optoelectronics for processing semiconducting materials [1, 2]. Examples are laser annealing, amorphization, recrystallization, and application of the films. It is known that laser pulses acting on the surface of solids may generate lattice defects at the surface, such as vacancies and interstitials [3, 4]. Their concentration may increase several-fold in comparison with the initial value and become as high as 10^{19}–10^{21} cm^{-3}. Such considerable defect concentrations uncontrollably affect the result of laser processing and make the production of a material with given properties impossible. In addition, the defects deteriorate the properties of the surface. Therefore, there is a need for finding mechanisms and conditions for defect generation under laser action.

Mechanisms of laser-induced defect generation depend on irradiation conditions. Below the melting point of a solid, the point defects are generated via an electron–deformation–thermal mechanism [4, 5]. Its essence is as follows. Laser emission excites the electron subsystem and increases the free carrier concentration at the surface. When the electrons pass to the excited state, the energy of defect formation diminishes. Moreover, the relaxation of the energy of the excited states causes lattice heating. The nonuniform distribution of the electrons excited and lattice heating result in the deformation of the surface layer. This triad—local excitation of electrons, heating, and deformation—is responsible for an increase in the defect generation rate according to the expression

$$\frac{\partial n}{\partial t} \sim \exp\left(-\frac{E_0 - E_e - \Theta_d \xi}{k_B(T_0 + \Delta T)}\right).$$

Here, n is the concentration of the point defects, E_0 is the initial energy of defect formation, E_e is the energy of local electron excitation, ξ is the strain, Θ_d is the deformation potential, and ΔT is a temperature increment due to laser heating.

As the concentration of the point defects grows (up to 10^{19}–10^{21} cm^{-3}), the interaction between their elastic strain fields becomes more and more pronounced. It may be a reason for collective (correlation) effects. This, in turn, results (under certain conditions) in the formation of periodic defect structures or extended defects (pores or dislocation loops), if the formation threshold of the latter is overcome [6, 7]. When the extended defects combine to produce dislocation or pore clusters, microcracks, which initiate surface damage below the melting point, may originate. Another factor associated with defects is a change in the surface absorptivity. As a rule, the absorptivity of the defect part of the surface rises, the larger the defects (pores, dislocations, and microcracks), the greater the rise. Thus, laser emission uncontrollably changes the temperature in the vicinity of these defects.

It is the aim of this article to study the generation and accumulation of defects at the surface of single-crystal silicon subjected to short laser pulses with a subthreshold power $I < I_m$, where I_m is the threshold of surface melting. Solid-phase damage of the silicon surface because of the accumulation of dislocations is considered. The critical number N_c of pulses (the least number of pulses that causes surface damage) vs. power density I and pulse repetition period τ is obtained.

EXPERIMENTAL SETUP

An experimental setup is depicted in Fig. 1. A mirror-surface single-crystal Si(100) sample 0.5 mm thick was placed into a vacuum chamber kept at a pressure of $\approx 10^{-2}$ torr. Low-pressure conditions prevent the effect

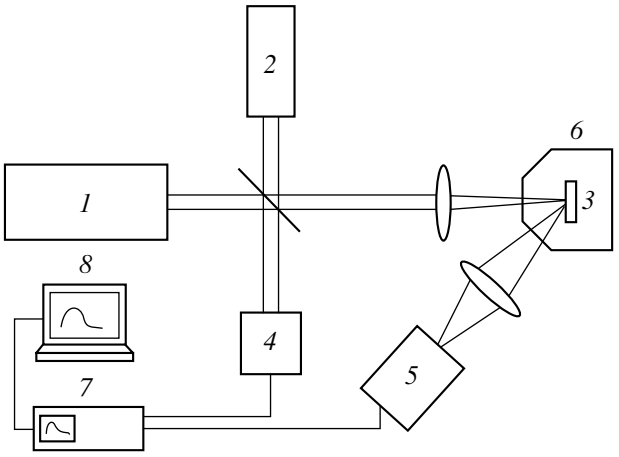

Fig. 1. Experimental setup: (*1*) YAG : Nd^{3+} laser; (*2*) He–Ne laser; (*3*) sample; (*4*) photodetector; (*5*) monochromator; (*6*) vacuum chamber ($p \approx 10^{-2}$ torr); (*7*) oscilloscope; and (*8*) PC.

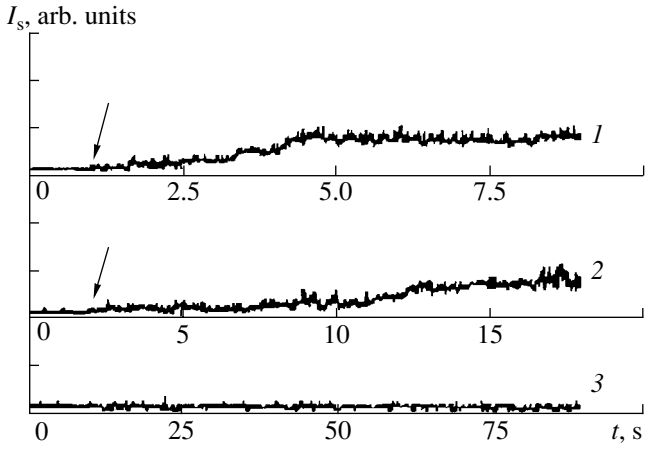

Fig. 2. Typical variations of the scattering intensity of the probing radiation during the pulse–periodic laser action on the surface. $I = 3.4 \times 10^{10}$ W/m^2, τ = (*1*) 50, (*2*) 100, and (*3*) 200 ms.

of oxidation on the surface damage. The sample was subjected to short pulses ($\tau_p \approx 3 \times 10^{-7}$ s, $E_p \approx 0.5$–1.2 mJ) of unpolarized radiation from a YAG : Nd^{3+} laser. The radiation was focused into a spot of radius $r_s = 0.3$–0.6 mm. The damage was monitored by probing with a beam of a He–Ne laser. The scattered radiation of the He–Ne laser was detected at an angle of 45° to the surface with a monochromator and an FÉU-79 photoelectric multiplier. Signals to be studied were applied to an S9-8 oscilloscope and then to a PC.

After the laser action, the surface was examined with an optical microscope and then processed in a selective etchant that reveals dislocations on the silicon surface [8]. After etching, the sample was examined in the optical microscope again.

EXPERIMENTAL RESULTS

The power density of the pulses was $I = (2.5–3.4) \times 10^{10}$ W/m^2. Figure 2 shows typical variations of the scattered intensity of the probing laser when the pulses of the YAG : Nd^{3+} laser damaged the surface. The time instant when the scattered radiation started to grow (marked by arrows) was taken as the time to damage Δt. The upper bound of I was defined as the surface melting threshold, $I < I_m$. The lower bound depended on the recording time, since the time to damage Δt rapidly extended with decreasing I.

Figure 3 demonstrates the images of the samples processed in the etchant after being subjected to laser pulses with $I \approx 2.8 \times 10^{10}$ W/m^2 and $\tau \approx 20$ ms. Etch pits are sites where dislocations reach the surface. Early dislocations are seen to appear within ≈10 s after irradiation. For our irradiation conditions, this corresponds to $N_d(I, \tau) \approx 500$ pulses (N_d is the least number of the pulses after which dislocations emerge). The dislocation density grows with irradiation time, and their distribution over the surface is random. The scattered intensity of the probing beam increases within $\Delta t \approx 20$ s after the beginning of irradiation, i.e., after the application of $N_c \approx 1000$ pulses. By this time, the dislocation density reaches 10^{10}–10^{11} m^{-2}.

The critical number of the pulses N_c vs. their repetition period τ for different I is shown in Fig. 4. The value of N_c was defined as $N_c = \Delta t/\tau$, where Δt is the averaged (over ten measurements) time delay of the growth of the scattered radiation. From the $N_c = N(I, \tau)$ curves, one can determine (for each of I) the upper limit of τ_l, above

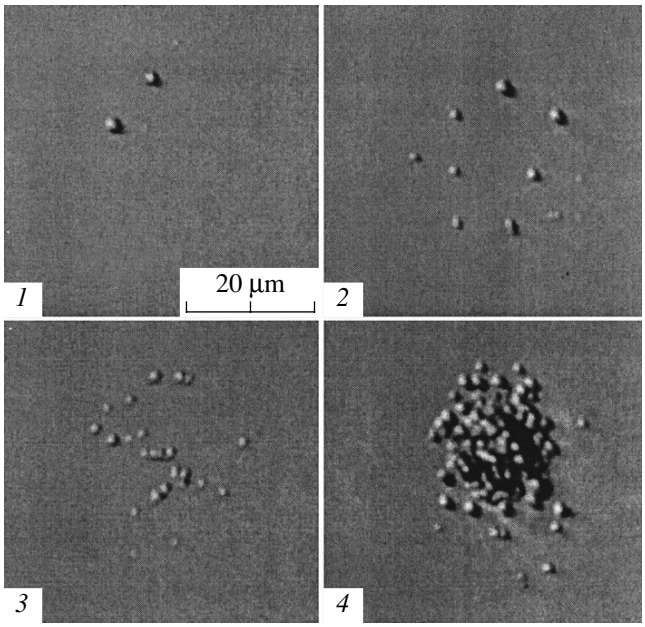

Fig. 3. Micrograph of the surface after irradiation and etching. The irradiation time is (*1*) 10, (*2*) 20, (*3*) 50, and (*4*) 100 s.

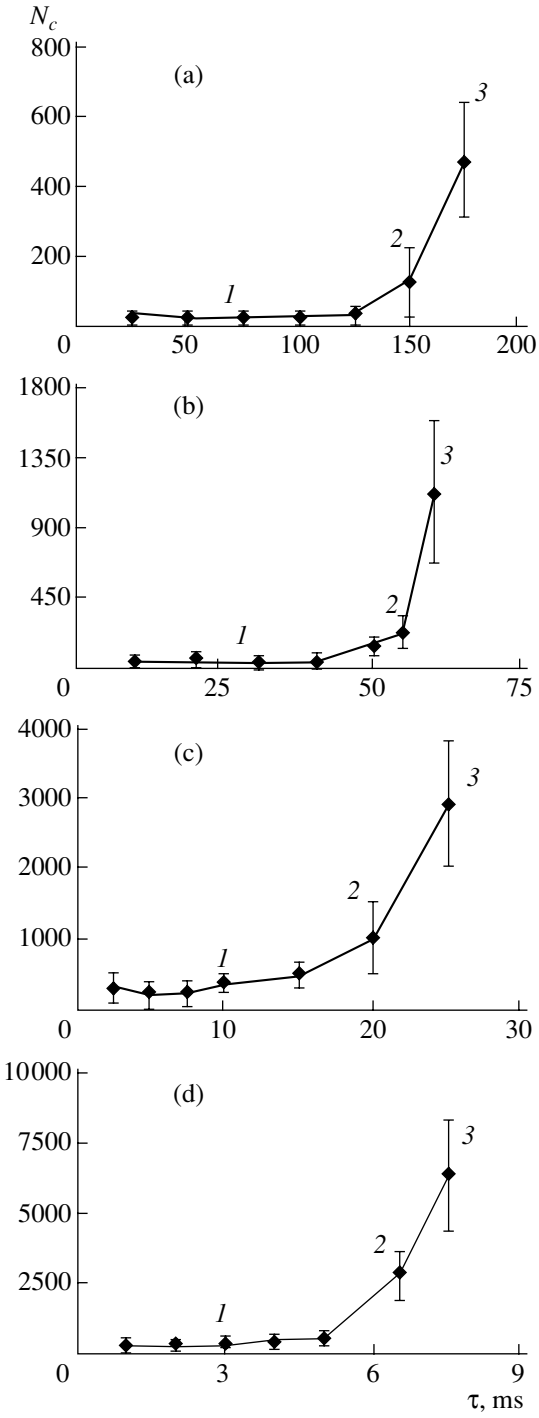

Fig. 4. Critical number of pulses N_c vs. power density I and pulse repetition period τ. I = (a) 3.4×10^{10}, (b) 3.1×10^{10}, (c) 2.8×10^{10}, and (d) 2.5×10^{10} W/m^2; τ_s = (a) 100, (b) 40, (c) 10, and (d) 4 ms; τ_l = (a) 175, (b) 60, (c) 25, and (d) 8 ms.

which ($\tau > \tau_l$) the surface remains intact (for example, at $I = 3.4 \times 10^{10}$ W/m^2 and $\tau = 200$ ms, the surface remained intact after 5 min of irradiation; therefore, one can put by convention Δt and $N_c \longrightarrow \infty$) and also its lower limit, τ_s, below which N_c is virtually independent of τ. Thus, three regimes of laser irradiation where the surface is damaged in different ways can be distinguished (Fig. 4). (1) $\tau \le \tau_s(I)$, high-frequency regime. Here, at a given I, we have $N_c \approx \Delta t/\tau \approx$ const; i.e., the number of pulses to damage the surface is $N_c(I)$, this number being independent of τ; (2) $\tau_s(I) \le \tau \le \tau_l(I)$; the critical number of pulses depends on τ ($N_c(I, \tau)$ grows with τ); and (3) $\tau > \tau_l(I)$, low-frequency regime. The surface remains intact, and no dislocations are revealed after etching and subsequent examination in the microscope. As is seen in Fig. 4, N_c rapidly drops with increasing I and equals only $N_c = 20$–40 for $I = 3.4 \times 10^{10}$ W/m^2 and $\tau \le 100$ ms. As I approaches the melting threshold of the surface ($I_m \approx 3.6 \times 10^{10}$ W/m^2), melting occurs prior to solid-phase damage due to the generation of dislocations. After the surface had been subjected to individual shots with I close to I_m, no dislocations were observed at the sample surface.

DISCUSSION

According to the aforesaid, short laser shots with I up to the melting threshold I_m do not generate dislocations in the surface layer. At the same time, long shots with $I < I_m$ generate individual dislocations or even dislocation structures. The authors of [6, 9–11] observed dislocation structures when they applied millisecond laser pulses and continuous radiation with a subthreshold power density. As follows from estimates, the application of short laser pulses with $2.6 \times 10^{10} \le I \le 3.4 \times 10^{10}$ W/m^2 raises the surface temperature and thermal stresses to

$$T_s \approx \frac{2IA}{\lambda}\left(\frac{\chi\tau_p}{\pi}\right)^{1/2} \approx 1300\text{–}1670 \text{ K},$$

$$\sigma_s \approx \frac{\alpha G \Delta T}{1-\mu} \approx (4\text{–}5) \times 10^8 \text{ N/m}^2.$$

Here, $\lambda \approx 66$ W/m, K is the thermal conductivity, $\chi \approx 0.32 \times 10^{-4}$ m^2/s is the thermal diffusivity, $\alpha \approx 4 \times 10^{-6}$ K^{-1}, $G \approx 0.66 \times 10^{11}$ N/m^2, $\mu \approx 0.2$, and $A \approx 0.74$ is the absorption factor.

As a result, the surface temperature exceeds the brittle-to-ductile transition temperature of silicon (according to [6], silicon becomes ductile at $T \ge 800$ K); hence, thermal stresses must plastically deform the material with the formation of dislocations. However, dislocations do not appear when short pulses are applied. This indicates that the formation of dislocations considerably depends on the pulse duration τ_p. One can suggest that the number and the size of dislocations (dislocation loops) vary as τ_p and that only large dislocations (of size greater than the thickness of the surface layer etched) are revealed by etching. If we assume that the thickness of this layer is roughly equal to the maximal size of the etch pits d ($d \approx 0.5$–1 μm in our experiments), then the size of the dislocations resulting under the action of a short pulse is less than 1 μm. As the num-

ber of pulses k increases, the dislocations grow and their size R_k (R_k is the radius of a dislocation loop after the application of k pulses) reaches $R_k \approx d = 0.5$–1 μm at $N_d < k < N_c$. Recall that both N_d and N_c depend on I and τ. It should be noted that the functions $N_d(\tau)$ and $N_c(\tau)$ do not depend on the rise in the temperature from pulse to pulse, since the time interval between the pulses is much greater than the time of surface cooling.

Qualitatively, the origination and growth of dislocations with increasing number of pulses can be explained as follows. During a pulse, a thin surface layer of thickness $h \sim (\chi\tau_p)^{1/2} \approx 3 \times 10^{-6}$ m is heated, and point defects of concentrations up to $n \sim 10^{25}$–10^{27} m^{-3} are generated. Concentration and thermal stresses initiate the growth of dislocations. Within the time between pulses, the temperature rapidly drops to its initial value and the concentration of the defects diminishes because of recombination, diffusion, and drainage; as a result, the growth of dislocations is terminated and the reverse (relaxation) process starts. The competition between the growth and relaxation of the dislocations eventually causes surface damage. The experimental $N_c = N_c(I, \tau)$ curves (Fig. 4) and the observations of the laser-processes surface in the microscope lead to the following conclusions.

(1) There exists a correlation between the concentration n of point defects and the dislocation size R_k.

(2) During the kth laser pulse, the dislocation size increases by ΔR_k, whereas within the time between pulses, the size decreases (a dislocation relaxes). We have $(R_k - R_{k0}) \approx (R_k^+ - R_{k0})\exp(-\tau/\tau_0)$, where τ_0 is the time constant of dislocation relaxation, R_k^+ is the dislocation size by the end of the kth pulse, $R_{k0} \approx R_k^+ \exp(-\tau_r/\tau_0)$ is the residual dislocation size after the pulse ceases, and τ_r is the relaxation time.

Let us assume that a dislocation absorbs a point defect when the latter is at a distance less than r_c from the dislocation core. Then, for the growth rate $V_k(n, T)$ of the radius R_k of a dislocation loop due to absorption of point defects, we can write

$$V_k = \frac{dR_k}{dt} \approx 2a^2 r_c J, \tag{1}$$

where a is the interatomic distance in silicon and J is the resulting flux of defects.

As follows from (1), the growth rate of dislocations depends on J and does not depend on R_k. During the kth pulse, the increment of the dislocation size is

$$\Delta R_k = \int_0^{\tau_p} V_k dt.$$

Hence, we can assume that ΔR_k is also independent of R_k and pulse no.; that is, $\Delta R_k \approx \Delta R$.

In view of the above assumptions, the dislocation size at the end of the kth pulse is given by

$$R_k^+ \approx \Delta R \sum_{p=0}^{k-1} \left[\exp\left(-\frac{\tau_r}{\tau_0}\right) + \exp\left(-\frac{\tau}{\tau_0}\right) - \exp\left(-\frac{\tau_r + \tau}{\tau_0}\right) \right]^p. \tag{2}$$

To find ΔR, we evaluate the flux J of vacancies during a pulse (for interstitials, the procedure is similar).

Since our experiment meets the condition $r_s/h \gg 1$, we can hereafter consider a one-dimensional flux $J(z, t)$ directed along the coordinate z normally to the surface. Basically, the flux is the sum of three components [3, 4]:

$$J = j_1 + j_2 + j_3, \tag{3}$$

where

$$j_1 = -D\frac{dn}{dz}, \quad j_2 = -\frac{2(1+\mu)G(\Delta\Omega)^2}{3(1-2\mu)}\frac{Dn}{k_B T}\frac{dn}{dz}, \quad j_3 = \frac{4(1-\mu^2)G\Delta\Omega\alpha}{3(1-2\mu)^2}\frac{Dn}{k_B T}\frac{dT}{dz}. \tag{4}$$

Here, $n(z, t)$ is the concentration of vacancies, $D(z, t)$ is the diffusion coefficient, G is the shear modulus, μ is Poisson's ratio, α is the coefficient of thermal expansion, $\Delta\Omega = (0.3$–$0.6)a^3$ is the dilatation ($\Delta\Omega < 0$ for vacancies), and k_b is the Boltzmann constant. The flux j_1 is due to the vacancy concentration gradient (normal diffusion) and is directed inward to the sample. The flux j_2 is the additional vacancy flux arising when the strain due to the concentration gradient is taken into account (it is directed toward the surface). Finally, the vacancy flux j_3 is due to the temperature gradient and is directed toward the surface.

Let us evaluate the increment ΔR of the dislocation loop during a laser pulse. We assume that the concentration of vacancies within the pulse duration is

$$n(z, t) = n_0 \exp\left[\frac{-E}{k_b T(z, t)}\right],$$

where $E \approx E_0 - (E_e + E_t + E_n)$. Here, E_0 is the initial energy of vacancy formation, E_e is the increment in the vacancy energy due to the generation of electron–hole pairs, E_t is the increment due to a rise in the temperature, and E_n is the increment due to a rise in the concentration. The energy E, the renormed energy of formation of vacancies, is a complex function of fast-varying parameters: temperature, concentration, and electron excitation. For silicon subjected to short laser pulses, the value of E was estimated at $E \approx 1$ eV [4]. Substituting the expression

$$\frac{dn}{dz} = \frac{nE}{k_b T^2}\frac{dT}{dz} \approx \frac{nE\Delta T}{k_b T^2 h}$$

($\Delta T = T - T_0$) into Eqs. (4), we obtain

$$\Delta R \approx 2a^2 L_c \int_0^{\tau_p} (j_1 + j_2 + j_3)dt, \qquad (5)$$

where

$$j_1 = -\frac{DnE}{k_b T^2}\frac{\Delta T}{h}, \quad j_2 = \frac{2(1+\mu)G(\Delta\Omega)^2}{3(1-2\mu)}\frac{Dn^2 E}{k_b^2 T^3}\frac{\Delta T}{h},$$

$$j_3 = \frac{4(1-\mu^2)G\Delta\Omega\alpha}{3(1-2\mu)^2}\frac{Dn}{k_b T}\frac{\Delta T}{h},$$

$$D = D_0 \exp\left(-\frac{E_m}{k_b T}\right), \quad n = n_0 \exp\left(\frac{-E}{k_b T}\right).$$

Rearranging the expression for $T(r, t)$ from [12] for the one-dimensional case, we come to

$$T(z, t) = \frac{2AI}{c\rho}\int_0^t f(\tau^*)\frac{\exp\left[\frac{-z^2}{4\chi(t-\tau^*)}\right]}{[4\pi\chi(t-\tau^*)]^{1/2}}d\tau^*, \qquad (6)$$

where

$$f(\tau) = K\left(\frac{\tau^*}{\tau_p}\right)^b \exp\left(\frac{-\tau^*}{\tau_p}\right)^c$$

is the pulse shape.

We obtained $K = 12.5$, $b = 1$, and $c = 3$ by fitting to the actual pulse shape and also by fitting $T(z, t)$ calculated from (6) for $I \approx I_m$ (I_m is the experimentally found surface melting threshold) to the known melting point T_m. To find ΔR from (5) is a challenge, since D and n depend on the temperature, which varies during a pulse. Therefore, we used computer methods to evaluate ΔR. Substituting $I = 3.4 \times 10^{10}$ W/m^2, $D_0 = a^2\nu_D$ ($a = 5.4 \times 10^{-10}$ m and $\nu_D = 2 \times 10^{13}$ s^{-1} is the Debye frequency), $E_m = 0.33$ eV (energy of vacancy migration [13]), $E = 1$ eV, $n_0 = 5 \times 10^{28}$ m^{-3}, $T_0 = 300$ K, $h = 3 \times 10^{-6}$ m, $\Delta\Omega = (0.3–0.6)a^3$ [14], and $k = 1.38 \times 10^{-23}$ J/K into (4) for $z = 0–10^{-6}$ m, we obtain $\Delta R = (12–0.2)r_c$. If the condition for the absorption of a vacancy by a dislocation is assumed to be $U_{\text{def}}(r_c) \approx E_m$, where

$$U_{\text{def}}(r_c) \approx \frac{(1+\mu)G\Delta\Omega a}{5\pi(1-\mu)r_c}$$

is the increase in the energy of a vacancy in the deformation field of the dislocation, then $r_c \approx 5 \times 10^{-9}$ m; hence, $\Delta R = (60–1) \times 10^{-9}$ m.

The estimates were made for I near the surface melting threshold. However, even in this case, $\Delta R \ll 1$ μm during a pulse. Moreover, ΔR rapidly decreases with increasing distance to the surface, as follows from the estimates.

Now let us evaluate the size of arising dislocations using expressions (2) and (5) and the experimental curves (Fig. 4).

(1) $\tau \le \tau_s$; weak τ dependence of N_c (Fig. 4, regime *1*). In this case, the increment ΔR during a pulse far exceeds the relaxation between pulses; therefore, $R_k^+ (k = N_c) \approx N\Delta R$. From Eq. (5) ($z = 0$), we find $\Delta R(I_1) \approx 6 \times 10^{-8}$ m, $\Delta R(I_2) \approx 2 \times 10^{-8}$ m, $\Delta R(I_3) \approx 4 \times 10^{-9}$ m, and $\Delta R(I_4) \approx 1 \times 10^{-9}$ m. For the given I, we find from Fig. 4 $N_c(I_1) \approx 20$, $N_c(I_2) \approx 40$, $N_c(I_3) \approx 250$, and $N_c(I_4) \approx 400$. Then, $R_k^+(I_1) \approx 1$ μm, $R_k^+(I_2) \approx 0.8$ μm, $R_k^+(I_3) \approx 1$ μm, and $R_k^+(I_4) \approx 0.4$ μm. These values are in qualitative agreement with the experimental fact that, after the application of N_c pulses, the scattering grows, since the size of scatterers (dislocations) must be comparable to the probing wavelength under these conditions.

(2) $\tau_s \le \tau \le \tau_l$. Here, the relaxation processes become appreciable and the R_k vs. number of pulses follows Eq. (2). At $\tau = \tau_s$ and $k = N_c$, R_k equals 0.8 μm on average (see above). Substituting $R_l^+ = 0.8$ μm and the associated values of $\tau = \tau_s$, $k = N_c$, and ΔR for any two values of I in Fig. 4 [for example, $\tau_s(I_1) = 10^{-1}$ s, $N_c(I_1) = 20$, $\Delta R(I_1) = 6 \times 10^{-8}$ m and $\tau_s(I_2) = 4 \times 10^{-2}$ s, $N_c(I_2) = 40$, $\Delta R(I_2) = 2 \times 10^{-8}$ m] into (2) yields $\tau_0 \approx 1$ ns and $\tau_r \approx 1.2$ s.

(3) $\tau > \tau_l$. Substituting $\tau_0 = 1$ s and $\tau_r = 1.2$ s into Eq. (2), we find that the size of a dislocation loop is less than 0.5 μm for any τ and k. That is a possible reason why such dislocations do not scatter the probing radiation and, therefore, are not revealed in the microscope.

CONCLUSION

We studied the damage of the silicon surface subjected to short laser pulses. It is shown that the solid-phase damage is associated with the generation, growth, and accumulation of dislocations. It is established that a single shot with a power density up to the melting threshold does not damage the surface. $N_c = N_c(I, \tau)$ curves, where N_c is the critical number of laser pulses that causes damage, I is the power density, and τ is the pulse repetition period, are derived. The curves are explained using experimental data and numerical evaluation.

ACKNOWLEDGMENTS

The authors thank V.I. Emel'yanov for the valuable discussion.

REFERENCES

1. V. P. Veĭko and S. M. Metev, *Laser Technology in Microelectronics* (Bolgarsk. Akad. Nauk, Sofia, 1991).

2. S. Yu. Karpov, Yu. V. Koval'chuk, and Yu. V. Pogorel'skiĭ, Itogi Nauki Tekh., Ser. Fiz. Osn. Lazer. Puchkovoĭ Tekhnol. **1**, 5 (1988).
3. V. I. Boĭko, B. S. Luk'yanchuk, and E. R. Tsarev, Tr. Inst. Obshch. Fiz. Akad. Nauk SSSR **30**, 6 (1991).
4. B. L. Volodin, V. I. Emel'yanov, and Yu. G. Shlykov, Kvantovaya Élektron. (Moscow) **20**, 57 (1993).
5. V. I. Emel'yanov and P. K. Kashkarov, Appl. Phys. A: Solids Surf. **A55**, 161 (1992).
6. V. P. Veĭko, Ya. A. Imas, M. N. Libenson, *et al.*, Izv. Akad. Nauk SSSR, Ser. Fiz. **49**, 1236 (1985).
7. A. F. Banishev, V. I. Emel'yanov, and M. M. Novikov, Laser Phys. **2**, 178 (1992).
8. B. D. Luft, V. A. Perevozchikov, *et al.*, in *Physicochemical Methods for Treatment of Semiconductor Surface*, Ed. by B. D. Luft (Radio i Svyaz', Moscow, 1982).
9. A. F. Banishev and L. V. Novikova, Fiz. Khim. Obrab. Mater., No. 4, 55 (1992).
10. A. F. Banishev, V. I. Emel'yanov, B. L. Volodin, and K. S. Merzlyakov, Fiz. Tverd. Tela (Leningrad) **32**, 2529 (1990) [Sov. Phys. Solid State **32**, 1469 (1990)].
11. A. V. Demchuk, N. I. Danilovich, and V. A. Labunov, Poverkhnost, No. 11, 26 (1985).
12. S. V. Buntsents, S. G. Dmitriev, and O. G. Shagimuratov, Fiz. Tverd. Tela (St. Petersburg) **38**, 993 (1996) [Phys. Solid State **38**, 552 (1996)].
13. V. V. Mikhnovich and T. V. Firsova, Fiz. Tekh. Poluprovodn. (Leningrad) **24**, 181 (1990) [Sov. Phys. Semicond. **24**, 108 (1990)].
14. J. D. Eshelby, Solid State Phys. **3**, 79 (1956).

Translated by V. Isaakyan

Technical Physics, Vol. 46, No. 8, 2001, pp. 968–976. Translated from Zhurnal Tekhnicheskoĭ Fiziki, Vol. 71, No. 8, 2001, pp. 39–47.

SOLID-STATE ELECTRONICS

Dielectric Response Function of GaPAs Solid Solutions in the Vibrational Absorption Region

A. V. Goncharenko*, O. S. Gorea, N. L. Dmitruk*, A. A. Mikhaĭlik***, and V. R. Romanyuk***

** Institute of Semiconductor Physics, National Academy of Sciences of Ukraine, Kiev, 03028 Ukraine*
e-mail: avg@isp.kiev.ua
*** Moldova State University, ul. A. Matteevich 60, Chisinau, MD 2009 Moldova*
**** Institute of Material Sciences, National Academy of Sciences of Ukraine, Kiev, 03142 Ukraine*
Received July 27, 2000; in final form, February 19, 2001

Abstract—By taking spectra of IR transmission and reflection, attenuated total reflection, and Raman scattering, different models of the dielectric response function of GaPAs solid solutions are tested. It is demonstrated that the models accounting for the difference in the times of transverse and longitudinal vibrational relaxations, as well as the frequency distribution of TO phonons, make possible the prediction of the experimental spectra with a reasonable accuracy. *© 2001 MAIK "Nauka/Interperiodica".*

INTRODUCTION

Solid solutions with a composition-dependent lattice constant (GaPAs, InGaAs, etc.) are widely used in band engineering and in heterostructures. In the latter case, they serve as transition (buffer) layers for the dislocation-free matching of epitaxial films with greatly differing lattice constants. The lattice constants of GaAs and GaP (the components of GaPAs solid solutions) differ by 3.6% [1]. It is known that mechanical stresses in the lattice result in a frequency shift of transverse optical (TO) and longitudinal optical (LO) phonons [2, 3]. Dislocations and other defects due to stress relaxation adversely affect the electrical and optical parameters of the system. However, even in the absence of mechanical stresses and dislocations, the lattice of the solid solutions is disordered. This means that the number of configurations in the nearest vicinity of atoms may be equal to three or four. Direct experimental methods for the study of local inhomogeneities in the structure of solid solutions are still in the developmental stage. The basic issues to be tackled are the arrangement of the substituents (degree of order) and the type and degree of lattice distortions. The complex structural transformations in GaPAs solid solutions and the effect of process conditions have been touched upon in [4]. The complex structure of the solid solutions makes the simulation of their macroscopic dielectric response function, which is necessary for the interpretation of the optical spectra, difficult.

The broadening of the optical excitation band (of an exciton, polariton, or phonon) is often observed in photoluminescence, transmission, and Raman scattering spectra of solids. In most cases, it is qualitatively explained by the structural imperfection of laboratory samples [5–7] and natural objects [8] or by artificially introduced disorder [9, 10]. The reasons for the experimentally observed broadening of the excitation bands may be the point-spread function of an instrument or fluctuations of the thin layer thickness. Physically, the broadening can be related to a decrease in the relaxation time (enhanced damping) of the excitations. The nonuniform distribution of some local material characteristics along those distances or within those time periods over which these characteristics are averaged may also be a factor. Note that, in this case, the penetration (or localization) depth of light is likely to have a noticeable effect on results obtained (see, e.g., [11, 12]).

GaAs and GaP form a continuous series of solid solutions GaP_xAs_{1-x}. The GaAs and GaP compounds are polar cubic crystals that have the zinc-blend structure and two atoms in the unit cell and are characterized by one dipole-active infrared (IR) vibration. The damping parameter of this vibration is $\Gamma_T = 2.6$ cm^{-1} for GaAs and $\Gamma_T = 1.1$–1.3 cm^{-1} for GaP at room temperature [13, 14]. In the optical phonon region, the GaPAs solid solution displays the two-mode behavior and the parameters of its dielectric response function are well described by the modified model of random element isodisplacements [15]. In studying the optical properties of GaAs/GaPAs superlattices [16], good agreement between the IR reflection and attenuated total reflection (ATR) spectra has been obtained in the reststrahlen range of the GaAs component. At the same time, the band of the bulk and surface phonon polaritons related to the GaP-like vibration was considerably broaden. It was assumed that the damping parameters of the surface optical phonons in the solid solutions are greater than the bulk values because of the atomic disorder. Moreover, they vary with concentration [17–20] and

are approximately proportional to the concentration variance $(\Delta x)^2 = x(1-x)$ [21].

In [22], the optical properties of GaPAs solid solutions were described by the cluster model, which gives eight active optical phonons. By fitting the experimental reflectance spectra, the GaP-like modes were found to have $\Gamma_j = 0.02\omega_{Tj} \approx 7.3$ cm^{-1}, whereas the GaAs-like modes have $\Gamma_j = (0.03–0.05)\omega_{Tj} \approx 8.1–13.5$ cm^{-1}. The same amount of LO peaks would be expected in the Raman scattering spectra of these compounds. However, experimental results [3, 23] and our measurements show that only one LO phonon in the restsrahlen region of gallium phosphide and one in the restsrahlen region of gallium arsenide are excited. This is a typical two-mode behavior of the solid solution, which is adequately described by the model of random element isodisplacements [15]. At the same time, a similar cluster approach [24] has turned out to be quite appropriate when the phonon state density in HgCdTe at different temperatures were calculated using Green's function method.

With time-resolved coherent anti-Stokes Raman spectroscopy (TR CARS) and Raman spectroscopy (RS), one can determine the phonon relaxation (lifetime τ) either directly or through the excitation bandwidth as $\tau = (2\pi c\Gamma)^{-1}$ [25]. It should be noted, however, that the relaxation of TO phonons has been studied by these methods much less than that of LO phonons.

The shape of the TO and LO bands for GaP that were obtained from IR reflectance and RS spectra [14, 26] implies that the peak of $\mathrm{Im}[\varepsilon(\omega)]$ (at the TO phonon frequency) is strongly asymmetric and broadens toward low frequencies, whereas the peak of $\mathrm{Im}[-1/\varepsilon(\omega)]$ (at the LO phonon frequency) is narrow and symmetric. It has been suggested that the asymmetric broadening of the GaP band results from strong interaction between the TO phonon at $\omega_{TO} = 366$ cm^{-1} and the nearby combined absorption band TA(X) + LA(X) = 357 cm^{-1} (at $T = 300$ K), and the frequency-dependent damping function $\Gamma(\omega)$ has been introduced [14].

In mixed crystals (solid solutions), two cases are distinguished [27]: (1) the concentration of impurities is small and the approximation of isolated impurity atoms is valid and (2) disordered systems with a high concentration of substituting impurities. Disorder can be introduced by a variety of ways. The whole set of implementations of disordered lattice results in the statistic distribution of the phonon parameters. Investigations of the AlGaAs solid solution have shown that the random distribution of Al and Ga in the cation sublattice breaks the translation symmetry at the atomic level and decreases the correlation length (≈10 nm). This effect shows up as the broadening and asymmetry of the LO phonon band in RS spectra [28]. Therefore, in ternary compounds, where the constituent atoms are distributed randomly, the phonon lifetime is affected by both spontaneous anharmonic decay into low-energy phonons (τ_d) and elastic scattering by isotopic disorder (τ_{dis}). It has been shown [23] that the latter mechanism becomes significant when the impurity concentration is high.

The quality and, hence, the electrical and optical properties of multilayer solid solution systems are strongly dependent on process-related factors, such as interdiffusion, the formation of transition layers, interface roughness, and mechanical stresses. To elucidate the role of each of them, we study the optical properties of single-layer GaPAs epitaxial films grown on a gallium arsenide substrate. Another aim of this work is to verify models for the permittivity of the GaPAs solid solution in the fundamental lattice vibration band both with and without using the continuous distribution of the transverse optical phonon frequency.

MODEL APPROXIMATIONS

The dielectric response function in the optical phonon band of a crystal that has N IR-active oscillators is most frequently described within the model of noninteracting (harmonic) Lorentz oscillators [29]:

$$\varepsilon(\omega) = \varepsilon_\infty + \sum_{j=1}^{N} \frac{4\pi\rho_j\omega_{Tj}^2}{\omega_{Tj}^2 - \omega^2 - i\omega\Gamma_j}, \qquad (1)$$

where ε_∞ is the high-frequency permittivity and $4\pi\rho_j$, ω_{Tj}, and Γ_j are the strength, frequency, and damping parameter, respectively, of the jth transverse mode. Model (1) adequately describes the dielectric response of GaAs and GaP crystals in the IR region [13].

An important generalization of (1) is the four-parametric semiquantum (or factorized) model [30], which includes the difference in the decay of the transverse and longitudinal optical phonons:

$$\varepsilon(\omega) = \varepsilon_\infty \prod_j \frac{\omega_{Lj}^2 - \omega^2 - i\omega\Gamma_{Lj}}{\omega_{Tj}^2 - \omega^2 - i\omega\Gamma_{Tj}}. \qquad (2)$$

Here, each jth oscillator is characterized by four parameters. These are the frequencies of the transverse and longitudinal optical vibrations, ω_{Tj} and ω_{Lj}, and their dampings, Γ_{Tj} and Γ_{Lj} (generally, $\Gamma_{Tj} \neq \Gamma_{Lj}$). For GaP, it was found that $\Gamma_{TO} = \Gamma_{LO} = 1.3$ cm^{-1} [31]. By applying this model to studying the optical properties of AlGaAs solid solution, it was found [17] that $\Gamma_{Lj} < \Gamma_{Tj}$, with Γ_{Tj} increasing with a decrease in the content of the corresponding component.

The transverse and longitudinal optical phonons in the pure binary components of the GaPAs solid solution have different lifetimes. At $T = 300$ K, $\tau_{LO} = 3.5$ ps [32] and $\tau_{TO} = 1.4$ ps [33] for GaAs, $\tau_{LO} = 9$ ps [25] and 4.24 ps [23] and $\tau_{TO} < 0.1$ ps [34] for GaP, and $\tau_{TO} = 3.86$ ps [23] for the GaP-like TO-mode in $GaP_{0.9}As_{0.1}$. It is evident from these data that the TO vibration in

GaP has a very small lifetime presumably because of the strong anharmonicity of Ga–P vibrations both in the pure bulk crystal [35] and in GaPAs solid solution [18]. With regard for the above lifetimes of the TO and LO phonons and in view of the fact that the phonons have different decay channels, it appears that the factorized model (2) of the dielectric response function is more appropriate. Taking into account the different dampings of the TO and LO vibrations within this model enables us to obtain the asymmetric peak in Im[$\varepsilon(\omega)$]. Below, however, we will show that this is insufficient for the experimental reflectance spectra of the GaP_xAs_{1-x} epitaxial films to be in satisfactory agreement with the simulations in a wide range of x.

Ternary semiconductors $A_xB_{1-x}C$ are a mixture of binary components AC and BC taken in a certain proportion. The macroscopically uniform crystal lattice with substitutional defects is formed when As ions are replaced by P ones. The distribution of phosphorus atoms in the lattice is random, and the nearest vicinity of atoms in the solid solution is not necessarily reduced to one or two configurations unambiguously related to the composition. The disordered structure, resulting in the different nearest vicinities of the atoms or molecules, specifies the probabilistic nature of all local characteristics and the statistical character of the experimentally measured values. In spectroscopy, this causes the nonuniform (fluctuation) broadening of the bands, i.e., broadening stemming from the fact that each spectral band is a superposition of many narrower bands. If the film thickness is larger than a critical value, stress relaxation may lead to a uniform strain distribution across the film. Since the optical diagnostic techniques are largely integral, they give averaged microscopic characteristics. Note that the penetration depth of the probing radiation in the IR reflection method is much greater than in RS. At the same time, the ATR method with the excitation of surface waves enables one to control the light penetration depth by varying the angle of incidence onto the sample [12].

The effect of structure disorder or the variation of a certain parameter about its average value on the complex permittivity $\varepsilon(\omega)$ and on the optical spectra of solids has been considered elsewhere [8, 36, 37]. In the general case, the shape of a nonuniformly broadened band depends on the distribution of this parameter. If the number of oscillators of each type is assumed to obey the Gaussian distribution over the variable resonance frequency, the dispersion relation for the complex permittivity is written as the convolution of the Lorentzian and Gaussian functions [36]:

$$\varepsilon(\omega) = \varepsilon_\infty + \sum_j \frac{4\pi\rho_j}{\sqrt{2\pi}\sigma_j} \times \int_{-\infty}^{+\infty} \frac{\exp[-(\omega' - \omega_j)^2/(2\sigma_j^2)]}{\omega'^2 - \omega^2 - i\omega\Gamma_j} d\omega'. \quad (3)$$

As a first approximation, we assume that the oscillator strength $4\pi\rho_j$ is frequency-independent and that the distribution width σ_j depends on the oscillator type. The non-Gaussian contribution is assumed to be insignificant.

Obviously, the real fluctuations of the vibrational frequencies in crystals should have narrow spectral intervals. The concept of the Gaussian distribution of local parameter values is common in the characterization of the dielectric properties of disordered media. Equation (3) encompasses virtually any feasible degree of random disorder. A similar approach was used for the interpretation of the IR reflectance spectra from the near-surface SiC layer [37]. It might be expected that this equation is also valid for other classes of condensed disordered media, such as solid solutions, noncrystalline semiconductors, polymer melts, etc.

SAMPLES AND MEASUREMENT PROCEDURE

GaP_xAs_{1-x} epitaxial films were grown on GaAs substrates by chloride vapor-phase epitaxy [38]. The substrates were both undoped and doped GaAs(001) single crystals about 0.4 mm thick. From the reflectance spectra taken on the substrate side in the plasma minimum range, the plasma frequency ω_p and the plasmon damping parameter γ_{pl} in the substrate were determined. The component sources were undoped (high-resistivity) GaAs and GaP n-type ($n \approx 5 \times 10^{15}$ cm^{-3}) single crystals. The film growth rate was 2–5 Å/s. From the photoluminescence spectra, it was found that the actual composition may differ from the desired (rated) composition by no more than $\Delta x = \pm 0.05$. According to our estimates, with such a spread, $\Delta x = \pm 0.05$, the uncertainty in the transverse phonon frequency is no more than $\Delta\omega_T = \pm 1$ cm^{-1}. The thicknesses of the epitaxial layers (see Table) far exceed the critical value for such a system (approximately 250 Å [1]); therefore, the strains may have a minor effect on the film properties.

Near-normal (the angle of incidence on the sample plane is 16.5°) IR reflection, R_{NIR}, and transmission (normal incidence), T, spectra were taken with a KSDI-82 grating spectrometer and an Goley detector. The spectral slit width did not exceed 1.5 cm^{-1}. ATR spectra R_P in p-polarized light were taken in the Otto geometry [39]. The sample and the CsI semicylinder (refractive index $n = 1.71$, critical angle $\varphi_{cr} = 36°$) were separated by the vacuum gap d_{gap} provided by calibrated spacers. The Raman backscattering spectra were measured at an angle of incidence of the exciting radiation (Ar laser, $\lambda = 488$ nm) close to the Brewster angle. All spectra were recorded at room temperature.

The samples parameters were determined by solving the inverse spectral problem. The reflectance, transmission, and ATR spectra were calculated using the matrix formalism [40] with regard for the point-spread

function of the reflection attachments. The permittivity of the substrate was calculated from Eq. (1) with regard (if necessary) for the contribution of free carriers, and that of the epitaxial film was determined from Eq. (2) or (3) including the GaAs- and GaP-like oscillators. Hereafter, the subscripts $j = 1, 2$ refer to the GaAs-like and GaP-like mode, respectively, in the GaPAs solid solution. The optical parameters of bulk GaAs and GaP crystals were taken from [13].

The GaPAs films grown were also examined by X-ray diffraction with a DRON-UM1 powder diffractometer (CuK_α radiation). The 002_{GaPAs} and 004_{GaPAs} reflections were recorded in the 2Θ–Θ geometry.

RESULTS AND DISCUSSION

Two additional peaks are observed in the vicinity of the 004_{GaAs} and 002_{GaAs} reflections (Fig. 1). One of them, at 67° (32.2°), corresponds to the GaP_xAs_{1-x} lattice for the respective x. The broadening of the 002 and 004 peaks implies, according to [41], that the microstress fields in the GaP_xAs_{1-x} epitaxial film are insignificant. The intensity of the second peak (at smaller angles) is several orders of magnitude lower, and the peak is very broad (between 60° and 70° for 004_{GaAs} and between 29° and 33° for 002_{GaAs}). The nature of this peak is still unclear. It may be associated with fine crystallites present in the film. One can assume the formation of variously oriented domains and subdomains, as well as the occurrence of displacement anisotropy, which reduces the total symmetry of the structure (see, e.g., [4]).

A feature of our system is that gallium arsenide is the substrate and simultaneously the component of the epitaxial film. This affects the results of optical measurements. The TO–LO splitting bands of the GaAs substrate and the film superpose, these bands for the GaAs component of the solid solution being narrower. The reflection in the restsrahlen range of GaAs will be enhanced by the signal from the substrate, since the light partially penetrates through the film. At the same time, the transmission spectra of the film on the undoped GaAs substrate will have a nontransparent region in the restsrahlen range (240–320 cm^{-1}) because of the large thickness of the substrate. It can be shown that a 0.5-mm-thick GaAs substrate will be transparent in the restsrahlen region of GaP at a doping level $n \leq 10^{16}$ cm^{-3}, which corresponds to $\omega_p \leq 30$ cm^{-1}. The effect of the substrate is the reason why the parameters of the Ga–P vibration alone can reliably be determined from the IR reflectance or transmission spectra. The same situation for GaAs/AlAs superlattices on GaAs substrates has been analyzed in detail in [42].

In Fig. 2, the reflectance and transmission spectra of the $GaP_{0.02}As_{0.98}$ epitaxial film (sample 1) are presented. The phosphorus content in this sample is very low; therefore, phosphorus atoms can be considered as impurities in the GaAs matrix that do not interact with each other. It has been found [18] that, at $x \leq 0.03$, the frequency and the bandwidth are independent of the concentration. Such a Ga–P vibration is known to be local [43]. Its amplitude vanishes at a distance of several lattice constants. The reflectance spectrum has a distinct band in the GaAs restsrahlen range and also an oscillator-induced band in the range of the GaP component. Since the substrate is transparent for IR radiation above 330 cm^{-1}, we determined directly from the trans-

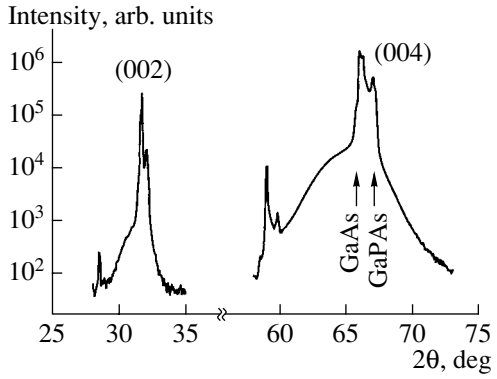

Fig. 1. Angular dependencies of the 002_{GaAs} and 004_{GaAs} X-ray diffraction intensity for sample 6 (CuK_α radiation).

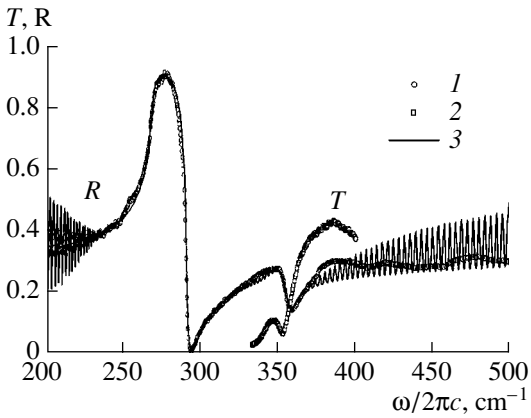

Fig. 2. Experimental IR (*1*) reflection (φ = 16.5°) and (*2*) transmission spectra for sample 1. (*3*) Simulated reflectance spectrum obtained using model (2) for the dielectric response function of the GaPAs film.

Growth parameters for GaP_xAs_{1-x} epitaxial films on GaAs substrates

Sample no.	x	d, μm	ω_p of the substrate, cm^{-1}
1	0.02	2.3	~10
2	0.15	1.62	450
3	0.24	1.3	~10
4	0.24	1.8	430
5	0.26	1.4	~10
6	0.31	1.5	150

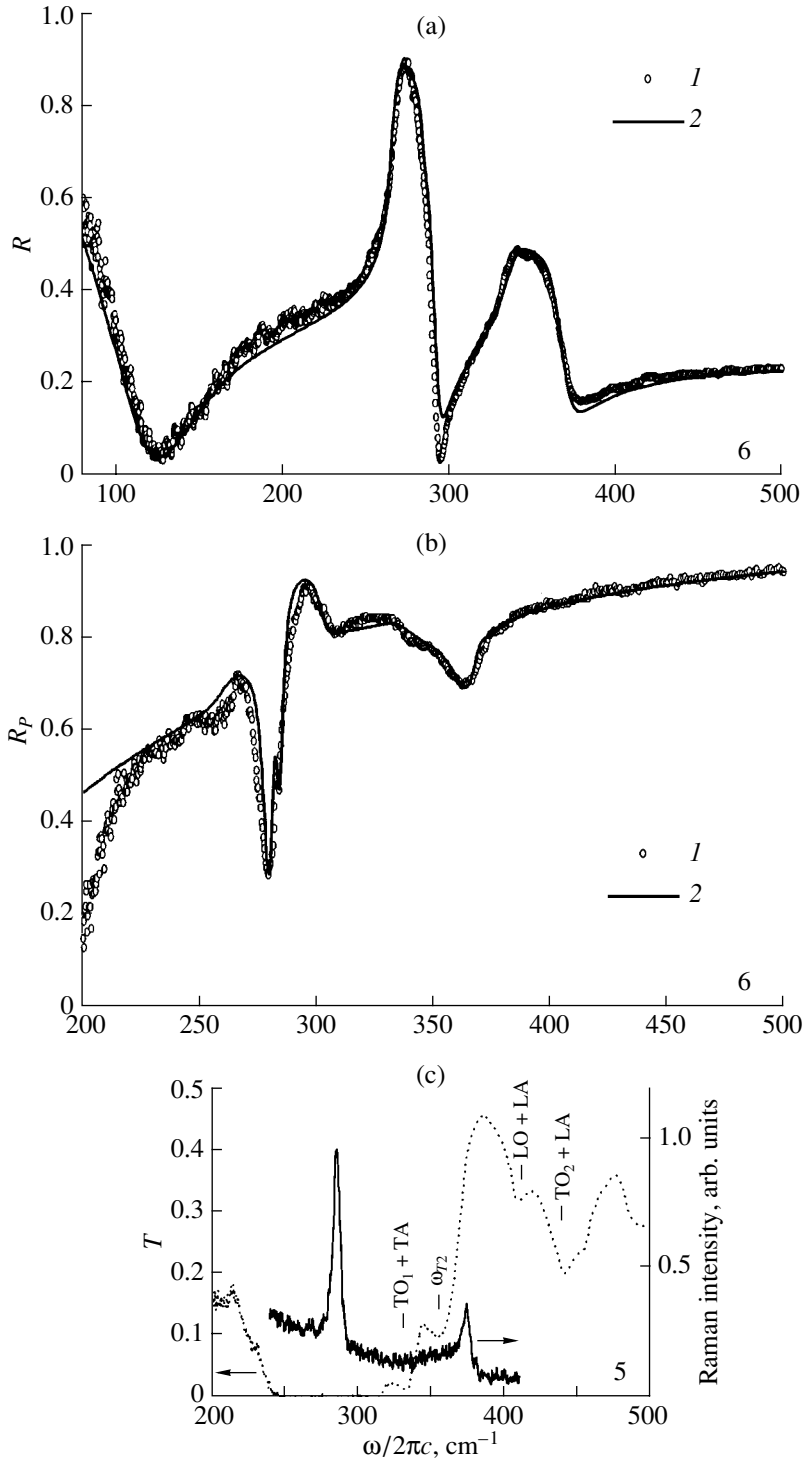

Fig. 3. (a) IR reflection (φ = 16.5°) and (b) ATR (φ = 41°, d_{gap} = 17 μm) spectra for sample 6: (*1*) experiment and (*2*) simulation. (c) Transmission and Raman spectra for sample 5. Arrows in the transmission spectrum indicate (according to [13]) two-phonon absorption bands of the GaAs substrate.

mission spectrum the transverse frequency of the local Ga–P vibrations: $\omega_{T\text{loc}}$ = 353.3 cm^{-1}. The factorized model (2) of the dielectric response function provides better agreement with the experiment than the model of noninteracting harmonic oscillators (1). From the former, Γ_{T2} = 8.3 cm^{-1}, Γ_{L2} = 6.5 cm^{-1}, and $\omega_{L\text{loc}}$ = 354.9 cm^{-1}. Thus, the inequality $\Gamma_L < \Gamma_T$ obtained for the localized vibrations of noninteracting P atoms in the

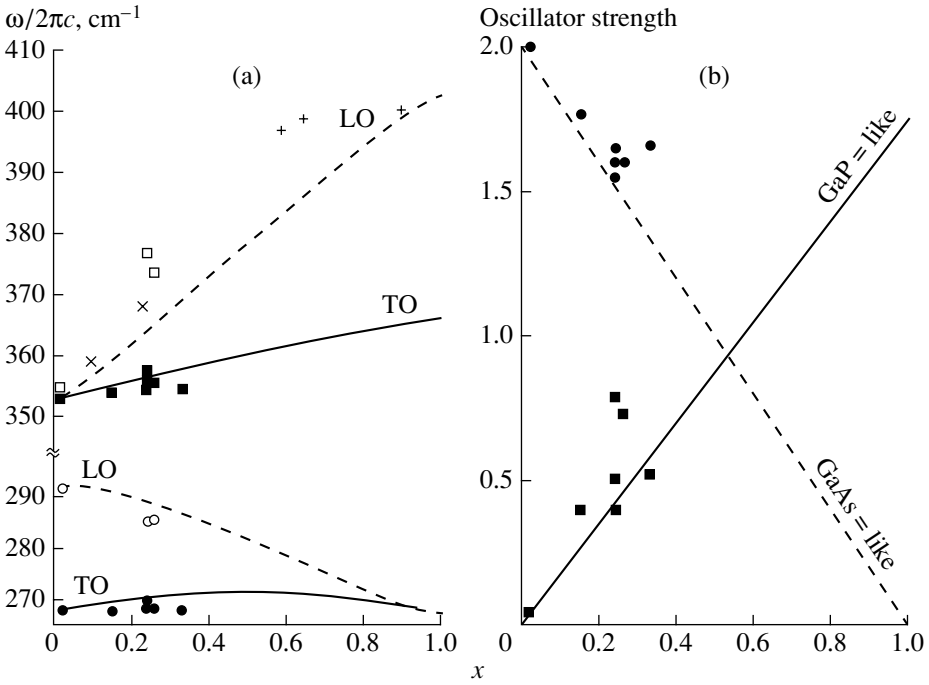

Fig. 4. (a) Frequencies of (○, □) LO and (●, ■) TO phonons and (b) oscillator strengths $4\pi\rho_1$ and $4\pi\rho_2$ for the GaAs and GaP components, respectively, of the GaP_xAs_{1-x} solid solution vs. phosphorus content x. Continuous and dashed lines, calculation by the model of isodisplacements. Shown are also the experimental values of ω_{L2} obtained in (+) [3] and (×) [23].

GaAs matrix is similar to data for pure bulk GaP [25, 34], because it means that $\tau_{LO} > \tau_{TO}$. The weak structure in the experimental reflectance spectra in the range 380–500 cm^{-1} stems from the contribution of combined (two-phonon) absorption to the permittivity of the substrate [13], which is ignored in the models used.

The samples with a higher phosphorus content in the film of the solid solution have a GaP phonon bandwidth in the reflectance spectra that corresponds to $\Gamma_T \simeq 11$–13 cm^{-1} (note that, for bulk GaP, $\Gamma_T \simeq 1.1$–1.3 cm^{-1} [14, 31]). The fitting of such reflectance spectra with factorized model (2) does not yield a stable and unique solution. Apparently, at high phosphorus concentrations in the crystal lattice, the P–P interaction and microfluctuations of x throughout the volume become significant. For fitting to yield a physically meaningful result, the values of ω_T and ω_L should be obtained from independent experiments. Moreover, analysis of model (2) [30, 41] shows that the difference between Γ_T and Γ_L is reliably detected if the gap between ω_{Lj} and ω_{Tj} far exceeds Γ_{Tj} and Γ_{Lj}. Therefore, we fitted the parameters ω_{T1}, $4\pi\rho_1$, σ_1, ω_{T2}, $4\pi\rho_2$, and σ_2 for model (3), which specify the dielectric response of the GaPAs epitaxial film at fixed damping parameters of individual GaAs and GaP oscillators: $\Gamma_{T1} = 2.6$ cm^{-1} and $\Gamma_{T2} = 2.0$ cm^{-1}, respectively. These values were obtained from the reflectance measurements in the restsrahlen region of 0.5-mm-thick undoped GaAs and GaP wafers and well correlate with data in [13].

In Fig. 3, typical reflectance, transmission, ATR, and Raman spectra of the GaPAs/GaAs films are presented. At very low x, as in the previous case, two intense reflectance bands appear in the reflectance spectra (Fig. 3a): one, more intense, in the restsrahlen region of GaAs, while the other, in the region of GaP. Since at lower-than-plasma frequencies the doped substrate becomes nontransparent and high-reflecting, interference modes (with a minimum at 125 cm^{-1}) may arise in the transparent film. Figure 3b shows an ATR spectrum in p-polarized light. The ATR method makes it possible to excite surface waves that propagate over the surface and are confined near the interface within distances of the order of the wavelength in the medium. In multilayer structures, surface phonon–polariton, mixed phonon–plasmon, and waveguide modes can be excited under the conditions ATR [16]. These are sensitive to the phonon parameters of the medium. The GaAs-like surface phonon–polariton mode (at a frequency near 280 cm^{-1}) has the considerably smaller half-width than the GaP-like mode (at a frequency near 360 cm^{-1}). In Figs. 3a and 3b, theoretical spectra for which the dielectric response function was simulated using model (3) are presented as well. The calculation is seen to adequately describe the reflectance spectra in the restsrahlen region of both solid solution components. In Fig. 3c, the transmission spectrum for one of the samples grown on the undoped GaAs substrate is depicted. The transmission of such a system is determined mainly by the transmission of the thick (much thicker

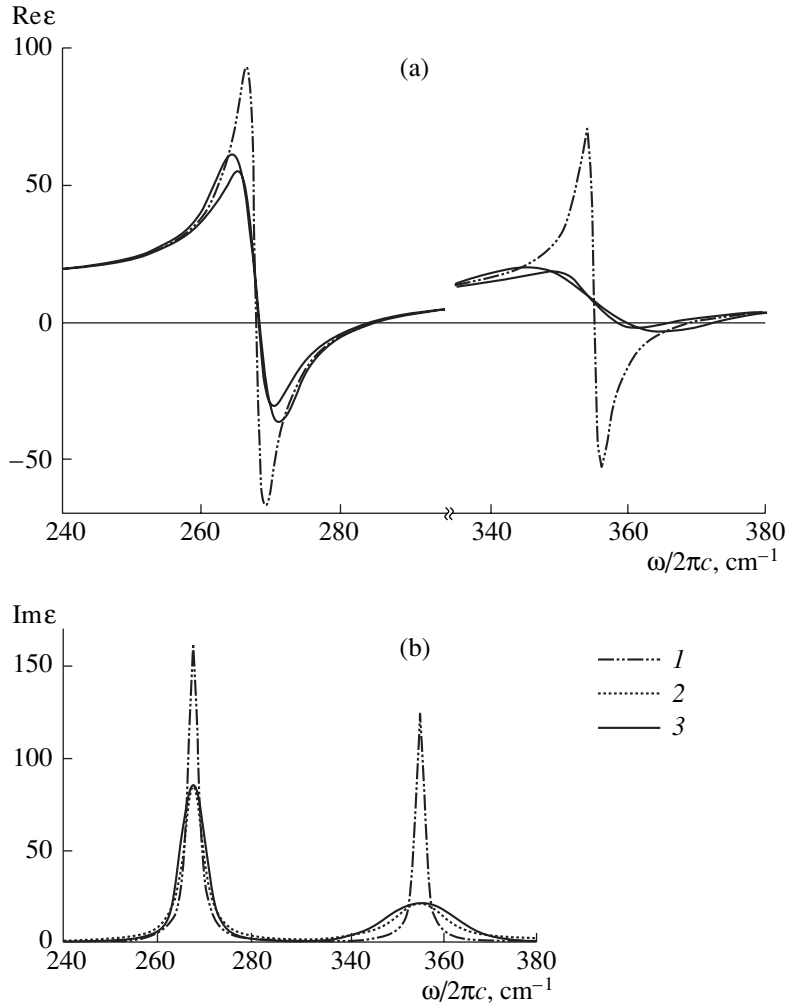

Fig. 5. Permittivity of the $GaP_{0.26}As_{0.74}$ solid solution in the optical phonon range calculated by Eq. (1). Bulk values of the damping parameters are (*1*) $\Gamma_{T1} = 2.6$ cm^{-1}, $\Gamma_{T2} = 2$ cm^{-1} and (*2*) $\Gamma_{T1} = 5.0$ cm^{-1}, $\Gamma_{T2} = 12.5$ cm^{-1}. Curves *3* correspond to Eq. (3) at $\Gamma_{T1} = 2.6$ cm^{-1}, $\sigma_1 = 2.0$ cm^{-1}, $\Gamma_{T2} = 2.0$ cm^{-1}, and $\sigma_2 = 7.0$ cm^{-1}.

than the film) substrate, which is nontransparent in the restsrahlen region 240–320 cm^{-1}. At higher frequencies, combined absorption bands appear as well. They were identified according to [13]. At the same time, the GaP-like TO vibration in the solid solution ($\omega_T = 355.5$ cm^{-1}) falls into the transparence region between these bands and is clearly observed. In the Raman spectrum of this sample that is also presented in Fig. 3c, only two LO modes are excited: one in the restsrahlen region of either component of the solid solution. In pure GaP, the excitation band for the GaP-like LO phonon in the Raman spectra [23] is symmetric, whereas, in the solid solution, it becomes asymmetric. The asymmetry grows as the phosphorus content in GaPAs decreases. The asymmetry of the GaP-like band is larger than that of the GaAs-like one. The effect of mechanical stresses on the phonon spectrum of GaPAs was studied with Raman scattering in [3]. It was found that Ga–As bonds are deformed more strongly than Ga–P bonds in strained GaPAs layers.

Thus, applying the fitting procedure to the near-normal reflection and ATR spectra, we obtained the parameters ω_{T1}, $4\pi\rho_1$, σ_1, ω_{T2}, $4\pi\rho_2$, and σ_2 for the GaAs- and GaP-like optical phonon vibrations in the GaP_xAs_{1-x} solid solution with a phosphorus content within $0.02 \le x \le 0.31$. The frequencies of the transverse vibrations and the oscillator strengths of the components are presented in Fig. 4 together with the calculations from the model of isodisplacements [15]. For the reason mentioned above, we cannot judge the variation of ω_{T1} with x. However, we can argue that the values of ω_{T2} obtained lie somewhat below (approximately by 1–2 cm^{-1}) the calculated ones. In the model of isodisplacements, it is assumed that the oscillator strength in the two-mode solid solution depends linearly on the content of the corresponding component: $4\pi\rho_j(x) = x4\pi\rho_{0j}$,

where $4\pi\rho_{0j}$ is the corresponding value for the bulk material. The actual oscillator strengths are somewhat higher; for the GaP component, the deviation is greater. Figure 4a shows also the values of ω_{L2} obtained from the Raman spectra for other x at $T = 300$ K [3, 23]. The experimental data [3, 23] fall above the calculated curve. This also indicates that the strength of the phonon GaP-like oscillator is higher than that following from the model of isodisplacements. Generally speaking, the assumption on the linear dependence of the oscillator strength on the content of the corresponding component in a solid solution is poorly justified [20, 43]. In [17], better agreement with the experiment was demonstrated for an AlGaAs solid solution when $4\pi\rho_j(x)$ was a nonlinear function. Here, we omit this complex problem. Just note that the knowledge of the exact dependence $\omega_L(x)$ is also of applied interest, since the frequency of the longitudinal vibration is more concentration-dependent than the frequency of the transverse vibration (Fig. 4a). It was also found that $\sigma_1 < 2$ cm^{-1} and $\sigma_2 = 7$–9 cm^{-1}. Hence, in the range of x under consideration, the band of the GaP component (i.e., the component whose content in the solid solution is lower) is more broadened compared with the bulk values for the binary components. Moreover, the ratio $\sigma_2/\omega_{T2} \approx 1.5\%$, whereas in [8], a similar approach gave the value 9% for amorphous silicon dioxide.

In Figs. 5a and 5b, the dielectric response function of the GaPAs solid solution in the optical phonon range is presented. It was calculated using Eqs. (1) and (3) with the parameters obtained by fitting. It is evident that one cannot derive the functional dependence of the permittivity described by an equation like (3) by merely increasing the damping in the model of harmonic oscillators, since (3) is the convolution of the Lorentzian and Gaussian functions. Finally, it should be noted that the agreement achieved is not perfect, in particular, near the maximum of the reflectance band, as follows from Fig. 3. However, with function (3) for the permittivity of the GaPAs solid solution, one can better characterize the IR reflection spectra of multilayer heterostructures based on this solid solution (particularly, GaAs/GaPAs superlattices). Physically, the model of dielectric response function with the asymmetric distribution at large x seems to be more reasonable (especially, in the range of Ga–P vibrations). It enables one to take into account not only the parameter spread over an ensemble of oscillators but also the considerably different lifetimes of the longitudinal and transverse optical vibrations in the components.

CONCLUSION

We studied optical phonon spectra in epitaxial GaPAs/GaAs films. The spectra exhibit the broadened bands of the bulk and surface phonon–polariton excitations. The crystals have a disordered lattice, which can be formed by a variety of ways. Each realization of such a lattice results in a set (distribution) of the parameters of phonon oscillators. X-ray diffraction analysis shows the absence of mechanical stresses and good crystal quality of the films. Moreover, the X-ray diffraction pattern has an additional broadened peak. Its origin is likely to be related to the formation of domain and subdomain structures [4]. The subdomains may reduce the symmetry of the structure and break long-range order in the crystal, thus affecting the optical properties of the solid solution. To describe the optical properties of such disordered systems, the model with the Gaussian frequency distribution of oscillators is used. This model fits experimental spectra much better than the model of harmonic oscillators without increasing the number of fitting parameters. The distribution function parameters obtained from the solution of the inverse spectral problem take physically reasonable values. The aforesaid is valid not only for the optical properties of GaPAs but to some extent for the properties of other ternary compounds based on III–V semiconductors. If the system parameters (in our case, the optical phonon frequencies) are distributed, fine structures in the optical phonon spectra, for example, localized modes or Berreman modes, are difficult to observe.

ACKNOWLEDGMENTS

The authors are grateful to V. Vysotsky for recording Raman spectra.

REFERENCES

1. J. W. Matthews and A. E. Blakeslee, J. Cryst. Growth **27**, 118 (1974).
2. T. Kato, T. Matsumoto, M. Hosoki, and T. Ishida, Jpn. J. Appl. Phys. **26**, L1597 (1987).
3. G. Armelles, M. J. Sanjuan, L. Conzalez, and Y. Gonzalez, Appl. Phys. Lett. **68**, 1805 (1996).
4. A. A. Vaĭpolin and D. Melebaev, Fiz. Tverd. Tela (St. Petersburg) **36**, 2107 (1994) [Phys. Solid State **36**, 1150 (1994)].
5. H. Lee, D. Biswas, M. V. Klein, *et al.*, J. Appl. Phys. **75**, 5040 (1994).
6. A. H. Kachare, W. C. Spitzer, F. K. Euler, and A. Kahan, J. Appl. Phys. **45**, 2938 (1974).
7. P. V. Santos and L. Ley, Superlattices Microstruct. **5**, 43 (1989).
8. D. K. Lynch, Astrophys. J. **467**, 894 (1996).
9. K. Ishioka, K. G. Nalamura, and M. Kitajima, Phys. Rev. B **52**, 2539 (1995).
10. D. Kirillov, P. Ho, and G. A. Davis, Appl. Phys. Lett. **48**, 53 (1986).
11. T. Takeuchi, C. Maezava, T. Nomura, *et al.*, Appl. Surf. Sci. **41/42**, 530 (1989).
12. N. L. Dmitruk, A. V. Goncharenko, O. S. Gorea, *et al.*, Proc. SPIE **2648**, 138 (1995).
13. R. K. Willardson and A. C. Beer, in *Semiconductors and Semimetals* (Academic, New York, 1967), Vol. 3.
14. A. S. Barker, Jr., Phys. Rev. **165**, 917 (1968).

15. I. F. Chang and S. S. Mitra, Phys. Rev. **172**, 924 (1968).
16. E. F. Venger, A. V. Goncharenko, O. S. Gorea, *et al.*, Zh. Prikl. Spektrosk. **66**, 460 (1999).
17. O. K. Kim and W. G. Spitzer, J. Appl. Phys. **50**, 4362 (1979).
18. W. G. Spitzer, J. Phys. Chem. Solids **28**, 33 (1967).
19. G. Irmer, M. Herms, J. Monecke, and H. Bock, Phys. Status Solidi B **145**, K79 (1988).
20. M. H. Brodsky, G. Lucovsky, M. F. Chen, and T. S. Plaskett, Phys. Rev. B **2**, 3303 (1970).
21. B. Samson, T. Dumelow, A. A. Hamilton, *et al.*, Phys. Rev. B **46**, 2375 (1992).
22. H. W. Verleur and A. S. Barker, Jr., Phys. Rev. **149**, 715 (1966).
23. C. Ramkumar, K. P. Jain, and S. C. Abbi, Phys. Rev. B **53**, 13 672 (1996).
24. V. N. Pyrkov, S. P. Kozyrev, and L. K. Vodop'yanov, Fiz. Tverd. Tela (St. Petersburg) **35**, 2479 (1993) [Phys. Solid State **35**, 1228 (1993)].
25. J. Kuhl and W. E. Bron, Solid State Commun. **49**, 935 (1984).
26. B. A. Weinstein and G. I. Piermarini, Phys. Rev. B **12**, 1172 (1975).
27. A. A. Maradudin, E. W. Montroll, G. H. Weiss, and I. P. Ipatova, *Theory of Lattice Dynamics in the Harmonic Approximation* (Academic, New York, 1971).
28. J. A. Kash and J. C. Tsang, Solid-State Electron. **31**, 419 (1988).
29. M. Born and E. Wolf, *Principles of Optics* (Pergamon, Oxford, 1969; Nauka, Moscow, 1970).
30. F. Gervais and B. Piriou, J. Phys. C **7**, 2374 (1974).
31. M. Giehler and E. Jahne, Phys. Status Solidi B **73**, 503 (1976).
32. A. R. Bhatt, K. W. Kim, and M. A. Stroscio, J. Appl. Phys. **76**, 3905 (1994).
33. F. Ganikhanov and F. Vallee, Phys. Rev. B **55**, 15 614 (1997).
34. J. Qu and W. E. Bron, Phys. Rev. B **48**, 6720 (1993).
35. B. Bendow, S. P. Yukon, and S. C. Ying, Phys. Rev. B **10**, 2286 (1974).
36. Yu. I. Kopilevich and E. G. Makarova, Opt. Spektrosk. **63**, 147 (1987) [Opt. Spectrosc. **63**, 86 (1987)].
37. A. V. Goncharenko, E. F. Venger, and S. I. Vlaskina, Inst. Phys. Conf. Ser. **142**, 369 (1996).
38. O. S. Gorea, V. V. Zelenin, O. V. Koval, and A. V. Simashkevich, J. Cryst. Prop. Prepar. **32/34**, 503 (1991).
39. *Surface Polaritons: Electromagnetic Waves at Surfaces and Interfaces*, Ed. by V. M. Agranovich and D. L. Mills (North-Holland, Amsterdam, 1982; Nauka, Moscow, 1985).
40. A. R. El-Cohary, T. J. Parker, N. Raj, *et al.*, Semicond. Sci. Technol. **4**, 388 (1989).
41. J. K. Williamson and W. H. Hall, Acta Metall. **1**, 22 (1953).
42. M. M. Dvoynenko, A. V. Goncharenko, V. R. Romaniuk, and E. F. Venger, Superlatt. Microstruct. **26**, 333 (1999).
43. I. F. Chang and S. S. Mitra, Adv. Phys. **20**, 359 (1971).
44. F. Gervais and B. Piriou, Phys. Rev. B **11**, 3944 (1975).

Translated by M. Lebedev

Technical Physics, Vol. 46, No. 8, 2001, pp. 977–987. Translated from Zhurnal Tekhnicheskoĭ Fiziki, Vol. 71, No. 8, 2001, pp. 48–58.

SOLID-STATE ELECTRONICS

The Effect of Space Charge on the Characteristics of ZnS Thin-Film Electroluminescent Devices

N. T. Gurin, O. Yu. Sabitov, and A. V. Shlyapin

Ul'yanovsk State University, Ul'yanovsk, 432700 Russia

e-mail: soy@sv.uven.ru

Received August 3, 2000

Abstract—From experimental time dependences of the instantaneous brightness and the total current passing through a ZnS : Mn thin-film electroluminescent device, capacitance–voltage, charge–voltage, and current–voltage characteristics of the device are calculated. Conditions for negative differential resistance (NDR) of *S* and *N* types are found. An NDR mechanism that exploits the ionization and the recharge of deep donors and acceptors (zinc and sulfur vacancies) with the formation of space charge at the cathodic and anodic interfaces of the phosphor is suggested. © *2001 MAIK "Nauka/Interperiodica".*

Thin-film (TF) electroluminescent (EL) devices feature nonuniformity in structure and properties. This is especially true for those devices that are fabricated by atomic layer epitaxy and offer the best illumination parameters [1–3]. The reason for this nonuniformity is the nonuniform distribution of lattice defects and impurities (hence, associated donor and acceptor centers) across the phosphor layer. It is known [1–5] that the space charge due to these centers may substantially affect the electroluminescence kinetics in TF EL devices. Specifically, the dependence of the current passing through the phosphor layer in the emission mode on the mean field F_p in this layer may exhibit *S*-type NDR [5–7]. At the same time, there is evidence [4] that, under certain conditions, this dependence may show *N*-type NDR, whose nature still remains unclear.

It is therefore the aim of this article to study the electrical performance of TF EL devices with the phosphor layer containing the space charge. Emphasis will be given to conditions under which *S*- or *N*-type NDR arises.

It is common practice [5, 8] to represent a TF EL device as series-connected capacitors, C_i and C_p, made by two insulating layers and the phosphor layer. Such an approach is valid if the exciting voltage does not exceed the luminescence threshold. Once the threshold has been reached, electrons subjected to the high electric field tunnel from states at the phosphor–insulator interface and are accelerated in the field. Simultaneously, Mn^{2+} luminescence centers are excited and other centers associated with crystal defects and impurities experience impact ionization. As a result, under the above-threshold conditions, the current $I_p(t)$ passes through the phosphor layer of thickness d_p. This current is the sum of the displacement current and the conduction current, which define the kinetics of charge carrier transfer, excitation of luminescence centers, formation of space charge, and field redistribution in the layer.

If the time variation of the exciting voltage $V(t)$ is known, the mean field $F_p(t)$ in the phosphor is given by

$$F_p(t) = \frac{1}{d_p}\left[V(t) - \frac{1}{C_i}\int_0^t I_e(t)dt\right], \qquad (1)$$

where $I_e(t)$ is the current in the external circuit.

Formula (1) is valid for the zero initial conditions, i.e., during the first half-cycle of the exciting voltage. Under nonzero initial conditions, it is necessary to take into consideration the remanent polarization field after the preceding voltage half-cycle of opposite polarity:

$$F_p(t) = \frac{1}{d_p}\left[V(t) - \frac{1}{C_i}\int_0^t I_e(t)dt\right] + F_{\text{pol}}. \qquad (2)$$

The field F_{pol} includes the field F_{pi} due to the polarization charge Q_{pi} accumulated by the states at the phosphor–insulator interface and the field F_{ps} due to the space charge in the phosphor layer. In general, the field F_{ps} may have several components that are associated with different space charges and are variously oriented with respect to the field F_{pi}. The field F_{pol} drops with time between two successive intervals when a TF EL device is in the active (emitting) mode and the current $I_p(t)$ passes.

In the absence of recombination losses and carrier trapping, the charge transferred through the phosphor Q_p equals that accumulated at the interface states. The charge Q_p and the charge passing in the external circuit

1063-7842/01/4608-0977$21.00

Q_e are related as [6]

$$Q_p(t) = \frac{C_i + C_p}{C_i}[Q_e(t) - C_e V(t)], \quad (3)$$

where

$$Q_e(t) = \int_0^t I_e(t)dt. \quad (4)$$

The charge Q_e passing in the external circuit can be determined if the initial conditions are known.

Under the above conditions, $Q_p(t)$ and $F_p(t)$ are related as [6]

$$F_p(t) = \frac{1}{d_p(C_i + C_p)}[C_i V(t) - Q_p(t)]. \quad (5)$$

Eventually, the field applied to the phosphor layer decreases by an amount proportional to $Q_p = Q_{pi}$. The field of this charge, remanent polarization field, is retained by the instant of the next excitation cycle and may stay for up to several hours [6]. At $V(t) = 0$,

$$F_{pi}(t) = -\frac{Q_{pi}(t)}{d_p(C_i + C_p)}. \quad (6)$$

In this case, we have

$$Q_p = \frac{C_i + C_p}{C_i} Q_e. \quad (7)$$

The mean threshold field in the phosphor layer F_{pt}, which initiates luminescence, can be determined from the formula

$$F_{pt} = \frac{1}{d_p}\left[V_t - \frac{Q_{et}}{C_i}\right] + F_{\text{pol}}, \quad (8)$$

in view of (2). Here, V_t and Q_{et} are the threshold voltage and charge, respectively, in a TF EL device.

If the exciting voltage varies linearly, i.e., $V(t) = (V_m/t_m)t$, where V_m and t_m are the amplitude of the exciting voltage and the time during which the voltage rises from 0 to V_m, we can write $V_t = (V_m/t_m)t_t$, where t_t is the time during which the voltages reaches the threshold value. The time instant when luminescence starts, as well as the threshold parameters V_t, t_t, and Q_{et}, are usually found by arbitrarily specifying some threshold value of the mean brightness of the device (1 or 10 cd/m^2). Then, from the dependences $L(t)$ and $I_e(t)$, one can refine this parameters, for example, by specifying some small fixed current increment $\Delta I_{et}(t)$ relative to the subthreshold value or brightness increment $\Delta L(t)$ relative to the initial value. The initial value of brightness is defined by the time discretization period that corresponds to the amplitude quantizing level and measurement accuracy. Since $I_e(0) = C_e(dV(t)/dt) = C_e V_m/t_m = \text{const}$ before luminescence,

$$\begin{aligned} F_{pt} &= \frac{1}{d_p}\left[\frac{V_m}{t_m}t_t - \frac{C_e}{C_i}\frac{V_m}{t_m}t_t - \frac{\Delta I_{et} t_t}{C_i}\right] + F_{\text{pol}} \\ &= \frac{1}{d_p}\left(\frac{C_i - C_e}{C_i}\frac{V_m}{t_m} - \frac{\Delta I_{et} t}{C_i}\right)t_t + F_{\text{pol}}. \end{aligned} \quad (9)$$

At $(C_i - C_e)(V_m/t_m) \gg \Delta I_{et}$ and taking into account that $C_e = C_p C_i/(C_p + C_i)$, we reduce expression (9) to

$$F_{pt} \approx \frac{C_i V_m}{d_p(C_i + C_p)t_m}t_t + F_{\text{pol}}. \quad (10)$$

The conduction current passing through the phosphor layer at above-threshold voltages and in the absence of the space charge in it is given by [4]

$$\begin{aligned} I_p(t) &= I_e(t)\frac{C_i + C_p}{C_i} - C_p\frac{dV(t)}{dt} \\ &= \frac{C_i + C_p}{C_i}[I_e(t) - I_e(0)]. \end{aligned} \quad (11)$$

Because of the space charges appearing in the layer, the current $I_p(t)$ [Eq. (11)] will have the reactive component and thus contain information on the space charges in the phosphor. In this case, under the assumption that the insulator is ideal (i.e., conduction current and space charges in it are absent), the capacitance C_i of the insulating layers in a TF EL device can be considered as constant for any operating mode of the device. Then, the dependence $I_p(F_p)$ obtained from formulas (1) or (2) and (11),

$$I_p(t) = C_i\frac{dV(t)}{dt} - (C_i + C_p)d_p\frac{dF_p(t)}{dt} \quad (12)$$

would characterize some conventional semiconductor device that includes a phosphor layer with the phosphor–insulator interfaces. The initial thickness and geometric capacitance of this layer, as well as the voltage across it, are d_p, C_p, and $V_p(t) = F_p(t)d_p$, respectively.

From formulas (2) and (12), it follows that the current $I_p(t)$ can be considered as F_{pol}-independent if the field F_{pol} varies with time much weaker than $V(t)$ and $F_p(t)$. If the field F_p is constant in the active mode of operation, i.e., $dF_p/dt = 0$, and the voltage $V(t)$ grows linearly, the current I_p must be time-independent. When the rate of change of the field $F_p(t)$ declines, the current $I_p(t)$ increases; when dF_p/dt changes sign (after the function $F_p(t)$ has passed through a maximum), the current $I_p(t)$ continues growing and peaks when the rate of fall of $F_p(t)$ is the highest. Subsequently, the current $I_p(t)$ decreases as the rate of fall of $F_p(t)$ diminishes.

In the active mode of the device, its capacitance C_e is given by

$$C_e(t) = \frac{I_e(t)}{dV(t)/dt} = \frac{C_i C_p(t)}{C_i + C_p(t)} = C_i\left[1 + C_i/\frac{dQ_p(t)}{dV_p(t)}\right]^{-1}. \quad (13)$$

The passage of the conduction current in the active luminescent mode means that the capacitance $C_p(t)$ drastically increased [4]. If the mean field F_p in the phosphor layer is fixed, $C_p(t) = dQ_p(t)/dV_p(t)$ tends to infinity and $C_e(t) \approx C_i$; in other words, in the active mode, there should be a region where $C_e \approx C_i$ and does not depend on V [2, 3]. If, in this case, the exciting voltage increases linearly, the current $I_e(t)$, as well as $I_p(t)$ [Eq. (12)], is also constant in this region [8] and the dependence $Q_p(V_p)$ or $Q_p(F_p)$ runs vertically (parallel to the ordinate axis).

With the space charges in the phosphor layer, F_p is no longer constant in the active mode and the behavior of the characteristic $C_e(V)$ depends on the value of $C_p(t) = dQ_p/dV_p(t)$.

(1) $dQ_p/dV_p > C_p$ and grows with V, however, remaining finite. In this case, $C_e(V)$ increases but does not reach C_i. If subsequently dQ_p/dV_p drops with increasing V, $C_e(V)$ also drops. Then, according to (13), if $dV(t)/dt$ remains positive in this range of V (including the linearly increasing voltage), the dependence $I_e(V)$ [and also $I_p(V_p)$ or $I_p(F_p)$, according to (1) or (11)] will have the same form. This means that the I–V characteristic of the phosphor has the N-type NDR region. In the specific case $dQ_p/dV_p = C_i$, $C_e(V) = C_i/2$.

(2) $dQ_p/dV_p \longrightarrow 0$ and $C_e(V)$ also tends to zero. This, in particular, takes place when the exciting voltage V grows, reaches the amplitude value V_m, and then declines.

(3) $dQ_p/dV_p < 0$ and $|dQ_p/dV_p| > C_i$. For a finite value of dQ_p/dV_p, $C_e(V)$ is always greater than C_i. In this case, the smaller (closer to C_i) $|dQ_p/dV_p|$, the greater $C_e(V)$. If, as V increases, $|dQ_p/dV_p|$ grows, starting from some minimal value, $C_e(V)$ decreases from some maximal value, tending to C_i as $dQ_p/dV_p \longrightarrow \infty$. In this case, the vertical portion of the curve $Q_p(V_p)$ or $Q_p(F_p)$ is approached from the left. According to the theory of negative-resistance semiconductor devices [9], negative capacitance always corresponds to NDR of the S type. That is, if $C_e(V) > C_i$, the curves $I_p(V_p)$ or $I_p(F_p)$ must always have an S-type NDR region.

If $|dQ_p/dV_p| = 2C_i$, $C_e(V) = 2C_i$; if $|dQ_p/dV_p| = C_i$, $C_e(V) \longrightarrow \infty$; and if $|dQ_p/dV_p| < C_i$, the values of $C_e(V)$ become negative, which corresponds to a decline in the $Q_e(t)$ curve in the interval where $V(t)$ grows. Positive values of $dV(t)/dt$ would mean the reversal of the current $I_e(t)$, which is unrealistic.

We experimented with metal–insulator–semiconductor–insulator–metal (MISIM) TF EL devices. Here, M is either the 0.2-μm-thick lower transparent SnO_2 electrode applied on a glass substrate or the 0.15-μm-thick upper opaque TF Al electrode 1.5 mm in diameter, I is the 0.15-μm-thick $ZrO_2 + Y_2O_3$ (13 wt %) insulating layer, and S is 0.54-μm-thick the ZnS : Mn (0.5 wt %). The phosphor layer was applied by thermal evaporation in a quasi-closed space, followed by annealing at 250°C for 1 h. The opaque electrode and the TF insulating layers were applied also by thermal evaporation and electron-beam evaporation, respectively.

The time dependences of the current and the instantaneous brightness were taken by applying an alternating-sign triangular voltage from a G6-34 generator equipped with a driver amplifier and an external G5-89 trigger generator. The pulse amplitude was 160–170 V, and the coefficient of voltage nonlinearity was no more than 2%. In the pulse triggering mode, a train of pulses with a repetition rate of 2, 10, 50, 200, 500, or 1000 Hz was used. The time between the pulses T_s was varied between 0.1 and 100 s. In the continuous triggering mode, the voltage frequency was varied from 10 to 1000 Hz. The current through the device was measured with a 0.1- to 10-kΩ resistor series-connected to the device. The voltage drop across the resistor was no higher than 1 V. The instantaneous brightness L was an FÉU-84-3 photoelectric multiplier. The exciting voltage V, current through the device I_e, and the instantaneous brightness L vs. time t were recorded by means of an S9-16 dual-trace storage oscilloscope connected to a PC. Measurement data for 2048 points within the discretization period selected (to an accuracy of 2%) were stored. The data were mathematically and graphically processed with Maple V Release 4 Version 4.00b and GRAPHER Version 1.06 2-D Graphing System packed application programs and formulas (1)–(13) at C_i = 986 pF and C_p = 250 pF. The voltage across the resistor was subtracted from the voltage $V(t)$. The values of C_i and C_p were determined the total capacitance C_e = 200 pF, which was measured with an E7-14 immitance meter, and the geometric sizes of the device.

The curves in Figs. 1 and 2 run in a different way when the voltage polarity is changed. This is typical of the curves $L(t)$, $I_e(t)$, $I_p(t)$, and $F_p(t)$ irrespective of the voltage frequency [10]. The reason is the specifics of TF EL device fabrication; namely, surface states and lattice defects in the phosphor are variously distributed at the upper and the lower phosphor–insulator interfaces [10]. In the pulse triggering mode, both I_e and I_p currents exhibit an additional peak during the first half-cycle of the exciting voltage. Its amplitude grows with triggering (start-up) period T_s. The brightness L increases to a certain level much faster than I_e and I_p. This can be explained by the high probability of exciting the luminescence centers even if the current $I_p(t)$ is relatively low. Starting from the second half-cycle of

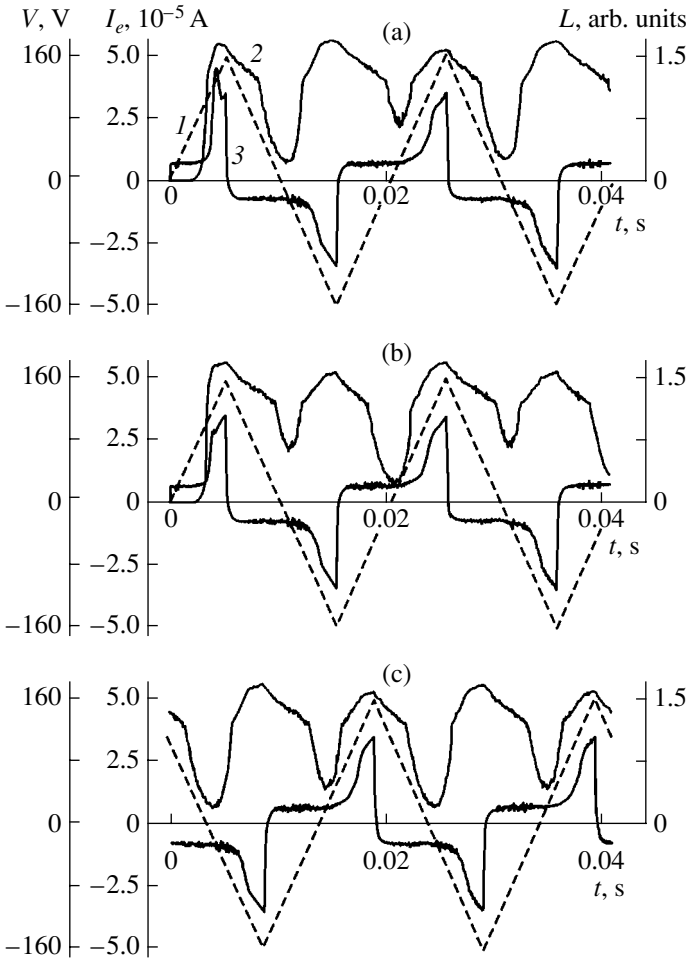

Fig. 1. (*1*) $V(t)$, (*2*) $L(t)$, and (*3*) I_e curves at f = 50 Hz and V_m = 160 V. (a) Pulse triggering with T_s = 100 s and the negative half-wave (half-cycle) applied to the upper electrode (–Al conditions), (b) the same with the positively charged upper electrode (+Al conditions), and (c) continuous triggering (positive amplitude $V(t)$ corresponds to the –Al conditions).

the exciting voltage in the pulse triggering mode, the curves $L(t)$ and $I_e(t)$ run identically to those in the continuous triggering mode (within the measurement accuracy). This indicates that the quasi-steady-state (continuous) mode is set after the first half-cycle of excitation.

This circumstance allowed us to find the initial conditions upon calculating the $F_p(t)$, $Q_p(t)$, $I_p(F_p)$, and $Q_p(F_p)$ curves from formulas (2)–(12), as well as the value of F_{pt} for the pulse triggering mode. Through the value of F_{pt}, one can evaluate the residual polarization charge Q_{pol} and the residual polarization field F_{pol} in the phosphor layer by the instant the next train of pulses is applied. In the steady-state triggering mode, the charges passing during the different half-cycles are equal in magnitude because of the capacitor structure of the device. Therefore, first, Q_{pol} and F_{pol} in the pulse triggering mode were calculated from formulas (1), (3), and (4) for $Q_e(t)$ and $F_p(t)$ with the zero initial conditions. Then, the values of $|Q_e(t_m)|$ corresponding to the voltage V_m in the third and the fourth half-cycles were equated to each other. Finally, the true positions of the curves $Q_e(t)$ and $F_p(t)$ relative to the abscissa axis were found and the values of $Q_p(t) = Q_{\text{pol}}$ for $V(0)$ (i.e., at the instant of triggering) from (7) and $F_p(0) = F_{\text{pol}}$ for all the periods T_s were obtained. The error in determining Q_{pol} and F_{pol} was ±2%.

As follows from the curves $L(t)$, $I_p(t)$, and $F_p(t)$ in Fig. 2, the field F_p after the beginning of emission varies, indicating the presence of the space charges in the phosphor layer. The additional peak of $I_p(t)$corresponds to the highest rate of fall of $F_p(t)$ (Figs. 2b, 2c). This is completely consistent with expression (12). To this additional peak, there corresponds a similar peak in the curve $L(t)$. This can be explained by an increase in the excitation probability of the luminescence centers (the excitation probability varies as the density of the current passing through the phosphor [8]). There are regions where $I_p(t)$ rises and $F_p(t)$ drops. Hence, the *S*-type NDR portions are present in the curves $I_p(F_p)$. When the first half-cycle of the exciting voltage applied

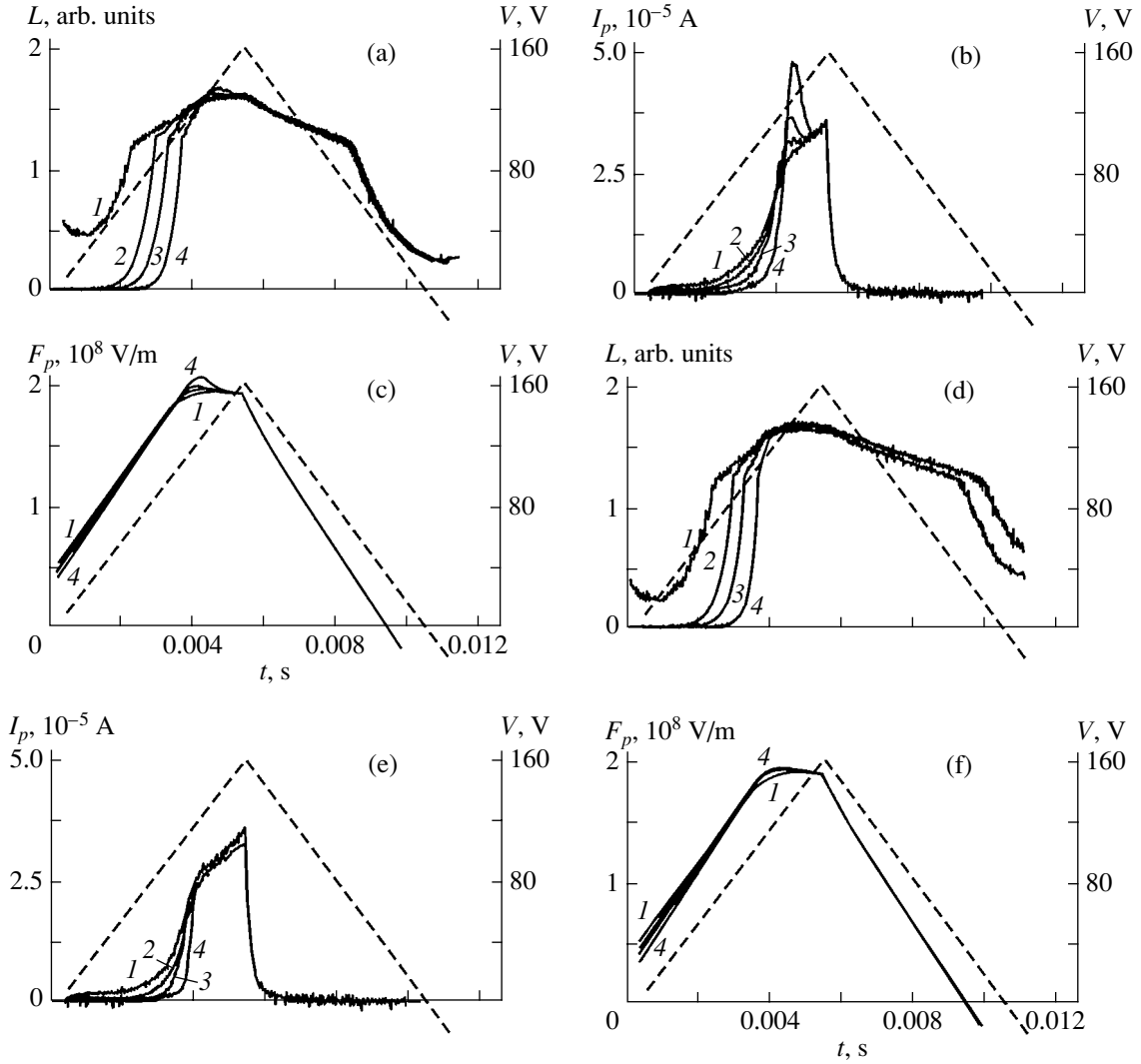

Fig. 2. $L(t)$, $I_p(t)$, and $F_p(t)$ curves at $f = 50$ Hz. (*1*) Continuous triggering and single triggering with T_s = (*2*) 0.5, (*3*) 5, and (*4*) 100 s. (a, d) $L(t)$, (b, e) $I_p(t)$, and (c, f) $F_p(t)$. (a–c) –Al conditions and (d, e) +Al conditions.

to the upper electrode (+Al conditions) is positive, there exist regions where $I_p(t)$ declines and $F_p(t)$ grows. This is typical of *N*-type NDR.

The C_e vs. applied voltage dependences calculated by formula (13) (Fig. 3) also differ when taken at the opposite voltage polarities. This difference builds up in going from the continuous triggering mode to the pulse triggering mode, especially for large triggering periods T_s and high voltage frequencies f. Note that, unlike [2, 3], the curves $C_e(V)$ for the opposite half-waves of the exciting voltage applied to the upper electrode in the first half-cycle here are shown merging for clarity. They are depicted for the complete cycle of the exciting voltage. Arrows indicate the run of $C_e(V)$ when $V(t)$ increases from 0 at $t = 0$ to V_m at $t = t_m$; the sharp drop of C_e down to zero within the time interval from t_m to the instant the current I_e passes through zero (Fig. 1); and the subsequent rise in C_e to $C_e(0)$, following the variation of the current I_e. Such behavior is in complete agreement with the explanation given in item 2 above. As follows from Fig. 3, along with the basic peak at $t = t_m$, there appears an additional peak whose amplitude grows with T_s and f. This is observed in the active (above-threshold) mode when both the negative and the positive half-waves are applied to the upper electrode (±Al conditions). However, in the latter case (+Al), the amplitude of the additional peak of $C_e(V)$ is much lower than for –Al. This peak is virtually absent at the pulse repetition rates 2, 10, and 50 Hz. At these frequencies under the –Al conditions, both the basic peak $C_e(V_m)$ and the additional peak of C_e (for certain T_s) far exceed the value of C_i. This, as noted above, means not only the considerable increase in the capacitance C_p of the phosphor layer but also that this capacitance becomes negative and $|C_p(t)| > C_i$. At the higher frequencies (f = 200, 500, and 1000 Hz), the basic peak

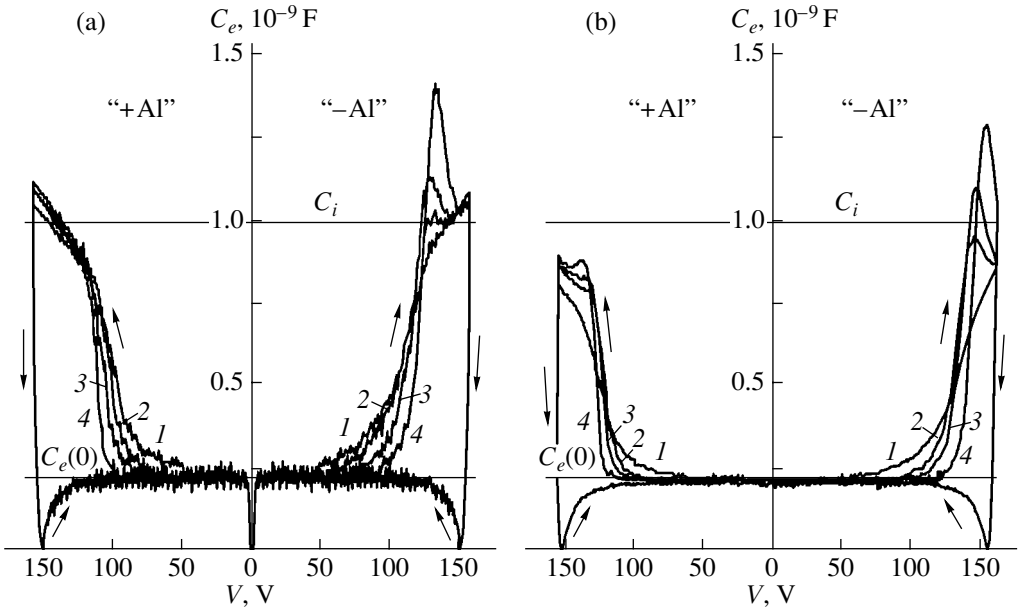

Fig. 3. $C_e(V)$ for the exciting voltage frequencies (a) 50 and (b) 1000 Hz. (*1*) Continuous triggering and pulse triggering with T_s = (*2*) 0.5, (*3*) 5, and (*4*) 100 s. $C_e(0)$ is the device capacitance in the subthreshold region.

$C_e(V_m)$, as well as the additional peaks $C_e(V)$ or any of T_s under the +Al conditions and the additional peaks $C_e(V)$ for T_s = 0.1, 0.5, and 1 s under the –Al conditions, are lower than C_i; hence, one could not expect the appearance of *S*-type NFR in the curves $I_p(F_p)$ under the above conditions. At the same time, the additional peaks $C_e(V)$ that do not reach the value of C_i are observed for the above frequencies when T_s = 0.5 and 1 s under the –Al conditions and T_s = 1, 5, 20, and 100 s under the +Al conditions. According to item 1 of our analysis, this implies the presence of *N*-type NDR in the *I*–*V* characteristic of the phosphor.

Curves $Q_p(F_p)$ depicted in Fig. 4 for two repetition rates in the pulse triggering mode also show (1) the asymmetry of the TF EL structure, (2) regions where F_p drops but Q_p rises, and (3) regions where both the sign and the value of dQ_p/dF_p change. They also suggest that the fields F_p and the charges Q_p in the third and the fourth half-cycles of the excitation voltage are the same and that the amount of charge Q_p transferred through the phosphor layer markedly decreases with increasing *f*. However, these curves are much less informative than the curves $C_e(V)$; in particular, the former cannot reliably detect *N*-type NDR in the $I_p(F_p)$ curves.

The *I*–*V* characteristics of the phosphor that were obtained before the voltage $V(t)$ reached its amplitude value V_m (Figs. 5, 6) totally support the presence of *S*- and *N*-type NDR regions. Under the –Al conditions, the curves $I_p(F_p)$ in Figs. 5a, 5c, 6a, and 6c show, along with the "smooth" *S*-type NDR region, the portion where I_p falls with decreasing F_p (for all T_s at f = 2, 10, and 50 Hz and for $T_s \geq 2$ s at f = 200, 500, and 1000 Hz). This portion expands with T_s (Figs. 5a, 6a). At the low excitation frequencies 2, 10, and 50 Hz, the current after the fall starts increasing again at V_m = 170 V (Fig. 5a). For the higher frequencies, at the same value of V_m, this portion first shrinks and then totally disappears (Fig. 6a). This correlates with the disappearance of the basic peak in the curves $C_e(V)$ in Fig. 3b. At T_s = 0.1 and 0.5 s and f = 200, 500, and 1000 Hz, the curve $I_p(F_p)$ (–Al conditions) exhibits the *N*-type NDR region (Fig. 6a). As T_s increases to ≥1 s, NDR changes to the *S* type. This is consistent with the shape of the curves $C_e(V)$ in Fig. 3b. Under the +Al conditions, the curve $I_p(F_p)$ exhibits the *N*-type NDR region (Figs. 5c and 6c). The NDR value grows with T_s and f. At the low frequencies f = 2, 10, and 50 Hz (Fig. 5c), NDR changes to the *S* type and disappears with increasing frequency (Fig. 6c). The value of T_s at which the *N*-type region appears drops when f increases: from T_s = 50 s at f = 10 Hz to T_s = 5 s at f = 1000 Hz.

For the continuous triggering mode, the *S*-type NDR region is observed at the low frequencies f = 2, 10, and 50 Hz under both conditions (±Al). The shapes of the curves $I_p(F_p)$ discussed above fully correlate with those of the curves $C_e(V)$ in Figs. 3a and 3b. In the pulse triggering mode, the increase in T_s causes the former curves to shift toward larger F_p as compared with the curves taken in the continuous triggering mode. At the high frequencies f = 200, 500, and 1000 Hz in the pulse triggering mode, the curves $I_p(F_p)$ in Fig. 6 also tend to larger F_p; however, in the continuous triggering mode, these curves exhibit neither *S*- nor *N*-type NDR

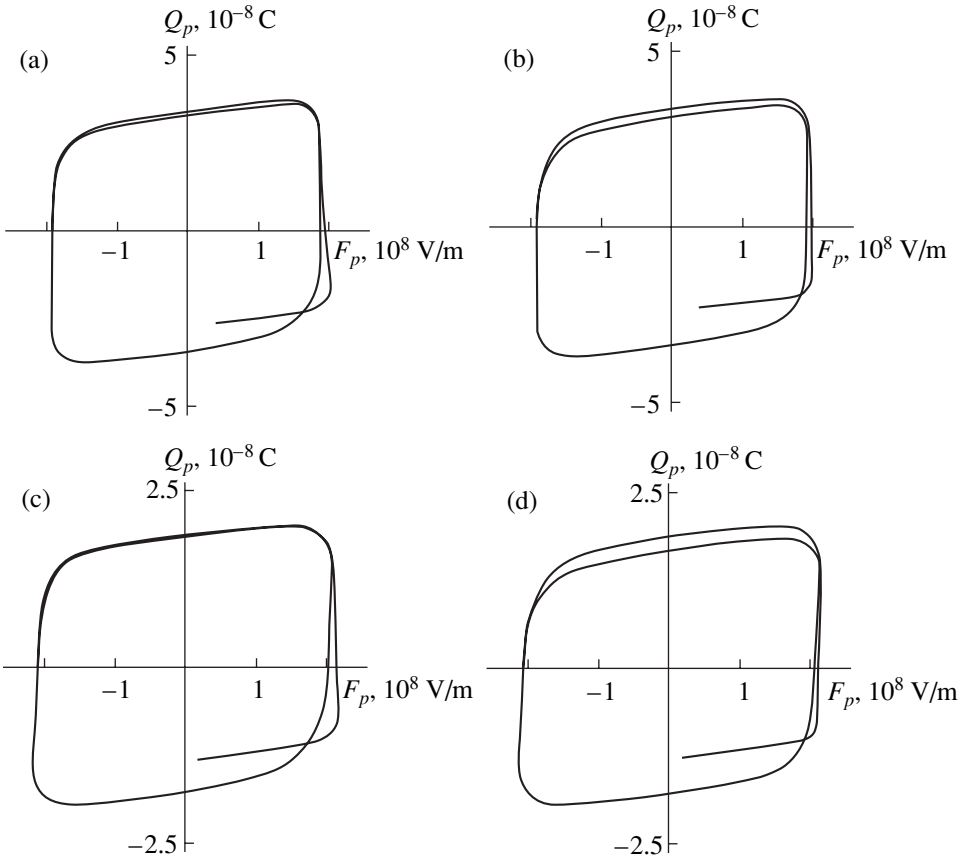

Fig. 4. $Q_p(F_p)$ curves for pulse triggering with T_s = 100 s. f = (a, b) 50 and (c, d) 1000 Hz. (a, c) –Al and (b, d) +Al conditions.

(Figs. 3a, 3b) and the growth of I_p with F_p is weaker than in the pulse triggering case.

The common features of the curves $I_p(F_p)$ (Figs. 5, 6) at all the frequencies f are as follows. (1) The peak of the current I_p for the –Al conditions in the pulse triggering mode is higher because of the appearance of the additional peak in the +Al conditions; (2) the curves shift toward higher values of the mean field F_p for the –Al conditions; (3) the lesser asymmetry of I_p and F_p between the ±Al conditions in the continuous triggering mode because of the absence of the additional I_p peak; (4) the current I_p and the field F_p grow with f because of the increase in $dV(t)/dt$ [see (1), (2), 12)].

The appearance and growth of the additional peaks in the $I_p(t)$ curves and the associated S- and N-type regions are clearly related to the triggering pulse period T_s. Therefore, we studied the T_s-dependences of the remanent polarization charge Q_{pol}, remanent polarization field F_{pol}, threshold field F_{pt} [see (9) and (10)], and field F_{pn} at which the N- and S-type NDR regions start (at f = 1000 Hz) in Figs. 5 and 6. The values of Q_{pol} and F_{pol} were found with the above initial conditions for $F_p(t)$, $Q_p(t)$, $I_p(F_p)$, and $Q_p(F_p)$. The values of F_{pt} were those when the curves $L(t)$ and $I_p(t)$ in Fig. 2 exceeded the background noise by two quantizing levels of the L or I_p amplitude for the total numbers of quantizing levels 100–200. The thus-obtained value of F_{pt} was accurate within ±3%. Eventually, the curves $F_{\text{pol}}(T_s)$, $F_{pt}(T_s)$, and $F_{pn}(T_s)$ were found to be well approximated by the expression

$$F = A\left[1 - \exp\left(-\frac{T_s}{\tau_A}\right)\right] + B\left[1 - \exp\left(-\frac{T_s}{\tau_B}\right)\right] + C \tag{14}$$

for all the frequencies f. Here, A and B for $F_{\text{pol}}(T_s)$ were negative and for $F_{pt}(T_s)$ and $F_{pn}(T_s)$, positive. The constants C were positive for all the functions.

For $F_{\text{pol}}(T_s)$, $|A|$ decreases from $\approx 7.3 \times 10^6$ to $\approx 1.6 \times 10^6$ V/m as f grows from 10 to 1000 Hz, C decreases from 5.5×10^7 to 2.6×10^7 V/m for the –Al conditions and to $\approx 2.4 \times 10^7$ V/m for +Al, and $|B| = (6.8 \pm 3) \times 10^6$ V/m. The time constants are τ_A = 0.2–3 s and $\tau_B = 32 \pm 7$ s. For $F_{pt}(T_s)$, A, B, and C are frequency-independent: $A = (3.4 \pm 0.6) \times 10^7$ V/m, $B = (1.6 \pm 0.4) \times 10^7$ V/m, and $C = (9.3 \pm 0.6) \times 10^7$ V/m. The time constants are τ_A = 0.4–4 s and τ_B = 30–100 s. For $F_{pn}(T_s)$, A,

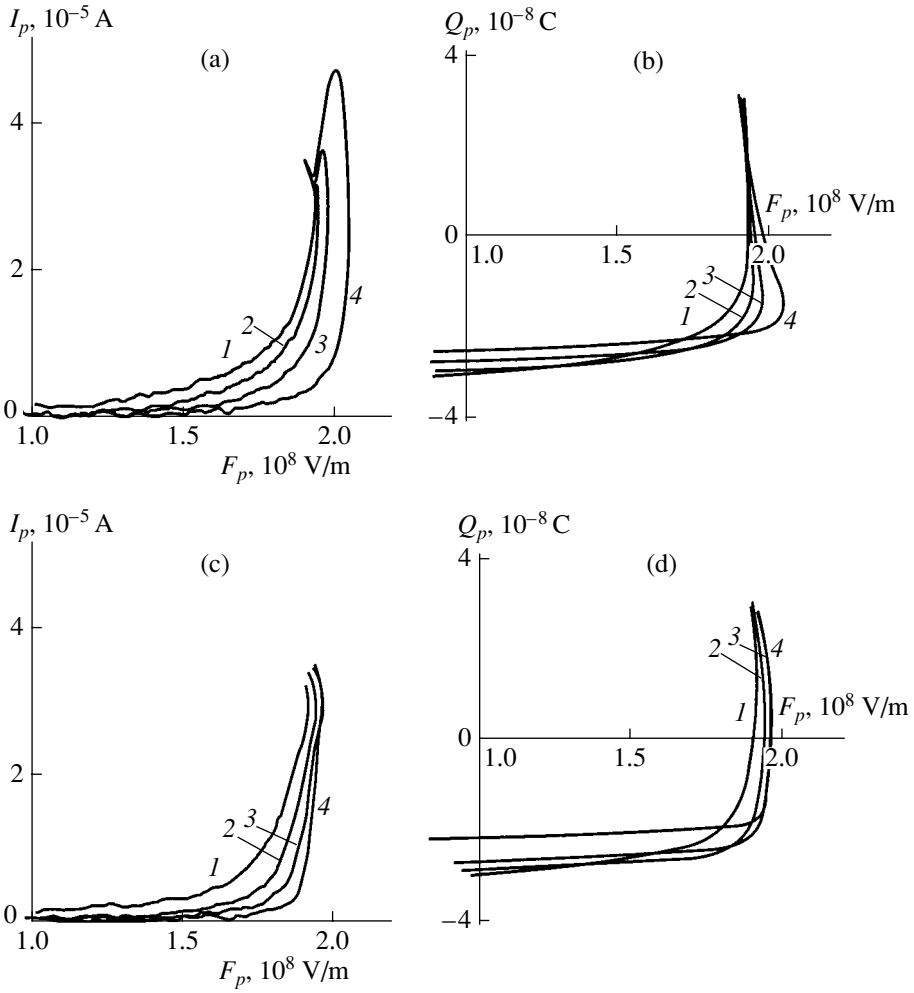

Fig. 5. (a, c) $I_p(F_p)$ and (b, d) $Q_p(F_p)$ for f = 50 Hz. (*1–4*) The same as in Fig. 3. (a, b) –Al and (c, d) +Al conditions.

C weakly grow as the frequency f rises from 10 to 1000 Hz: A, from $\approx 3.1 \times 10^6$ to 4.5×10^6 V/m; C, from 1.91×10^8 to 2.1×10^8 V/m for –Al and from 1.87×10^8 (f = 10 Hz) to 1.91×10^8 V/m (f = 50 Hz) for +Al. The values of B are $(9.5 \pm 3) \times 10^6$ V/m for –Al and $(2 \pm 0.35) \times 10^6$ V/m for +Al. The time constants are τ_A = 0.7–4 s and τ_B = 35–110 s.

Thus, the curve $F_{\text{pol}}(T_s)$ has two exponentially descending portions, while the curves $F_{pt}(T_s)$ and $F_{pn}(T_s)$ have exponentially ascending portions with the time constants $\tau_A \approx 1$ s and τ_B = 30–100 s. The spread in the values of τ_A, τ_B, A, B, and C is due to the small number of the T_s values taken into consideration. The depolarization time for the phosphor–insulator interface states was determined by increasing T_s to 60 min. The results obtained indicate that the additional peaks of I_e and the instantaneous brightness L (Figs. 1a, 2a, 2b) continue growing according to the law $1 - \exp(-T_s/\tau_i)$ with τ_i = 40 min, which is consistent with data in [6]. Since $\tau_i \gg \tau_A$ and τ_B, the effect of the field $F_{pi}(T_s)$ on the characteristics under study [expressions (2) and (12)] can be ignored.

The dependences of F_{pt} and F_{pn} on the residual field F_{pol} (Fig. 7) are direct evidence for the validity of formulas (2) and (8)–(10). As follows from Fig. 7, the field F_{pn} approximated by a straight line up to the measurement and computational errors declines with increasing F_{pol}. For the +Al conditions, the fields F_{pn} are always smaller (Figs. 5, 6) and the $F_{pn}(F_{\text{pol}})$ dependence is weaker. For the same T_s, F_{pn} also grows with f because the absolute value of F_{pol} decreases with increasing f. Accordingly, the F_{pn} vs. F_{pol} dependence becomes stronger as f rises.

The curves $F_{pt}(F_{\text{pol}})$ behave similarly to the curves $F_{pn}(F_{\text{pol}})$. The only difference is that F_{pt} rises much sharper when F_{pol} diminishes. Note that the rate of growth increases with f, while the absolute values of F_{pt} depend on f only weakly at the same values of T_s.

The results obtained can be explained as follows. The technology of phosphor preparation, like atomic

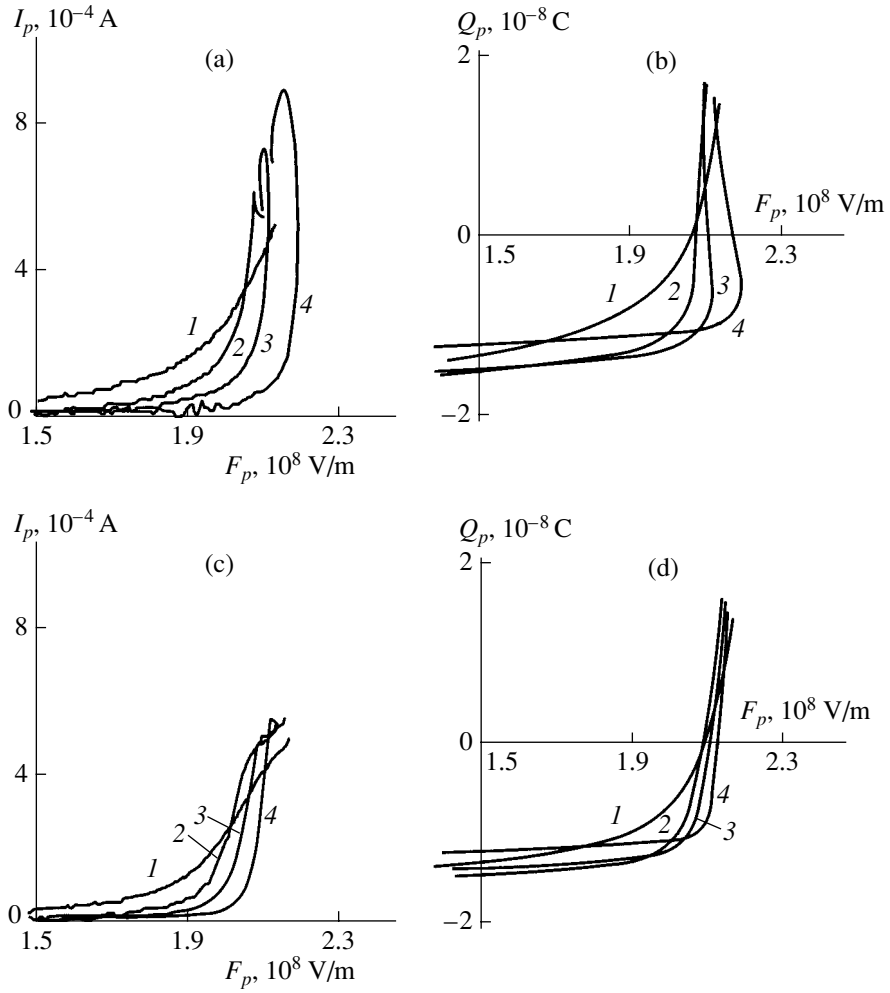

Fig. 6. (a, c) $I_p(F_p)$ and (b, d) $Q_p(F_p)$ for f = 1000 Hz. (*1–4*) The same as in Fig. 3.

layer epitaxy [2, 3], is such that a zinc deficiency arises at the lower phosphor–insulator interface. Accordingly, various lattice defects (zinc and sulfur vacancies, interstitial zinc, etc.), complexes, and their associated shallow and deep centers appear. Since the ZnS layer is polycrystalline, one could expect that the deep centers are nonuniformly distributed across the phosphor layer. In particular, the concentration of the zinc vacancies V_{Zn} is likely to decrease from the lower to the upper interface. On the contrary, that of the sulfur vacancies V_S rises. That the zinc vacancies play a major part in the formation of the space charge in the ZnS layer is corroborated by experimentally observing blue luminescence [5, 11]. For the donors V_{Zn}^- and V_{Zn}^{2-} due to the zinc vacancies, this corresponds to the energy positions 0.5–1.25 and 1.5–1.9 eV, respectively, above the valence band top E_v [12, 13]. The sulfur vacancies V_S^0 and V_S^+ may have the energy positions 0.2–1.6 and 0.6–2.0 eV, respectively, below the conduction band bottom E_c [12, 14]. They are deep acceptors. In a high electric field, these centers ionize and exchange charge with the formation of the space charge regions near the cathode and the anode. The mean field F_p in the phosphor is a superposition of the growing external field; growing and oppositely directed field F_{pi} due to charged states at the phosphor–insulator interface; and fields due to the space charges near the electrodes, F_{pc} and F_{pa}.

In the continuous triggering mode under the –Al conditions, once the carrier have tunneled from the interface states and the threshold field necessary to ionize the Mn^{2+} luminescent centers has been attained (as indicated by the increase in the instantaneous brightness, Figs. 1 and 2), the deep donors V_{Zn} at the anode begin to ionize [3]. The energy of ionization for them is higher than the energy of excitation of the Mn^{2+} centers (≈2.4 eV). As a result, the current I_p increases and the mean field F_p in the phosphor layer drops, since the field of the space charge of the ionized vacancies V_{Zn} is directed oppositely to the external field. This causes the *S*-type NDR region to appear in the *I–V* curves at low frequencies ($f \le 50$ Hz). At high frequencies ($f \ge$

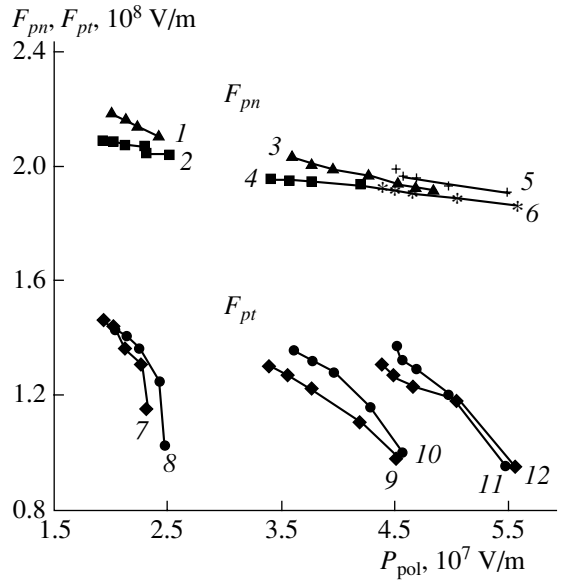

Fig. 7. (*1–6*) $F_{ps}(F_{pol})$ and (*7–12*) $F_{pt}(F_{pol})$. f = (*1, 2, 7, 8*) 1000, (*3, 4, 9, 10*) 50, and (*5, 6, 11, 12*) 10 Hz. (*1, 3, 5, 8, 10, 12*) –Al and (*2, 4, 6, 7, 9, 11*) +Al conditions.

200 Hz), the charge Q_p transferred through the phosphor (hence, the amount of the ionized centers and the space charge fields) is smaller than at the low frequencies. Therefore, higher external fields are necessary for the associated regions in the *I–V* curves to be observed. That is why *S*-type NDR is absent in the *I–V* curve (Fig. 6a).

In the continuous triggering mode under the +Al conditions, an additional space charge field exists near the cathode (lower interface). Here, the space charge is that of the donors V_{Zn} ionized in the preceding cycle. This causes tunnel emission form the interface states, the emission current being maximal in the continuous mode (Figs. 5c, 6c). As the external field and the field F_{pc} grow, the ionization of the acceptors V_S (or, more probably, the tunnel emission of holes into the valence band) near the cathode begins. Accordingly, the field F_{pc} decreases. Simultaneously, the rate of growth of the tunnel emission current and of the current I_p declines with increasing F_p, which, in turn, increases with frequency (Figs. 5c, 6c). At a further increase in the external field, the V_{Zn} vacancies at the anode ionize and the *S*-type NDR region appears at the low frequencies ($f \le$ 50 Hz) (Fig. 5c). As noted above, at the high frequencies ($f \ge 200$ Hz), the near-anode field does not reach the ionization field for the V_{Zn} vacancies, so that the *S*-type NDR region is absent (Fig. 6c). In the –Al conditions, the field of the V_S acceptors ionized in the preceding (+Al) excitation half-cycle enhances the near-anode field F_{pa}. Therefore, under the –Al conditions, the V_{Zn} vacancies ionize at the low frequencies $f \le$ 50 Hz.

In the pulse triggering mode, the deep centers acquire their initial charge state with increasing T_s once the external field has been off. For the donors, this process takes place with $\tau_A \approx 1$ s and includes hole tunneling from these centers into the valence band due to the remanent polarization field and the field of the space charge at the lower interface [5]. For the acceptors, this process ($\tau_B \ge 30$ s) includes electron tunneling from these centers into the conduction band. Under the +Al conditions, the tunnel emission current drops as the space charge field of the ionized V_{Zn} donors near the cathode decreases. When the external field grows, F_{pc} first increases and the acceptors exchange charge. For certain T_s, the field F_{pc}, tunnel emission current, and current I_p start decreasing, hence, the *N*-type NDR region in Figs. 5c and 6c. With a further increase in the external field at the low frequencies, the near-anode field reaches the ionization field of the V_{Zn} donors and the *S*-type NDR region appears (Fig. 5c). Under the –Al conditions, as T_s expands, the field of the ionized donors V_{Zn} near the cathode and that of the ionized acceptors V_S near the anode decrease; as a result, so do the tunnel emission current and current I_p (Figs. 5a, 6a). As the external field increases, first the V_{Zn} donors ionize, the current I_p near the anode grows, the mean field F_p drops, and the *S*-type NDR region appears. Then, the V_S acceptors near the cathode ionize, causing the tunnel emission current and the current I_p to decrease. With a subsequent growth of the external field at the low frequencies, I_p rises again but the field F_p drops because of the continuing ionization of the donor centers at the anode and the expansion of the space charge region associated with V_{Zn}. At the high frequencies ($f \ge$ 200 Hz) and small T_s ($T_s \le 1$ s), where some donors V_{Zn} had no time to recover the initial charge state and their field enhances the near-cathode field F_{pc}, the acceptors V_S ionize at the cathode and the *I–V* characteristic exhibits the *N*-type NDR (Fig. 6a). At long T_s, the near-cathode space charge field of the donors V_{Zn} declines, the acceptors do not ionize, and the *I–V* characteristic has only the *S*-type NDR with the subsequent decay of the current (Fig. 6a). The next region where I_p grows is not achieved because the external field is insufficient.

It is worthy to note that, in the continuous triggering mode, the tunnel emission current, current I_p, and instantaneous brightness *L* start growing from the lesser value of the mean field F_p (Figs. 1, 2, 5a, 5c, 6a, 6c). This is due to the reversal of the external field, which is absent in the pulse triggering mode with $V(t) = 0$ because of the time delay between the pulses.

Note also that the increase in the instantaneous brightness when the additional peaks of the current I_p due to the appearance of the space charges appear (Figs. 1, 2) indicates that the brightness can be increased by increasing the concentration of zinc vacancies and selecting special triggering modes.

Thus, we found that the operating (emission) mode of TF EL devices includes the ionization and recharge of deep centers of two types: V_{Zn} donors and V_S acceptors. They form space charges at the cathodic and the anodic parts of the phosphor layer. Because of the nonuniform distribution of the centers and the dopant across the layer, the electric performance and the illumination parameters of the device (including the appearance of *S*- and *N*-type NDR regions) depend on the polarity of the exciting voltage.

REFERENCES

1. A. Abu-Dayah, S. Kobayashi, and J. F. Wager, Appl. Phys. Lett. **62**, 744 (1993).
2. A. Abu-Dayah, J. F. Wager, and S. Kobayashi, J. Appl. Phys. **74**, 5575 (1993).
3. A. Abu-Dayah and J. F. Wager, J. Appl. Phys. **75**, 3593 (1994).
4. V. P. Singh and S. Krishna, J. Appl. Phys. **70**, 1811 (1991).
5. K. A. Neyts, D. Corlatan, P. De Visschere, *et al.*, J. Appl. Phys. **75**, 5339 (1994).
6. E. Bringuier, J. Appl. Phys. **66**, 1314 (1989).
7. E. Bringuier, Philos. Mag. B **75**, 209 (1997).
8. N. T. Gurin and O. Yu. Sabitov, Zh. Tekh. Fiz. **69** (5), 65 (1999) [Tech. Phys. **44**, 537 (1999)].
9. S. A. Garyainov and I. D. Abezgauz, *Semiconductor Devices with Negative Resistance* (Énergiya, Moscow, 1970).
10. N. T. Gurin, A. V. Shlyapin, and O. Yu. Sabitov, Pis'ma Zh. Tekh. Fiz. **27** (4), 12 (2001) [Tech. Phys. Lett. **27**, 138 (2001)].
11. K.-W. C. Yang and S. J. T. Owen, IEEE Trans. Electron Devices **ED-30**, 452 (1983).
12. F. A. Kröger, *The Chemistry of Imperfect Crystals* (Wiley, New York, 1964; Mir, Moscow, 1969).
13. J. D. Joseph and R. C. Neville, J. Appl. Phys. **48**, 1941 (1977).
14. I. K. Morozova and V. A. Kuznetsov, *Zinc Sulfide: Production and Properties* (Nauka, Moscow, 1987).

Translated by V. Isaakyan

Technical Physics, Vol. 46, No. 8, 2001, pp. 988–994. Translated from Zhurnal Tekhnicheskoĭ Fiziki, Vol. 71, No. 8, 2001, pp. 59–65.

OPTICS, QUANTUM ELECTRONICS

Interference Effects in X-ray Radiation from Relativistic Electrons Moving at a Small Angle to an Atomic Plane

N. N. Nasonov*, G. P. Pokhil, and A. F. Tulinov****

** Kharkov Institute of Physics and Technology, Ukranian Scientific Center, Akademicheskaya ul. 1, Kharkov, 61108 Ukraine*

*** Skobeltsyn Research Institute of Nuclear Physics, Moscow State University, Vorob'evy gory, Moscow, 119899 Russia*

e-mail: pokhil@anna19.npi.msu.su

Received September 26, 1999

Abstract—X-ray radiation of relativistic electrons interacting with a set of parallel atomic planes is considered. The anomalous behavior of the radiation due to the interplay of parametric and coherent bremsstrahlung emission mechanisms, which simultaneously occur under specific conditions, is studied. © *2001 MAIK "Nauka/Interperiodica".*

INTRODUCTION

Synchrotrons—currently main sources of quasimonochromatic pencil X-ray beams, employed in research and applications—are very complex and expensive. Therefore, alternative methods of generating such radiation are needed. The use of parametric X-ray radiation (PXR) from relativistic electrons interacting with a crystal [1–3] seems to be a promising approach in this area. The energy of PXR quanta increases with decreasing the angle of orientation of the electron momentum with respect to a reflecting crystallographic plane. This allows one to reduce the electron energy. As a result, it can be one to two orders of magnitude lower than in synchrotrons. If the orientation angle is comparable to the characteristic emission angle of a relativistic particle $\gamma^{-1} = m/\varepsilon$ (m and ε are the mass and the energy of an emitting electron, respectively), the interference with coherent bremsstrahlung of the electron becomes significant [4, 5].

This article reports in-depth analysis of this interference effect. Unlike [4], the smallness of the orientation angle is used in the explicit form, which provides a clearer insight into the radiation mechanism and properties. We also consider the effect of multiple scattering of emitting electrons. Finally, the feasibility of raising the spectral and angular densities of the radiation via the interference effect is discussed.

RADIATION AMPLITUDE

Let us consider the structure of an electromagnetic field generated by a relativistic particle of charge q that moves in a crystal. The Maxwell equation in this case is given by

$$(k^2 - \omega^2)\mathbf{E}_{\mathbf{k}\omega} - \mathbf{k}(\mathbf{k}, \mathbf{E}_{\mathbf{k}\omega}) = 4\pi i\omega\left(\mathbf{j}_{\mathbf{k}\omega} + \frac{q}{(2\pi)^4}\int dt\mathbf{v}_q e^{i\omega t - i\mathbf{k}\mathbf{r}_q}\right). \quad (1)$$

Here, $\mathbf{E}_{\mathbf{k}\omega}$ is the Fourier transform of the electric field, $\mathbf{r}_q(t)$ is the fast particle path, $\mathbf{v}_q = (d/dt)\mathbf{r}_q$, $\mathbf{j}_{\mathbf{k}\omega}$ is the Fourier transform of the density of the particle-field-induced electron current, and $(\mathbf{k}, \mathbf{E}_{\mathbf{k}\omega})$ is the scalar product. In the energy range characteristic of X-rays,

$$I \ll \omega \ll m \quad (2)$$

(where I is the mean ionization potential of atoms in the crystal and m is the mass of an electron), both the binding energy of an electron in the atom and the comptonization ω due to fast particle scattering by the atom can be neglected. Then, the operator of the electron current density is described by the expression [6]

$$\hat{\mathbf{j}} = -\frac{e^2}{m}\mathbf{A}(\mathbf{r}, t)\hat{n}, \quad \hat{n} = \sum_{\alpha}\sum_{\beta=1}^{M}\delta(\mathbf{r} - \mathbf{r}_\alpha - \mathbf{r}_{\alpha\beta}), \quad (3)$$

which is common in the theory of X-ray scattering. Here, $\mathbf{A}$ is the potential vector of the field, $\mathbf{r}_\alpha$ are the coordinates of nuclei, and $\mathbf{r}_{\alpha\beta}$ are the coordinates of electrons in the atom.

From (1) and (3), we obtain

$$(k^2 - \omega^2)\mathbf{E}_{\mathbf{k}\omega} - \mathbf{k}(\mathbf{k}, \mathbf{E}_{\pi\omega}) + \int dk' G(\mathbf{k}' - \mathbf{k})\mathbf{E}_{\pi'\omega} = \frac{i\omega q}{4\pi^3}\int dt\mathbf{v}_q e^{i\omega t - i\mathbf{k}\mathbf{r}_q}, \quad (4)$$

1063-7842/01/4608-0988$21.00

$$G(\mathbf{k}'-\mathbf{k}) = \frac{e^2}{2\pi^2 m}\sum_{\alpha}\sum_{\beta=1}^{Z}\delta(\mathbf{r}-\mathbf{r}_\alpha-\mathbf{r}_{\alpha\beta}).$$

This equation describes both scattering and refractive properties of a crystal. To proceed to the analysis, we must separate the coherent component from the function $G(\mathbf{k}' - k)$. This component is responsible for refraction. Averaging $G(\mathbf{k}' - k)$ over the nuclear and electron coordinates, we come to

$$\begin{gathered} G(\mathbf{k}'-\mathbf{k}) \equiv \langle G(\mathbf{k}'-\mathbf{k})\rangle + \tilde{G}(\mathbf{k}'-\mathbf{k}), \\ \langle G(\mathbf{k}'-\mathbf{k})\rangle = \omega_0^2\delta(\mathbf{k}'-\mathbf{k}), \quad \omega_0^2 = \frac{4\pi Z e^2 n_0}{m}, \end{gathered} \tag{5}$$

where ω_0 is the plasma frequency of the medium.

Substituting (5) into (4) yields an equation that differs from (4) in designations:

$$\begin{gathered} G(\mathbf{k}'-\mathbf{k}) \longrightarrow \tilde{G}(\mathbf{k}'-\mathbf{k}), \quad k^2-\omega^2 \longrightarrow k^2-k_0^2, \\ k_0^2 = \omega^2\left(1-\frac{\omega_0^2}{\omega^2}\right) = \omega^2\varepsilon(\omega). \end{gathered} \tag{6}$$

If scattering is assumed to be weak (the kinematic approximation in the theory of diffraction), a solution to Eq. (4) is found by iteration:

$$\begin{aligned} \mathbf{E}_{\mathbf{k}\omega} \approx \frac{i\omega q}{4\pi^3}\frac{1}{k^2-k_0^2}\int dt e^{i\omega t}\Bigg[\left(\mathbf{v}_q-\frac{\mathbf{k}}{k_0^2}\mathbf{k}\mathbf{v}_q\right)e^{-i\mathbf{k}\mathbf{r}_q} \\ -\int\frac{d\mathbf{k}'}{k'^2-k}\tilde{G}(\mathbf{k}'-k)\left(\mathbf{v}_q-\frac{\mathbf{k}'}{k_0^2}\mathbf{k}'\mathbf{v}_q-\frac{\mathbf{k}'}{k_0^2} \right. \\ \left.\times\left(\mathbf{k}\mathbf{v}_q-\frac{\mathbf{k}\mathbf{k}'}{k_0^2}\mathbf{k}'\mathbf{v}_q\right)\right)e^{-i\mathbf{k}'\mathbf{r}_q}\Bigg]. \end{aligned} \tag{7}$$

It is easy to check that the first term in (7), which is proportional to $e^{-i\mathbf{k}\mathbf{r}_q}$, describes the equilibrium electromagnetic field of a fast particle moving in a medium of permittivity $\varepsilon(\omega)$; the second term stands for the scattering of this field by fluctuations of the electron density of the medium.

To find the spectral–angular distribution of the radiation, it is necessary to take the Fourier integral $\mathbf{E}_\omega(\mathbf{r}) = \int d^3k E_{\mathbf{k}\omega}e^{i\mathbf{k}\mathbf{r}}$. We are interested in the radiation field in the wave zone and integrate over d^3k by using asymptotic methods:

$$\mathbf{E}_\omega = \int d^3k\mathbf{E}_{\mathbf{k}\omega}e^{i\mathbf{k}\mathbf{r}} = \mathbf{A}_\mathbf{n}\frac{e^{ik_0 r}}{r},$$

$$\begin{aligned} \mathbf{A}_\mathbf{n} = \frac{i\omega q}{2\pi}\int dt e^{i\omega t}\Bigg[(\mathbf{v}_q-\mathbf{n}\mathbf{n}\mathbf{v}_q)e^{-ik_0\mathbf{n}\mathbf{r}_q}-\int\frac{d^3k}{k^2-k_0^2} \\ \times\tilde{G}(\mathbf{k}-k_0\mathbf{n})\left(\mathbf{v}_q-\frac{\mathbf{k}}{k_0^2}\mathbf{k}\mathbf{v}_q-\mathbf{n}\left(\mathbf{n}\mathbf{v}_q-\frac{\mathbf{n}\mathbf{k}}{k_0^2}\mathbf{k}\mathbf{v}_q\right)\right)e^{-i\mathbf{k}\mathbf{r}_q}\Bigg], \end{aligned}$$

where $\mathbf{n}$ is the unit vector in the direction of radiation.

It is easy to see that the first term in (8) does not contribute to the radiation if the fast particle moves uniformly and rectilinearly. To estimate the contribution from bremsstrahlung, we take the integral in the first term by parts and express the resulting acceleration of the fast particle in terms of the crystalline potential using the equation of motion. If we assume that the trajectory $\mathbf{r}_q(t)$ in the resulting expression for the amplitude $\mathbf{A}_\mathbf{n}$ is rectilinear (the dipole approximation in theory of radiation, which is valid if the scattering angle of the particle is less than γ^{-1} [7]), the final expression for radiation amplitude takes the form

$$\begin{aligned} \mathbf{A}_\mathbf{n} = -iq\int d^3k\left[\frac{1}{k^2}Q(\mathbf{k})\mathbf{a}_\mathbf{k}+\frac{1}{k^2 2k_0\mathbf{n}\mathbf{k}}\tilde{G}(\mathbf{k})\mathbf{b}_\mathbf{k}\right] \\ \times\delta[\omega(1-\sqrt{\varepsilon}\mathbf{n}\mathbf{v})-\mathbf{k}\mathbf{v}], \\ Q(\mathbf{k}) = \frac{eq}{2\pi^2 m\gamma}\sum_\alpha e^{i\mathbf{k}\mathbf{r}_\alpha}\left(Z-\sum_{\beta=1}^{Z}e^{i\mathbf{k}\mathbf{r}_{\alpha\beta}}\right), \\ \mathbf{a}_\mathbf{k} = \frac{\mathbf{k}-\mathbf{v}\cdot\mathbf{k}\mathbf{v}}{1-\sqrt{\varepsilon}\mathbf{n}\mathbf{v}}-\frac{\mathbf{n}-\sqrt{\varepsilon}\mathbf{v}}{(1-\sqrt{\varepsilon}\mathbf{n}\mathbf{v})^2}(\mathbf{n}\mathbf{k}-\mathbf{n}\mathbf{v}\mathbf{n}\mathbf{k}), \end{aligned} \tag{8}$$

$$\begin{aligned} \tilde{G}(\mathbf{k}) = \frac{e^2}{2\pi^2 m}\sum_\alpha\sum_{\beta=1}^{Z}e^{i\mathbf{k}(\mathbf{r}_\alpha+\mathbf{r}_{\alpha\beta})}-\omega_0^2\delta(\mathbf{k}), \\ \mathbf{b}_\mathbf{k} = \mathbf{v}\frac{\mathbf{k}\mathbf{v}}{1-\sqrt{\varepsilon}\mathbf{n}\mathbf{v}}-\mathbf{k}\frac{1}{\varepsilon}-\mathbf{n}\left(\mathbf{n}\mathbf{v}\frac{\mathbf{k}\mathbf{v}}{1-\sqrt{\varepsilon}\mathbf{n}\mathbf{v}}-\mathbf{n}\mathbf{k}\frac{1}{\varepsilon}\right). \end{aligned} \tag{9}$$

Note that expression (9) does not include any suggestions about the structure of the medium. Therefore, it applies to any crystalline matter where the emission properties of fast electrons are studied.

The term proportional to $Q(\mathbf{k})$ corresponds to the bremsstrahlung of a fast particle scattered by nuclei and atomic electrons; the term proportional to $\tilde{G}(\mathbf{k})$ refers to the polarization bremsstrahlung of the particle scattered by atomic electrons [8]. Before entering into a study of the spectral–angular properties of the radiation, we note that, in the nonrelativistic limit ($v \ll 1$), amplitude (9) correctly describes the well-known interference effect [9] of mutual suppression of polarization bremsstrahlung and bremsstrahlung due to scattering by electrons when a nonrelativistic electron emits. Indeed, at $v \ll 1$, it follows from (9) that $\mathbf{a}_\mathbf{k} \approx -\mathbf{b}_\mathbf{k} \approx \mathbf{k} - \mathbf{n}\cdot\mathbf{n}\mathbf{k}(\varepsilon \approx 1)$ and $k^2 + 2\omega\sqrt{\varepsilon}\,\mathbf{n}\mathbf{k} \approx k^2$; therefore, at $q = -e$ ($e > 0$), the contributions from the electrons of the

medium to bremsstrahlung and polarization bremsstrahlung cancel out. As a result, the total radiation is reduced to the bremsstrahlung of the nonrelativistic electron scattered by nuclei [9].

SPECTRAL–ANGULAR DISTRIBUTION OF THE RADIATION

From (9), an expression for the spectral–angular distribution of the number of emitted quanta has the form

$$\omega\frac{dN}{d\omega dO} = \langle|\mathbf{A_n}|^2\rangle = \sum_{j=1}^{3}\omega\frac{dN^{(j)}}{d\omega dO}, \qquad (10)$$

where the first term is bremsstrahlung, the second is polarization bremsstrahlung, and the third describes the interference of the bremsstrahlung and polarization bremsstrahlung amplitudes.

Let us first consider the properties of bremsstrahlung:

$$\omega\frac{dN^1}{d\omega dO} = \omega\frac{dN^{br}}{d\omega dO} = q^2\int\frac{d^3k}{k^2}\frac{d^3k'}{k'^2}\langle Q(\mathbf{k})Q^*(\mathbf{k}')\rangle \qquad (11)$$

$$\times\mathbf{a_k}\mathbf{a_{k'}}\delta[\omega(1-\sqrt{\varepsilon}\mathbf{nv})-\mathbf{kv}]\delta[\omega(1-\sqrt{\varepsilon}\mathbf{nv})-\mathbf{k}'\mathbf{v}].$$

Here, angular brackets mean averaging over the random quantities $\mathbf{r}_\alpha$ and $\mathbf{r}_{\alpha\beta}$. In our case (crystalline medium), $\mathbf{r}_\alpha = \mathbf{r}_n + \mathbf{r}_{nl} + \mathbf{u}_{nl}$, where $\mathbf{r}_n$ is the position of the nth unit cell of the crystal, $\mathbf{r}_{nl}$ is the equilibrium position of the lth atom in the nth unit cell, and $\mathbf{u}_{nl}$ is the thermal displacement of the atom. Averaging over the thermal displacements $\mathbf{u}_{nl}$ yields the conventional Debye–Waller factor. Averaging over the electron coordinates $\mathbf{r}_{nl\beta}$ within the statistical model of atom with exponential shielding yields

$$\langle Q(\mathbf{k})Q^*(\mathbf{k}')\rangle = \frac{2e^2n_0}{\pi m^2\gamma^2}\left\{Z^2\frac{k^4R^4}{(1+k^2R^2)^2}\right.$$

$$\times\left[(2\pi)^3n_0|S(\mathbf{k})|^2e^{-k^2u^2}\sum_{\mathbf{g}}\delta(\mathbf{k}-\mathbf{g})+1-e^{-k^2u^2}\right] \qquad (12)$$

$$\left.+Z\left(1-\frac{1}{(1+k^2R^2)^2}\right)\right\}\delta(\mathbf{k}-\mathbf{k}')\equiv\frac{2e^4n_0}{\pi m^2\gamma^2}F^{br}(\mathbf{k})\delta(\mathbf{k}-\mathbf{k}'),$$

where R is the shielding radius in the statistical model of atom,

$$S(\mathbf{k}) = \frac{1}{N}\sum_{l=1}^{N}e^{i\mathbf{k}\mathbf{r}_{nl}},$$

N is the number of atoms in the unit cell of volume Ω, $n_0 = N/\Omega$, u is the rms amplitude of the thermal displacements of the atom, and $\mathbf{g}$ is the vector of the reciprocal crystal lattice.

The terms in (12) that contain the delta function $\delta(\mathbf{k}-\mathbf{g})$ refer to the coherent bremsstrahlung of a fast particle in the crystal. The term proportional to the factor $(1-e^{-k^2u^2})$ stands for the noncoherent bremsstrahlung of shielded crystal atoms. The term proportional to the number of atomic electrons Z separates out the contribution of the electrons of the medium to the bremsstrahlung (Landau–Rumer correction [10]).

Substituting (12) into general formula (11) yields the following spectral–angular distribution of the bremsstrahlung intensity:

$$\omega\frac{dN^{br}}{dtd\omega dO} = \frac{e^6n_0}{\pi^2m^2\gamma^2(1-\sqrt{\varepsilon}\mathbf{nv})^2}$$

$$\times\int\frac{d^3k}{k^4}\left(\mathbf{k}-\mathbf{v}\cdot\mathbf{kv}-\frac{\mathbf{n}-\sqrt{\varepsilon}\mathbf{v}}{1-\sqrt{\varepsilon}\mathbf{nv}}(\mathbf{nk}-\mathbf{nvnk})\right)^2 \qquad (13)$$

$$\times F^{br}(\mathbf{k})\delta[\omega(1-\sqrt{\varepsilon}\mathbf{nv})-\mathbf{kv}].$$

The distribution for the polarization bremsstrahlung intensity is obtained in a similar way:

$$\omega\frac{dN^{(2)}}{dtd\omega dO} = \omega\frac{dN^{pb}}{dtd\omega dO} = \frac{e^6n_0}{\pi^2m^2}\int\frac{d^3k'}{(k^2+2\omega\sqrt{\varepsilon}\mathbf{nk})^2}$$

$$\times\left(\mathbf{v}\omega-\mathbf{k}\frac{1}{\varepsilon}-\mathbf{n}\left(\mathbf{nv}\omega-\mathbf{nk}\frac{1}{\varepsilon}\right)\right)^2$$

$$\times F^{pb}(\mathbf{k})\delta(\omega(1-\sqrt{\varepsilon}\mathbf{nv})-\mathbf{kv}), \qquad (14)$$

$$F^{pb}(\mathbf{k}) = Z^2\frac{1}{(1+k^2R^2)^2}\left[(2\pi)^3n_0|S(\mathbf{k})|^2e^{-k^2u^2}\right.$$

$$\left.\times\sum_{\mathbf{g}}\delta(\mathbf{k}-\mathbf{g})+1-e^{-k^2u^2}\right]+Z\left(1-\frac{1}{(1+k^2R^2)^2}\right).$$

The interference term in (10) turns out to be proportional to the sign of the charge of the fast particle:

$$\omega\frac{dN^{(3)}}{dtd\omega dO}\equiv\omega\frac{dN^{\mathrm{int}}}{dtd\omega dO} = \mathrm{sgn}(q)\frac{2e^6n_0}{\pi^2m^2\gamma(1-\sqrt{\varepsilon}\mathbf{nv})}$$

$$\times\int\frac{d^3k}{k^2(k^2+2\omega\sqrt{\varepsilon}\mathbf{nk})}\left(\mathbf{v}\omega-\mathbf{k}\frac{1}{\varepsilon}-\mathbf{n}\left(\mathbf{nv}\omega-\mathbf{nk}\frac{1}{\varepsilon}\right)\right)$$

$$\times\left(\mathbf{k}-\mathbf{vkv}-\frac{\mathbf{n}-\sqrt{\varepsilon}\mathbf{v}}{1-\sqrt{\varepsilon}\mathbf{nv}}(\mathbf{nk}-\mathbf{nvkv})\right)F^{\mathrm{int}}(\mathbf{k}) \qquad (15)$$

$$\times\delta(\omega(1-\sqrt{\varepsilon}\mathbf{nv})-\mathbf{kv}),$$

$$F^{\text{int}}(\mathbf{k}) = Z^2\frac{k^2R^2}{(1+k^2R^2)^2}\Bigg[(2\pi)^3 n_0|S(\mathbf{k})|^2 e^{-k^2u^2} \times \sum_{\mathbf{g}}\delta(\mathbf{k}-\mathbf{g}) + 1 - e^{-k^2u^2}\Bigg] - Z\left(1-\frac{1}{(1+k^2R^2)^2}\right).$$

It is worthy to note some general properties of the radiation studied. First [11], the polarization bremsstrahlung component in (14) that is coherent throughout the crystal is adequate to well-known PXR [1–3]. The latter is usually considered in terms of the macroscopic approach [12–14]. When comparing the bremsstrahlung and polarization bremsstrahlung components that are incoherent over the crystal but coherent over the atomic electrons, we observe the drastically different effects of the thermal vibrations of crystal atoms on the above radiation mechanisms. From the expression for $F^{br}(\mathbf{k})$, it follows that the basic contribution to the bremsstrahlung is due to large transferred momenta, $k > R^{-1}$, i.e., particle–atom collisions with small impact parameters, $b < R^{-1}$ (the contribution from the collisions with $b \gg R^{-1}$ is suppressed because the nuclei are shielded by the atomic electrons). On the other hand, the same expression shows that the polarization bremsstrahlung yield depends largely on the collisions with impact parameters $b > R^{-1}$. The contribution of the collisions with $b < R^{-1}$ to the polarization bremsstrahlung component that is coherent over the atomic electrons is suppressed, since the parts of the electron coat on the opposite sides of the fast particle trajectory shift in the opposite directions, decreasing the coherent induced current of the atomic electrons responsible for polarization bremsstrahlung. Because of these differences, the factor $(1 - e^{-k^2u^2})$ entering into the cross sections is close to unity for bremsstrahlung and is negligible for polarization bremsstrahlung. Thus, the incoherent component of the polarization bremsstrahlung is sharply suppressed [15] unlike the same component of the bremsstrahlung.

Note also that the incoherent parts of the cross sections of bremsstrahlung and polarization bremsstrahlung and the interference cross section have opposite signs. To explain this fact, we note that the last-listed cross section [see (15)] is proportional to the averaged product of the varying current of a fast particle scattered by the electrons of the medium times the electron current induced by the particle. Obviously, these currents are oppositely directed; hence, the sign "minus" in the formula for $F^{\text{int}}(\mathbf{k})$. On the other hand, the correlators $\langle Q(\mathbf{k})Q^*(\mathbf{k}')\rangle$ and $\langle G(\mathbf{k})G^*(\mathbf{k}')\rangle$ average the quantities of a similar physical nature, hence, the sign "plus" in the associated terms in (12) and (14).

In this article, we will consider only the radiation component that is coherent throughout the crystal. It is due to the scattering of both the fast particle and its field by a set of parallel crystallographic planes. The planes are specified by the reciprocal lattice vector $\mathbf{g}$. The general expression for completely coherent radiation follows from (12)–(15):

$$\omega\frac{dN_{\mathbf{g}}}{dtd\omega dO} = \frac{8\pi Z^2e^6n_0^2|S(\mathbf{g})|^2e^{-g^2u^2}}{m^2(1+g^2R^2)^2}\Bigg[\text{sgn}(q)\frac{R^2}{\gamma(1-\sqrt{\varepsilon}\mathbf{nv})} \times\left(\mathbf{g}-\mathbf{v}\cdot\mathbf{gv}-\frac{\mathbf{n}-\sqrt{\varepsilon}\mathbf{v}}{1-\sqrt{\varepsilon}\mathbf{nv}}(\mathbf{ng}-\mathbf{nvgv})\right) + \frac{1}{g^2+2\omega\sqrt{\varepsilon}\mathbf{ng}} \times\left(\mathbf{v}\omega-\mathbf{g}\frac{1}{\varepsilon}-\mathbf{n}\left(\mathbf{nv}\omega-\mathbf{ng}\frac{1}{\varepsilon}\right)\right)\Bigg]^2\delta(\omega(1-\sqrt{\varepsilon}\mathbf{nv})-\mathbf{gv}). \quad (16)$$

Note that this expression includes the interference of the bremsstrahlung and polarization bremsstrahlung components in the explicit form.

For further analysis, it is convenient to introduce two-dimensional variables $\mathbf{\Psi}$ and $\mathbf{\Theta}$, which characterize the angular spread of a fast particle beam and the angular distribution of emitted photons, respectively. We assume that

$$\mathbf{v} = \mathbf{e}_1\left(1-\frac{1}{2}\gamma^2-\frac{1}{4}\Psi^2\right)+\mathbf{\Psi},\quad \mathbf{e}_1\mathbf{\Psi}=0,$$
$$\mathbf{n} = \mathbf{e}_2\left(1-\frac{1}{2}\Theta^2\right)+\mathbf{\Theta},\quad \mathbf{e}_2\mathbf{\Theta}=0, \quad (17)$$

where the unit vector $\mathbf{e}_1$ is aligned with the axis of a beam of emitting particles and the unit vector $\mathbf{e}_2$, with the detector axis. In experiments, the positions of both vectors are fixed; as a rule, $\mathbf{e}_1\mathbf{e}_2 = \cos\varphi$ (φ = const, parentheses mean the scalar product). However, the crystal can rotate about the beam axis by means of a goniometer (in this case, the direction of the reciprocal lattice vector $\mathbf{g}$ is changed). Note also that the vectors $\mathbf{e}_1$, $\mathbf{e}_2$, and $\mathbf{g}$ are usually coplanar in experiments. Here, of particular interest is the dependence of the distribution of the energy (or the number of quanta) emitted on the angle between a fast particle and a reflecting crystallographic plane. In the problem considered, the particle orientation is specified by the angle Θ' that is reckoned from the reflecting plane and strictly corresponds to the Bragg resonance condition (in Fig. 1, the directions of change of the components $\Psi_\parallel$ and $\Theta_\parallel$ are also shown; the components $\Psi_\perp$ and $\Theta_\perp$ vary in the plane normal to the plane of the figure).

When substituting expressions (17) into general formula (16), we assume that φ^2 is much smaller than unity but much larger than the parameter γ^{-2} (the angular range $\varphi \approx \gamma^{-1}$ calls for special consideration and is

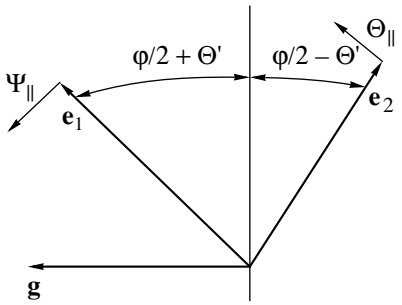

Fig. 1. Angular variables of the problem.

beyond the scope of our report). In the new variables, the spectral–angular distribution of the total radiation takes the form

$$\omega\frac{dN_{\mathbf{g}}}{dtd\omega d^2\Theta} = W_{\mathbf{g}}P(\Theta', \mathbf{\Omega})\delta\left(\omega - \frac{g}{\varphi}\left(1 + \frac{2\Theta'}{\varphi}\right)\right),$$

$$W_{\mathbf{g}} = \frac{e^2\omega_0^4|S(\mathbf{g})|^2 e^{-g^2u^2}}{\pi g^2}\frac{}{(1 + g^2R^2)^2},$$

$$P = \frac{4g^4R^4}{\gamma^2\varphi^6} + \frac{\Omega^2}{(\gamma^{-2} + \chi + \Omega^2)^2} \qquad (18)$$

$$- \mathrm{sgn}(q)\frac{4g^2R^2}{\gamma\varphi^3}\frac{\Omega_\parallel}{\gamma^{-2} + \chi + \Omega^2}.$$

In this expression,

$$\chi = \frac{\omega_0^2}{\omega^2}, \quad \Omega^2 = \Omega_\parallel^2 + \Omega_\perp^2, \quad \Omega_\parallel = 2\Theta' + \Theta_\parallel + \Psi_\parallel,$$

$$\Omega_\perp = \Theta_\perp - \Psi_\perp.$$

THE EFFECT OF INTERFERENCE ON THE ORIENTATION DEPENDENCE OF THE RADIATION YIELD

Let us take advantage of expression (18) in order to analyze the radiation yield vs. orientation angle dependence. We first consider the yield of collimated radiation ($\Theta^2 \ll \gamma^{-2}$; in actual conditions, the aperture angle Θ_d of X-ray detectors is usually much smaller than γ^{-1}) generated by a beam with a small initial divergence, $\Psi_0 \ll \gamma^{-1}$, in a thin crystal (the multiple scattering angle of emitting particles across the crystal thickness L must be less than γ^{-1}). Under these conditions, the number of quanta emitted vs. Θ' is given by the simple function

$$N_{\mathbf{g}} = \pi\gamma^2\Theta_d^2 W_{\mathbf{g}}\frac{L\varphi}{g}T(\alpha, \xi, x),$$

$$T = \frac{1}{1 + \frac{x}{\xi}}\left(-\mathrm{sgn}(q)\alpha + \frac{x}{1 + x^2}\right)^2, \qquad (19)$$

where $\alpha = (2g^2R^2)/(\gamma^2\varphi^3)$, $\xi = \gamma\varphi$, and $x = 2\gamma\Theta'$.

In (19), it is taken into account that the quantity

$$\gamma^2\chi = \frac{\gamma^2\varphi^2\omega_0^2}{g^2}$$

should be small within the kinematic approximation used to derive (16) [15].

Orientation curves $T(x)$ constructed at various values of α and $\xi = 20$ for electrons and positrons are shown in Figs. 2 and 3, respectively. Here, also shown are orientation dependences of the polarization bremsstrahlung yield without regard for the bremsstrahlung ($\alpha = 0$).

The significant effect of interference on the polarization bremsstrahlung behavior is obvious. In terms of the X-ray source efficiency, of most importance is the

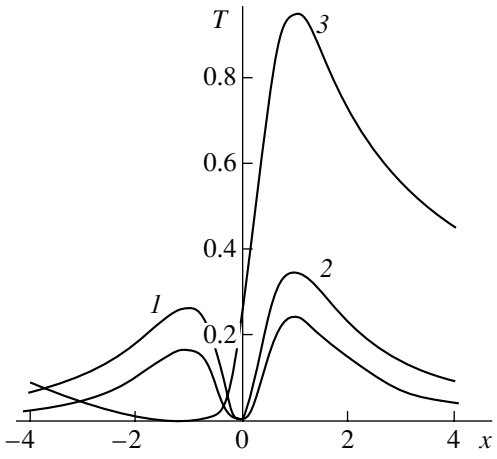

Fig. 2. Orientation dependence of the radiation emitted by electrons. α = (*1*) 0, (*2*) 0.1, and (*3*) 0.5. ξ = 20.

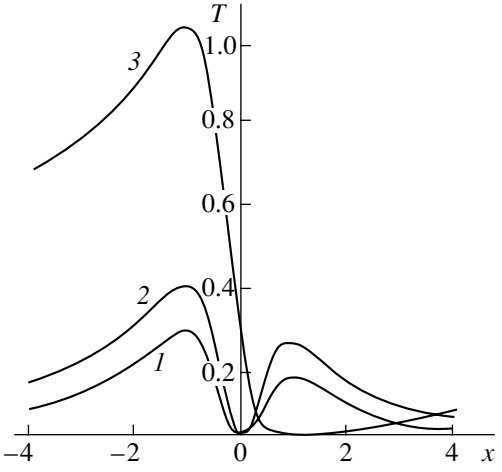

Fig. 3. Orientation dependence of the radiation emitted by positrons. The parameters are the same as in Fig. 2.

possibility of increasing the spectral–angular radiation density in the range of hard X-ray quanta (for emitting electrons, as follows from Fig. 2).

The simple function $T(0, \xi, x)$ allows us to easily estimate the optimum values of the X-ray source parameters. For the exact calculation of the parameters, one should take into consideration the initial divergence of the multiple scattering of an emitting particle beam, as well as the photoabsorption of X-ray quanta. When considering hard quanta [their characteristic energy $\omega_{\text{eff}} = \omega_b = g/\varphi$ grows with decreasing the radiation angle φ according to (18)], we will assume that the photoabsorption length is much greater than the crystal thickness L. Using the beam particle distribution function

$$f(t, \boldsymbol{\Psi}) = \frac{1}{\pi(\Psi_0^2 + \Psi_S^2 t)} \exp\left(-\frac{\Psi^2}{\Psi_0^2 + \Psi_S^2 t}\right)$$

(Ψ_0 is the initial divergence of the beam and Ψ_S is the rms angle of multiple scattering per unit length) and assuming that the condition of strong collimation $\gamma^2\Theta_d^2 \ll 1$ is met, we find a more general result from (18):

$$N_{\mathbf{g}} = \frac{\pi\Theta_d^2}{\Psi_S} W_{\mathbf{g}} \frac{\varphi}{g} \frac{1}{1 + \frac{x}{\xi}} \int_0^\infty dt \left[E_1\left(\frac{t}{\gamma^2\Psi_0^2 + \gamma^2\Psi_S^2 L}\right) - E_1\left(\frac{t}{\gamma^2\Psi_0^2}\right)\right] \left[\alpha^2 + \frac{1}{\beta^{\frac{1}{2}}} - \frac{1 + x^2 + t}{\beta^{\frac{3}{2}}} - \text{sign}(q)\frac{\alpha}{x}\left(1 - \frac{1 - x^2 + t}{\beta^{\frac{1}{2}}}\right)\right], \quad (20)$$

where $\beta = (1 + x^2 + t)^2 - 4x^2 t$.

It is easy to check that formula (20) passes into simpler formula (19) if the initial divergence of the beam is small ($\gamma^2\Psi_0^2 \ll 1$) and the crystal is thin ($\gamma^2\Psi_S^2 L \ll 1$).

THE EFFECT OF INTERFERENCE ON RADIATION POLARIZATION

To describe the polarization properties of the radiation, we revert to general formula (16) and expand the vector in the brackets of this formula in the unit vectors of polarization $\mathbf{e}_\perp = [\mathbf{n}, \mathbf{g}]/\sqrt{g^2 - (\mathbf{ng})^2}$ and $\mathbf{e}_\parallel = [\mathbf{n}, \mathbf{e}_\perp]$ (here, brackets mean the vector product). We will consider the polarization of collimated radiation without regard for the initial divergence and multiple scattering [conditions where formula (19) applies]. As before, the orientation dependence of the number of quanta emitted is given by formula (19), where the function T has the form

$$T = \frac{1}{1 + \frac{x_\parallel}{\xi}} \left[\frac{x_\perp}{1 + x^2}\mathbf{e}_\perp - \left(-\text{sign}(q)\alpha + \frac{x_\parallel}{1 + x^2}\right)\mathbf{e}_\parallel\right]^2, \quad (21)$$

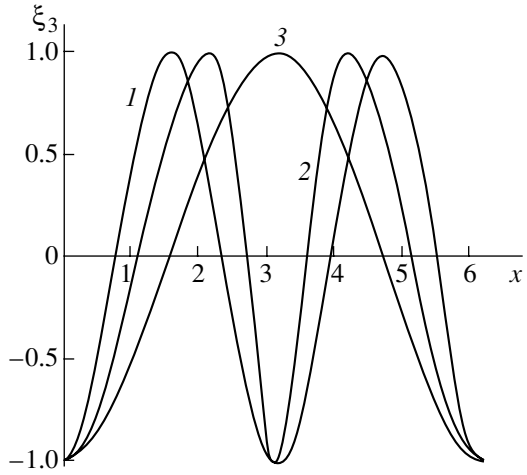

Fig. 4. Polarization asymmetry of the radiation emitted by electrons. λ = (*1*) 0, (*2*) 0.5, and (*3*) 1.

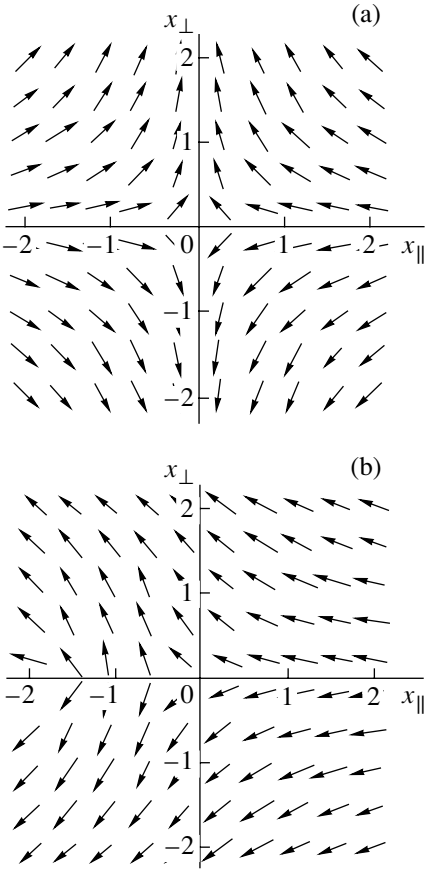

Fig. 5. Vector field of the polarization for the radiation emitted by electrons. α = (a) 0 and (b) 0.5.

where $x^2 = x_\perp^2 + x_\parallel^2$, $x_\perp = \gamma\Theta_\perp$, and $x_\parallel = \gamma(2\Theta' + \Theta_\parallel)$.

Expression (21) shows that the radiation is completely linearly polarized. The third Stokes coefficient ξ_3, usually found experimentally, is defined by the expression

$$\xi_3(x, \eta, \alpha) = \frac{\sin^2\eta - \left(\cos\eta - \mathrm{sgn}(q)\alpha\frac{1+x^2}{x}\right)^2}{\sin^2\eta + \left(\cos\eta - \mathrm{sgn}(q)\alpha\frac{1+x^2}{x}\right)}, \quad (22)$$

which follows from (21). Here, $x_\perp = x\sin\eta$ and $x_\parallel = x\cos\eta$.

According to (22), interference has an effect on the polarization through the single parameter

$$\lambda = \alpha\frac{1+x^2}{x}.$$

Curves $\xi_3(\eta)$ for emitting electrons at various λ are depicted in Fig. 4. It is seen that interference may greatly affect the polarization state.

Note that the vector in the brackets of (21) specifies the direction of the electromagnetic field of a quantum emitted, i.e., the direction of polarization. Figure 5 demonstrates the distribution of the vector field

$$\mathbf{e}(\mathbf{x}, \alpha) = \frac{\mathbf{e}_\perp x_\perp - \mathbf{e}_\parallel(x_\parallel - \mathrm{sgn}(q)\alpha(1+x^2))}{\sqrt{x_\perp^2 + (x_\parallel - \mathrm{sgn}(q)\alpha(1+x^2))^2}} \quad (23)$$

on the plane of the angular variables $x_\parallel$ and $x_\perp$. Interference markedly modifies the structure of the polarization vector field $\mathbf{e}(\mathbf{x}, \alpha)$ both for large x, where coherent bremsstrahlung dominates, and for $x \le 1$, where the amplitudes of bremsstrahlung and polarization bremsstrahlung may have the same order of magnitude.

CONCLUSION

From our analysis of X-ray emission due to relativistic electrons (positrons) moving at a small angle to a set of crystallographic planes, one can infer the following.

Under the conditions considered, the effective interference of both coherent and incoherent components of bremsstrahlung and polarization bremsstrahlung of a fast particle takes place.

The interference markedly modifies the spectral–angular distribution of the radiation. The modification depends on the sign of the charge of an emitting particle. A great increase in the radiation intensity (brightness) is a possibility in this case.

The interference drastically changes the angular dependence of the polarization of the resulting radiation.

ACKNOWLEDGMENTS

This work was partially supported by the STSU Foundation (grant no. 285) and by the Russian Foundation for Basic Research (grant no. 98-02-17238).

REFERENCES

1. M. L. Ter-Mikaelian, *High Energy Electromagnetic Processes in Condensed Media* (Wiley, New York, 1972).
2. V. G. Baryshevskiĭ and I. D. Feranchuk, Zh. Éksp. Teor. Fiz. **61**, 944 (1971) [Sov. Phys. JETP **34**, 502 (1972)].
3. G. M. Garibyan and Y. Shi, Zh. Éksp. Teor. Fiz. **61**, 930 (1971) [Sov. Phys. JETP **34**, 495 (1972)].
4. V. L. Kleiner, N. N. Nasonov, and A. G. Safronov, Phys. Status Solidi B **181**, 223 (1994).
5. S. V. Blazhevich, G. I. Bochek, V. I. Kulibaba, *et al.*, Phys. Lett. A **195**, 210 (1994).
6. Z. G. Pinsker, *Dynamic Scattering of X-rays in Crystals* (Nauka, Moscow, 1974; Springer-Verlag, Berlin, 1978).
7. L. D. Landau and E. M. Lifshitz, *The Classical Theory of Fields* (Nauka, Moscow, 1973; Pergamon, Oxford, 1975).
8. M. Ya. Amus'ya, I. M. Buĭmistrov, B. A. Zon, *et al.*, *Polarization Bremsstrahlung of Particles and Atoms* (Nauka, Moscow, 1978).
9. V. M. Buĭmistrov and L. I. Trakhtenberg, Zh. Éksp. Teor. Fiz. **69**, 108 (1975) [Sov. Phys. JETP **42**, 54 (1975)].
10. L. Landau and G. Rumer, Proc. R. Soc. London **166**, 213 (1938).
11. V. L. Lapko and N. N. Nasonov, Zh. Tekh. Fiz. **55** (1), 160 (1990) [Sov. Phys. Tech. Phys. **35**, 633 (1990)].
12. V. G. Baryshevsky and I. D. Feranchuk, J. Phys. (Paris) **44**, 913 (1983).
13. G. M. Garibian and C. Yang, Nucl. Instrum. Methods Phys. Res. A **248**, 29 (1986).
14. A. Caticha, Phys. Rev. B **45**, 9541 (1992).
15. N. N. Nasonov and A. G. Safronov, in *Proceedings of the International Symposium RREPS-93, Tomsk, 1993*, p. 113.

Translated by V. Isaakyan

Technical Physics, Vol. 46, No. 8, 2001, pp. 995–1000. Translated from Zhurnal Tekhnicheskoĭ Fiziki, Vol. 71, No. 8, 2001, pp. 66–71.

Scattering of CO_2 Laser Beam by a Plasma of Air Breakdown at Pressures of 1–300 torr

E. A. Meshalkin

Lebedev Institute of Physics, Russian Academy of Sciences, Leninskiĭ pr. 53, Moscow, 117924 Russia

Received July 31, 2000; in final form, January 23, 2001

Abstract—Results from experiments with a TEA CO_2 laser with an unstable cavity and a power of 10^7 W are presented. Laser radiation was focused by a lens with a focal length of 100 or 150 mm in air free of dust (grains larger than 0.1 μm were filtered out). The power and energy of radiation scattered within a central cone of an annular laser beam was recorded. The dependences of the threshold (for scattering) laser power and the scattered power on pressure were determined. The angular divergence of the collimated scattered beam was found to be 3.9 mrad, which was close to the divergence of the laser beam (2.5 mrad). The amplification of the scattered radiation pulse was performed. © *2001 MAIK "Nauka/Interperiodica".*

INTRODUCTION

It is well known [1–5] that the plasma produced by an optical breakdown in gas scatters laser radiation. Depending on the experimental conditions, the scattering may be attributed to the self-focusing of laser radiation in plasma [6–9], to reflection from the plasma boundaries [10], to refraction of the laser beam in plasma [11–13], or to Mie scattering by a small plasma object (PO) with a radius of $r_0 \sim \lambda$ [1, 14, 15]. The latter mechanism is dominant in the initial phase of the discharge at the laser beam intensities close to the breakdown threshold.

The scattered radiation is mainly concentrated within the solid angle Ω with the apex angle Θ_m, which is calculated from the beam propagation direction and depends on the gas pressure p [7, 13]. Scattering was observed within both the solid angle of laser beam and the inner solid angle of an annular focused beam [4, 5, 16]. The duration of the scattered pulse may be shorter than that of the laser pulse by one order of magnitude owing to both the threshold nature of scattering and the absorption of some of the laser energy in the plasma [2, 4, 5, 17, 18].

In this paper, we study the small-angle scattering of an annular CO_2 laser beam by a plasma produced by an optical breakdown in air at pressures of 1–300 torr.

EXPERIMENTAL SETUP

In our experiments (black diagram shown in Fig. 1), we used a TEA CO_2 laser ($\lambda = 10.6$ μm) with an unstable cavity. The magnification coefficient of the cavity was 1.7. The laser energy was measured with an IMO-2n *9* and VChD-2 *18* calorimeters. The shape of the laser pulses was monitored with FP-5 *8*, FP-1, and FP-0.5 photodetectors *18* and an S8-14 oscillograph with a transient-characteristic rise time of 7 ns.

The laser radiation was directed into a telescope formed by two antireflection meniscus germanium lenses *12*, *15* with focal lengths of $F_1 = 100$ mm and $F_2 = 150$ mm. The beam waist $D_1(F_1) = 3.8 \times 10^{-2}$ cm was located either in evacuated cell *2* or in air. The laser beam had a 40×40 mm cross section with a central aperture 25 mm in diameter. The laser beam power was attenuated by CaF_2 plates *7*. To avoid the direct propagation of laser radiation through the telescope, an opaque screen 25 mm in diameter was placed at the beam axis. After passing through the telescope, the laser beam was cut off by diaphragm *13* with a variable diameter of 1–22 mm. The parallel beam of scattered radiation, after passing through the telescope, was directed by lens *16* ($F = 200$ mm) onto the detector with a time resolution of 1 ns. When the beam divergence Θ_0 was measured with collecting mirror *16* ($F'_m = 5$ m), the radiation was focused onto diaphragm *17* and calorimeter *18*. Before reaching the cell, the value of Θ_0 (at a level of $1/e^2$) was 2.5 mrad.

Breakdown in atmospheric air *4* occurred spontaneously in the focal region of lens *12*. In experiments with a cell, breakdown was sometimes initiated [18] by laser plasma *3* arising at the end of a metal rod.

To amplify the scattered radiation pulses, we used another TE CO_2 laser operating in the four-pass or regeneration amplifier mode. In the latter case, the amplifier was equipped with an unstable cavity with a magnification coefficient of 2. The scattered pulse was introduced into the cavity with the help of a deflecting mirror (with a reflection coefficient of 45%), which was positioned outside the cavity and which directed the input pulse precisely toward the output beam of this

1063-7842/01/4608-0995$21.00 © 2001 MAIK "Nauka/Interperiodica"

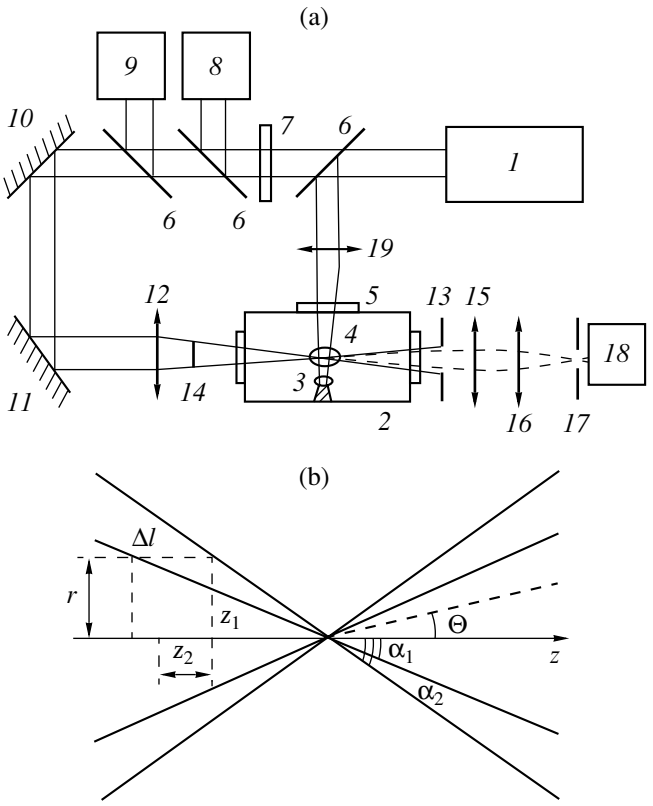

Fig. 1. (a) Experimental setup: (*1*) TEA CO_2 laser, (*2*) low-pressure cell, (*3*) plasma on a target for laser initiation of breakdown, (*4*) plasma of laser-induced air breakdown, (*5*) cell window, (*6*) laser-beam splitters, (*7*) CaF_2 absorbing plate, (*8*) photodetector, (*9*) calorimeter, (*10*, *11*) deflecting mirrors, (*12*) lens, (*13*) aperture, (*14*) screen, (*15*) lens, (*16*) lens or focusing mirror, (*17*) aperture, and (*18*) photodetector or calorimeter. (b) Geometric parameters characterizing the focused annular laser beam.

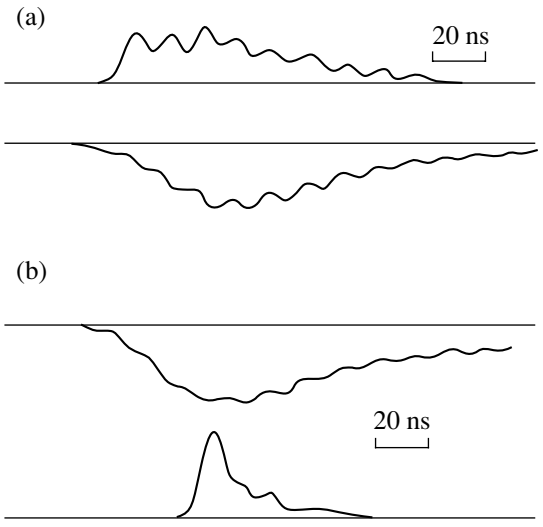

Fig. 2. Waveforms of the laser pulse power [(a) lower and (b) upper curves] and the scattered power [(a) upper curve (b) lower curve] for p = 70 torr.

laser. There were twice as many passes in this amplifier than in an amplifier with an aperture in the center of the mirror. When the driving signal was high enough, the reflection coefficient of the deflecting mirror could be decreased. The air filling the cell was cleaned of dust using a Petryanov filter, which filtered out grains larger than 0.1 μm.

EXPERIMENTAL RESULTS

In our experiments, scattered radiation was detected only when we visually observed a light burst from the laser plasma. When no burst occurred, no scattered signal was detected at a detector response level of 2 kW and a diaphragm diameter of D = 16 mm.

Within the air pressure range 0.7–300 torr, the duration of the leading edge of the scattered pulse τ_r (Fig. 2b) was determined by the rise time of the transition characteristic of the S8-14 oscillograph (7 ns), and the characteristic time of exponential decay was 7–20 ns. The visual observation of this pulse on the screen of the S1-75 oscillograph showed that the leading edge of most pulses was no longer than 2 ns. The shape and duration of the signal were independent of the diameter of diaphragm *13*. At the trailing edge, we sometimes observed oscillations caused by variations in the laser power.

At atmospheric pressure, the scattered pulse also had a rapidly increasing leading edge, but the pulse duration at half-maximum increased to 50 ns for F_1 = 100 and 250 mm (the beam was focused by a spherical mirror in air). The energy of this pulse (1.3 mJ for F_1 = 100 mm) was 3 time lower than the total energy scattered into the central region of the laser beam (Fig. 3b). The energy scattered into the outer region of the beam at angles greater than the given angle Θ was independent of F_1. The scattered energy was concentrated within an angle of $\Theta_m = 21°$. These measurements were performed with the help of an opaque screen with a variable diameter replacing diaphragm *13* and intercepting the laser beam.

The measurements of the angular divergence Θ_{ds} of the scattered beam that had passed through diaphragm *13* and been collimated by lens *15* showed that $\Theta_{ds} > 16$ mrad. This divergence corresponds to a source of scattered radiation whose diameter is no more than 2.4 mm; i.e., the scattered pulse (Fig. 2a) has a low-power tail containing 70% of the energy and arising due to scattering from the expanding plasma.

The pressure dependence (Fig. 4) of the laser beam power P_0 measured at the instant when the scattered power reaches its maximum is close to the curve describing the threshold power for breakdown in filtered air [19, 20]. The delay of the scattered pulse (at a level of 0.1 of the maximum value of P_0) from the beginning of the laser pulse remained constant (τ_d = 30 ns).

At $50 \le p \le 300$ torr, breakdown was unstable; in this case, we had $P_0 \sim p^{-0.9}$ [21]. The plasma object was initiated by dust grains present in air [15]. In the pressure range $25 < p \le 50$ torr, we observed the dependence $P_0 \sim S_b/\nu_m \sim p^{-1.8}$, where S_b is the area of the cross section of the laser beam containing an initiating grain and ν_m is the frequency of electron–molecule collisions. In this case, the pressure at which the dependence $P_0(p)$ undergoes a modification varies in the range 35–50 torr upon renewing the gas in the chamber. At $p = 20$ torr, scattering is not observed for each laser pulse in spite of the presence of light bursts. In the pressure range $4 \le p \le 20$ torr, primary electrons were produced by UV plasma radiation (the initiating laser beam did not pass through the waist of the main beam). The delay in scattering could be kept constant (30 ns) up to $p = 9$ torr. At lower pressures, the value of τ_d increased from 50 to 90 ns. At $p < 4$ torr, the scattering was observed only when the igniting laser beam intersected the main beam, so that the plasma moving from the target approached the waist of the main beam and could intersect it. The value of τ_d was 50–60 ns. The scattered power decreased below the detector response level at $p = 0.2$ torr.

The plasma radiation measured in the spectral region 285–530 nm at right angles to the laser beam axis within a solid angle of $\Omega \sim 0.26$ sr at $p = 70$ torr has an exponentially growing front (Fig. 5), associated with an avalanche growth of the electron density around the initiating center. Then the exponential growth transforms into the dependence t^3, associated with the three-dimensional expansion of the PO [15].

The divergence of the scattered light measured at the same pressure (Fig. 6) was equal to $\Theta = 3.9$ mrad. For the laser beam that passed through the telescope, it was equal to $\Theta_{db} = 2.5$ mrad (at a level of $1/e^2$). The energy of the collimated scattered beam (0.8 mJ) was equal to the energy of the scattered pulse that passed through diaphragm *13* (Fig. 2b).

Within the range $1.8 < \Theta < 3.6$ mrad ($0.9 < D < 1.8$ cm), the dependence $E(\Theta_d)$ (Fig. 6) can be approximated by the function $E \sim \Theta_d$; i.e., in this range of angles, for the energy scattered within the solid angle $d\Omega$, we have $dE/d\Omega \sim \Theta^{-1}$. The optical system (Fig. 1a) consisting of lens *15* and spherical mirror *16* with a focal length of $F' = 5$ m forms a magnified ($m = 33$) image of the scattering PO in the plane of diaphragm *17* with the radius $R = D/2$. Hence, the dependence of the luminosity of the plasma that scatters light within the focal region of lens *12* must take the form $M_s \sim r^{-1}$, where r is the distance from the beam axis in the PO plane (Fig. 1b). The maximum estimate of the radial displacement d_m of the PO is equal to $d_m = \Theta_{ds} F'_m/m = 6 \times 10^{-2}$ cm; i.e., it is larger than the diameter of the focal region of lens *12*, which is equal to 3.8×10^{-2} cm. Consequently, scattering centers arise at distances from the center of the laser beam waist up to $Z_m = d_m/2\tan\alpha_1 = 2.4$ mm, so that it is necessary to take into account the defocusing effect, which increases the diameter of the scattering circle in the plane of diaphragm *17*. Calculations with allowance for defocusing and spherical aberration showed that, with a maximum diaphragm diameter of $D = 25$ mm, the measuring system could detect scattering centers located at distances up to 5×10^{-2} cm from the Z axis. In this case, the magnitude of defocusing reached 0.4 cm, and the system resolution in the PO plane was no worse than 3×10^{-3} cm for distances from the Z axis shorter than 3×10^{-2} cm.

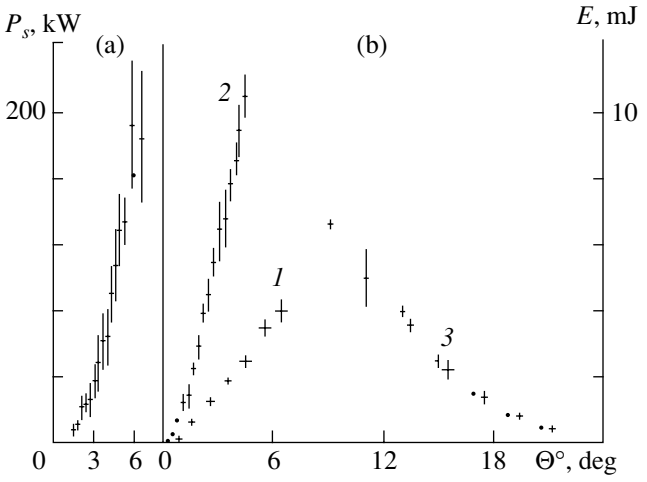

Fig. 3. (a) Scattered power P_s within the scattering angle Θ ($p = 5.4$ torr); (b) the scattered energy E within the scattering angle Θ for F_1 = (*1*, +) 100 and (*2*, ·) 150 mm and (*3*) the laser energy scattered at angles wider than the angle Θ, but narrower than 29° for F_1 = 100 and 150 mm (750 torr).

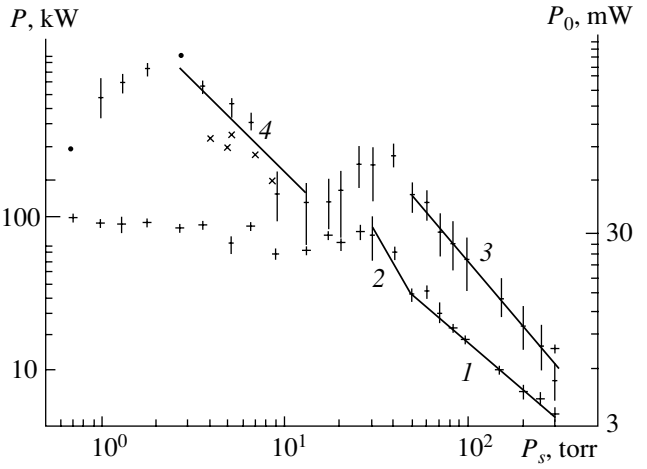

Fig. 4. Pressure dependences of the threshold power P_0 for the initiation of scattering of laser radiation (+): (*1*) $p^{-0.9}$ and (*2*) $p^{-1.8}$; the scattered power P (·): (*3*) $p^{-1.2}$ and (*4*) p^{-1}; and the scattered power P_s (UV breakdown initiation) (×).

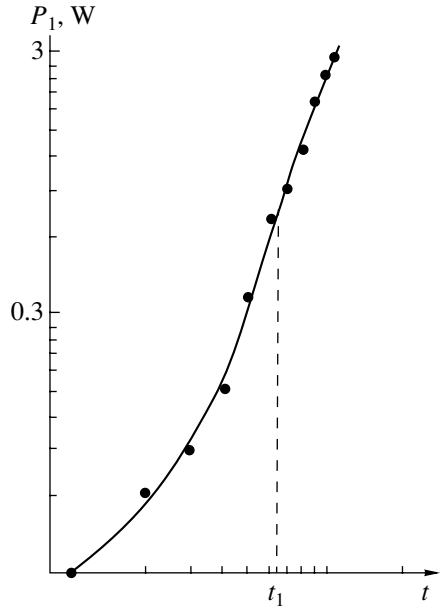

Fig. 5. The leading edge of the pulse of intrinsic radiation from a plasma produced by a laser breakdown in air: P_1 is the radiation power, and t is time (1 ns/division). The solid curve shows the exponential dependence on time, and the dashed line ($t > t_1$) shows the dependence t^3.

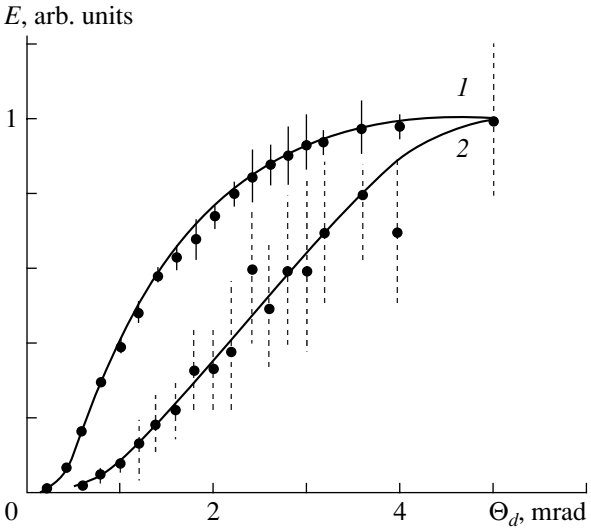

Fig. 6. Energy E of (*1*) laser and (*2*) scattered radiation within the divergence angle Θ_d for p = 70 torr.

The presence of a single short scattered pulse corresponds to scattering by a single PO. Therefore, let us consider the scattering of laser radiation by a single PO of radius r_0 arising at an arbitrary point near the focal region of lens *12*.

The maximum power scattered in a single pulse is equal to

$$P = I_b(r, Z_2)\eta\pi r_0^2, \quad (1)$$

where $\sigma_0 = \eta\pi r_0^2$ is the scattering cross section of the plasma object and η is the scattering efficiency.

Since each point in the dependences presented in Figs. 4 and 6 is an average over a series of N_0 = 10 pulses, the average scattered power is equal to

$$P_1 = \frac{1}{N_0}\int_0^{N_0} PdN = \frac{2\eta\pi r_0^2}{V_f}\int_0^{S_m(Z_1+\Delta l)}\int_{Z_1} I_b(r, Z_2)dZ_2dS. \quad (2)$$

Here, $dS = 2\pi rdr$ is the element of the area of the laser-beam cross section; $dN = ndSdZ_2$ is the differential of the number of pulses; $n = N_0/V_f$ is the spatial density of the realizations of breakdowns in a series of experiments; V_f is the volume of the focal region of the lens, determined by the condition $I_b \geq I_{th}$ (where I_{th} is the threshold intensity for the breakdown of the gas for a time delay of τ_d = 30 ns after initiation); and S_m is the area of the laser-beam cross section orthogonal to the Z axis and containing the breakdown region most distant from the axis.

The average luminosity of the volume V_f in a series of N_0 pulses can be written in the form

$$M = \xi\frac{dP_1}{dS}, \quad (3)$$

where $\xi = P_s/P_1$ is the fraction of the average power P_1 received by the measuring system in the solid angle Ω_0 resting on diaphragm *13*.

Then, the illuminance E' of the image in the plane of diaphragm *17* takes the form

$$E' = \frac{dP'}{dS'} = \frac{\tau M}{m^2}. \quad (4)$$

Taking into account that all the scattering centers arising at a distance r from the Z axis form a ring of radius R in the image produced by the optical system, it is necessary to integrate expression (2) over Z_2 (Fig. 1b). The laser radiation is absorbed by an ionization wave (at $t > \tau_d$) propagating from the PO [22]. Consequently, according to experiments, the intensity of laser radiation scattered by a PO can be written as

$$I(r, Z_2) = I_0(r, Z_2)e^{-t/\tau_s},$$

where τ_s is the scattered-pulse duration.

We will assume that the intensity I_0 in an arbitrary cross section $S_b = P_0/I_b$ orthogonal to the mean rays of the focused laser beam is constant. Then, we can write

$$I_0 = \frac{P_0}{S_b} = \frac{P_0}{(Z_1 + Z_2)^2} \times \frac{\cos\alpha}{\pi\tan^2\alpha_2\left[1 - \left(1 - \frac{2\sin(\Delta\alpha/2)}{\cos\alpha}\right)^2\right]} = \frac{P_0\chi}{(Z_1 + Z_2)^2}, \quad (5)$$

where P_0 is the laser radiation power at the instant of breakdown ($t = \tau_3$), $\Delta\alpha = \alpha_2 - \alpha_1$, $\alpha = (\alpha_1 + \alpha_2)/2$, and $Z_1 = r/\tan\alpha_2$.

Integrating expression (2) over Z_2, we obtain

$$\int_{Z_1}^{Z_1+\Delta l} I_0(r, Z_2)dZ_2 = \frac{\chi P_0 \Delta l}{Z_1(Z_1+\Delta l)} = \frac{\chi P_0}{r}(\tan\alpha_2 - \tan\alpha_1) = \gamma\frac{P_0}{r}, \quad (6)$$

where $\gamma = 4.4$.

From Eqs. (3), (4), and (6), we have

$$E' = \frac{2\tau\xi\gamma\eta\pi r_0^2}{m^2 V_f}\frac{P_0}{r}e^{-t/\tau_s}, \quad (7)$$

where $r = D/2m = F'_m\Theta_d/2m$ and Θ_d is the divergence of the light beam formed by lens *15*.

Integrating expression (7) over $dS' = (\pi/4)F'^2_m d(\Theta_d^2)$, we arrive at the following dependence of the scattered energy E on D (for $r > d_w/2$, i.e., for $\Theta_d > 1.8 \times 10^{-3}$ rad):

$$E = \frac{2\pi^2\tau\gamma}{mV_f}\xi\eta r_0^2 P_0\tau_s D, \quad (8)$$

which corresponds to the experiment (Fig. 6). For $p =$ 70 torr, $\Delta E = 1.4 \times 10^{-4}$ J (Fig. 6), $m = 33$, $\tau = 0.7$ s, $\tau_s = 10^{-8}$ s, $P_0 = 1.1 \times 10^7$ W, $\Delta D = 0.6$ cm, and $V_f = 2 \times 10^{-4}$ cm^3 (calculated from the value d_m), we obtain from expression (8) that $\xi\eta r_0^2 = 2.3 \times 10^{-7}$ cm^2; i.e., for $\xi \sim$ 0.1 (Fig. 3) and $\eta = 0.1$–1, we have $r_0 \sim 50$–15 μm.

For small beam divergences $\Theta_d < 1.8$ mrad $= \Theta_w$ ($p = 70$ torr), we have $E \sim \Theta_d^2$. This case corresponds to the scattering from the focal region because $2r = \Theta_w F'_m/m = 2.7 \times 10^{-2}$ cm $\sim 2r_w = d_w$.

By analogy to the derivation of formula (8), we can show that this dependence corresponds to the case of a constant intensity of laser radiation in the focal region of lens *12*,

$$E = \frac{\pi^2\tau}{4m^2 S_w^2}\xi\eta r_0^2 P_0\tau_s D^2, \quad (9)$$

where S_w is the area of the cross section of the focal region.

For $E = 1.2 \times 10^{-4}$ J (Fig. 6), $D = 0.9$ cm, $P_0 = 1.1 \times 10^7$ W, and $\tau_s = 10^{-8}$ s, we obtain $\xi\eta r_0^2 = 3.0 \times 10^{-7}$ cm^2 which coincides with that given by formula (8). This means that the values of ξ and r_0 are independent of the position of the PO in the laser beam; i.e., $r_0 < r_w$ and $\Theta_D \ll \Theta_m$, where Θ_D is half of the angle at which diaphragm *13* is seen from the focal region.

The results of the measurements of the value P_s were interpreted using formulas (1), (2), and (6) and the equation

$$\frac{dn_e}{dt} = \nu_i n_e,$$

where n_e is the electron density, $\nu_i = B\nu_m I_b$ is the rate of electron-impact ionization of molecules in the laser field, B is a constant factor under our experimental conditions, and ν_m is the frequency of electron–molecule collisions.

From this equation, assuming a linear increase in the laser beam power with time, $P_0 = b_1 t$, we obtain the relation

$$\frac{\nu_m P_0(\tau_d)\tau_d}{S_b} = b, \quad (10)$$

where $b = 2B^{-1}\ln(n_1/n_0)$; n_0 and n_1 are the initial and final electron densities in the PO.

The value of ξ is related to r_0 by the dependence $\xi \sim (\Theta_D/\Theta_{diffr})^2 \sim (r_0/\lambda)^2$, where $\Theta_{diffr} \sim \lambda/r_0$ is the effective angle within which the radiation power is scattered.

The measurements of P_s at $p = 69$ and 39 torr for $F_1 = 100$ and 150 mm showed that the value of $\xi\eta r_0^2$ is independent of S_b, which can vary as p, F_1, and P_0 vary.

At $p = 39$ torr, when passing from $F_1 = 100$ mm to $F_1 = 150$ mm at a constant value of P_0, the values of τ_d and S_b do not change, whereas the value of $\xi\eta r_0^2$ decreases by a factor of 4, which can be explained as a decrease in r_0 by a factor of ~1.4 assuming that η is constant. At $p = 69$ torr, the fall time of the pulse increases by a factor of 1.6 as F_1 increases. The fact that r_0 decreases while the average intensity remains constant and the laser focusing angle decreases can be attributed to a decrease in the light intensity in maximums that are present in the near and distant zones of the laser beam.

When passing from $p = 69$ torr to $p = 39$ torr at $F_1 =$ 150 nm and a at constant value of P_0, P_s decreases by 40% (unlike when $F_1 = 100$ mm), which is due to an insufficient increase (by a factor of 1.5) in the average intensity of the laser beam. A similar experiment with $F_1 = 100$ mm, in which the variation in $I_b(p)$ nearly corresponded to the variation in $I_{th}(p)$, showed that the value of $\xi\eta r_0^2$ was independent of the gas pressure. The amplitude of oscillations at the trailing edge of the scattering pulse increases substantially, possibly because the transparency of the ionization wave front increases [23]. At $p \geq 50$ torr, a similar inference follows from the dependence $P_p(p)$ (Fig. 4): since $\xi\eta r_0^2 \sim p^{-0.3}$, we have $r_0 \sim p^{-0.08}$; i.e., the PO radius is independent of the air

pressure and is determined by the size of the perturbations in the laser beam intensity.

The increase in the scattered power in the pressure range $2.7 < p < 13$ torr is observed for two methods of breakdown initiation and obeys the law $P_s \sim p^{-1}$. In accordance with this dependence, the PO radius increases as $r_0 \sim p^{-1/4}$. Since no dependence of r_0 on τ_d was observed, the PO expansion time was estimated as $\Delta t \sim \tau_r$, which is considerably shorter than the ambipolar diffusion time of the PO plasma. Therefore, the PO expansion at $p < 13$ torr may be attributed to the propagation of a shock wave from the PO: in accordance with the point-explosion theory [24], we have $r_0 \sim p^{-1/5}t^{2/5}$.

This assumption is also supported by the dependence $P_s(t) \sim t^{1.6}$ observed at $p = 15$ torr for some pulses with a front duration substantially exceeding the rise time of the oscillograph transient characteristic. This dependence coincides with the predictions of the point-explosion theory, because $P_s \sim r_0^4$.

The angular (over Θ) distribution of the scattered power averaged over six pulses is described by the dependence $P_s(\Theta) \sim \Theta^2$ (Fig. 3a).

A rapid decrease in the detected scattered power for $p < 2.7$ torr may be explained either by the further contraction of the scattering cone toward the laser beam propagation direction because of the increase in r_0 or by the decrease in the size of the initial breakdown region and the energy released in it (i.e., the decrease in r_0).

A 10- to 20-ns light pulse scattered by the laser plasma was amplified in a four-pass amplifier (with a working-mixture pressure of 0.6 atm) to a peak power of ~600 kW. For amplification, we also used a laser with an unstable cavity The duration of the amplified pulse was equal to that of the input signal.

In summary, we have shown that the scattered power increases as the air pressure decreases (from 300 to 40 torr), primarily, because the threshold intensity for laser breakdown increases. The increase in P_s at $2.7 < p < 13$ torr, is apparently associated with the propagation of a shock wave from the PO (i.e., with the increase in the PO radius). The scattered radiation was collimated into a beam with an angular divergence (averaged over 10 pulses) of 3.9 mrad, which was limited by variations in the PO position inside the lens focal region, and then was amplified.

REFERENCES

1. M. Young, M. Hercher, and C.-Y. Wu, J. Appl. Phys. **37**, 4938 (1966).
2. V. V. Korobkin and A. J. Alcock, Phys. Rev. Lett. **21**, 1433 (1968).
3. R. G. Tomlinson, IEEE J. Quantum Electron. **QE-5**, 591 (1969).
4. L. C. Johnson and T. K. Chu, Phys. Rev. Lett. **32**, 517 (1974).
5. D. R. Cohn, G. J. Raff, R. L. Brooks, *et al.*, Phys. Lett. A **49A**, 95 (1974).
6. A. J. Alcock, C. DeMichelis, V. V. Korobkin, *et al.*, Appl. Phys. Lett. **14** (5), 145 (1969).
7. A. J. Alcock, C. DeMichelis, and M. C. Richardson, IEEE J. Quantum Electron. **QE-6**, 622 (1970).
8. J. S. Bakos, I. B. Foldes, and Z. Sorlei, J. Appl. Phys. **52**, 627 (1981).
9. M. Luochesi, F. Cornolti, A. Giulietti, *et al.*, Nuovo Cimento Soc. Ital. Fis. B **82B** (1), 111 (1984).
10. N. Ahmad, B. C. Gale, and M. H. Key, J. Phys. B **2**, 403 (1969).
11. G. A. Askar'yan and M. A. Mukhamadzhanov, Pis'ma Zh. Éksp. Teor. Fiz. **33**, 48 (1981) [JETP Lett. **33**, 44 (1981)].
12. D. Giulietti, Opt. Commun. **68** (6), 399 (1988).
13. I. A. Bufetov, G. A. Bufetova, and V. B. Fedorov, Kvantovaya Élektron. (Moscow) **21**, 1177 (1994).
14. C. C. Wang and L. I. Davis, Phys. Rev. Lett. **26**, 822 (1971).
15. Yu. D. Kopytin, Yu. M. Sorokin, A. M. Skripkin, *et al.*, *Optical Discharges in Aerosols* (Nauka, Novosibirsk, 1990).
16. M. Autric, J. P. Caressa, D. Dufresne, and Ph. Bournot, AIAA Pap., No. 79-0250 (1979).
17. L. B. Glebov, O. M. Efimov, G. T. Petrovskiĭ, *et al.*, Kvantovaya Élektron. (Moscow) **12**, 2077 (1985).
18. E. Yablonovitch, Phys. Rev. A **10**, 1888 (1974).
19. D. C. Smith and R. J. Brown, J. Appl. Phys. **46**, 1146 (1975); *Principles of Laser Plasmas*, Ed. by G. Bekefi (Wiley, New York, 1976; Énergoizdat, Moscow, 1982).
20. S. V. Zakharchenko, L. P. Semenov, and G. A. Sintyurin, Kvantovaya Élektron. (Moscow) **13**, 1040 (1986).
21. Yu. P. Raizer, *Laser-Induced Discharge Phenomena* (Nauka, Moscow, 1974; Consultants Bureau, New York, 1977).
22. D. E. Lencioni and L. G. Pettingill, J. Appl. Phys. **48**, 1848 (1977).
23. V. N. Anisimov, V. A. Vorob'ev, V. G. Grishina, *et al.*, Kvantovaya Élektron. (Moscow) **22**, 900 (1995).
24. L. I. Sedov, *Similarity and Dimensionality Methods in Mechanics* (Nauka, Moscow, 1977).

Translated by N. Larionova